Probing Inhibitor Binding Sites in the Gastric H/K-ATPase

Jude Anthony Watts

Thesis submitted to the Board of the Faculty of Biological Sciences in partial fulfilment of the requirements for the Degree of Doctor of Philosophy at the University of Oxford

St Hugh's College, Oxford

Trinity, 2001

ABSTRACT

The H/K-ATPase, a 150 kDa αβ glycosylated membrane-bound ion-transporter, forms the last stage of acid secretion by pumping protons into gastric glands against a pH gradient of units. As such, the gastric H/K-ATPase is an important therapeutic target for peptic ulcer disease which can be treated with a number of highly specific reversible inhibitors including substituted imidazo[1,2-*a*]pyridines. Here, a number of novel substituted imidazo[1,2-*a*]pyridines has been synthesized carrying NMR-visible isotopes for use in structural studies in the solid and at their site of action. Their biochemical properties have been characterized *in vitro* to assess their suitability for ^{2}H NMR and rotational echo double resonance (REDOR) NMR in the solid state. Broad line solid state ^{2}H NMR experiments have been performed on a range of these inhibitors to examine the dynamics of the deuterated functional groups in the ligand binding pocket and to reveal information about the binding mechanism of this class of inhibitors. Precise ^{13}C-^{19}F interatomic distances have been measured using REDOR NMR to determine the 3-dimensional structure of these compounds within their high-affinity binding sites in an intact, native membrane environment. The data presented analysed, for the first time, in structural models of these pharmacologically important inhibitors in theirs sites of action. The biochemical characterization, ^{2}H and REDOR NMR studies have been combined with a novel reappraisal of the transmembrane topology of the H/K-ATPase based on the recent high-resolution structure of the sarcoplasmic endoplasmic Ca-ATPase (Toyoshima *et al*, (2000) *Nature* **405**: 647-655) to suggest models of these inhibitors in the H/K-ATPase binding pocket. Additionally, the orientation of an analogue of acetylcholine, the agonist of the nicotinic acetylcholine receptor, has been determined with respect to the membrane normal in macroscopically oriented enriched membranes. The structure of this protein, a 280 kDa membrane integral $\alpha_2\beta\delta\gamma$ multimer, has been determined to medium resolution (Miyasawa *et al*, (1999) *J. Mol. Biol.* **288(4)**: 765-86) and the orientation of the ligand has been correlated to the putative binding pocket in the acetylcholine receptor. The success of this experiment has demonstrated that it is possible to determine the orientation of ligands in the binding sites of large membrane proteins and that this approach might be adopted to refine the models of substituted imidazo[1,2-*a*]pyridines in the H/K-ATPase for which there is currently no orientational information.

Work in this thesis has appeared in:

Gröbner, G., Taylor, A., Williamson, P.T.F., Choi, G., Glaubitz, C., Watts, J.A., de Grip, W.J. & Watts, A. () Macroscopic orientation of natural and model membranes for structural studies. *Analytical Biochemistry*, 1997. **254**: p. 132-136.

Watts, A., Burnett, I.J., Glaubitz, C.,Gröbner, G., Middleton, D.A., Spooner, P.J.R., Watts, J.A. & Williamson, P.T.F. Membrane protein structure determination by solid state NMR. *Natural Product Reports*. 1999, **16**: p. 419-423.

Williamson, P.T.F., Watts, J.A., Addona, G.H. Miller, K.W. and Watts, A. Dynamics and orientation of $N^{+}(CD_3)_3$-bromoacetylcholine bound to its binding site on the nicotinic acetylcholine receptor. *PNAS*, 2001. **98**: p. 2346-2351.

Watts, J.A., Watts, A., and Middleton, D.A., A model of reversible inhibitors in the gastric H^{+}/K^{+}-ATPase binding site determined by REDOR NMR. *J. Biol. Chem.* 2001. **276(46)**: p. 43197-43204

TABLE OF CONTENTS

Chapter 1
Biological Membranes 1
Characteristics of Biological Membranes 1
The Importance of the Proteins in Biological Membranes 4
The Structure and Arrangement of Membrane Components 6
Basic Principles of Solid State NMR 14
Biological membranes as targets in the therapy of disease 18
Introduction 18
Gastroesophegael Reflux Disease and Gastric Ulcer Disease 19
Regulation of Acid Secretion 23
The Gastric H/K-ATPase 25
Inhibition of the gastric proton pump 30
Irreversible Inhibition 30
Reversible Inhibition 31
Aims of the Thesis 36

Chapter 2
Introduction 38
Aims of This Study 41
Materials and Methods 43
Enrichment of Porcine Gastric H/K-ATPase Membranes 43
Characterisation of Enriched Porcine Gastric H/K-ATPase Membranes 44
Determination of Protein Composition 44
Determination of Protein Concentration 44
Determination of H/K-ATPase Activity 45
Determination of Inhibitor Activity 45
Preparation of Substituted Imidazo[1,2-a]pyridines 46

Synthesis of 2-methyl,8-(phenylmethoxy)imidazo[1,2-a]pyridine (MMPIP) (R1 = H): Reaction 1 50

Synthesis of 2,3 Dimethyl,8-(phenylmethoxy)imidazo[1,2-a]pyridine (DMPIP) (R1 = CH_3): Reaction 1 50

Synthesis of 2-methylimidazo[1,2-a]pyridin-8-ol (R1=H) and 2,3-dimethylimidazo[1,2-a]pyridin-8-ol (R1=CH_3): Reaction 2 51

Synthesis of 8-aryl substituted imidazopyridines: Reaction 3a..... 52

Synthesis of 8-acyl substituted imidazopyridines: Reaction 3b 53

Synthesis of N-methylated substituted imidazopyridines: Reactions 4a and 4b 53

Results 54

Enrichment of Porcine Gastric H/K-ATPase Membranes..... 54

Determination of inhibitory activity of substituted imidazopyridines 57

C8 Aryl analogues of SCH28080..... 59

R2-R6 substitututions: the effet of fluorination on activity..... 61

C8- acyl analogues of SCH28080 61

Discussion..... 65

Conclusions 79

Chapter 3

Introduction 80

The Deuterium NMR Spectrum 82

Aims of this study 87

Materials and Methods..... 88

Synthesis of TEMPO-ITC-labelled Substituted Imidazo[1,2-*a*]pyridines..... 88

Generation of 3-amino-2-methyl-8-(phenylmethoxy)imidazo[1,2-a]pyridine and labelling with TEMPO-ITC 88

Generation of 2,3-dimethylimidazo[1,2-a]pyridine and labelling with TEMPO-ITC..... 90

Synthesis of Deuterated Substituted Imidazo[1,2-*a*]pyridines 91

Preparation of GI Membranes for NMR 92

Preparation of Gastric Membrane Lipids..... 92

Addition of Inhibitors to Membranes and Lipids..... 93

Broadline Deuterium NMR Measurements 94
Data analysis 94
Results and Discussion..... 95
Dynamics of d_3-Substituted Imidazopyridines in the Gastric Membrane 95
Gastric H/K-ATPase Membranes Labelled with d_3-TM2FPIP... 102
Gastric H/K-ATPase Membranes Labeled with d_7-TMPIP 104
Gastric H/K-ATPase Membranes Labelled with d_3-DMPIP..... 107
Gastric H/K-ATPase Membranes Labelled with d_3-TMTFBIP.. 109
Gastric Membranes Labelled with d_3-TMCHIP 112
Conclusions 117

Chapter 4
Introduction 120
Rotational Echo Double Resonance (REDOR) NMR 124
Aims of this study 129
Materials and Methods..... 131
Synthesis of N-$^{13}CH_3$ Labelled Substituted Imidazo[1,2-a]pyridines 131
Sample Preparation for NMR 131
REDOR NMR Experiments 132
Results and Discussion..... 133
Structural Analysis of Solid Fluorinated SIPs by REDOR NMR 133
Structural Analysis of the H/K-ATPase-Inhibitor Complex by REDOR NMR..... 137
Conclusions 146

Chapter 5
Introduction 148
Aims of this study 150
Methods 150
The Binding Site of SCH28080..... 151
Residues that define the binding site of SCH28080 151

The High Resolution Structure of the Sarcoplasmic Endoreticular Ca-ATPase as a Template for the H/K-ATPase 160

Models of Substituted Imidazo[1,2-*a*]pyridines at their Binding Sites in the Gastric H/K-ATPase 171

Conclusions 176

Chapter 6

Introduction 177

The Nicotinic Acetylcholine Receptor (AChR) 178

Information from the Deuterium Spectrum 180

Information from the static ^{31}P NMR spectrum 184

Aims of this study 187

Materials and Methods 188

Synthesis of Bromoacetylcholine bromide-d_9 (BrAChBr-d_9) 188

Purification and Labelling of Enriched Nicotinic Acetylcholine Receptor Membranes 188

Orientation of Enriched Nicotinic Acetylcholine Receptor Membranes 189

Static ^{31}P and ^{2}H NMR Spectroscopy 190

Lineshape Simulations 190

Results and Discussion 192

Dynamics of Bromoacetylcholine-d_9 Bromide Bound in the Nicotinic Acetylcholine Receptor 192

Acetylcholine Receptor-Enriched Membranes labelled with Bromoacetlycholine bromide-d_9 194

Static ^{31}P NMR of Oriented AChR-Enriched Native Membranes 197

Static ^{2}H NMR of Bromoacetylcholine Bromide-d_9 in Orientated Nicotinic Acetylcholine Receptor Enriched Membranes 199

Conclusions 203

Chapter 7

Synthesis and Functional Characterisation of Reversible Inhibitors of the Gastric H/K-ATPase 207

^{2}H Solid State NMR of Inhibitors of the Gastric H/K-ATPase 208

^{13}C-^{19}F REDOR NMR Studies of the Conformation of Substituted Imidazo[1,2-*a*]pyridines in H/K-ATPase Enriched Membranes..... 210

A Model of TMPFPIP at its Binding Site in the Gastric H/K-ATPase 211

Dynamic and Structural Information from Macroscopic Orientation of Native Membrane Samples..... 212

ACKNOWLEDGMENTS

This work was supported by the Biotechnology and Biological Sciences Research Council.

There are many people that have provided helped, supported, and advised me during the course of this thesis. As an undergraduate and then post-graduate, I have been associated with Professor Anthony Watts in one guise or form for the past 8 years. Professor Watts' support has been fundamental during this time, whether it has been for a novel and unpredictable approach to an experimental problem that I might have suggested, for encouraging advice and critical appraisal of my work even in the darkest hours after a reaction had failed into an oily goo, or simply for a fiver to buy lunch when the moths were living in my wallet. I would like to express my gratitude especially for his assistance and tolerance in developing my career at the Bench both scientific and otherwise. Not all supervisors would be quite so generous with their time and their resources. I would like to thank Dr. David Middleton at UMIST for his encouragement and direction throughout the project. He has patiently explained (again and again) various of the NMR concepts until some of them found root in this biochemist's stony mind. His help with the simulation of the NMR spectra and possible choice of synthetic routes has been particularly appreciated as has his reviewing of this thesis and the helpful suggestions he has peppered on the pages of the draft documents. In true cryptic acknowledgement: *The Yorkshire cowboy heard sheep expressed gratitude (5-3)*.

For his help and accommodation at his lab, I would like to thank Prof. Keith Miller of Harvard Medical School for permitting me to run riot with his equipment early in my research career and for his generous supply of protein.

And so to the Lab and beyond, many of whom have moved on to other pastures but whose presence still resonates in the benches and the bars of Oxford. For their chemical assistance, technical know-how and often programming wizardry, I would like to thank Drs. Boyan Bonev, Ian Burnett, Stephan Grage, Richard Kemp-Harper, Paul Spooner, Rene Verel and Phil Williamson. Phil is especially acknowledged for his help with the work on the acetylcholine receptor. Thanks are extended to Dr. Clemens Glaubitz for the "Discussions" and Stick Figure Death Theatre; to Dr. Gerhard Grobner, whose quotations are lab. legend and whose pate-coleslaw baguettes were infamous; to James and Jonny being such fine sports when they were sport (their collection of stars would distress an Astronomer Royal); to Scott for his rowing anecdotes and crème brulee; to Mark, for doing all the hard work, enjoying it and having to endure late-night food stops after RAL; to Zareen, for injecting a little spark of craziness into the lab.; to Pete, whose scrimper's tips and bicycle expertise have saved me on many and various occasions; to Liz, without whom *nothing* would be done – *ever*; and to everyone else who has made the working in the lab such a peculiarly enjoyable experience. The stamina for this work has come from several sources, most of them seen in double. Thanks George and Steve and Huw and Andy: the next round is on me, even the lemonade.

My parents have always been there, encouraging me, tutting at the strange work hours and showing polite enthusiasm for the bizarre experiments and their outcomes. Thank-you for the providing the perspective and love.

Thank-you Kat for your love – you're a star somewhere near Delphinus. *Laudate Dominum!*

ABBREVIATIONS AND SYMBOLS

ADP, ATP	Adenosine diphosphate, adenosine triphosphate
ACh	Acetylcholine
AChR	Nicotinic acetylcholine receptor
BrAChBr-*d_9*	Bromoacetylcholine bromide-d9
B_0	Static magnetic field
CP MAS	Cross polarization magic angle spinning
DCCD	Dicyclohexylcarbodiimide
DMPIP	2,3-dimethyl-8-(phenylmethoxy)imidazo[1,2-a]pyridinium iodide
DDF	p-(dimethylamin)-benzenediazonium fluoroborate
DFP	Di-isopropylfluorophsophate
$\Delta\upsilon_Q$	Quadrupole splitting
$\Delta\sigma$	Shielding anisotropy
EDTA	Ethylenediamine tetraacetic acid
E_1, E2	Conformations of the P-type ATPases sensitive to cytoplasmic and extracytoplasmic ions, respectively
ESR	Electron spin resonance
FITC	Fluorescein isothiocyanate
GI	Sealed, H/K-ATPase enriched microsomes
η	Asymmtry parameter
[^{3}H]mDAZIP	8-[(4-azidophenyl0methoxy]-1-tritiumethyl-2,3-dimethylamidazo[1,2-a]pyridinium iodide

IC_{50}	Concentration of inhibitor which inhibits 50% if H/K-ATPase activity
Lα	Lamellar liquid crystalline phase lipids
MBTA	4-(N-maleimido0benzyltrimethylammonium
NMR	Nuclear magnetic resonance
P_i	Inorganic phosphate
ppm	Parts per million
σ_{11}, σ_{22}, σ_{33}	Principal elements of a tensor
σ_{iso}	Isotropic chemical shift
SCH28080	2-methyl-3-cyanomethyl-8-(phenylmethoxy)imidazo[1,2-a]pyridine
SDS	Sodium dodecylsulphate
SDS-PAGE	Sodium dodecylsulphate-polyacrylamide gel electrophoresis
τ_1, τ_2	Refocusing and evolution delays respectively, in the ^2H NMR quadrupole echo pulse sequence
TEMPO-ITC	2,2,6,6-tetramethylpiperidinyloxyisothiocyanate
TLC	Thin layer chromatography
TMCHIP	1,2,3-trimethyl-8-(cyclohexylmethoxy)imidazo[1,2-a]pyridinium iodide
TMPIP	1,2,3-trimethyl-8-(phenylmethoxy)imidazo[1,2-a]pyridinium iodide
TM2FPIP	1,2,3-trimethyl-8-(2-fluorophenylmethoxy)imidazo[1,2-a]pyridinium iodide
TM4FPIP	1,2,3-trimethyl-8-(4-fluorophenylmethoxy)imidazo[1,2-a]pyridinium iodide

TMPFPIP	1,2,3-trimethyl-8-(pentafluorophenylmethoxy)-imidazo[1,2-a]pyridinium iodide
TMTFBIP	1,2,3-trimethyl-8-(trifluorobutylmethoxy)imidazo[1,2-a]pyridinium iodide
τ_r	Magic angle spinning rotor period
TRIS	Tris-[hydroxymethyl]-aminomethane
ω_0	Larmor (precessional) frequency
ω_R	Magic angle spinning rotor frequency

Chapter 1

INTRODUCTION

Biological Membranes

Characteristics of Biological Membranes

The importance of biological membranes to cellular function has long been appreciated. Study of membrane structure has developed from the Langmuir trough experiments of Gorter and Grendel which, in 1925, showed the bilayer nature of the erythrocyte membrane, to the application of electron microscopy and X-ray and neutron diffraction experiments to show the bilayer arrangement of amphipathic lipids in biological membranes [1] (Figure 1-1).

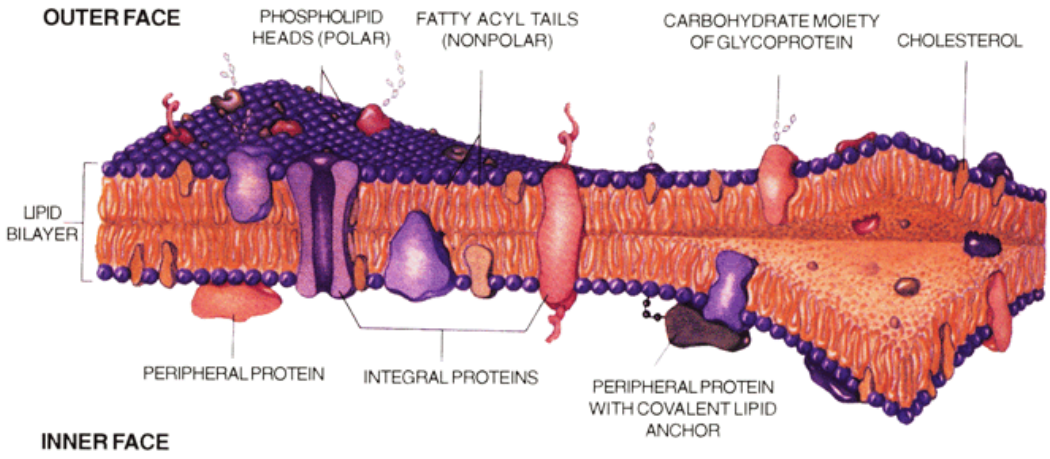

Figure 1-1 Schematic representation of a cell plasma membrane showing amphipathic lipids arranged in a bilayer: polar headgroups exposed to the aqueous cell interior and exterior, non-polar carbon chain tails self-associated and interdigitated in the membrane core. Proteins are peripherally or integrally associated with the membrane and are free to move laterally in the plane of the membrane. Movement from one leaflet of the bilayer to the other is restricted. Reproduced from *Principles in Biochemistry*, Lehninger, Nelson & Cox, 1992 .

Understanding of the protein arrangement in membranes has evolved from the models of Danielli and Davson [2], who proposed that membrane proteins existed on either side of, but did not span, the lipid bilayer to the Singer and Nicholson fluid mosaic model (1972) [3] and determination of the first membrane protein structure, that of bacteriorhodopsin, by Henderson and Unwin in 1975 [4]. Now, the Singer and Nicholson model of membrane-intergral proteins traversing a lipid bilayer in the fluid phase via hydrophobic interactions is being further refined to accommodate lipid rafting phenomena [5]. Other membrane structures are considered: instances when biological membranes undergo phase transitions from the normal lamellar (Lα) bilayer phase to adopt non-bilayer structures due to changes in temperature, hydration, and lipid constitution. An example is seen when the membrane adopts a non-bilayer phase similar to that observed in the hexagonal (H_{II}) phase, which is proposed to be implicated in cell fusion and endo- and exo-cytosis events and has been observed by X-ray diffraction techniques [6] and ^{31}P-NMR [7].

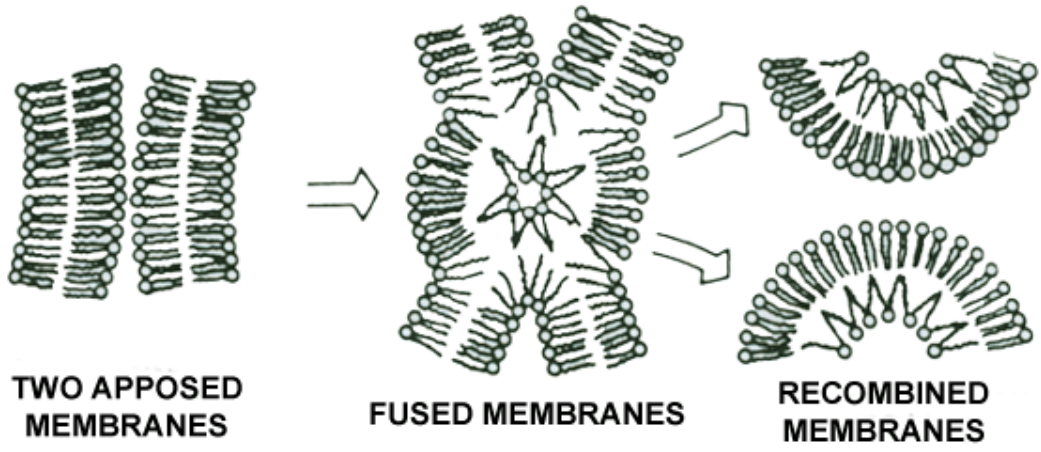

Figure 1-2 A model of the hexagonal (H_{II}) phase intermediate formation during membrane fusion. Reproduced from *A Comprehensive Introduction to Membrane Biology*, Datta, 1987.

Under physiological conditions, amphipathic lipids form stable sheet-like structures. The lipid bilayer assembles such that the polar lipid head groups present themselves externally to a core of hydrophobic acyl chains (Figure 1-1). This arrangement provides a formidable but selective barrier to the influx and efflux of molecules and charged species. The membrane sieving effect imposes steric limitations on the size of uncharged molecules that might be solvated by the hydrophobic core and pass dissolved across the bilayer; the large positive free energy considerations of moving even a small charged group from an aqueous environment (dielectric constant $\varepsilon = 80$) through a regime with small dielectric constant ($\varepsilon = 2$) [8] permit lipid bilayers to form effective envelopes around cells and cellular organelles that serve to contain and protect cellular processes.

Simple membranes allow the storage of water-soluble metabolites at particularly high concentrations in condensing vesicles, vacuoles, and lysosomes. For example, the cholinergic presynapse contains membrane-enclosed packets of 0.8 M acetylcholine that permit the quantised release of the neurotransmitter into the synaptic space by fusion with the pre-synaptic membrane. The membranes of the storage granules in pancreatic β cells permit insulin to store at concentrations that cause precipitation into small crystals [9].

A lipid bilayer which possesses high capacitance is fully utilized as a battery in cellular energy production. This vectoral storage and discharge of electrochemical potential energy is observed across the bacterial periplasmic membrane, thylakoid and mitochondrial inner membranes and the plasma membranes of Schwann cells [10].

Biological membranes permit reaction space of three-dimensions to be reduced to approach two-dimensions [11]. This feature allows the membrane to localize

the reacting machinery and thus act as a concentration zone for metabolism and cell signaling [12].

The Importance of the Proteins in Biological Membranes

It is estimated that 80% of all cellular signals are triggered by membrane proteins. GTP-binding protein-coupled receptors (GPCRs) are targets for hormones, neurotransmitters, chemokines and sensory stimuli [13]. The binding of a ligand such as epinephrine, histamine, chemokine CCR5 to or the incidence of a stimulus such as a photon of light on a GCPR results in a cellular response mediated by the associated G proteins [14]. At least 2000 GCPRs have been reported since bovine opsin was cloned in 1983 [15] and this class of integral membrane proteins has been subdivided into over 100 subfamilies [16]. GCPRs alone have been implicated in a wide number of diseases and pathologies of the central nervous system. Drug targeting of these receptors has been important in treatment of Schizophrenia [17], depression and migraine [18], Alzheimer's and Parkinson's [19]. The efficiency of membrane receptor communication relay can be palpable as part of signal amplification. Upon activation by a single photon, a single rhodopsin molecule can in turn activate nearly 1000 transducin molecules in 1 second [20] and the total number of transducins that can be activated by a single photoreceptor may reach 37,000, leading to hyperpolarization of rod cells [21]. In contrast, stimulation of the β-adrenergic receptor results in the activation of only 20 molecules of Gs, a G-protein that stimulates adenylate cyclase in the signal cascade [22]. There may be membrane-mediated communication within the cell. Nuclear import signal sequences rich in lysine, arginine, and proline stimulate the dilation of nuclear pores from 10 nm up to 26 nm such that large

molecular weight (greater than 50 kDa) molecules can be trafficked across the membrane via an energy-dependent, gated, channel mechanism. Members of the importin-β family of transport receptors mediate Nuclear Pore Complex passage of cargo by interacting with Nuclear Pore Complex proteins (nucleoporins) and a small GTPase, Ran [23].

Integral membrane proteins do not have the monopoly role for cellular communication: membrane lipids contribute to a number of recognition events. Anionic phospholipids have been demonstrated to have numerous roles in the regulation of cell functions [24]. Phosphatidylserine (PS) is normally located on the inner leaflet of the plasma membrane and its asymmetric distribution is maintained by an aminophospholipid translocase [25]. A breakdown in the asymmetric distribution of PS such that it becomes displayed on the external cell surface is characteristic of platelet activation [26] and apoptosis [27]. Phosphatidic acid in the external monolayer of the plasma membrane may be the preferred substrate for human phospholipase A2. The primary physiological role of human phospholipase A2 is considered to be in the removal of infectious micro-organisms and damaged cells. The enzyme may contribute to the pathology of rheumatoid arthritis by attacking the membranes of normal cells in the synovial joints of patients and act to inflame the joint.

The Structure and Arrangement of Membrane Components

To understand further the molecular basis for important cellular and organellar functions that biological membranes and their components regulate, structural information is required for the molecules that act as receptors, transport substrates, flag the cell as "self" during an immune response, provide connectivity between other cells and tissues, propel a motile cell and so on. The quest for atomic level three-dimensional structure is one of the main driving forces of protein science [28]. High-resolution data has been obtained for many globular, water-soluble proteins using well-established diffraction techniques such as X-ray crystallography and cryo-electron microscopy and spectroscopic methods such as high-resolution solution state nuclear magnetic resonance (NMR). The number of structures deposited in the Protein Data Bank (PDB) has grown exponentially since its inception [29]. There are currently more than 15000 entries, more than 14000 of which relate to protein structures. More than 80% of the data is derived from diffraction experiments, 15% of the structures were obtained using NMR techniques and the remainder were submitted from theoretical modeling studies [30] (Figure 1-3).

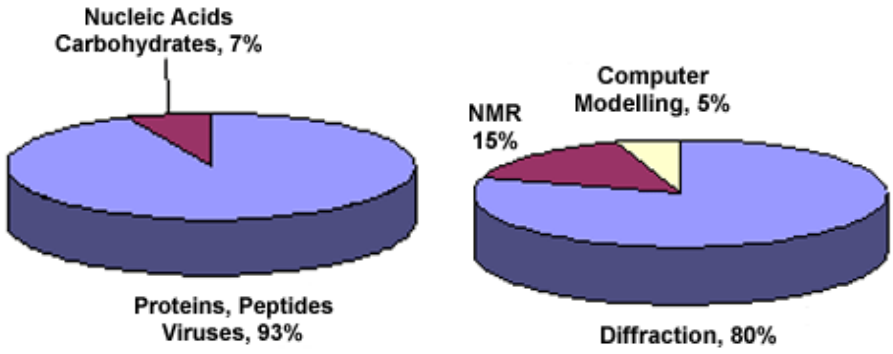

Figure 1-3 Pie chart representations of the distribution of Protein Data Bank structure holdings. The chart on the left shows the distribution of the ~15000 species for which there are structures deposited with the Data Bank. The chart on the right represents the proportion of structures using diffraction, NMR and computer modeling techniques. Data compiled from [30].

Only a very small proportion of these PDB entries relates to membrane integral proteins since the various experimental techniques required for high resolution data are frustrated by heterogeneity and low levels of expression in the membrane environment.

Diffraction methods, aside from usually necessitating isomorphous replacement to resolve the phase problem, rely on the availability of an ordered (crystalline) array of the molecule under examination. Membrane proteins and associated lipids, in their two-dimensional bilayer environment are entropically constrained by the hydrophobic effect and the imposition of further order requires a significant energy barrier to be overcome before a crystal will form in two or three dimensions. Packing of membrane proteins in 3D is not possible in an intact bilayer. Furthermore, detergents have only a limited ability to manipulate proteins with hydrophobic/amphipathic surfaces that are normally enveloped with membrane lipid. Frequently, the protein packs as an intractable aggregate. Some success has been had with electron microscopy of two-dimensional crystals [4, 31, 32], where the protein has been removed from the native

membrane by detergent and then reconstituted into intact membranes. With 3D crystallization, detergents solubilised the protein permanently away from the membrane [33]. In one naturally formed example, bacteriorhodopsin in the plasma membrane of *Halobacter halobium* obligingly forms a crystalline array under conditions of low oxygen and high salt concentration. The so-called purple membrane of the bacterium has a high packing density of bacteriorhodopsin (bR) and as a result, the light-driven H^+-pump has been studied extensively. New techniques, such as the use of the cubic lipid polymorphic phase as a pseudo isotropic environment [34, 35], have been developed to accommodate membrane proteins such as porins for diffraction studies but only one GPCR has been crystallized in this manner. The number of high resolution structures that have been obtained for membrane proteins is still small and is currently two orders of magnitude lower than the number of structures obtained for globular proteins.

High resolution NMR has provided over two thousand protein structures [30]. NMR is an effective and established method for structural determination of soluble proteins as resolution and tractable size of protein improves along with increases in magnetic field strength. Full structure elucidation is limited to well-folded systems of molecular weights less than 30000-40000 Da. Molecular motions have a profound influence on the NMR analysis of proteins. The effect may be direct, through motional averaging of lineshapes, or indirect, through relaxation effects. The NMR spectrum is determined by a number of interactions. The chemical shift is an interaction of a nuclear spin with the electronic environment created by the surrounding electrons. The scalar interaction is a nuclear spin-spin interaction mediated through the Fermi contacts of electrons in neighbouring nuclei. The dipolar coupling is a distance- and orientation-

dependent through-space interaction between nuclear magnetic dipoles. The quadrupolar effect is an orientation-dependent interaction between nuclei with nuclear spin $I \geq 1$ and the electric field gradient surrounding the nucleus. The interaction is created by the charges around the nucleus in question. In solution experiments, the lineshapes are averaged out to their isotropic values by fast molecular motion: only the indirect effects are seen. If the correlation time of the molecular motion is long on the NMR timescale (μs to ms) the lineshapes broaden and may overlap due to anisotropic magnetic interactions [36]. The correlation time for molecular tumbling is given by:

$$\tau_c = \frac{4\pi\eta r^3}{3kT}$$ **Equation 1-1**

and

$$\eta \propto M_w^{\alpha}$$ **Equation 1-2**

where τ_c is the correlation time, η is intrinsic viscosity, r is the Stoke's radius of the complex of molecular weight M_w, k is the Boltzmann constant, α is an empirically-determined constant that varies with shape of the species and T is the absolute temperature. Since τ_c varies with r, even a small integral membrane protein such as bR (M_w = 26 kDa) will be too large to tumble sufficiently rapidly to average out the chemical shift anisotropy and dipolar interactions of μs to ms when associated with membrane lipids.

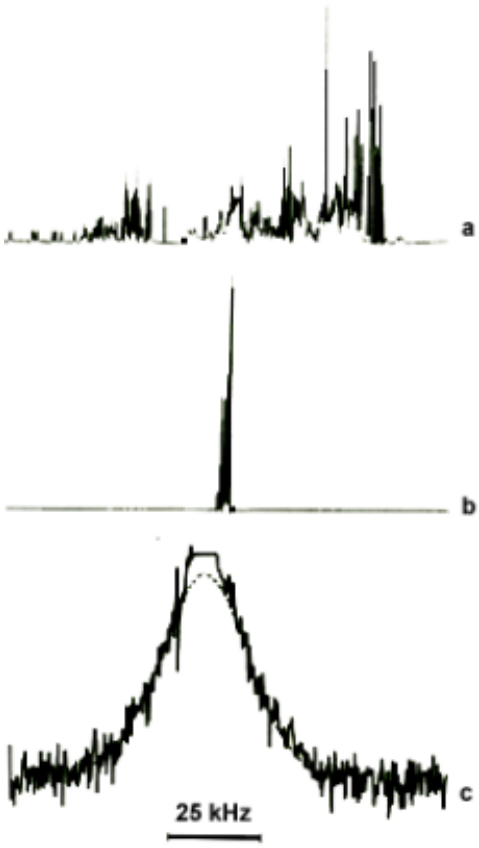

Figure 1-4 Comparison of ^{1}H-NMR spectra of water-soluble and membrane-integral proteins. (a) High resolution spectrum of bovine pancreas trypsin inhibitor (BPTI), a small (M_w ~ 7 kDa) rapidly isotropically tumbling protein, exhibiting sharp lines from which the complete three-dimensional structure was resolved. (b) The spectrum of (a) on the same scale as (c). (c) The broad powder spectrum of bovine rhodopsin (M_w ~ 39 kDa) reconstituted into deuterated lipid bilayers. The broad lineshape results from the slow, anisotropic rotations of the protein in the membranes. The protein and lipid together have an effective M_w >> MDa and the resultant spectrum is dominated by the relatively large ^{1}H-^{1}H dipolar interactions, which are not averaged to zero by the slow tumbling of the protein-membrane complex. Adapted from [37].

The protein-membrane complex produces broad, poorly resolved spectra (Figure 1-4). The resulting overlap of lineshapes may make it impossible to interpret the spectrum to provide information about the system.

Some modest success has been gained by using selectively ^{13}C-labelling and optimising solubilisation of large membrane proteins in detergent micelles [38]. Usually, however, the line-broadening due to incomplete averaging of the dipolar interaction and chemical shift anisotropy constitutes a significant problem for structural studies by solution state ^{1}H and ^{13}C NMR, where dipolar relaxations in

the form of nuclear Overhuaser effects are required to give structural information at the atomic level. It is in these cases that NMR methods developed for the analysis of solids have become useful.

The solid-state NMR technique of Magic Angle Sample spinning (MAS NMR) effectively reproduces the narrow lineshapes obtained for small molecules tumbling in solution for rare nuclei like ^{13}C, ^{15}N, ^{31}P and ^{19}F. Protons have a high gyromagnetic ratio which produces strong homonuclear dipolar couplings. Since the spectral width of the proton spectrum is narrow compared with the magnitude of the ^{1}H-^{1}H dipolar interaction, resolution of distinct resonances is rendered difficult.

Usually a sample is orientated at the so-called magic angle of $\theta = 54.7°$ to the applied magnetic field and set spinning in a rotor at high speed (2 - 22 kHz). In the MAS experiment, magnetic interactions such as the dipolar coupling that show orientational dependence which varies with $(3\cos^2\theta–1)$ are averaged to zero. The isotropic chemical shift information is recovered. Homonuclear dipolar interactions are only partially averaged since the interaction is in many cases larger ($d_{HH}.r^3 = 1.2x10^5$ Hz.Å^3) than the spinning speeds achievable using MAS. Proton decoupling at high power can overcome the strong homonuclear and heteronuclear dipolar interactions with concomitant improvement in spectral lineshapes.

There is much to be gained from heteronuclear couplings between protons and dilute nuclei whose NMR-sensitive isotopes are present in only low natural abundance. Transfer of magnetisation from the pool of protons dipolar decoupled to less sensitive dilute spins (^{13}C, ^{15}N) by cross-polarisation (CP) can enhance the observed signals from a protein and lipid sample. In addition, since cross-

polarisation does not take place in molecules undergoing rapid reorientation in aqueous solution, only motionally restricted molecules and ligands that interact with the membrane will be observed. Thus, the drug or cofactor retained at its binding site will be visible in the CP-MAS spectrum whereas the molecule that is not retained will remain invisible.

The strength of a dipolar coupling varies with $1/r^3$ of the distance (r) between the coupled nuclei. Measurement of the dipolar coupling is thus valuable in providing intra- and inter-molecular distance measurement. Dipolar couplings, having been averaged under MAS conditions, must be selectively re-introduced in order to extract structural information from the spectrum. Various techniques have been employed successfully to achieve this end: Rotational Resonance [39-41] and Rotational Echo Double Resonance (REDOR) [42-44] are most commonly used to obtain homonuclear and heteronuclear interatomic distance measurements with high precision (<Å). Rotational resonance relies on the fact that magnetization transfer between two homonuclear spins is most efficient when the shift difference equals an integral of the MAS frequency, which can place the spinning sideband of one resonance overlapping with the isotropic resonance of another [45]. If the homonuclear spins are sufficiently proximal to be strongly coupled by the dipolar interaction, their resonance intensities will vary as a magnetization mixing time is varied in the NMR experiment. Magnetization transfer is proportional to the dipolar coupling (D) and measurement of D (in Hz) can be used to calculate the internuclear distance (r) according to

$$D = \left(\frac{\mu_0}{4\pi}\right)\frac{\gamma_I \gamma_S \eta}{r^3}$$

Equation 1-3

where μ_0 is the permeability constant, γ_I and γ_S are the I and S gyromagnetic ratios, and h is Planck's constant. The same relationship is used in the REDOR experiment to measure distances between dipolar-coupled heteronculei. REDOR reintroduces the heteronuclear dipolar coupling that is averaged by MAS sample rotation, by application of a train of radio frequency pulses timed with the rotor cycles of the MAS rotor. The π-pulses interfere with averaging of the heteronuclear dipolar coupling and the observed spins accumulate phase which leads to a diminution of signal intensity in a distance-dependent manner. Systematic variation of the number of rotor cycles and observing the signals both with and without the occurrence of π-pulsed dipolar-dephasing in the REDOR experiment produces a time-domain REDOR dipolar dephasing signal from which internuclear couplings may be calculated directly.

Thus far, solid-state NMR has helped to determine the structure and orientation of prosthetic groups such as retinal [46], local structure and tilt angles of membrane-associated peptides [47, 48] and the orientation and structure of pharmacologically important site-specific agonists and inhibitors of membrane proteins such as the nicotinic acetylcholine receptor [49], the Na/K-ATPase [50] and the gastric H/K-ATPase (gHKA) [51]. Solid state NMR has established itself as a valuable tool for determining the structure and orientation of molecules that would be poorly defined using other methods on membrane systems and, as such, is a powerful method for characterising species in their sites of efficacy.

Basic Principles of Solid State NMR

This section provides a basic introduction to some of the NMR interactions investigated in this thesis.

Nuclear spins engage in a number of external and internal electromagnetic interactions to produce an NMR spectrum. The nuclear spin Hamiltonian (the energy-operator containing the terms for the internal and external interaction of the spin system under investigation) is given by [52]

$$H = H_{ZN} + H_{CS} + H_J + H_D + H_Q \qquad \textbf{Equation 1-4}$$

The Zeeman Hamiltonian (H_{ZN}) term reflects the interaction of the nucleus spin (I) with the magnetic field (B_0)

$$\mathrm{H}_{ZN} = \gamma\hbar\mathbf{B}_0\mathbf{I}_z \qquad \textbf{Equation 1-5}$$

where γ is the gyromagnetic ratio and $\boldsymbol{I_z}$ is the component of the macroscopic magnetisation operator aligned parallel to the direction of the applied magnetic field which is defined by convention as the z-axis of the laboratory reference frame.

The Hamiltonian for the chemical shift interaction is

$$H_{CS} = \gamma\hbar\mathbf{B}_0\sigma_{zz}^{labframe}\mathbf{I}_z \qquad \textbf{Equation 1-6}$$

where σ_{ij}, the chemical shift, is a second rank tensor with principle elements σ_{11}, σ_{22}, σ_{33}. The chemical shift Hamiltonian may be written explicitly as

$$H_{CS} = \gamma\hbar\left(\sigma_{11}\sin^2\theta\cos^2\phi + \sigma_{22}\sin^2\theta\cos^2\phi + \sigma_{33}\cos^2\theta\right)\mathbf{B}_0\mathbf{I}_z \qquad \textbf{Equation 1-7}$$

where θ and ϕ describe the angles formed between the principal axis and the laboratory fixed axis (Figure 1-5).

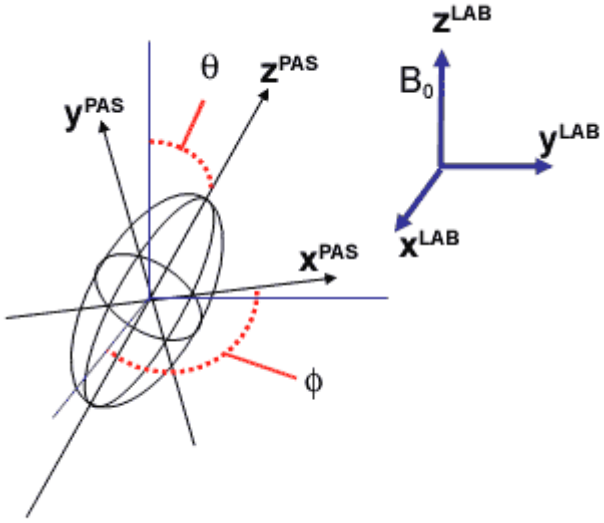

Figure 1-5 Chemical shielding ellipsoid with the geometric relationship between the Principal Axis System (PAS) of the nucleus and the laboratory fixed axis (LAB).

In addition, from these principal elements are defined the shielding anisotropy ($\Delta\sigma$), asymmetry parameter (η) and the isotropic chemical shift:

$$\Delta\sigma = \sigma_{33} - \frac{1}{2}(\sigma_{11} + \sigma_{22}) \qquad \textbf{Equation 1-8}$$

$$\sigma_{iso} = \frac{1}{3}(\sigma_{11} + \sigma_{22} + \sigma_{33}) \qquad \textbf{Equation 1-9}$$

$$\eta = \frac{\sigma_{22} - \sigma_{11}}{\sigma_{33} - \sigma_{iso}} \qquad \textbf{Equation 1-10}$$

Fermi-contact mediated interactions between nuclear spins give rise to the electron mediated, J coupling, Hamiltonian:

$$H_J = 2\pi \mathbf{I}\mathbf{J}\mathbf{I} \qquad \textbf{Equation 1-11}$$

characterised by the indirect spin coupling tensor **J**. The Hamiltonian can be divided into the isotropic and anisotropic components

$$H_J^{iso} = 2\pi J \mathbf{I}_1 \mathbf{I}_2$$ **Equation 1-12**

$$H_J^{aniso} = 2\pi \mathbf{I}_1 \mathbf{J}^{aniso} \mathbf{I}_2$$ **Equation 1-13**

The dipolar interaction may be written as an approximate (truncated) Hamiltonian. The Hamiltonian describing a homonuclear dipolar coupling is

$$H_D = \frac{1}{2}\frac{\gamma_1\gamma_2}{r^3}\left(1-3\cos^2\theta\right)\left(3I_zS_z - \mathbf{I}.\mathbf{S}\right)$$ **Equation 1-14**

and for a heteronuclear dipolar coupling is

$$H_D = \frac{1}{2}\frac{\gamma_1\gamma_2}{r^3}\left(1-3\cos^2\theta\right)\left(2\mathbf{I}_z\mathbf{S}_z\right)$$ **Equation 1-15**

where θ is the angle between the internuclear vector of length r and the applied field. The dipolar interaction may be exploited to measure dipolar distances (r) in solids. This aspect of the interaction of spins with each other will be explored further in Chapter 4.

The Hamiltonian for the quadrupolar interaction of a nucleus having spin ≥1 may be written in the form

$$H_Q = \mathbf{IQI}$$ **Equation 1-16**

where **Q** may be expressed in terms of the electric field gradient at the nucleus:

$$\mathbf{Q} = \frac{eQ}{2I(2I-1)\eta}\mathbf{V}$$ **Equation 1-17**

where eQ is the nuclear quadrupolar moment and **V** is the electric field gradient at the site of the nucleus. Under the high-field approximation, whereby it is assumed that the Zeeman interaction is larger than the quadrupolar interaction, non-secular terms may be neglected and

$$V_{zz}^{labframe} = \frac{1}{2}\left(3\cos^2\theta - 1\right)V_{zz}^{PAS} + \frac{1}{2}\sin^2\theta\cos 2\phi\left(V_{xx}^{PAS} - V_{yy}^{PAS}\right)$$ **Equation 1-18**

The asymmetry parameter η is given by

$$\eta = \frac{V_{xx} - V_{yy}}{V_{zz}}$$ **Equation 1-19**

where by convention $|V_{zz}| \geq |V_{xx}| \geq |V_{yy}|$. Thus

$$V^{(2,0)} = \frac{1}{2}\left(\left(3\cos^2\theta - 1\right) + \eta\sin^2\theta\cos 2\phi\right)$$ **Equation 1-20**

For an axially symmetric deuteron (η=0), the quadrupolar contribution may be written as

$$H_Q = \frac{e^2qQ\left(3I_z^2 - \mathbf{I}^2\right)}{4\eta}\left(3\cos^2\theta - 1\right)$$ **Equation 1-21**

Biological membranes as targets in the therapy of disease

Introduction

Given the diversity of the physiological processes in which biological membranes are implicated, they have become the focus of therapeutic targeting for the clinical treatment of disease. The goal of many therapeutic strategies in disease control and management is to intervene in the processes initiated at the biological membrane. The properties of the lipid bilayer may be modified to induce a pharmacological response: the general anaesthetics alphaxatone and halothane work by a poorly understood mechanism that involves expansion of the plasma membrane, depression of the phase transition point of the leaflets, and may be implicated in pore formation [53]. The principal mechanism of anaesthesia is more likely to involve interaction with ion channels in nervous tissue [54]. Small peptide antibiotics are thought to act by dissipating the electrochemical potential gradients of target cell by penetrating the lipid bilayer, often forming pores. Similarly, ionophores such as valinomycin, gramicidin and alemethicin act as carriers or form ion-conducting channels. They permit ion-specific flux down the electrochemical gradient and can result in cell lysis. Although toxic to mammalian cells, peptides such as gramicidin are still valuable as topical antibacterial agents [55].

A common strategy in disease control involves drug targeting of membrane proteins. A membrane target may be stimulated by agonist hormones such as insulin, which activate specific G-protein pathways upon binding their receptors. The effects of stimulation by insulin may be both short- and long-term: sugar and amino acid transport is rapidly activated, followed by receptor-internalisation and

ultimately a change in the protein expression profile of the cell. Regulators of membrane function may be targeted. Phospholamban, a 52-residue membrane-spanning protein, regulates the active transport of Ca^{2+} ions into the endoplasmic reticulum in cardiac myocytes by what is thought to be an inhibitory monomeric association with the SERCA2 isoform of the Ca-ATPase [56]. The peptide is of particular interest in the control of heart failure and its structure has been examined using solid-state NMR [48].

More usually, membrane proteins are targeted to inhibit their enzyme function or to prevent native antagonist ligand binding and activation of the protein, i.e., 5HT receptor antagonists. Acid secretion into the fundic region of the stomach, for example, may be prevented by direct, irreversible inhibition of a number of membrane proteins but the current favoured target is the gastric proton pump (H/K-ATPase) responsible for acid secretion into the lumen of gastric glands. Site-specific inactivation of the protein is achieved clinically by orally dosing or intravenously infusing the patient with substituted benzamidazoles such as omeprazole [57]. Regulation of stomach acidosis is a global preoccupation in the treatment of gastroesophagael reflux disease and gastric ulcer disease: global sales of Prilosec (omeprazole) were valued at $6.2 bn in 2000 [58].

Gastroesophegael Reflux Disease and Gastric Ulcer Disease

The lower esophagus, stomach and proximal duodenum are frequently exposed to extreme acidic pH. Malfunction of the lower esophagael sphincter may permit reflux of gastric acid into the esophagus [59] (Figure 1-6).

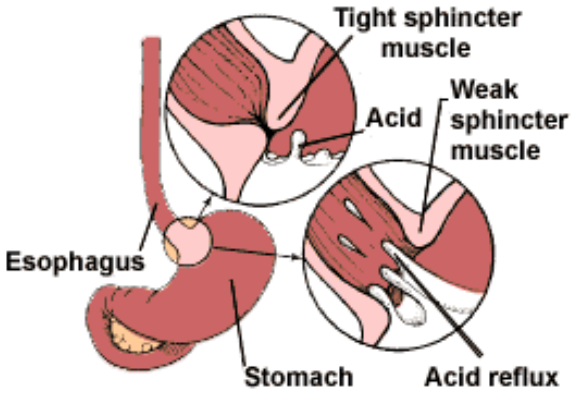

Figure 1-6 Schematic representation of acid reflux into the esophagus. A weakened lower esophagael sphincter permits gastric acid to reflux into the esophagus where it may overwhelm the HCO_3^- buffering capacity of the esophagael epithelium and damage the underlying layer of cells.

The esophagael epithelium is enervated into the superficial layers of the mucosa. There are no tight junctions to seal adjacent cells in the lower esophagael epithelium and the tissue is significantly more acid sensitive than the gastric epithelium, which is provided with "tight" tight junctions (Figure 1-7).

The esophagael epithelium is protected by an aqueous mucosa that is not considered to be a significant barrier to acid back diffusion, a secreted HCO_3^- buffer which provides surface neutralisation of acid and a Na/H anion exchange acid recovery mechanism. The pain fibres lack this recovery mechanism and have a lower threshold for acid than the epithelial tissue. Once damaged, the extracellular protection pathway is shortened and less effective; a lesion forms that increases sensitivity and discomfort to acid reflux.

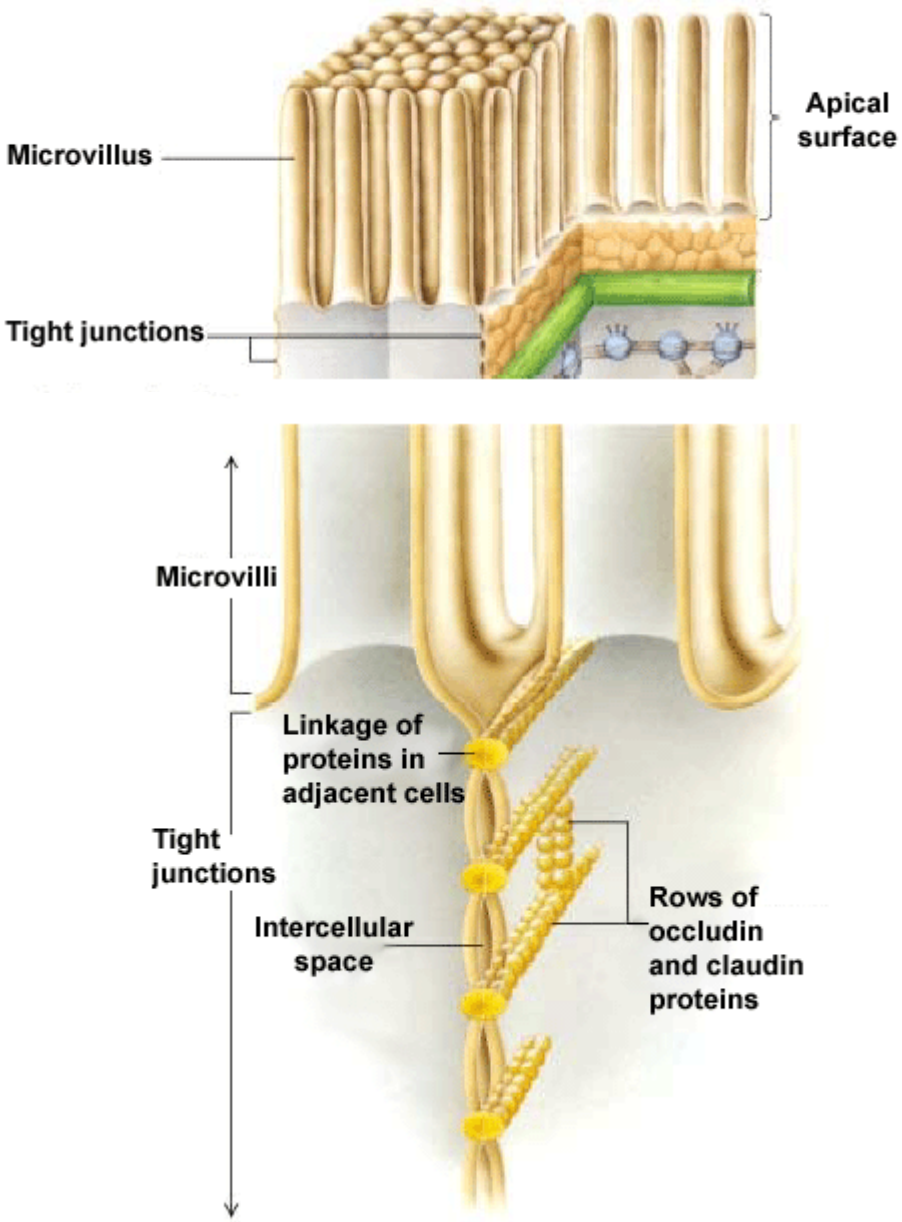

Figure 1-7 Schematic representation of gastrointestinal cell surfaces with tight junctions. Top figure shows projection of parietal cell microvilli into the gastric lumen. Bottom figure shows intercellular tight junction to prevent reflux of secreted acid into the underlying tissue (adapted from [60]).

Whereas surface buffering can accommodate a pH 4.0 load of acid (30 µmol acid/30 min/10 cm human esophagus), a tenfold increase (to 300 µmol acid/30 min/10 cm human esophagus) is beyond the buffering capacity of HCO_3^- (78 µmol/30 min/ 10 cm human esophagus) [61]. If the Na/H anion exchange

pathway is viable, the damage to the epithelium may be prevented but if pepsin is activated (by pH less than 3.0), the esophagus may suffer proteolytic damage.

The stomach has a median pH 1.4. Microelectrode measurements indicate that when the lumen has pH 2.0, the gastric surface has approximately neutral pH [62]. Buffering of gastric acid is through food, HCO_3^- secretion and the gastric mucous membrane. Nocturnally, when there is no food buffer, pH can fall below pH 1.0. *In vitro* application of the weakly basic ^{14}C-aminopyridine localised the radio label to the fundic glands, indication that the pH was lower than the atrial surface [63].

Infection by the Gram-negative bacterium *Helicobacter pylori* is now implicated in both duodenal and non-steroid induced anti-inflammatory drug (NSAID)-induced gastric ulcers [64]. About 550 000 new cases a year of stomach cancer - about 55% of the worldwide total - are attributable to *H. pylori* [65]. The bacteria are thought to disrupt the integrity of tight junctions and permit acid reflux across the apical membrane of the exposed tissue. Necrosis of the underlying tissue follows.

Treatment of lower gastroesophagael reflux disease is achieved by improving the response or structure of a weak lower esophagael sphincter that may have been permitting acid flow up the alimentary canal. Current treatment is relatively non-selective and has lower efficacy than acid inhibition [59]. This strategy is applied to treatment of gastric ulcer disease: effective inhibition of acid secretion allows tissue healing and symptom relief and is achieved through a range of site inhibitions that work at various stages of the acid secretory pathway.

Effective control of acid secretion allows tissue healing and symptom relief. This is the strategy adopted in treatment of gastric ulcer disease, where regulation of

the acid secretory pathway is coupled with a course of antibiotics to eliminate the *H.pylori* infection. The bacterium survives between pH 4.0 – 8.0 and grow (synthesise protein) between pH 6.0 – 8.0. Antibiotics such as clarithromycin and amoxicillin act only on growing organisms and non-dividing organisms will survive, being unaffected by the treatment. [66]

Regulation of Acid Secretion

Reduction of gastric acid secretion by the parietal cells of the fundus is the core strategy for the treatment of lower esophagael acid reflux disease, gastric ulcer disease and duodenal ulcer disease. There are many possible molecular sites of inhibition of acid secretion. The physiological regulation of gastric acid secretion from parietal cells is summarized in Figure 1-8.

Efferent fibres from the vagus nerve synapse with ganglions of the enteric nervous system. Three cell types are stimulated by the vagus nerve, proceeding with gastrin-containing (G) cells. Under negative control by somatostatin-releasing (D) cells of the fundus and atrium, G cells release gastrin to stimulate enterochromatin-like (ECL) cells. These cells are also subject to feedback control by D cells but are stimulated by acetylcholine, epinephrine and increases in cAMP levels. Histamine, released by ECL cells, binds H_2 receptors in the parietal cell membrane, which stimulates production of cAMP. The elevation of cAMP activates transferral of the gastric proton pump from fusion of tubulovesicles with the apical membrane, forming the secretory canaliculus. Acid secretion into the gastric lumen is then catalysed by the proton pump.

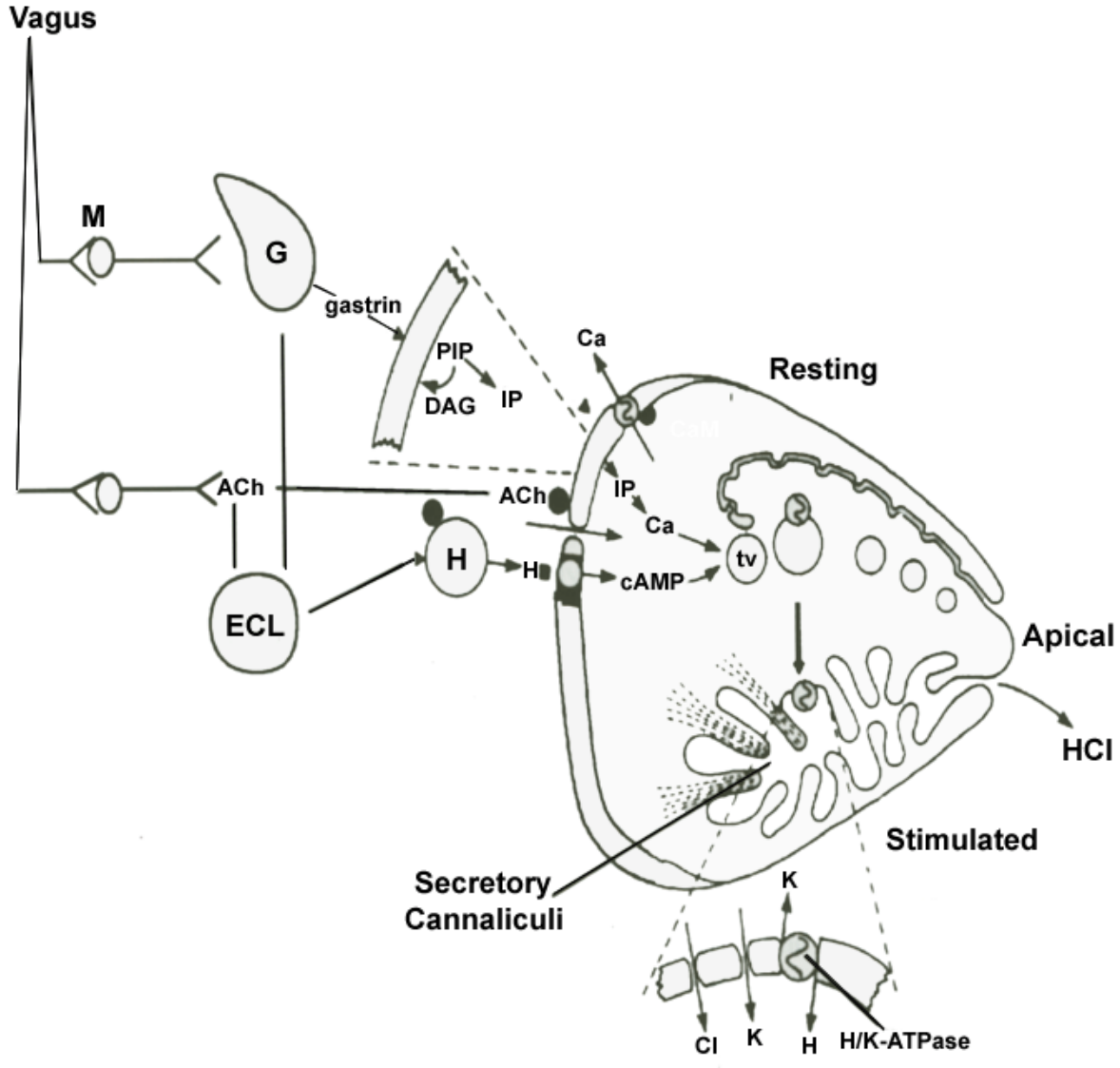

Figure 1-8 Schematic representation of physiological regulation of gastric acid secretion from parietal cells. Acetylcholine (ACh), released by the vagus nerve, activates a muscarinic M3 receptor on the parietal cell, which alters the cell permeability to Ca^{2+}. Release of gastrin from antral "G" cells and histamine from enterochromatin-like (ECL) cells is also stimulated by the vagus nerve. Gastrin binds the G receptor of the parietal cell, which triggers release of inositol triphosphate (IP) and thence intracellular Ca^{2+}. Histamine, upon binding parietal cell H_2 receptors, stimulates production of cyclic AMP (cAMP). Tubulovesicles (tv) in the cytosol are activated by cAMP and Ca^{2+} and, containing H/K-ATPase, are transformed into the microvilli of the secretory canaliculus, which also conducts K^+ and Cl^-. (Adapted from [67])

There are several pathways that may be inhibited to prevent acid secretion. Acetylcholine-stimulated secretion may be modified by muscarinic antagonists such as atropine and pirenzipine. These compounds inhibit 50% of the maximal

meal-stimulated acid production but produce side effects since they interfere with cholinergic receptors throughout the body [68]. Histamine-H_2 antagonists such as cimetidine and ranitidine have been found to protect the stomach and show some degree of selectivity [69] but the multiplicity of cell receptors means that 100% inhibition of acid secretion is difficult. Because it represents the final stage of acid secretion – all upstream pathways converge at this point - the gastric proton is now a successful target for the selective inhibition H^+-extrusion and the treatment of acid-related disorders by site-specific inhibitors such as substituted benzamidazoles and substituted imidazopyridines.

The Gastric H/K-ATPase

The gastric H/K-ATPase (EC 3.6.1.36) is an αβ heterodimer ion-motive phosphorylated (P-type) ATPase. It is found in the canalicular membrane of microvilli in parietal cells of the gastro-intestinal tract. The H/K-ATPase has been isolated from the parietal cells of human, rabbit, hog and cat gastric mucosa in which it was found to be present in similar amounts and with similar rates of catalysis [70]. Molecular cloning experiments have identified H/K-ATPase in colon and kidney from rat and rabbit [71]. In all cases, the transporting enzyme catalyses the electroneutral exchange of H^+ for K^+ across the membrane and, in the gastro-intestinal tract, this generates a million-fold concentration gradient across the canalicular membrane – the largest ion gradient known in mammals [72].

The H/K-ATPase contains a 1030 amino acid (114 kDa) catalytic α subunit that shares 62% sequence homology with the Na/K-ATPase [73]. A highly conserved

region is found at the aspartate phosphorylation site and nucleotide binding site, both in the very large cytoplasmic domain of the α subunit. By analogy with the Ca-ATPase three-dimensional crystal and Na/K-ATPase 2-D structures [74, 75], protein digest [76] and hydropathy mapping [73], the α subunit is suggested to have 10 membrane spanning helices (Figure 1-9).

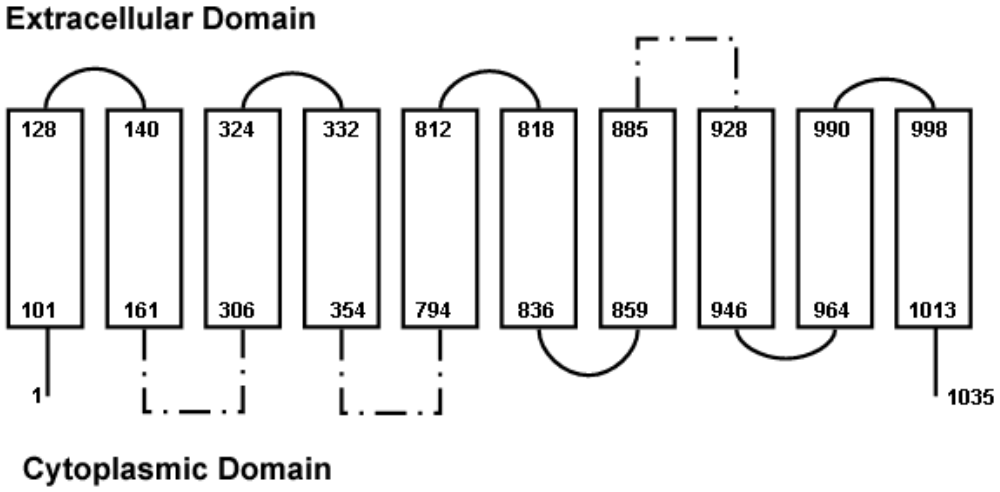

Figure 1-9 Schematic representation of the transmembrane region of the gastric H/K-ATPase showing the 10 putative membrane domains and their sequence boundaries (after [77]). Short interherlical loops are shown in solid lines whereas longer extramembranous segments are indicated by the broken lines.

Despite its molecular weight of 114 kDa, the α-subunit appears as a 94 kDa band on SDS PAGE [78]. The β subunit has about 300 amino acids and molecular weight of 35 kDa but due to extensive glycosylation, it runs at 60-80 kDa on SDS PAGE [79]. The β subunit contains a single transmembrane region with the main body of the protein on the luminal side of the membrane. The function of the β subunit is not clear but is essential for correct packing and stable membrane insertion of the H/K-ATPase α subunit [80]. The β subunit may be promiscuous and can act as a surrogate for the β subunit of the Na/K pumps in *Xenopus* oocytes [81]. Similar promiscuity has not been observed in mammalian cell expression systems [82]. Other lines of evidence suggest that there are common

regions of interaction between α and β subunits in gHKA and Na/K-ATPases [77, 83].

Little is known about the structure of the αβ heterodimer. The low resolution three-dimensional crystal structure of porcine gHKA (Figure 1-10) revealed little more than a pear-shaped domain measuring 60 x 45 $Å^2$, with a height of 50 Å measured perpendicular to the membrane plane. A small stalk segment, 20 Å in length, forms a connection to the transmembrane domain [84]. Proteinase K proteolysis of open gastric tubulovesicles followed by FTIR analysis suggested that the protease-resistant membrane-protected segment contained 35% α-helical, 35% β-sheet, 20% turn and 10-15% random structure [85]. The α-helical components were perpendicular to the membrane. Examination of the hydrogen/deuterium exchange rates of the membrane part of the protein indicates that solvent has access to a large fraction of the protein, perhaps through the membrane or a pore defined by the protein [85].

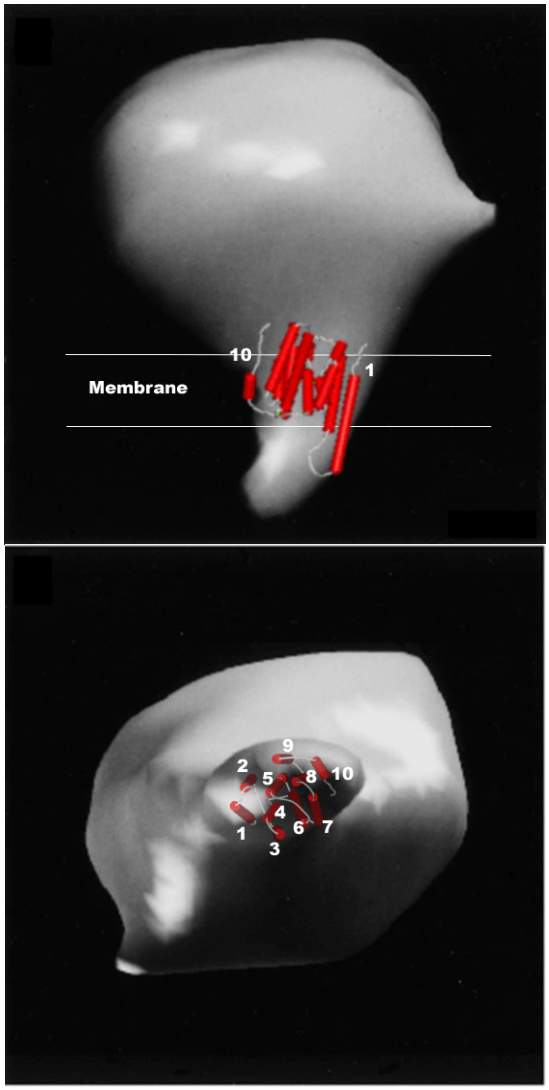

Figure 1-10 Schematic representations of gastric H/K-ATPase (after Xian *et al* [84]) with putative transmembrane region modelled from the Ca-ATPase [74] showing the large cytoplasmic domain of the proton pump, small transmembrane stalk with suggested arrangement of helices of the α-subunit, and small extracytoplasmic domain.

The H/K-ATPase is a P-type ATPase and, as such is phosphorylated at a conserved aspartate. Like the homologous Na/K- and Ca-ATPases, the H/K-ATPase exists as a phosphoenzyme during its catalytic cycle. Unlike the Na/K-ATPase, ion translocation by the H/K-ATPase is electroneutral [86] in the ratio $2K^+$:$2H^+$:1ATP. The enzyme has both a high- and a low-affinity site for ATP binding [87] and is also phosphorylated by inorganic phosphate in the presence of Mg^{2+} [88]. In the presence of Mg^{2+}, H/K-ATPase is phosphorylated at Asp 386

upon ATP hydrolysis [89]. There is Mg-stimulated basal activity involving slow dephosphorylation in the absence of K^+. With K^+ present, dephosphorylation is rapid and is coupled to the E_2P-E_2K^+-E_1K^+-E_1P transition (Figure 1-11). The overall catalytic cycle is accelerated by K^+, leading to rapid proton transport. The H/K-ATPase is also stimulated by a number of other monovalent cations in the order of effectiveness $Tl^+ > K^+ > NH_4^+ > Cs^+$ [90].

As with the homologous Na/K- and Ca-ATPases, H/K-ATPase exists as a phosphoenzyme during its catalytic cycle.

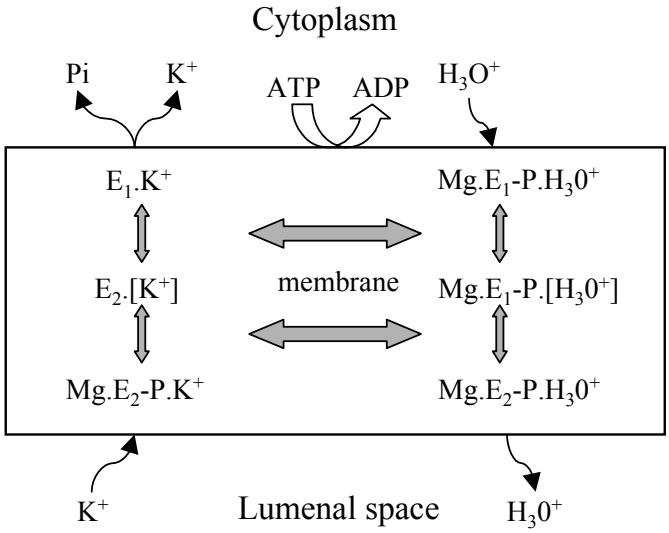

Figure 1-11 Model of the catalytic cycle of the gastric H/K-ATPase (after [91]). The low-affinity K^+-binding form E_1 has ion binding sites facing the cytoplasm. E_2, the high-affinity form for K^+ has ion binding sites facing the luminal space. A hydronium ion is thought to be transported into the gastric lumen upon conversion of the E_1.P to E_2.P. Binding of K^+ to the lumenal side of the protein results in dephosphorylation of the pump, the loss of bound Mg, and the conformational change to the $E_1.K^+$ form. Both ions are occluded (as $[K^+]$ and H_3O^+, above) during the transport cycle.

Upon phosphorylation, the outward-facing ion-binding site of high affinity [E1] changes to an outward-facing ion-binding site with low affinity [E2] [91, 92]. An intermediate state that occludes the hydronium ion, inferred from rate studies in Na/K-ATPase, Ca-ATPase, has also been eventually observed in H/K-ATPase

[93-95]. Following extrusion of the hydronium ion outside, the counter-ion binds enabling dephosphorylation of [E2]-phosphate. E2 in the bound counter-ion state makes the transition to the E1 state with release of the inwardly-transported ion. Chemical modification of the α subunit at Lys549 in the cytoplasmic region of the protein with the fluorescent probe fluorescein isothyocianate (FITC) suggested that about 70% of unliganded H/K-ATPase molecules reside in the E1 state [96].

Inhibition of the gastric proton pump

Irreversible Inhibition

P-type ATPases form a large family [97] and a putative inhibitor should be protein-specific. The compound should preferably act at the extra-cytoplasmic lumenal interface or within the membrane and not be absorbed into the cell and on into the blood. Moreover, a successful inhibitor should be concentrated in the the low pH fundic region where H/K-ATPase is most abundant. A weak, protonatable base with pKa < 6.0 will accumulate at pH 1.0 and ignore other acid spaces such as lysosomes and endosomes. Selective inhibition of H/K-ATPase by substituted benzamidazoles such as omeprazole and lanzoprazole has been reported [67]. Cysteine 813 in the lumenally-exposed M5-M6 interhelical loop has been implicated as the binding site of modification for omeprazole [98]. The high proton concentration is thought to increase the reactivity of C2 in the substituted benzamidazole, facilitating attack by the unprotected N of the pyridine ring (Figure 1-12). Through a common mechanism of molecular

rearrangement, an activated sulfenamide cation is formed that is membrane impermeable and stable at acidic pH.

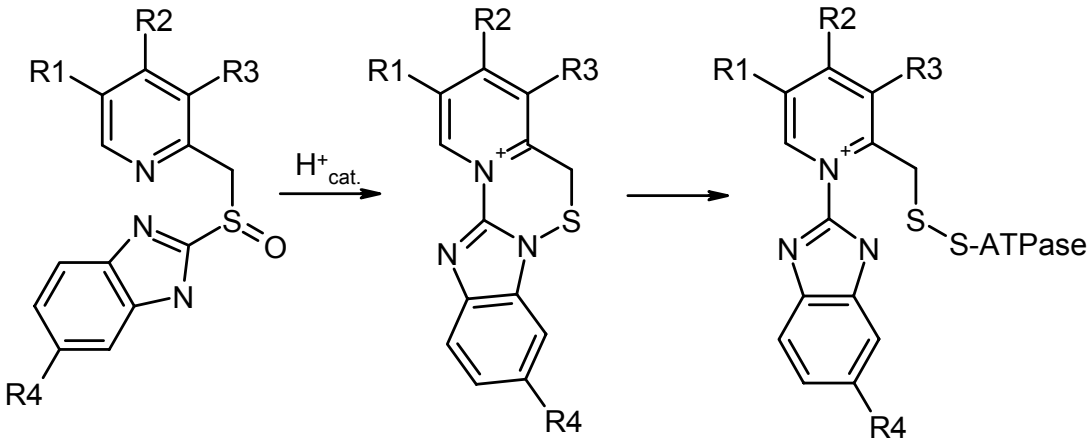

Figure 1-12 Acid catalysed rearrangement of subsitituted benzamidazoles. An activated sulfenamide intermediate is formed which then reacts with distinct free thiol groups in the lumenal side of the proton pump α subunit.

The active sulfenamide reacts with available thiols in the gastric lumen. Omeprazole modified a number of cysteines but only modification of Cys 813 is inhibitory [98].

Reversible Inhibition

There is concern about the suggested development of gastric carcinoid tumour types in patients undergoing chronic treatment and atrophic gastritis, a precursor of gastric cancer, has been reported with long-term omeprazole use in the presence of *H. pylori* [99].

The compound 2-methyl,3-cyanomethyl-8-[(phenylmethoxy)imidazo[1,2-*a*]pyridine (SCH28080) and its substituted imidazopyridine derivatives (Figure 1-13) are high-affinity reversible inhibitors of the gastric proton pump [100, 101]

and have a shorter-acting duration while retaining gastric anti-secretory and cytoprotective properties [102].

The compounds are K^+-competitive and bind in protonated form to the high-affinity K^+ site in the extra-cytoplasmic surface of the protein [103, 104] with a dissociation constant, K_D, of 45 nM. The most extensively studied is SCH28080, which was withdrawn as a drug candidate but is a valuable probe of the inhibitory binding site.

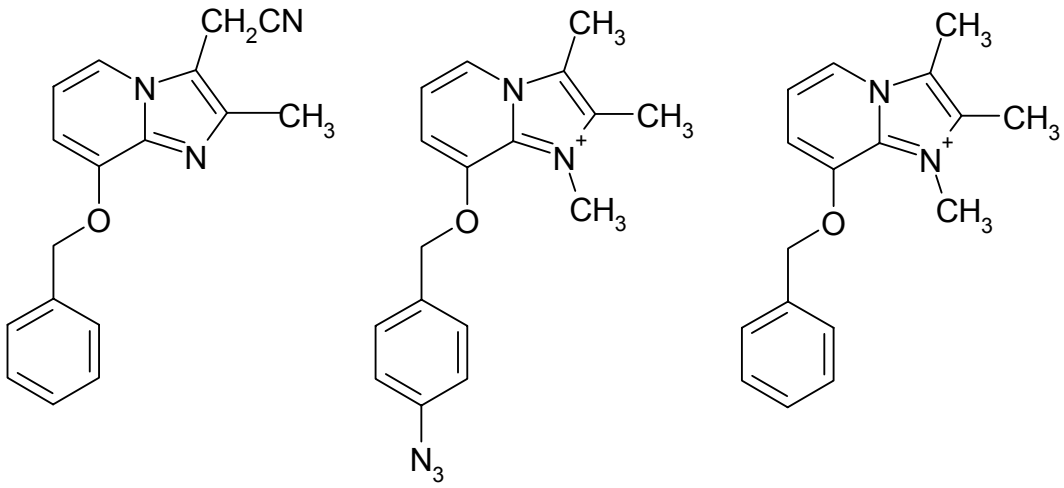

Figure 1-13 Chemical structures of some substituted imidazopyridines (SIPs): left to right, SCH28080, mDAZIP and TMPIP

The site of reversible inhibition is poorly defined. The photoaffinity ligand 2,3-dimethyl-8-[(4-azidophenyl)methoxy]imidazo[1,2-*a*]pyridine (mDAZIP), is an analogue of SCH28080 and acts as a K^+-competitive inhibitor in the dark. Irradiation produces irreversible loss of activity as the $-N_3$ group of the phenyl ring reacts covalently with neighbouring residues. Munson and co-workers [105, 106] localised mDAZIP to the first and second putative transmembrane helices (M1 and M2) of the α subunit by photoaffinity labelling and subsequent protein digests. A computer model based on the structure of mDAZIP considered Phe126 and Asp138 to be of importance in ion selection but site-directed mutagenesis of

these residues has cast doubt about their value in stabilising the ligand in the binding site [107].

Site-directed mutagenesis has implicated a number of residues in the putative transmembrane region of the α subunit (Figure 1-14). Glu822 was found to be important for ATPase function but the carboxyl residue was not indispensable, although it is suggested to be involved in determining the affinity of H/K-ATPase for K^+ [108]. Glu820 in rat gastric H/K-ATPase is the counterpart of rabbit Glu822. This residue and Glu795 were demonstrated by site-directed mutagenesis to have a significant role in K^+ binding and the transition to the E_2 form of the enzyme [109]. Recently, the M5-M6 helices were demonstrated to move from a proteolytically sensitive state to a stabilised form upon occlusion of K^+ [110]. Glu820 in the interhelical space between M5 and M6 has also been implicated as the site of interaction of SCH28080 [111]. A further contribution to an understanding of the binding site can be taken from the recent work of Munson and co-workers [112], which showed that the binding affinity of SCH28080 is reduced by mutations of residues Met330 and Met334 in the transmembrane domain M4. The M4 helix is of particular interest here because of its possible location adjacent to M1 and M6, and it is therefore possible that the methionine residues form part of the SCH28080 binding site.

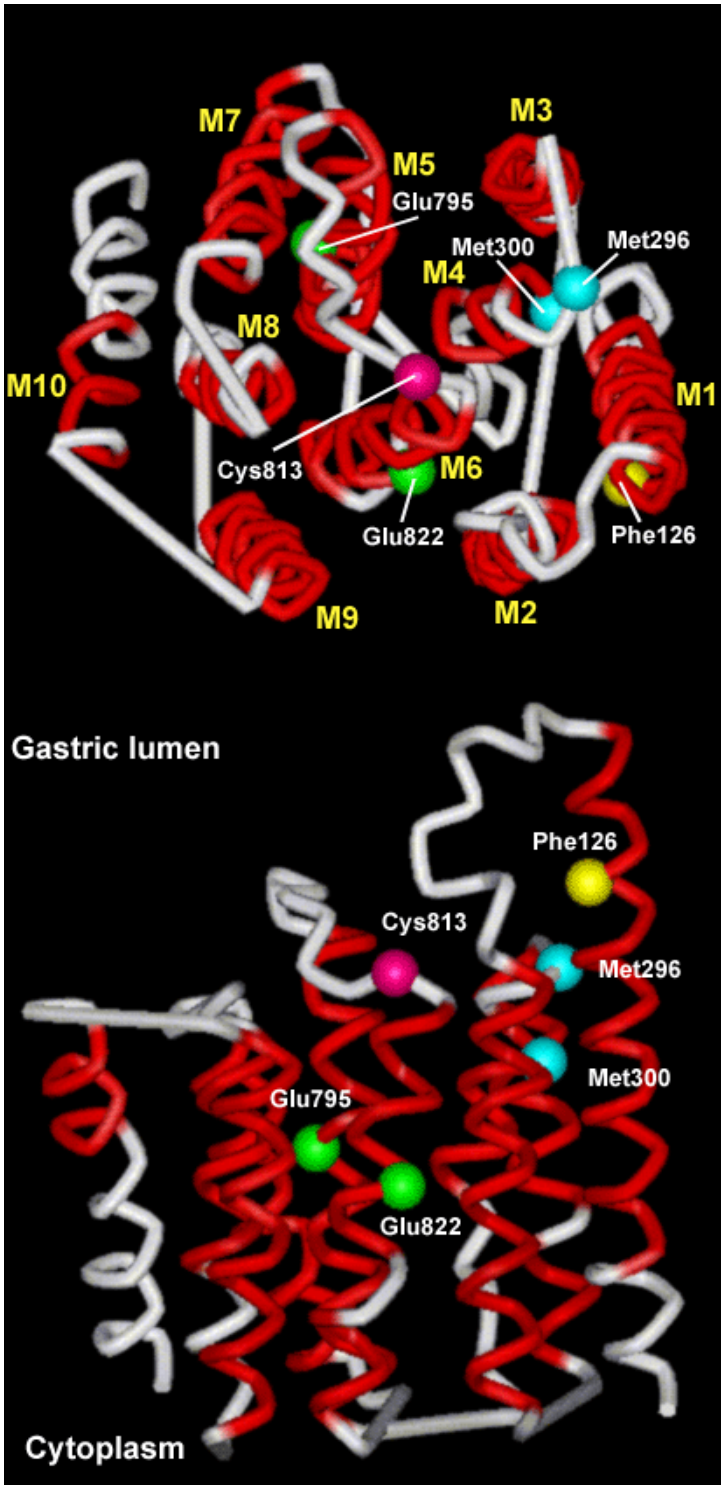

Figure 1-14 Molecular model of the transmembrane region of H/K-ATPase based on the co-ordinates of the SERCA1 Ca^{2+} ATPase structure [74]. Highlighted residues (F126, yellow; M296 and M300 blue; C813, pink; and E795 and E822 green) were positioned by sequence threading discussed in Chapter 5. Top image shows view from lumenal face and indicates relative positions of transmembrane helices M1-10. Bottom image shows side view through the membrane.

Although the recent Ca-ATPase structure is an important template, there is relatively little known about the organisation of the helices in the transmembrane segment of the catalytic α subunit and the binding sites for SIPs. An understanding of ligand conformations may reconcile the site-directed mutagenesis information with the photoaffinity studies and can impose constraints on helix-helix interactions and the environment of the inhibitor binding site which, despite the recent 8 Å three-dimensional crystal structure of the porcine H/K-ATPase [84], remain unobserved.

Aims of the Thesis

Chapter 2 describes the synthesis, characterisation of novel substituted imidazo[1,2-*a*]pyridines as inhibitors of the gastric H/K-ATPase and their appropriateness for study by deuterium and REDOR solid state NMR spectroscopy.

Chapter 3 introduces the theory of broad line deuterium NMR spectroscopy and its application to the investigation of the mechanism of association of substituted imidazo[1,2-*a*]pyridines with the gastric H/K-ATPase and gastric lipids and the correlation between observed motional restriction and inhibitory potency of site-specifically deuterated molecules.

Chapter 4 introduces the theory of REDOR NMR spectroscopy and its application to determining the structure of 1,2,3-trimethyl-8-(perfluorophenylmethoxy) imidazo[1,2-*a*]pyridinium iodide (TMPFPIP), a ^{13}C and ^{19}F site-specifically labelled K^+ competitive analogue of SCH28080 and inhibitor of the gastric H/K-ATPase at its high-affinity site of action. The study demonstrates the potency of using ^{13}C and ^{19}F as non-perturbing NMR probes in determining, to high precision, structures of ligands at their sites of efficacy in membrane proteins.

Chapter 5 reviews the structural data available for the gastric H/K-ATPase and, in combination with recent site-directed mutagenesis studies, presents an original model of the gastric H/K-ATPase that reconciles these bodies of information

with the REDOR NMR high-resolution structure available for TMPFPIP at its binding site in the ATPase. A new model generated using the recent 2.6 Å structure of the related Ca-ATPase considers the relative locations of antagonist binding residues in the gastric H/K-ATPase the possible available interactions with SCH28080 and its analogues.

Chapter 6 describes how macroscopic orientation of membrane proteins for solid state ^{31}P and ^{2}H NMR allows the dynamics and orientation of pharmacologically important ligands in their protein binding sites to be observed and measured, thus advancing understanding of the ligand binding mechanism when there may be little other available structural information for the membrane protein. The nicotinic acetylcholine receptor labelled with a deuterated acetylcholine analogue is used to demonstrate the value of this technique and in establishing a paradigm for future orientation of labelled gastric H/K-ATPase.

Chapter 7 draws together the findings of this thesis and suggests directions that may be followed as future considerations in order to understand more fully the H/K-ATPase and the interaction between the protein and its inhibitors.

Chapter 2

SYNTHESIS AND FUNCTIONAL CHARACTERISATION OF REVERSIBLE INHIBITORS OF THE H/K-ATPASE

Introduction

There are currently three approaches that may be taken in the current treatment of gastrointestinal ulcer disorders. Antibiotic eradication of *Helicobacter pylori* infection forms the core therapy; this can be coupled with drugs to suppress acid secretion by the parietal cells of the fundic region of the stomach and ameliorate ulceration. Drugs that lower gastric acidity (Figure 2-1) include histamine receptor antagonists (H_2RAs) and covalent proton pump inhibitors (substituted benzamidazoles). Proton pump antagonists (substituted imidazopyridines) would be a desirable new class of drugs that does not require regeneration of the cellular proton-pumping apparatus before efficient digestion can be resumed.

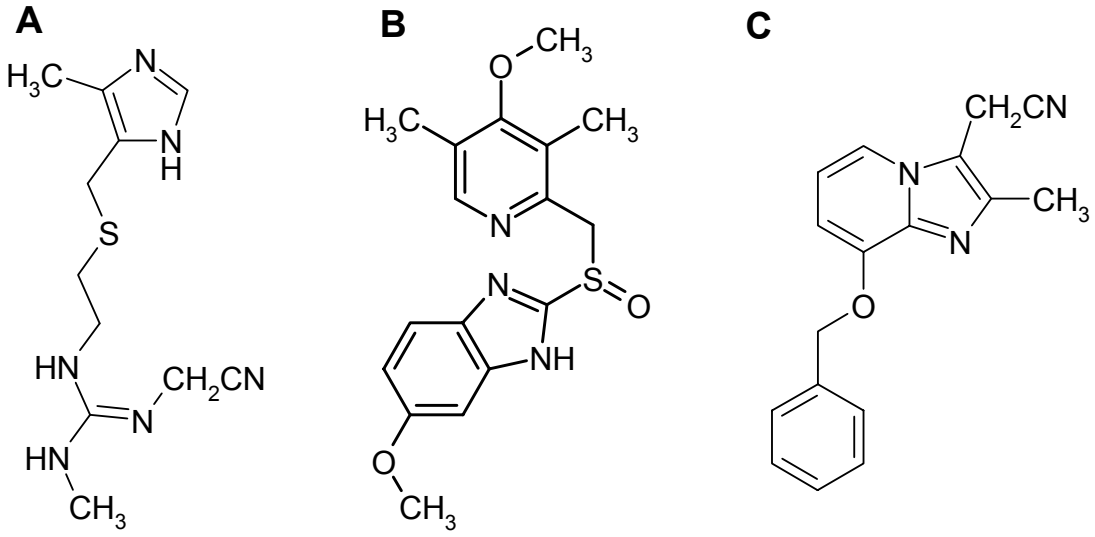

Figure 2-1 Antagonists and inhibitors of acid secretion: structures of (A) cimetidine [113], (B) omeprazole [67] and (C) SCH28080 [100, 101].

H_2RAs, such as cimetidine attenuate the sensory-stimulated feeding response and ultimate activation of acid secretion by the parietal cells. Receptor blocking by cimetidine leads to loss of cAMP/Ca^{2+} triggered recruitment of the H/K-ATPase, the enzyme responsible for acidification of the gastric lumen from tubulovesicles, to the parietal canalicular membrane. However, H_2RAs as targets have disadvantages. Since they antagonise histamine receptors, their effects are wide-ranging and not limited exclusively to inhibition of acid secretion. Hence, H^+-pumping is inhibited indirectly. For the treatment of gastroesophagael reflux disease (GERD), because they inhibit acid production at the site of secretion, covalent proton pump inhibitors (PPIs) such as omeprazole, and the close analogues pantoprazole and lanzoprazole, are much more effective than H_2RAs when given at dosages effective for healing duodenal and gastric ulcers [114]. As a comparison of the different treatments, symptomatic relief of GERD is observed in 27% of placebo-treated, 60% of H_2RA-treated and 83% of PPI-treated patients. In addition, esophagitis is healed in 24% placebo-treated, 50% H_2RA-treated and 78% PPI-treated patients [115]. Furthermore, patient adverse event withdrawals are higher with H_2RAs than with PPI treatment and healing is slower when the histamine pathway is targeted [116, 117].

Proton pump inhibitors and proton pump antagonists, when weakly basic, are active only in an acidic environment and act directly at the H/K-ATPase to limit extrusion of acid from the parietal cell. As such, inhibition of acid secretion is direct and targeted to the site of acid production. PPIs bind characteristically free cysteine sulphydryl groups of exposed cysteine residues at the luminal face of the protein. Common to all PPIs, and coincident with inhibition, is covalent

modification of Cys813 (Figure 1-11) in the loop between the 5th and 6th transmembrane segments [91].

Inhibition by substituted benzamidazoles is irreversible. These inhibitors undergo an acid-catalysed rearrangement which results in a profound decrease in acid secretion. The parietal cell must recycle the canalicular membrane to remove inactivated gastric H/K-ATPase and upregulate H/K-ATPase expression before acid secretion and efficient digestion may resume. The subsequent drop in luminal acidity results in increased gastrin production from antral G cells and sustained increases in serum gastrin, which assists histamine in expression and activation of the H/K-ATPase [118]. There is concern about the suggested development of gastric carcinoid tumour types in patients undergoing chronic treatment and atrophic gastritis, a precursor of gastric cancer, which has been reported with long-term omeprazole use in the presence of *H. pylori* [99]. PPIs are nonetheless prescribed for long-term use in gastric acid management and have been an extremely successful therapeutic strategy.

Substituted imidazopyridines, like SCH28080 (Figure 2-1) are K^+-competitive [100, 101], non-covalent reversible inhibitors of the H/K-ATPase which have a shorter-acting duration while having gastric anti-secretory and cytoprotective properties [102]. SCH28080 inhibits K^+-stimulated (5mM) ATP hydrolysis with an *in vitro* IC_{50} (concentration giving 50% inhibition of total activity) of 1.3 μM [100]. SCH28080 forms a complex with the phosphorylated (E2-P) form of the enzyme to prevent K^+-stimulated dephosphorylation of the ATPase. The inhibitors are weak bases (pK_a ~5.5) that concentrate in the acidic fundic region of the stomach and bind to the lumenal face of the enzyme. The molecular basis of inhibition by SCH28080 and its close analogues is unclear. Preincubation of

H/K-ATPase with SCH28080 prevents covalent binding of Cys813 by omeprazole [119], indicating that there is some overlap between the two sites of inhibition. Site-directed mutagenesis studies have implicated residues in M4 [112] and the M5/M6 loop region [108]. In order to reconcile these data and to construct a model of the active site of inhibition, the structure and dynamics of SCH28080 analogues have been examined, with subtle modifications in molecular composition providing valuable insight into the nature of the interaction of this class of inhibitors and their target, the gastric H/K-ATPase.

Aims of This Study

SCH28080 has been extensively studied but its mechanism of action remains poorly understood. The binding site for this inhibitor appears to embrace several regions of the transmembrane domain of the gHKA and the imposition of a full set of structural constraints of close analogues of SCH28080 would help resolve the importance of various residues suggested to be of significance at the site of inhibition. The aim of this study is to produce an analogue of SCH28080 that is both functionally active but is also isotopically labelled for structure determination and dynamic studies using solid state NMR. In order to measure precisely large (>8 Å) intramolecular distances in these analogues, ^{19}F and ^{13}C is site-specifically introduced into the compounds for later examination by rotational echo double resonance (REDOR) NMR. The chemistry for this process must be developed and the final SIPs must be assessed for inhibitory potency. To better understand the importance of functional groups in the binding mechanism of these inhibitors compounds have been synthesised to contain ^{2}H

such that the molecular dynamic information reported by wide line deuterium NMR may be exploited.

To explore the relationship between structure and activity, three classes of substitution have been considered: the effects of fluorine on the 8-aryl group; the influence of methyl substitution in the 3-position of the imidazo ring; the importance of π-interaction between the aryl group and available π systems of the protein (Figure 2-2).

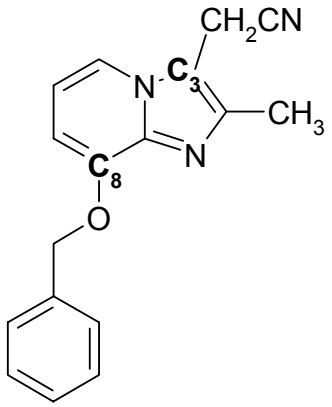

Figure 2-2 2-methyl-3-cyanomethyl-8-(phenylmethoxy)imidazo[1,2-*a*]pyridine (SCH28080) with sites of substitution indicated in bold. The cyanomethyl group is varied at position C3 to H- and CH_3-. A variety of fluorinated aryl compounds are substituted at the C8 position.

The results of these studies have determined the viability of fluorinated SCH28080 analogues for ^{13}C-^{19}F rotational echo double resonance (REDOR) NMR structure determination experiments and the suitability of these compounds for ^{2}H wide line static solid state NMR investigation of ligand dynamics in the binding site. The coalition of conventional structure-function relationships with conformation measurements and dynamic information allows construction of a coherent model of this pharmaceutically important class of proton pump antagonists at their site of inhibition.

Materials and Methods

Enrichment of Porcine Gastric H/K-ATPase Membranes

Gastric membrane vesicles enriched with H/K-ATPase were prepared according to a method modified from that previously described [78]. Fresh hog stomachs were obtained and transported on ice in a solution of saturated NaCl. Stomachs were selected which had highly folded fundic regions and which were free of tumours and ulcers. The stomach sac was washed of excess mucous and any remainder was removed by scraping the fundic region with the blunt edge of a knife and with vigorous rubbing with paper towelling. When no more mucous could be removed in this way, the trimmed tissue was laid out in ice-cold saturated NaCl solution which was 5 mM Tris/HCl, pH 7.4 and allowed to stand for five minutes before drying with paper towels. The scraping procedure was continued until no more mucous could be removed.

Membrane enrichment was carried out at 4 °C. Mucosal tissue slices were removed from the translucent basement membranes using a dulled kitchen knife. 60 g batches of crude fundic slices were minced through a press and suspended in Isolation Buffer (0.25 M sucrose, 5 mM PIPES, 5 mM Tris-HCl, pH 7.4). The parietal cell-rich suspension was homogenised using 5 strokes of a mechanical homogeniser operating at approximately 2000 rpm. The homogenate was separated by ultracentrifugation (14000 g, 20 min) and the resulting supernatant was centrifuged to form a pellet (125000 g, 45 min). The pellet was resuspended in Isolation Buffer and homogenised by 3 strokes of a tight-fitting hand-held homogeniser. The suspension was layered over a sucrose/Ficoll density gradient

(from bottom: 15 mL 30% (w/v) sucrose/5 mM Tris-HCl/5 mM PIPES, pH 7.4;/ 15 mL 7.5% Ficoll in Isolation buffer) and centrifuged (76000 g, 90 min).

GI microsomal membranes were collected as a brown band above the Ficoll/Isolation buffer interface, GII was collected as a volume of cloudy material below the GI band and above the Ficoll/30% sucrose buffer interface. The yields were maintained by 1:1 dilution in 60% (w/w) sucrose solution (5 mM TRIS-HCl/5 mM PIPES, pH 7.4) and were stored at –20 °C. A sample had been removed at each stage of the enrichment process to follow the purification procedure. Membranes prepared for lyophilisation were washed twice with 5 mM Tris/HCl, pH 7.4 and lyophilised overnight. The membranes were then resuspended in 5 mM Tris/HCl, pH 7.4 and stored at -20 °C.

Characterisation of Enriched Porcine Gastric H/K-ATPase Membranes

Determination of Protein Composition

Protein samples taken during the enrichment preparation (GI, GII) were analysed by 10-20% gradient Tricine SDS-PAGE [120] run against molecular weight markers (M_ws of 202, 133, 71.0, 41,8, 30.6, 17.8 kDa) and visualised by Coomassie Blue staining.

Determination of Protein Concentration

Protein concentration was determined using the modified method of Lowry [121] using bovine serum albumin as protein standards. Sucrose was removed from membrane samples by washing with centrifugation (247000 g, 60 min, 4

°C). The pellet was resuspended in 5 mM Tris-HCl/5 mM PIPES buffer at pH 7.4 prior to assaying.

Determination of H/K-ATPase Activity

Determination of ATPase activity was performed according to a method modified from that described by LeBel [122]. GI lyophilised membranes (10 μg) were added to 0.5 mL Assay Medium (2 mM $MgCl_2.6H_20$, 2 mM ATP, 20 mM Tris (pH 7.4), 40 mM KCl) and inhibitor. The mixture was incubated (37 °C, 30 min) and quenched by addition of 1 mL ice-cold acid-molybdate (4:1 5% ammonium molybdate: 60% perchloric acid). ATPase activity was estimated as a release of inorganic phosphate from ATP into butyl acetate at 320 nm. K^+-stimulated activity was estimated by subtracting basal activity due to Mg^{2+} stimulation from the activity of the enzyme in the presence of K^+ and Mg^{2+} and comparing to a standard curve produced by varied concentrations of inorganic phosphate in Assay Medium.

Determination of Inhibitor Activity

Substituted imidazo[1,2-*a*]pyridines were dissolved in ethanol to a maximum concentration of 5 mM. The final ethanol concentration upon pipetting an aliquot of inhibitor solution was 2% and was regarded to have no effect on the enzyme preparation [123]. The final concentration range of inhibitor assessed in the assay was 0.1 mM – 10 nM. Typically, between 2.5 – 10 μL of inhibitor solution were added to 10 μg protein in assay medium and incubated (30 min, 37 ˚C). After this time, the reaction was stopped by quenching by addition of 1

mL ice-cold acid-molybdate (4:1 5% ammonium molybdate: 60% perchloric acid). ATPase activity was estimated as a release of inorganic phosphate from ATP into butyl acetate at 320 nm. K^+-stimulated activity was estimated by subtracting basal activity due to Mg^{2+} stimulation from the activity of the enzyme in the presence of K^+ and Mg^{2+}. All assays were performed in triplicate on three preparations unless otherwise indicated. The IC_{50} values were defined as the inhibitor concentration that produced 50% inhibition of K^+-stimulated ATPase activity [32]. The IC_{50} values were calculated by non-linear least-squares fitting of a logistic sigmoidal function to the normalised experimental data using Microcal™ Origin™ 5.0. (Equation 2-1).

$$y = \min + \frac{(\max - \min)}{1 + e^{(-k(x - Xmid))}}$$ **Equation 2-1**

Where y and x are variables, k and $Xmid$ are constants varied in the simulation, and max and min define the range of the dataset. The sample size was based on three assays each measured in triplicate for each compound.

Preparation of Substituted Imidazo[1,2-*a*]pyridines

A series of analogues of the potent proton pump reversible inhibitor SCH28080 was synthesised using the methods of Kaminski [124-126] and adaptations thereof. The general structure is shown in Figure 2-3 and the compounds synthesised are presented in Figure 2-4. A generalised schematic overview for the synthesis is presented in Figure 2-5.

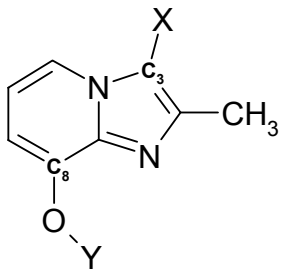

Figure 2-3 Template for imidazopyridine substitutions. SCH28080 contains a cyanomethyl substitution at X which is attached to C3 of the imidazo ring as indicated. CH_3- and H- substitutions were studied at C3 here. Y in SCH28080 is a phenyl ring. Substitutions at this C8 hydroxyl group include fluorinated aryl and butyl groups.

All compounds were derived from 2,3-dimethylimidazo[1,2-*a*]pyridin-8-ol (DMHIP) and 2-methylimidazo[1,2-*a*]pyridin-8-ol (MMHIP), which were synthesized by methods described previously [124] (steps 1 & 2 in Figure 2-4). Step 3 introduced a substituent at the 8-position of the fused ring. Step 4 produced the final pyridinium iodide salt of a given compound. Typical reactions are presented when the same reaction route is taken. The progress and purity of reactions and products was followed by thin-layer chromatography and product purity was determined by ^{1}H NMR and Atmospheric Pressure Chemical Ionisation (APCI) Mass Spectrometry.

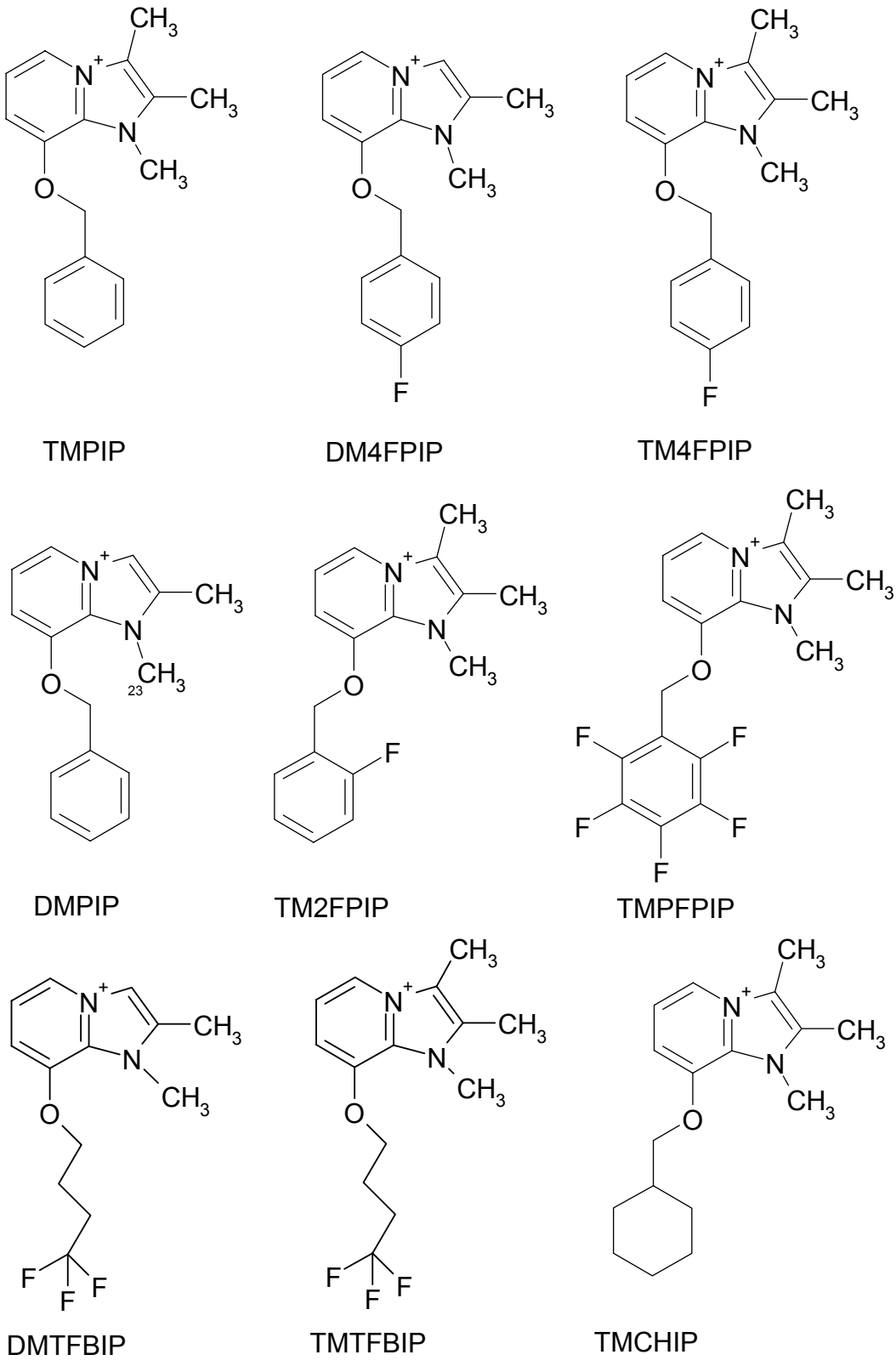

Figure 2-4 Combinations of substituted imidazopyridines considered in this study. Some species were isotopically-enriched labelled with either $^{13}CH_3$- or C^2H_3- (d_3-) groups for the purposes of experiments described in Chapters 3 & 4.

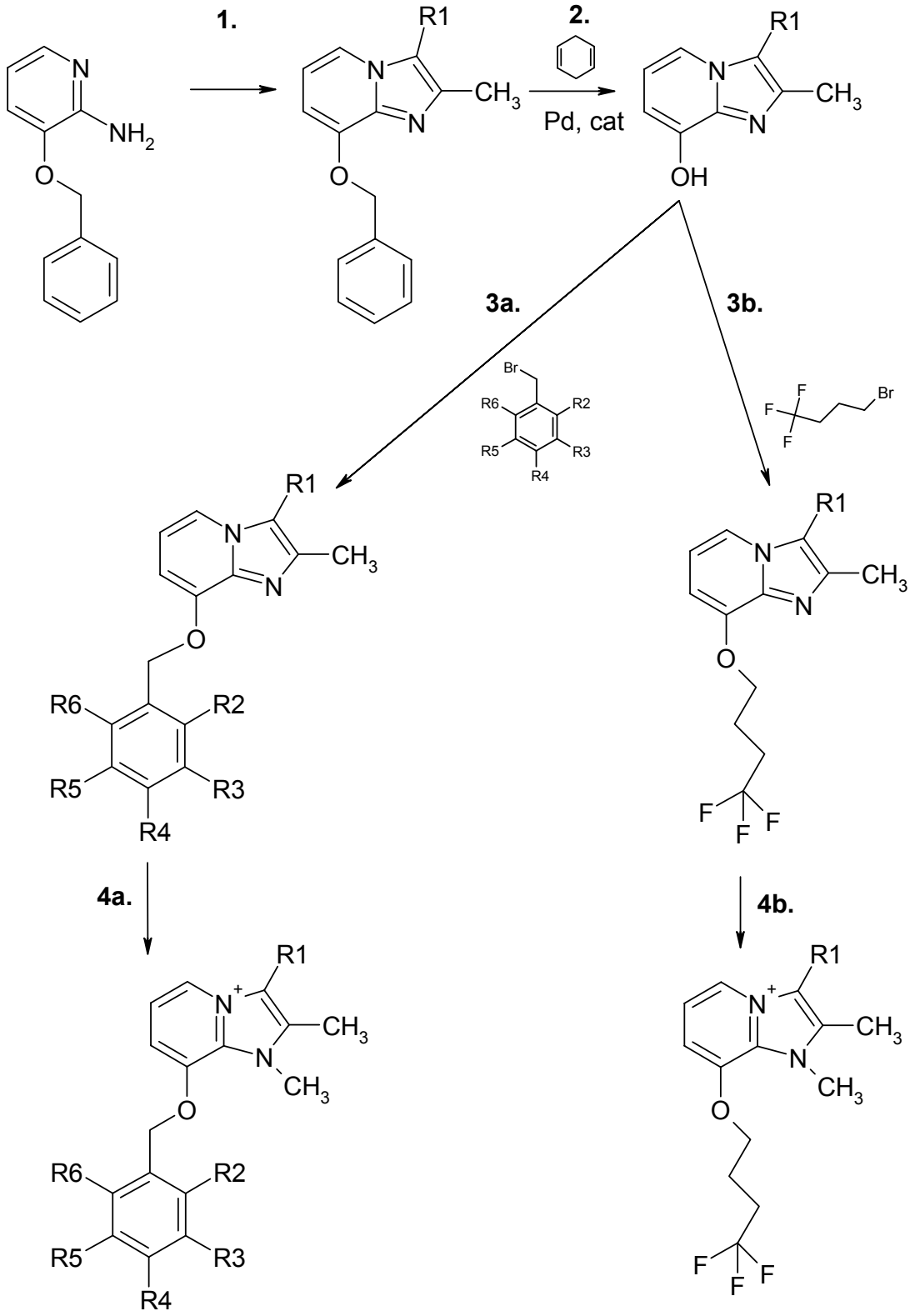

Figure 2-5 Reaction scheme for the preparation of substituted imidazo[1,2-*a*]pyridines. Steps 1 and 2 are common to the synthesis of all compounds in this study. Substitution of phenyl and fluorophenyl groups follows route 3a and 4a. The generation of a butyl compound follows the scheme presented in 3b and 4b. Reactive groups R1-R6 as indicated in the text describing synthesis.

Synthesis of 2-methyl,8-(phenylmethoxy)imidazo[1,2-a]pyridine (MMPIP) (R1 = H): Reaction 1

To 3 g (15.0 mmol) 2-amino-3-benzyloxypyridine in ethanol was added 3 mole equivalents (4.16 g) of chloroacetone (Aldrich Chemical Co., Gillingham, UK). The reaction was stirred under reflux for 20 hr after which a further mole equivalent of chloroacetone was added to the reaction mixture. The reaction was continued for 5 hr after which it was removed from the heat and the solvent was removed by rotary evaporation under reduced pressure. Crude residue was taken up in water and the pH adjusted to pH 11.5 – 12.0 with 50% (w,w) sodium hydroxide solution prior to extraction into chloroform. The aqueous phase was washed three times with 250 mL volumes of chloroform and the organic phases pooled. After concentrating the organic phase, the mixture was separated on a Si60 Keiselgel silica column (Merck, Darmstadt, Germany), eluting with chloroform/ethyl acetate in a 4:1 ratio. The first fraction was identified by Thin Layer Chromatography (TLC) and collected for concentration. The pure, dry residue gave 2.22 g (9.25 mmol) (62%) of 2-methyl,8-(phenylmethoxy)imidazopyridine.

Synthesis of *2,3* Dimethyl,8-(phenylmethoxy)imidazo[1,2-a]pyridine (DMPIP) (R1 = CH_3): Reaction 1

To 3 g (15 mmol) 2-amino-3-benzyloxypyridine in ethanol was added 3 mole equivalents (6.80 g) (45 mmol) 3-bromo-2-butanone (Lancaster Synthesis Ltd, Morecambe, UK). The mixture was stirred under reflux for 20 hr, after which a

further mole equivalent of 3-bromo-2-butanone was added. The reaction was stirred under reflux for 5 hr, allowed to cool. Removal of the solvent under reduced pressure rotary evaporation afforded a beige residue. Precipitation from water gave fine white crystals. The precipitate was filtered and 2.52 g (9.82 mmol) (67%) 2,3-dimethyl,8-(phenylmethoxy)imidazo[1,2-*a*]pyridine was obtained from recrystallisation of the residue from minimal hot methanol.

Synthesis of 2-methylimidazo[1,2-*a*]pyridin-8-ol (R1 = H) and 2,3-dimethylimidazo[1,2-*a*]pyridin-8-ol (R1 = CH_3): Reaction 2

Generation of the 8-ol compounds followed the same reaction route. The conditions for 2,3-dimethylimidazo[1,2-*a*]pyridin-8-ol are reported here.

To 2.63 g (10.4 mmol) 2,3-dimethyl,8-(phenylmethoxy)imidazo[1,2-*a*]pyridine in 50 mL dimethylformamide was added 5 mole equivalents (4.17 g) (52.0 mmol) 1,4-cyclohexadiene and 80 mg palladium black. The mixture was heated to 80 ˚C before removing from the heat and was then allowed to react for 2 hrs. After this time, palladium black was removed by filtration through PTFE (0.2 μm pore diameter) and solvent was removed by roatary evaporation under reduced pressure. Final recrystallisation from minimal hot methanol gave 1.56 g (9.51 mmol) (91%) 2,3-dimethylimidazo[1,2-*a*]pyridin-8-ol.

Recrystallisation of 2-methylimidazo[1,2-*a*]pyridin-8-ol from minimal hot methanol gave 893 mg (5.96 mmol) (70%).

Synthesis of 8-aryl substituted imidazopyridines: Reaction 3a.

2-Methyl,8-(*p*-fluorophenylmethoxy)imidazo[1,2-a]pyridine (R1=H, R2=F, R3-6=H), 2,3-dimethyl,8-(*m*-fluorophenylmethoxy)imidzo[1,2-a]pyridine (R1=CH_3, R2=F, R3-6=H), 2,3-dimethyl,8-(*p*-fluorophenylmethoxy)imidzo[1,2-a]pyridine (R1=CH_3, R2-3=H, R4=F, R5-6=H), 2,3-dimethyl,8-(pentafluorophenylmethoxy)imidzo[1,2-a]pyridine (R1=CH_3, R2-6=F) were prepared in the following way. To 1 mole equivalent 2-methylimidazo[1,2-*a*]pyridin-8-ol or 2,3-dimethylimidazo[1,2-*a*]pyridin-8-ol as appropriate, was added 5 mole equivalents potassium carbonate in dimethylformamide. After 30 minutes stirring under argon at room temperature, 1 mole equivalent 2-fluorobenzylbromide, 4-fluorobenzylbromide or pentafluorobenzylbromide (all Apollo Scientific Ltd, Whaley Bridge, UK) was added as appropriate and the reaction was allowed to stir for 48 hours during which a scarlet colour developed. The reaction was stopped by drop-wise neutralisation with 1.0 M HCl until the pH was reduced to below pH 7.0. The mixture was filtered and washed with chloroform. The organic phases were pooled and concentrated to give a crimson oil which was then separated on a Si60 Keiselgel silica column (Merck, Darmstadt, Germany), eluting with chloroform:ethylacetate (4:1). The first and second bands were typically inseparable and accounted for the beige-coloured products which, upon drying, yielded 2-methyl,8-(*p*-fluorophenylmethoxy)-imidazo[1,2-*a*]pyridine (47%), 2,3-Dimethyl,8-(*m*-fluorophenylmethoxy)imidazo[1,2-*a*]pyridine (59%), 2,3-Dimethyl,8-(*p*-fluorophenylmethoxy)imidazo[1,2-*a*]pyridine (13%), 2,3-Dimethyl,8-(pentafluorophenylmethoxy)imidazo[1,2-*a*]pyridine (21%).

Synthesis of 8-acyl substituted imidazopyridines: Reaction 3b

2-Methyl,8-(trifluorobutylmethoxy)imidazo[1,2-a]pyridine (R1=H), 2,3-dimethyl,8-(trifluorobutylmethoxy)imidzo[1,2-a]pyridine (R1=CH_3) and 2,3-dimethyl,8-(cyclohexamethyoxy)imidazo[1,2-a]pyridine (R1=CH3) were synthesised in the following way. To 1 mole equivalent 2-methylimidazo[1,2-*a*]pyridin-8-ol or 2,3-dimethylimidazo[1,2-*a*]pyridin-8-ol as appropriate, was added 5 mole equivalents potassium carbonate in dimethylformamide. After 30 minutes stirring under argon at room temperature, 1 mole equivalent 1,1,1-trifluoro-4-bromobutane or 1-bromomethylcyclohexane (Apollo Scientific Ltd, Whaley Bridge, UK) was added as appropriate and the reaction was allowed to stir for 48 hours during which a scarlet colour developed. The reaction was stopped by drop-wise neutralisation with 1.0 M HCl until the pH was reduced to below pH 7.0. The mixture was filtered and washed with chloroform. The organic phases were pooled, concentrated and decolourised with activated carbon before drying over anhydrous Mg_2SO_4. The solution was fritted through Keiselgel 60 silica (Merck, Darmstadt, Germany) and anhydrous Mg_2SO_4. This step removed the carbon and polar impurities.

Synthesis of *N*-methylated substituted imidazopyridines: Reactions 4a and 4b

The quaternary ammonium compounds TMPIP, DM4FPIP, TM4FPIP, DMPIP, TM2FPIP, TMPFPIP, DMTFBIP, TMTFBIP, TMCHIP (structures defined in

Figure 2-4) were prepared as iodide salts by reaction of the appropriate tertiary amine with 5 mole equivalents methyl iodide (Aldrich Chemical Co., Gillingham, UK) in 5 ml acetone. For ^{13}C labelled compounds, ^{13}C-methyl iodide was used in place of the natural isotope abundance reagent. Similarly, for *N*-C^2H_3 compounds, d_3-methyl iodide (Aldrich Chemical Co., Gillingham, UK) was used. The reaction was stirred under reflux until a precipitate had formed. The reaction was removed from the heat and allowed to cool with stirring. The mixture was filtered, washed with ether and recrystallized from water. Purity of compounds was assessed by ^1H-NMR and Pressure Chemical Ionisation (APCI) Mass Spectrometry. The ^1H NMR δ_H values of novel SIPs are presented below.

DM4FPIP ^1H-NMR (methanol-d_4, 200 MHz): δ_H 2.50 (s, 3H, 2-CH_3); 4.10 (d, 3H, N-$^{13}CH_3$; 5.35 (s, 2H, 10-CH_2); 7.20 (t, 2H, ArH); 7.30 (t, 1H, 6-CH); 7.45 (d,1H, 7-CH); 7.60 (m, 2H, ArH); 8.00 (s, 1H, 3-CH); 8.30 (d, 1H, 5-CH).

TM4FPIP ^1H-NMR (methanol-d_4, 200 MHz): δ_H 2.45 (s, 3H, 2-CH_3); 2.55 (s, 3H, 3-CH_3); 4.10 (d, 3H, N-$^{13}CH_3$; 5.35 (s, 2H, 10-CH_2); 7.20 (t, 2H, ArH); 7.30 (t, 1H, 6-CH); 7.45 (d,1H, 7-CH); 7.60 (m, 2H, ArH); 8.00 (s, 1H, 3-CH); 8.30 (d, 1H, 5-CH).

TM2FPIP ^1H-NMR (methanol-d_4, 200 MHz): δ_H 2.45 (s, 3H, 2CH_3); 2.55 (s, 3H, 3-CH_3); 4.10 (d, 3H, *N*-$^{13}CH_3$); 5.45 (s, 2H, 10-CH_2); 7.40 (m, 5H, ArH); 8.20 (d, 1H, 5-H).

TMPFPIP ^1H-NMR (methanol-d_4, 200 MHz): δ_H 2.45 (s, 3H, 2-CH_3); 2.55 (s, 3H, 3-CH_3); 4.05 (d, 3H, *N*-$^{13}CH_3$); 5.55 (s, 2H, 10-CH_2); 7.40 (d, 1H, 6-CH); 7.60 (d, 1H, 7-CH); 8.25 (d, 1H, 5-CH).

***d_3*-DMTFBIP** ^1H-NMR (methanol-d_4, 200 MHz): δ_H 2.20 (m, 2H, 13-CH_2); 2.55 (m, 5H, 2-CH_3 & 12-CH_2); 4.40 (t, 2H, 11-CH_2); 7.30 (t, 1H, 6-CH); 7.35 (d, 1H, 7-CH); 8.00 (s, 1H, 3-CH); 8.25 (d, 1H, 5-CH).

***d_3*-TMTFBIP** ^1H-NMR (methanol-d_4, 200 MHz): δ_H 2.25 (m, 2H, 13-CH_2); 2.45 (m, 2H, 12-CH_2); 2.50 (s, 3H, 2-CH_3); 2.55 (s, 3H, 3-CH_3); 4.40 (t, 2H, 11-CH_2); 7.35 (t, 1H, 6-CH); 7.4 (d, 1H, 7-CH); 8.15 (d, 1H, 5-CH).

***d3*-TMCHIP** ^1H-NMR (methanol-d_4, 200 MHz): δ_H 1.35 (m broad, 10H, C13-17-CH_2); 1.80 (m broad, 7H, 2-CH_3, 3-CH_3, C12-H); 4.15 (d, 2H, 11-CH_2); 7.35 (m, 2H, C7-CH & C6-CH); 8.15 (d, C5-CH).

Results

Enrichment of Porcine Gastric H/K-ATPase Membranes

GI and GII gastric membrane microsomes were obtained by differential and density gradient centrifugation [127]. GI and GII fractions were harvested from the interfaces of a discontinuous sucrose gradient and in principle differ in their protein content and in the leakiness. GI are sealed microsomes. The protein samples were separated by 10-20% gradient Tricine gel and stained with Coomassie Blue. A representative SDS-PAGE electrogram is presented in Figure 2-6.

A band corresponding to the 94 kDa α subunit of the H/K-ATPase was seen between the 83 and 175 kDa marker points (Figure 2-6). There was greater intensity in the GI lane than in GII indicating the greater enrichment of the subunit in the microsomal preparation. A band appeared between the 48 - 62 kDa marker points. This may be the glycosylated β subunit which is often unseen due to interference of the glycosylated site with Coomassie Blue staining [128]. Although predominantly H/K-ATPase-enriched, bands other than the 48-62 and 94 kDa bands were observed between the 17 - 25, and 33 - 48 kDa marker points, indicating contamination by either other proteins in the apical membrane or of other membranes in the GI and GII microsomal fractions.

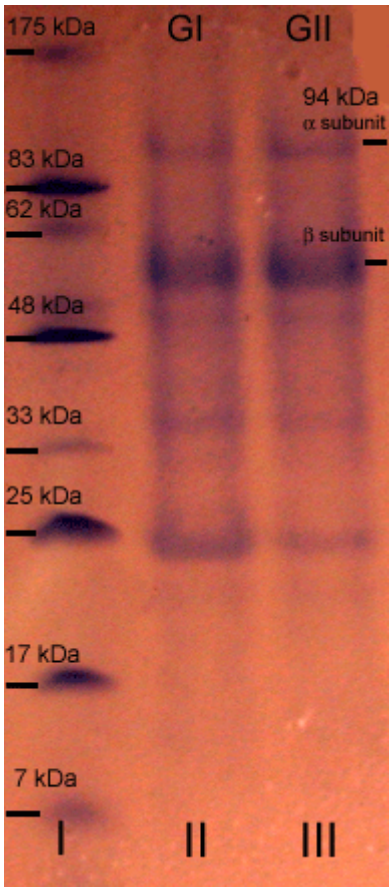

Figure 2-6 SDS-PAGE (10-20%) of gastric H/K-ATPase preparation showing molecular weight markers (Lane I: top to bottom – *E. coli* maltose-binding protein (MBP)-β-galactosidase, 175 kDa; *E. coli* MBP-paramyosin, 83 kDa; bovine liver glutamic dehydrogenase, 62 kDa; rabbit muscle aldolase, 48 kDa; rabbit muscle triosephosphate isomerase; 33 kDa, rabbit muscle triosephosphate isomerase; 25 kDa, bovine milk β-lactoglobulin A; 17 kDa, chicken egg white lysozyme; 7 kDa, bovine lung aprotinin. GI preparation (0.25 M sucrose/7.5% Ficoll interface) (Lane II) GII preparation (7.5% Ficoll/30% sucrose interface) (Lane III) after discontinuous density gradient ultracentrifugation as described in Materials and Methods.

Approximately 60 g of fundic mucosal tissue was used with each enrichment of H/K-ATPase. The final GI and GII protein yields were consistent between preparations. The protein specific activities are presented in Table 2-1. The mean protein concentrations are presented in Table 2-2.

K^+-stimulated specific activities (following subtraction of basal activity) (Table 2-1) were lower than those reported for preparation using zonal centrifugation and free-flow electrophoresis [129] but were nonetheless similar to those

obtained elsewhere (65.5 μmol Pi/mg protein/hr) [127]. In addition, Mg-stimulated (basal) specific activity was higher than that reported by Saccomani [129]. Hence, microsomal (GI) and non-microsomal (GII) membrane preparations were obtained which were highly enriched with hydrolytically-active H/K-ATPase in yields comparable to those preparations reported in the literature by Briving [127], but rather lower in purity to those of Saccomani [129].

Table 2-1 K^+-only stimulated and basal (Mg^{2+}) activities (μmole Pi/mg protein/hr) of lyophilised GI and GII microsomes at 37 °C in the presence and absence of K^+. ATPase reaction solutions were 20 mM Tris/HCl, pH 7.4, 2mM $MgCl_2.6H_20$, 2mM ATP and 40 mM KCl as appropriate. Figures in brackets are standard deviations.

Fraction	K^+ stimulated	Mg^{2+}
GI	98.74 (±22.47)	57.60 (±26.22)
GII	59.60 (±31.82)	43.77 (±36.65)

Table 2-2 Mean (Lowry) protein concentration (mg protein/ml/60g tissue) and mean total (Lowry) protein content of GI and GII gastric microsomes (6 datasets). Figures in brackets are standard deviations.

Fraction	Mean protein concentration (mg/ml/60 g tissue)	Total protein (mg)
GI	0.539 (± 0.195)	58.75 (± 17.37)
GII	0.696 (± 0.121)	63.62 (± 18.78)

Determination of inhibitory activity of substituted imidazopyridines

A series of analogues of the K^+-competitive inhibitor of the gastric H/K-ATPase, SCH28080, was synthesised to examine the roles of various substitutions on binding to gastric lipids and the proton pump itself. Here the structure-activity relationship of these analogues is examined. Two particular questions are addressed. First, is stabilisation of the pyridinium cation important for inhibitory potency? Second, is the interaction of –C8 substitutions with

residues in the inhibitor binding site governed primarily by steric considerations or an interaction between a π-electron system and the side groups of aromatic residues in the protein, as suggested by Munson and coworkers [106]?

The 3-methyl analogue of the SCH28080 cation (1,2,3-dimethy-8(phenylmethoxy)imidazo[1,2-*a*]pyridinium, TMPIP) (Figure 2-7) has been shown to have inhibitory potency of two orders of magnitude less than that of SCH28080 [130] but this reduction in inhibitory potency is offset by the unreactive methyl or hydrogen substituent at the –C3 position of the reactive cyanomethyl α carbon.

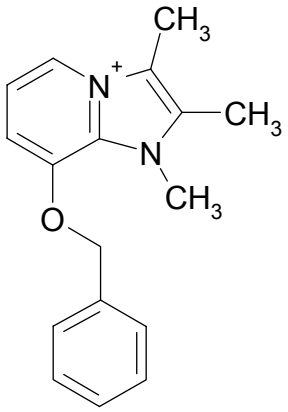

Figure 2-7 Chemical structure of TMPIP (1,2,3-dimethy-8-(phenyl-methoxy)imidazo[1,2-*a*]pyridinium), the 3-methyl analogue of the SCH28080 cation (c.f. Figure 2-1C).

The synthesis of TMPIP derivatives was more readily achieved and permitted greater and more reliable yields of conformationally-simple, isotopically-labelled compounds suitable for analysis by NMR. The inhibitory profiles of substituted imidazopyridines considered in this study are summarised in Table 2-3.

Table 2-3 Summary of the structure-activity relationship of substituted imidazo[1,2-*a*]pyridines. The IC_{50} values represent the half maximal concentrations for inhibition of K^+-stimulated ATPase activity in purified lyophilised GI fraction gastric membranes. (3 datasets). Figures in brackets are standard deviations. The IC_{50} plots for DMPIP, TM2FPIP, TM4FPIP, TMPFPIP and TMTFBIP are presented in Figures 2-9 to 2-11.

Compound	IC_{50} (μM)
TMPIP	2.8 ± 3.5
DMPIP	> 100
TM2FPIP	5.0 ± 0.9
TM4FPIP	3.5 ± 1.5
TMPFPIP	8.2 ± 4.0
TMTFBIP	> 100
TMCHIP	0.11 ± 0.51

C8 Aryl analogues of SCH28080

The groups (R1 – R6) substituted in this study are shown in Figure 2-8.

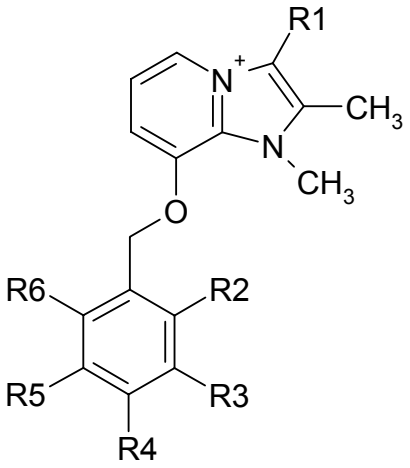

Figure 2-8 Schematic representation of a general analogue of SCH28080 with groups R1-6 varied in this study.

R1 substitutions and stabilisation of the imidazo conjugate ring

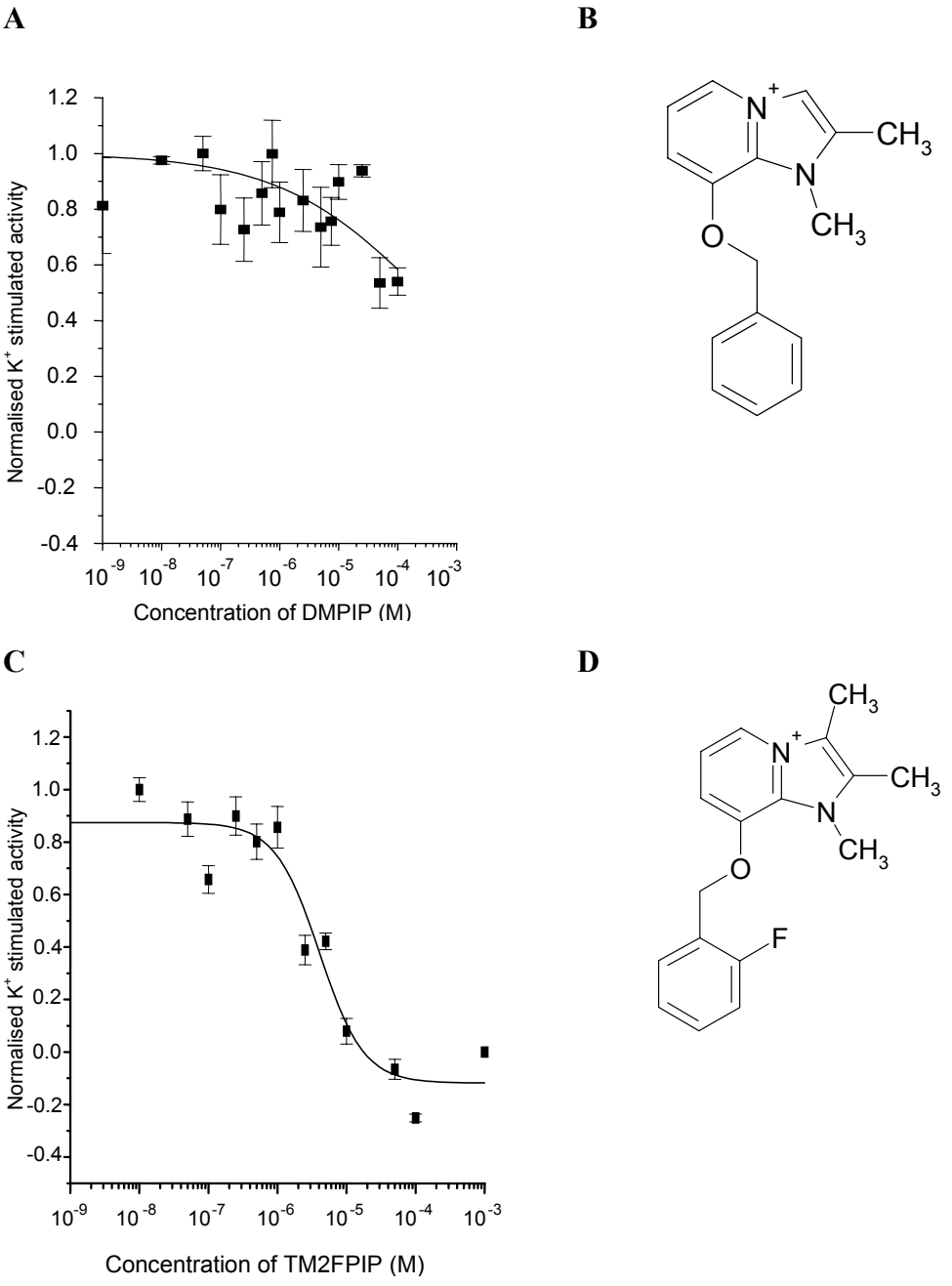

Figure 2-9 Dose response curves showing inhibition of K^+-stimulated ATPase activity of lyophilised GI microsomes by (A) DMPIP and (C) TM2FPIP. Specific activity was assayed by quantification of Pi liberated from ATP after incubation of microsomes at 37 °C for 30 min in standard reaction medium containing the stated concentrations of DMPIP. The IC_{50} value is given in Table 2-3. Chemical structures of DMPIP (B) and TM2FMPIP (D) are shown,

Replacement of a methyl group at the C3 (R1) position of TMPIP (Figure 2-8) by hydrogen produces an inhibitor with markedly reduced potency with respect to TMPIP. The reported IC_{50} of TMPIP, which has $–CH_3$ at C3, is 2.8 μM [130]. In contrast, the IC_{50} value of 2-methyl-8(phenylmethoxy)imidazo[1,2-*a*]pyridinium (DMPIP), with –H substituted at C3, is over 100 μM (Figure 2-9). This minor change in the substitution to the imidazo ring appears to have a profound effect on inhibitory activity, indicating the importance of this region of the molecule for activity.

R2-R6 substitutions: the effect of fluorination on activity

TMPIP, with an IC_{50} of 2.8 μM, exhibits a marginally higher activity than those activities exhibited by its fluorine-containing aryl analogues. The variation in activities is not statistically significant, however, with the potencies of the fluorinated analogues being in the rank order TM4FPIP (R4=F) > TM2FPIP (R2=F) > TMPFPIP (R2-6=F), with TMPFPIP having an IC_{50} of 8.2 μM (Figures 2-9 & 2-10). Hence, in contrast to changes to the imidazo ring, substitution of fluorine into the phenylmethoxy ring has little or no impact on the activity of the inhibitors.

C8 Acyl analogues of SCH28080

Introduction of an aliphatic group at the C8 position entirely removes the opportunity for the substituted imidazopyridine to engage either in association with quaternary ammonium groups by π-cation interactions [131, 132] or π-π stacking with protein residues. Substitution of the aryl group with a fluorobutyl, pentyl or cyclohexyl group allows the importance of steric interactions on

activity to be investigated, by reporting whether the space occupied by the carbon chain is important in docking the inhibitor in its binding site.

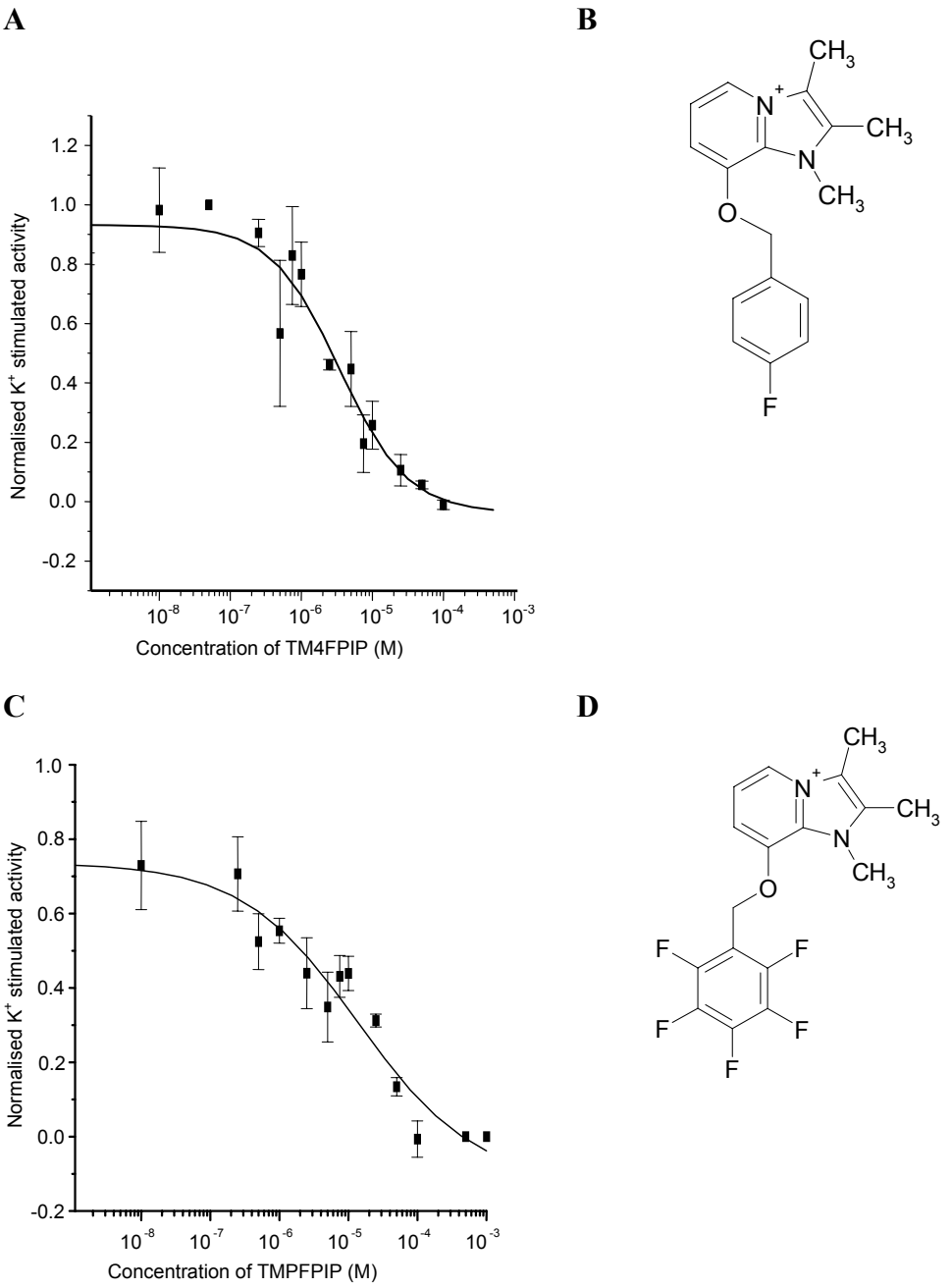

Figure 2-10 Dose response curve showing inhibition of K^+-stimulated ATPase activity of lyophilised GI microsomes by (A) TM4FPIP and (C) TMPFPIP. Specific activity was assayed by quantification of Pi liberated from ATP after incubation of microsomes at 37 °C for 30 min in standard reaction medium containing the stated concentrations of TM2FPIP. The IC_{50} value is given in Table 2-3. Chemical structures of TM4FPIP and (B) TMPFPIP (D) are shown.

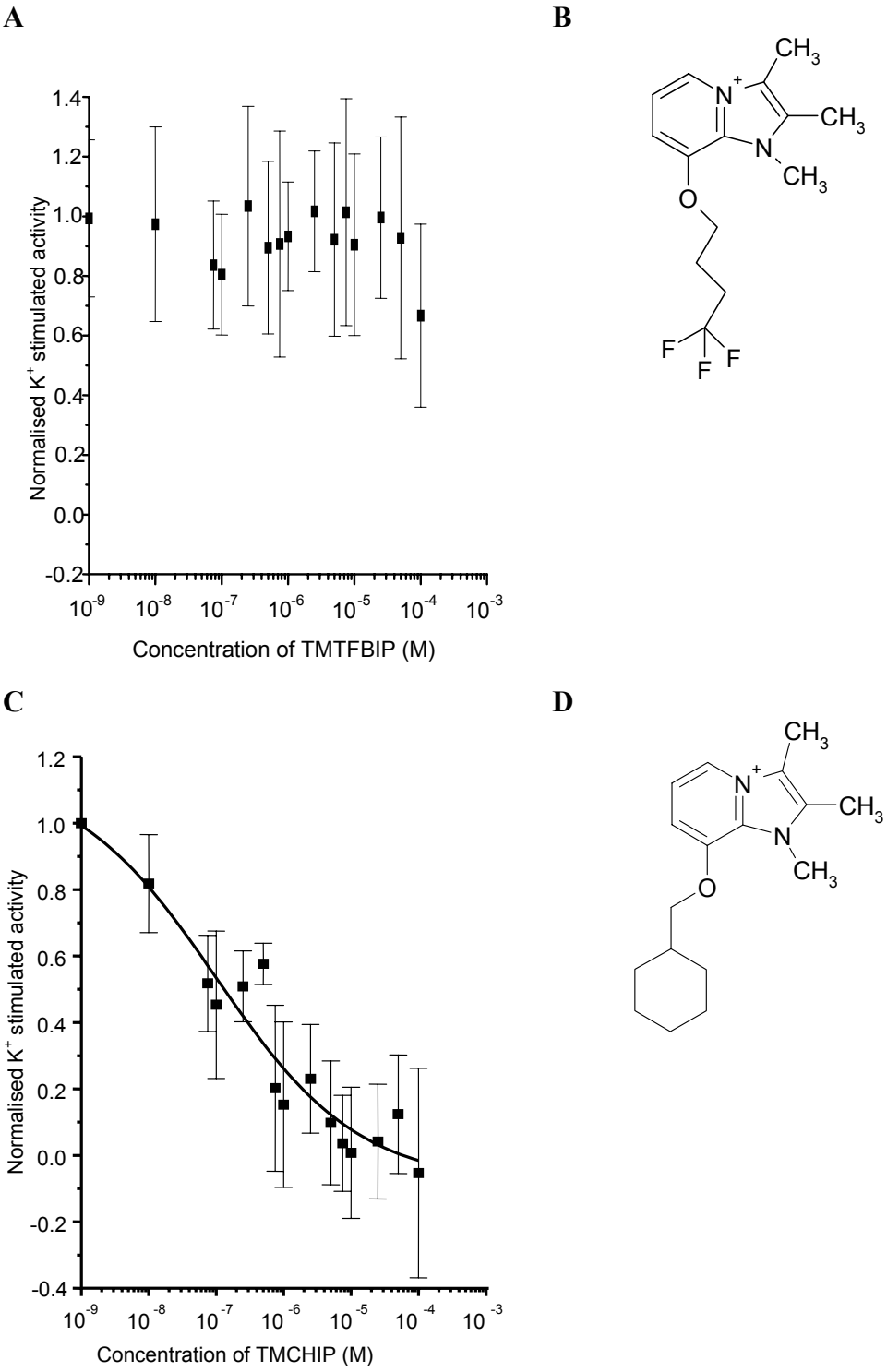

Figure 2-11 Dose response curve showing inhibition of K^+-stimulated ATPase activity of lyophilised GI microsomes by TMTFBIP(A) and TMCHIP (C). Specific activity was assayed by quantification of Pi liberated from ATP after incubation of microsomes at 37 °C for 30 min in standard reaction medium containing the stated concentrations of TM4FPIP. The IC_{50} value is given in Table 2-3. Chemical structures of (B) TMTFBIP and (D) TMCHIP are shown.

Reaction of 2,3-dimethylimidazo[1,2-*a*]pyridine-8-ol by 1,1,1-trifluorobutyl-4-bromobutane produced an inhibitor (TMTFBIP) with no appreciable inhibition of K^+-stimulated activity even at 1 mM concentration (Figure 2-11).

A butyl analogue substituted with H- at C3 of the imidazo ring had been prepared but was not examined for inhibitory potential given the low activity of the CH_3- C3 compound. Reprotection of 2,3-dimethylimidazo[1,2-*a*]pyridine-8-ol by 1-bromomethyl-cyclohexane produced a potent inhibitor of the gastric H/K-ATPase with IC_{50} of 0.11 μM (Figure 2-11). In this case loss of the delocalised electron ring of a phenyl group did not appear to affect inhibitory potency but seems to increase it slightly. This compound has a substituent with approximately the same size as a benzyl group but with no π-π capability and a non-planar configuration.

Discussion

Replacement of a methyl group at the C3 position by hydrogen produced an inhibitor with markedly reduced potency (Table 2-3, Figure 2-9). The effect may be steric or electronic. Methyl or acyl functional groups at this position will donate electrons to the N4 quaternary ammonium cation and thus maintain the aromaticity and planarity of the SIP. Previous studies have examined extensively functional group substitutions at this position [125, 127]. Substitution of $–CH_2CN$ by $-CH_2OH$ produced only a small variation in IC_{50} (0.87 and 2.2 μM, respectively) and the IC_{50} of TMPIP, which contains $–CH_3$ at the C3 position, is 2.8 μM. Solution ^{1}H-NMR of TMPIP indicates deshielding of the C5 hydrogen and thus that the cation positive charge resides preferentially on N4 rather than as a generalised delocalisation of charge in that ring system (Fig. 2-12). Since the –H at C3 cannot fulfil this function may indicate the importance of the conjugated ring in this portion of the molecule.

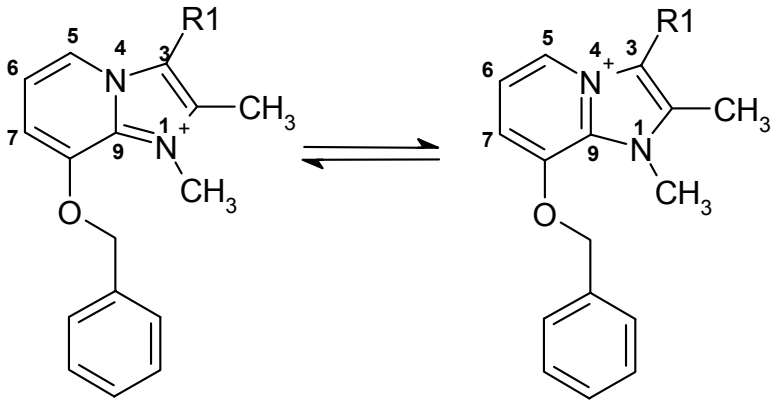

Figure 2-12 Conjugation of cation charge between N1 and N4 in a substituted imidazo[1,2-a]pyridinium species. Introduction of methyl or acyl functional groups as R1 at C3 may stabilise the aromaticity of the N_1, C_2, C_3, N_4, C_9 ring and positive charge bias at N4.

Two sterically equivalent analogues were synthesised containing $–CH_2OH$ at C3 and $–CH_3$ or $-CF_3$ at C2 (IC_{50} = 2.2 μM, no activity (respectively)) but no methyl substitution at N1 [127]. The compounds generated did not contain a methyl substituent at N1. Dramatic negative effects on inhibitor activity were observed when $–CF_3$ was present at C2 The pKa of the compound was reduced from 6.1 to 2. Hence, it is probable that the introduction of $–CF_3$ abolished inhibition by reducing the ability for protonation and concentration of the inhibitor at its active site. In this work, a permanent cation was prepared so that substituent effect on pKa would not lead to loss of activity is important for maintaining inhibitor potency as it is the cationic form that has inhibitory activity.

In order to relate charge distributions to inhibitory potency, the influence of substitutions at C3 and C8 (Figure 2-3) was predicted by modelling the distribution of the partial charge distribution in the pyridinium ions *in vacuo* using WebLab ViewerPro 4.0 (Molecular Simulations, Inc.). Figure 2-13 defines the atomic numbering system for SIPs considered in this study.

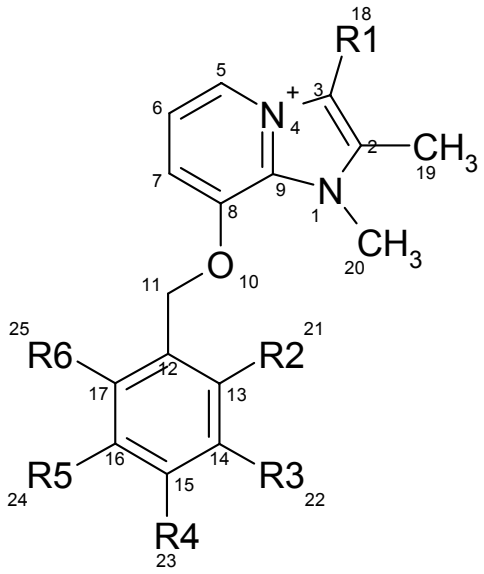

Figure 2-13 Chemical structure of generic substituted imidazo[1,2-*a*]pyridine with atomic numbering defined for non-hydrogen atoms.

Because of its structural simplicity, TMPIP was used as a template and changes in partial charge where considered at each non-hydrogen atom upon variation of the composition of functional groups R1-R6 in the aryl substitution at C8. The effect of an acyl group at C8 on the charge was also considered. For convenience of comparison, the C3 functional groups of acyl substituted compounds have retained the numbers assigned to the corresponding group in the aryl substituted compounds.

In Figure 2-14 TMPIP is shown with a map of partial charges at each non-hydrogen atom. The electropotential surface displays Gasteiger charges [133], which are partial equalisations of electronegativity between bonded atoms generated from generalisations about the effects of functional groups, for the atoms contained in the surface and maps the electrostatic potential representing these charges to the surface. Positive partial charges are shown in blue; regions of negative charge are shown in red. In subsequent figures the difference (Δ) in partial charges at each non-hydrogen site is calculated relative to the partial charge in TMPIP at the same location. In this way, the influence of substitution of various functional groups on the charge distribution may be compared. The pyridinium cationic charge is predicted to be distributed between N1 and N4 of the imidazo ring with a bias of positive charge at N4.

In the case of DMPIP (Figure 2-15), the presence of –H at C3 changes the distribution of partial charges and the electropotential of the imidazo fused ring. Positive charge resides at N1 and the partial charge at N4 is predicted to be negative. The difference (Δ) in partial charges at each non-hydrogen site relative to that of TMPIP is calculated and shown in Figure 2-15C. The same

comparison is made for the fluorinated SIPs TM2FPIP (Figure 2-16), TM4FPIP (Figure 2-17), TMPFPIP (Figure 2-18), TMTFBIP (Figure 2-19) and the non-fluorinated acyl substitution TMCHIP (Figure 2-20). See Figure 2-4 for a summary of these compounds.

A **B**

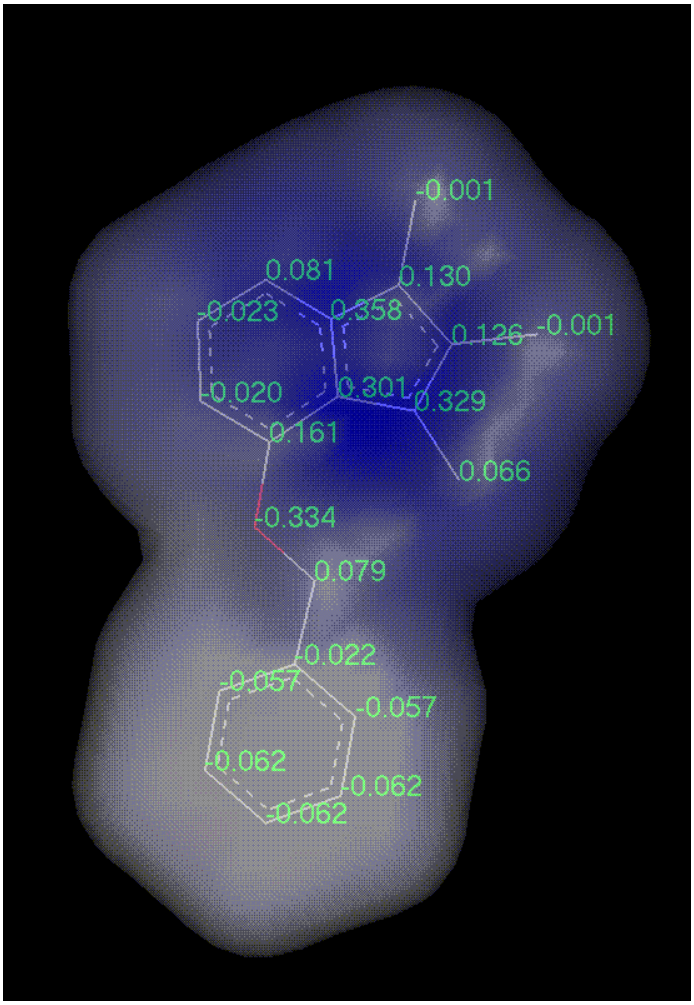

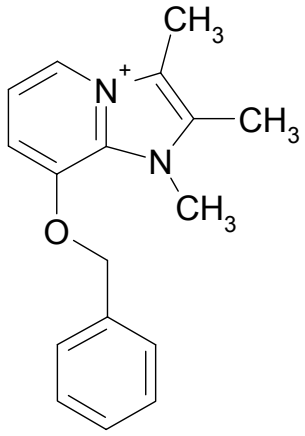

Figure 2-14 (A) Chemical structure of the 1,2,3-trimethyl,8-(phenylmethoxy)imidazo[1,2-a]pyridinium cation (TMPIP) with electropotential surface and partial charges of individual non-hydrogen atoms in the molecule. Electropotential surface varies as a charge gradient from positive (electron-poor, blue) to negative (electron-dense, red). (B) Conventional chemical structure of TM2FPIP for reference.

A **B**

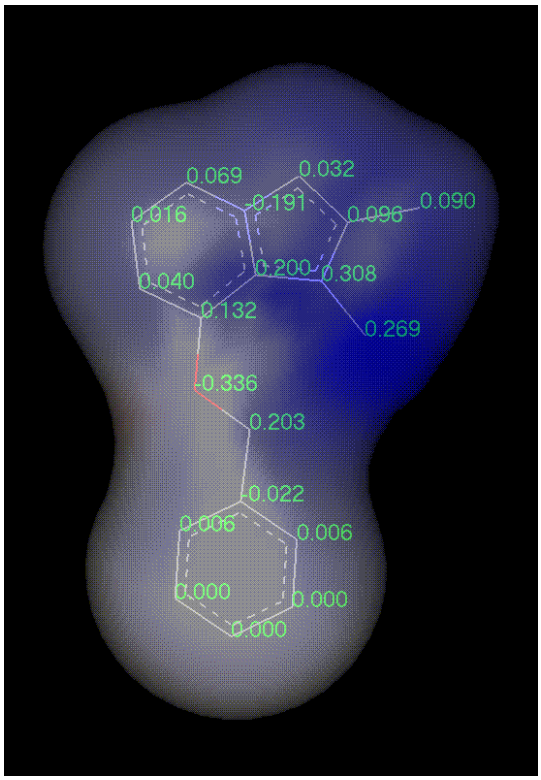

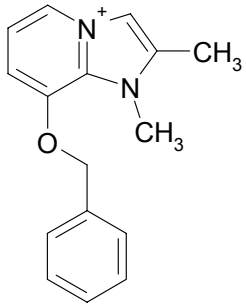

C

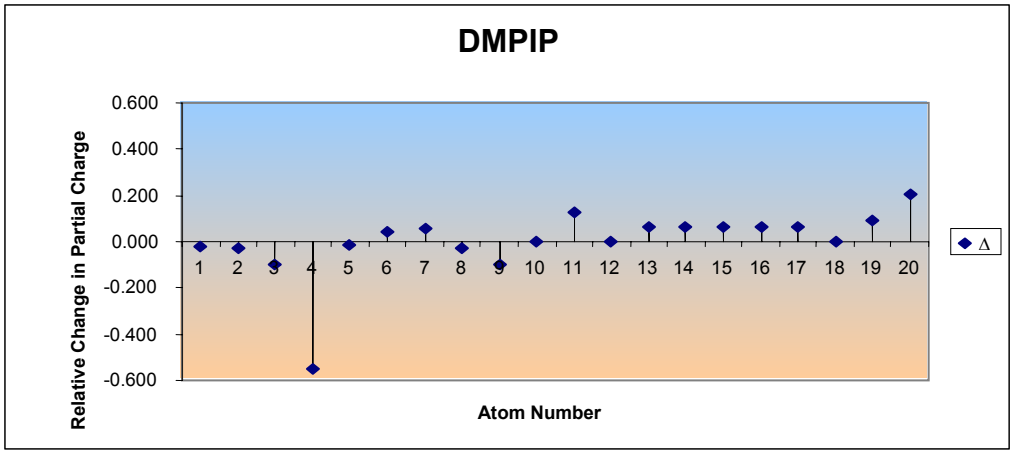

Figure 2-15 (A) Chemical structure of the 1,2-dimethyl,8-(phenylmethoxy)imidazo[1,2-a]pyridinium cation (DMPIP) with electropotential surface and partial charges of individual non-hydrogen atoms in the molecule. Electropotential surface varies as a charge gradient from positive (electron-poor, blue) to negative (electron-dense, red). (B) Conventional chemical structure of DMPIP for reference. (C) Change in partial charge in DMPIP relative to TMPIP. Blue region indicates increase in positive charge; red region corresponds to increasing negative charge. Refer to Figure 2-13 for definition of atom numbering system.

There are small variations in the calculated charge distribution in the phenyl ring of DMPIP (Figure 2-15) relative to TMPIP. The *N*-methyl group (C20) acquires more positive charge and the methyl substituents of the imidazo[1,2-*a*]pyridine fused ring become slightly more negative.

Stabilisation of positive charge on N4 by proximal electron-donating groups is apparently not essential for inhibitory potency. It is calculated that TMPFIP (Figure 2-18), with an IC_{50} in the same order of magnitude as TMPIP (Figure 2-14), and TMCHIP (Figure 2-20), but with a greater potency than TMPIP renders the relative partial charge at N4 as negative as N4 of DMPIP (Table 2-15C). The same phenomenon is observed with TMTFBIP (Figure 2-19), which has $–CH_3$ at C3. Removal of electron density from the phenyl ring by perfluorination or by saturation of the ring system is calculated to have a strong influence on the charge distribution of the imdazo conjugated ring system. There is also a minor increase in the electron density at C3, C8 and C9.

Disruption of the imidazo conjugate ring system cannot account solely for the loss of activity of DMPIP since TMPFPIP and TMCHIP are active. It is noted that there is a decrease in the local charge density of C19 and C20 that does not occur in either TMPFPIP or TMCHIP. Given the variation in electrostatic potential that is exhibited by the imidazo conjugate ring system, it is suggested that the profound loss of activity demonstrated for DMPIP is due to a steric effect at C3 rather than an electronic effect of cation stabilisation in the pyridinium moiety.

A

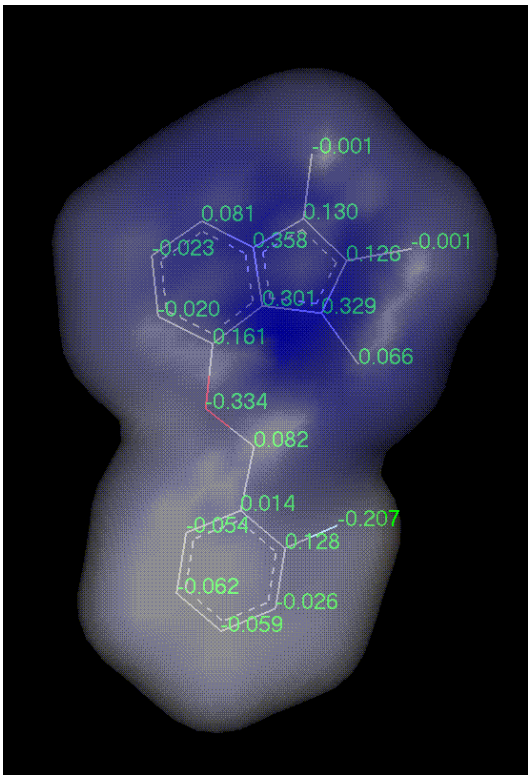

B

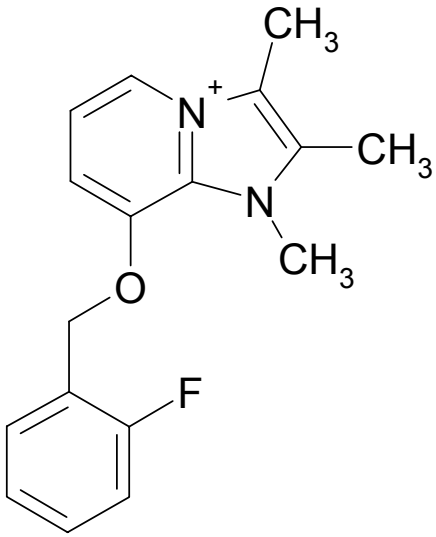

C

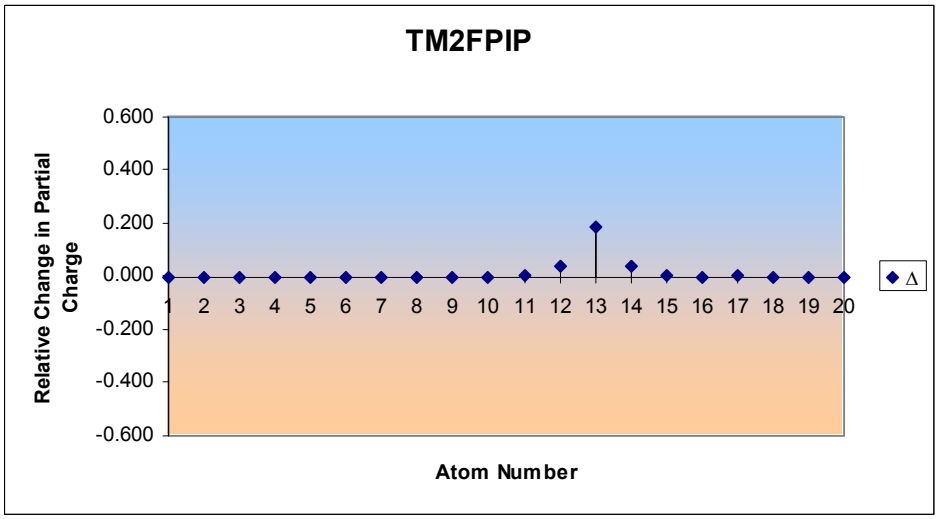

Figure 2-16 (A) Chemical structure of the 1,2,3-trimethyl,8-(o-fluorophenylmethoxy)-imidazo[1,2-a]pyridinium cation (TM2FPIP) with electropotential surface and partial charges of individual non-hydrogen atoms in the molecule. (B) Conventional chemical structure of TM2FPIP for reference. (C) Change in partial charge in TM2FPIP relative to TMPIP. Blue region indicates increase in positive charge; red region corresponds to increasing negative charge. Refer to Figure 2-13 for definition of atom numbering system.

A

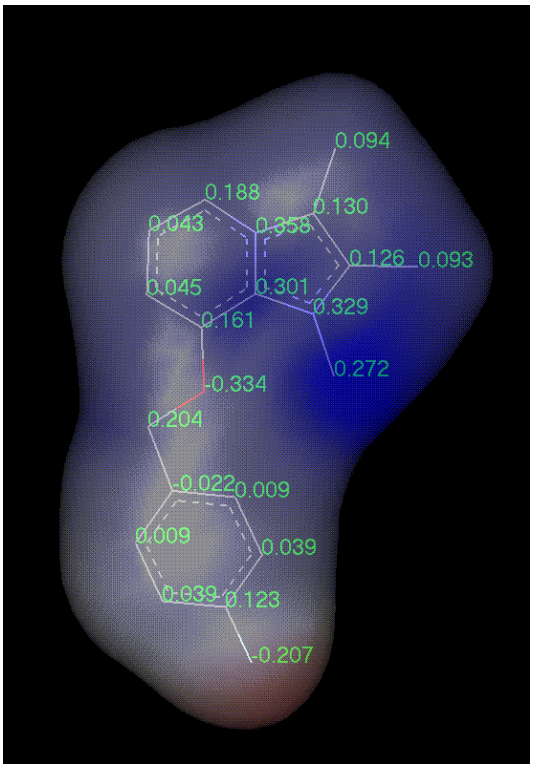

B

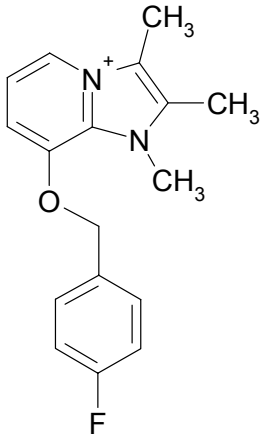

C

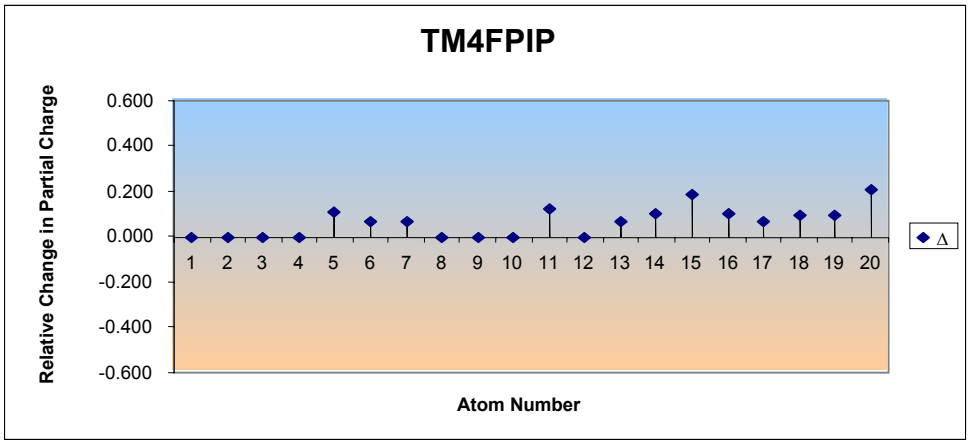

Figure 2-17 (A) Chemical structure of the 1,2,3-trimethyl,8-(p-fluorophenylmethoxy)-imidazo[1,2-a]pyridinium cation (TM4FPIP) with electropotential surface and partial charges of individual non-hydrogen atoms in the molecule. (B) Conventional chemical structure of TM4FPIP for reference. (C) Change in partial charge in TM4FPIP relative to TMPIP. Blue region indicates increase in positive charge; red region corresponds to increasing negative charge. Refer to Figure 2-13 for definition of atom numbering system.

A

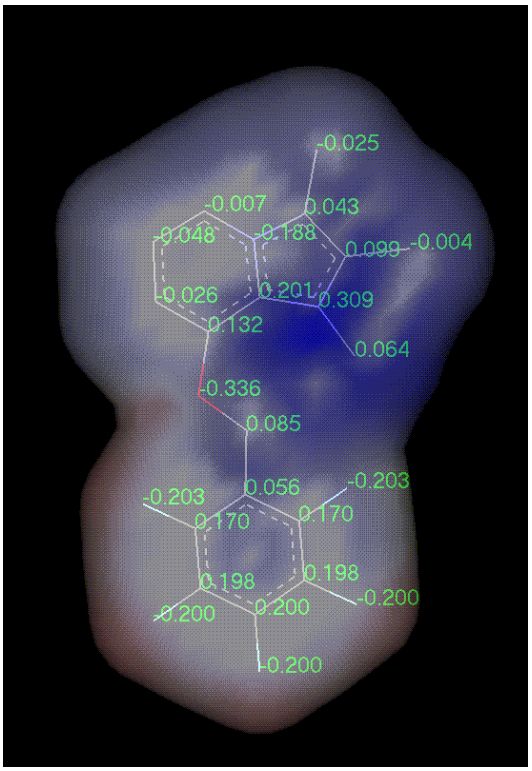

B

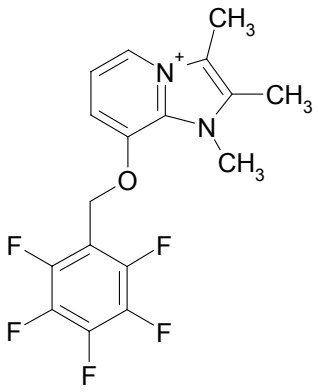

C

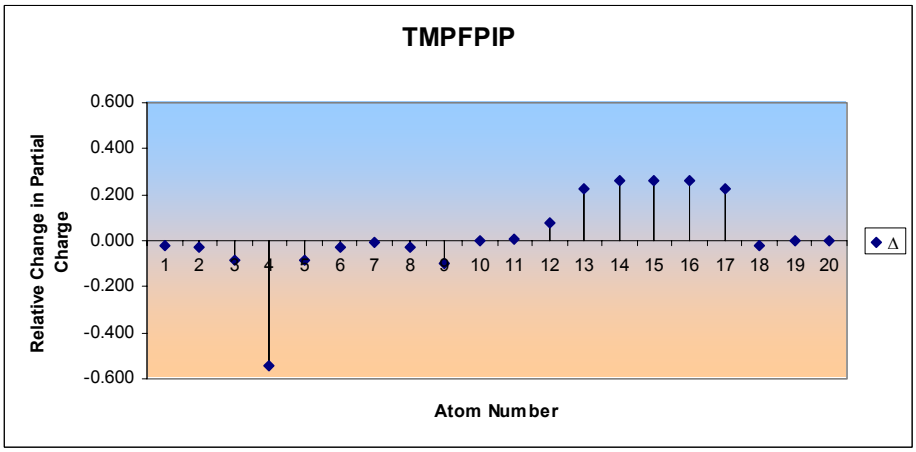

Figure 2-18 (A) Chemical structure of the 1,2,3-trimethyl,8-(perfluorophenylmethoxy)-imidazo[1,2-a]pyridinium cation (TMPFPIP) with electropotential surface and partial charges of individual non-hydrogen atoms in the molecule. (B) Conventional chemical structure of TMPFPIP for reference. (C) Change in partial charge in TMPFPIP relative to TMPIP. Blue region indicates increase in positive charge; red region corresponds to increasing negative charge. Refer to Figure 2-13 for definition of atom numbering system.

A

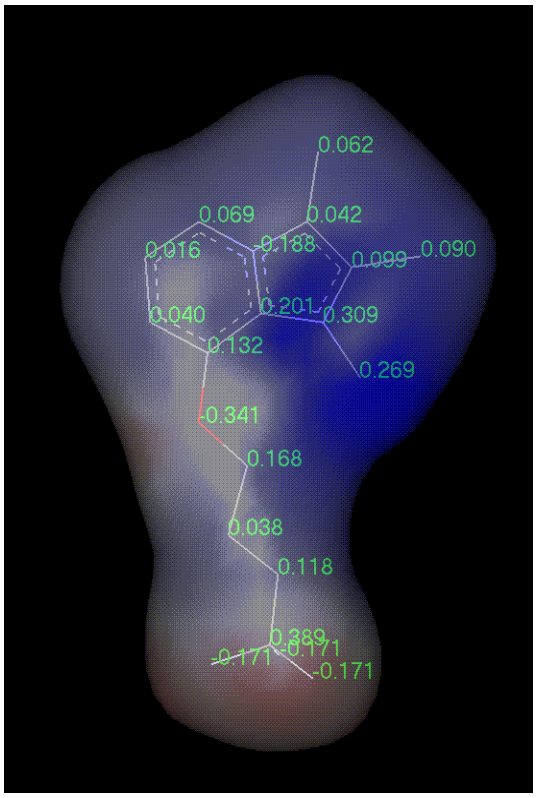

B

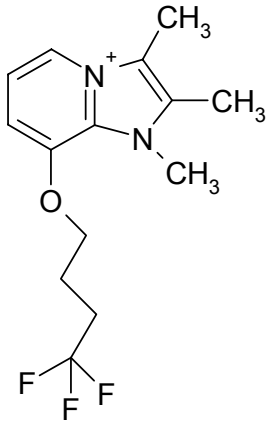

C

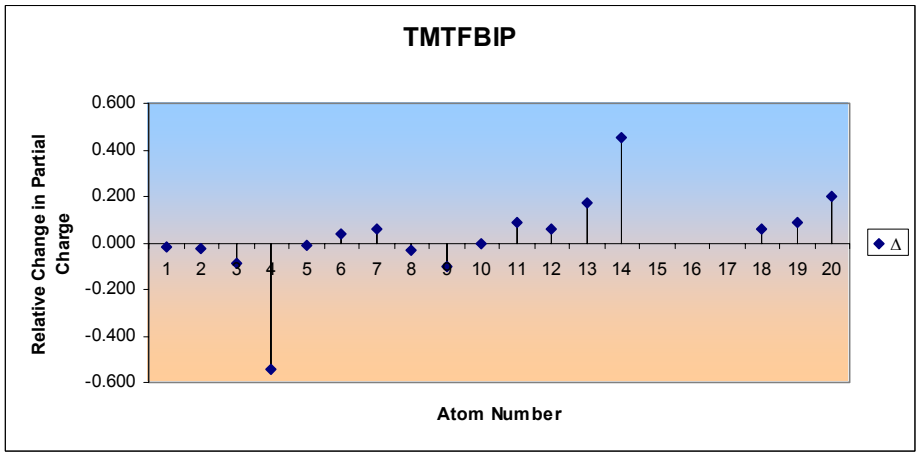

Figure 2-19 Chemical structure of the 1,2,3-trimethyl,8-(trifluorbutylmethoxy)imidazo[1,2-a]pyridinium cation (TMTFBIP) with electropotential surface and partial charges of individual non-hydrogen atoms in the molecule. (B) Conventional chemical structure of TMTFBIP for reference. (C) Change in partial charge in TMTFBIP relative to TMPIP. Blue region indicates increase in positive charge; red region corresponds to increasing negative charge. Refer to Figure 2-13 for definition of atom numbering system.

A **B**

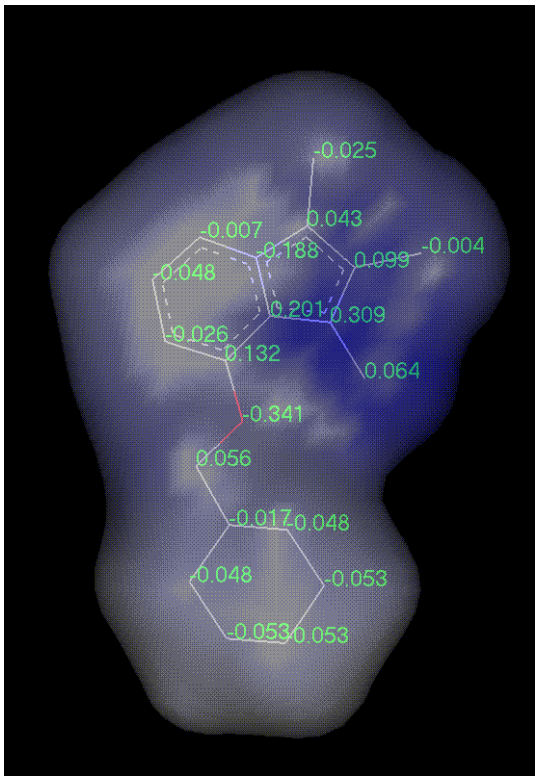

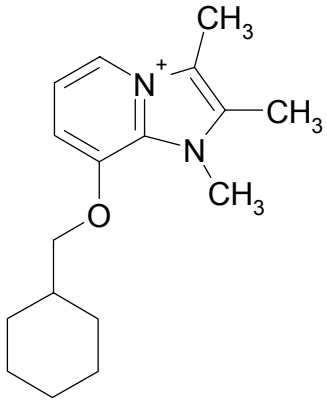

C

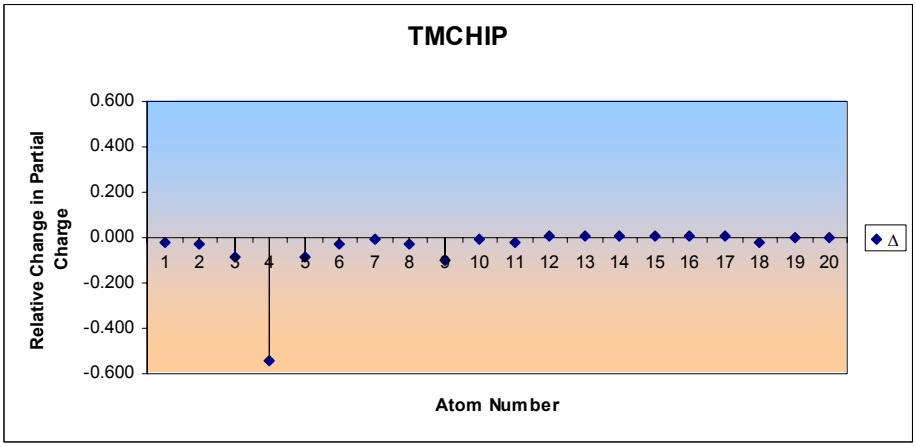

Figure 2-20 Chemical structure of the 1,2,3-trimethyl,8-(cyclohexyamethoxy)imidazo[1,2-a]pyridinium cation (TMCHIP) with electropotential surface and partial charges of individual non-hydrogen atoms in the molecule. (B) Conventional chemical structure of TMCHIP for reference. (C) Change in partial charge in TMCHIP relative to TMPIP. Blue region indicates increase in positive charge; red region corresponds to increasing negative charge. Refer to Figure 2-13 for definition of atom numbering system.

This study indicates that the presence of fluorine at the *ortho*- or *para*- position of a C8 phenyl group and as a pentafluoro- derivative has little effect on the ability of the species to act as a K^+-competitive, reversible inhibitor of the proton pump. As the number of fluorine substituents is increased, there is a lower propensity of the aryl π electrons to interact with neighbouring cationic groups [134]. There is evidence that introduction of fluorine into aromatic rings diminishes their ability to interact with quaternary cations, investigated by site-directed mutagenesis with unnatural amino acids [135]. A π-cation association is postulated for the interaction of nicotinic acetylcholine receptor Tyr198 with the quaternary ammonium group of acetylcholine through cation-π stabilisation, an association that has been further implicated in the stabilisation of secondary structure in dimethylamine dehydrogenase [132] and ion selectivity in K^+ channels [131]. In work on the nicotinic acetlycholine receptor containing fluorotyrosine or fluorotryptophan [135], variations in the EC_{50}s, the excitatory concentration of acetylcholine, could not be exclusively attributed to the change in *p*Ka of the modified amino acid due to the fluorine presence, however, but might also result from perturbations in the side chain ordering in the receptor protein. The EC_{50} of acetylcholine is reduced linearly with respect to the increasing numbers of ^{19}F atoms introduced into Trp in the binding site. The EC_{50} also show a linear relationship with the energy of π-cation interactions with F-Trp. Introduction of fluorine, which is strongly electron withdrawing, into an aromatic group has an effect on the electronic charge distribution of the new species. This effect is seen in the calculated partial charge distribution for atoms 11-17 of aryl SIPs. The least modified is 2FTMPIP (Figure 2-16), which shows a localised decrease in charge density at C13. A broader effect is

anticipated for TM4FPIP (Figure 2-17), with *meta*- and *para*- positions demonstrating an increase in partial charge as the F23 withdraws electrons from C15 and the aromatic ring. If π-cation interactions occur between the aryl group of the SIP and the protein side-groups, the inhibitor IC_{50} would be expected to decrease upon introduction of an increasing number of fluorines into the phenyl ring. Only a modest increase in IC_{50} was observed with TMPFPIP (Table 2-3) relative to that of TMPIP and the mono-fluorinated compounds. The ability to form π-cation interactions is greatly diminished in TMPFPIP. Perfluorination of the phenyl ring removes electrons from the aromatic ring (C12-C17) and leaves it containing an increased positive charge relative to TMPIP (Figure 2-18C). π–π association with other aromatic groups is reduced but nonetheless permitted and may be reflected in the higher IC_{50} of TMPFPIP relative to TMPIP.

The C8-acyl compounds TMTFBIP (Figure 2-19) and TMCHIP (Figure 2-20) have no π systems in the acyl moiety and the ability of these SIPs to engage in π-π stacking is abolished. TMTFBIP shows no inhibitory activity. The aliphatic group approximates to the length of a phenylmethoxy species substituted at C8 and thus occupies a substantial volume taken by a phenyl group. The steric occupation is not complete and is better approximated by the cyclohexyl group of TMCHIP, which exhibits good inhibitory potency. There is no scope for π-bonding by this SIP, which suggests that, if the manner of binding of this SIP is the same (K^+-competitive) as that of the aryl SIPs, the C8 substitution of an appropriate imidazo cation need only fulfil certain steric requirements for active inhibition. The mechanism of binding is, as yet, undetermined, and does not discount the ability of other aromatic SIPs studied here to engage with the π-

systems of neighbouring aromatic species in the H/K-ATPase as suggested by Munson and co-workers [106].

Conclusions

In summary, a series of novel substituted imidazo[1,2-*a*] pyridines has been synthesised and characterised to determine a structure-function relationship between the substitutions imposed on the system and the inhibitory potency of the novel inhibitors. It is proposed that the imidazo region of the pyridinium cation is primarily responsible for localisation and binding to the active site of the gastric H/K-ATPase. Substitutions in the imidazo group produce active inhibitors if a steric requirement is fulfilled at C3 of the imidazo conjugate ring system rather than if the delocalised cation is stabilised between N1 and N4. Incorporation of fluorine into the C8-phenyl region does not significantly affect inhibitory potency and permits the use of ^{19}F for later measurement of ^{13}C-^{19}F distances in structural studies of SIPs at their high-affinity binding sites. The cumulative electron-withdrawing effect of fluorine substituted into this ring system removes the scope for π-cation interactions with residues at the inhibitor binding site. That fluorinated inhibitors are active indicates that such an interaction is not important in stabilising the SIP in the protein. Upon complete loss of a π system for π-π bonding but with a steric requirement fulfilled, a C8-substituted cyclohexyl analogue of SCH28080 was nonetheless actively inhibitory but through an unknown mechanism. Thus it is concluded that the C8-substitution is less important than the C3 substitution in conferring inhibitory qualities on a substituted imidazo[1,2-*a*]pyridine and that the effect of these substitutions is governed primarily by steric rather than electronic considerations.

Chapter 3

^{2}H SOLID STATE NMR OF INHIBITORS OF THE GASTRIC H/K-ATPASE

Introduction

For reliable determination of the binding conformation of inhibitors using solid state NMR it is essential that the inhibitor be observed spectroscopically at its site of action. The aim of this chapter is to understand the possible mechanisms of binding of agents such as substituted imidazo[1,2-*a*]pyridine (SIP) inhibitors of the gastric H/K-ATPase. In general, drugs may associate strongly with the lipid bilayer and diffuse to the site of inhibition or may enter the protein directly from the aqueous phase and have little interaction with the membrane itself. An investigation of the molecular dynamics of inhibitors within their high-affinity binding sites would permit much information to be gained about the degrees of motional freedom available to the inhibitor and thus the identification of the regions or functional groups of the inhibitor most restrained at the active site. The dynamic information, combined with functional data for a range of inhibitors, would provide insight into the important functionalities for drug binding.

The motional behaviour of molecules can be determined spectroscopically using electron spin resonance (ESR) and nuclear magnetic resonance. Using spin labels, the degree of motional restraint is determined from the degree of averaging of anisotropy of the hyperfine splitting and rotational correlation times of proteins can be deduced from the linewidths of saturation transfer [137]. Deuterium magnetic resonance yields similar information to that given by spin label ESR, but without the

attachment of a bulky nitroxide group that might alter the molecular structure (Figure 3-1) and with a more restrictive dynamic time scale (~ μs – ms).

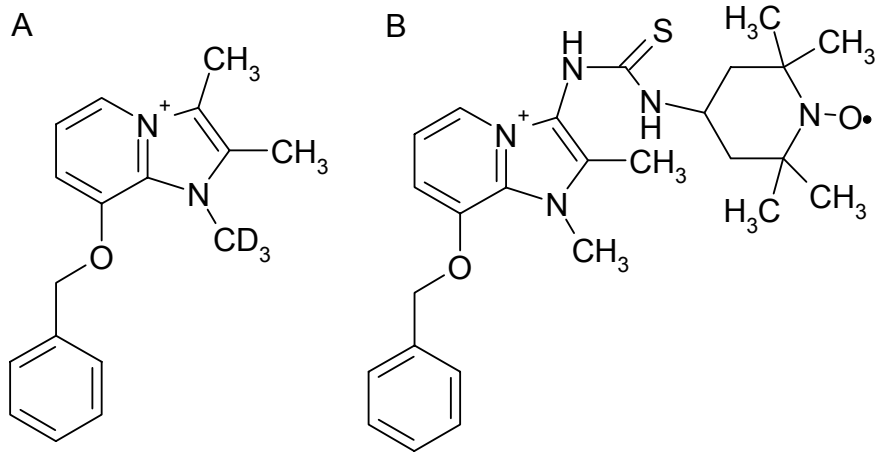

Figure 3-1 Substituted imidazo[1,2-*a*]pyridinium compounds with probes allowing the determination of the dynamics of the imidazo fused ring system. (A) d_3-TMPIP with a non-perturbing *N*-deuteromethyl group. (B) 1,2-dimethyl-3-amino-isothiocyanatoTEMP-8-(phenylmethyoxy)imidazo[1,2-*a*]pyridinium cation.

Through enrichment of selective sites with deuterium, which has a low natural abundance (0.01%), the problems of the comparatively low sensitivity of the deuterium nucleus in the NMR experiment are balanced by the ability to assign unambiguously the resonances in the deuterium spectrum. The small magnetic moment of the deuteron produces much reduced dipolar coupling compared to those that can dominate proton spectra of biological membranes, for example. The dominant interaction is quadrupolar which occurs in nuclei with $I \geq 1$ and influences the spectral lineshape markedly on the order of 100s kHz.

One of the values of deuterium NMR is its sensitivity to anisotropic motions. Rapid isotropic motion of a deuteron produces a single narrow line but anisotropic motion of a deuteron gives rise to a spectral "Pake" doublet due to only partial averaging of the quadrupolar interaction with the surrounding electric field gradient of the

nucleus [138]. The rate and amplitude of the anisotropic motion and the orientation of the deuteron with respect to the molecular symmetry axis define the doublet spacing, $\Delta\upsilon_{Q,}$ from which dynamic information may be obtained.

Deuterium NMR has been used extensively to examine the ordering and motion of the acyl chains of lipids in membrane [139, 141], to investigate lipid-protein interactions [139-146], soluble proteins in the solid state [147-149], integral membrane proteins in their native environments [136, 227, 228] and of ligand-protein interactions [147-149]. In an ensemble of lipids, e.g., in a vesicle, a spherical distribution of molecules gives rise to a ^{2}H powder patter. This is a superposition of Pake doublets for each orientation of the lipid with respect to the applied field B_0. In simple cases and model systems, line shape analysis can help determine the type of motional averaging [147-149]. Here, the spectra will be examined qualitatively to compare the mobility of different inhibitors with different potencies.

The Deuterium NMR Spectrum

Assuming the Zeeman interaction is much larger than the quadrupolar interaction (the high-field approximation), then the energy shifts of energy level *m* due to the quadrupolar interaction (ΔE_Q) for a single nucleus may be given as [150]:

$$\Delta E_Q = \frac{3}{8}\frac{e^2 qQ}{\eta}\left(3\cos^2\theta - 1\right)$$ **Equation 3-1**

where *eq* is the electric field gradient tensor.

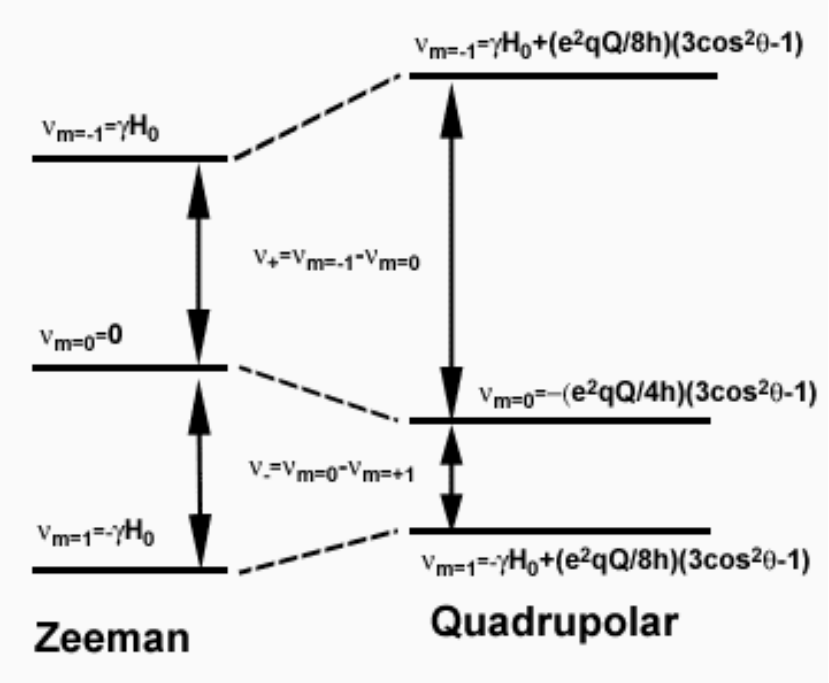

Figure 3-2 Energy level diagram for the combined Zeeman and quadrupolar interactions for a spin-1 nucleus in an applied magnetic field B_0.

The m = -1 and m = 1 levels of the energy diagram for the combined Zeeman and quadrupolar interactions are raised equally by the quadrupolar interaction (Figure 3-3). The energy for allowed transitions (m = 1 → m = 0; m = 0 → m = -1) is unequal, i.e., two lines appear in the spectrum. When Q is averaged to zero by isotropic tumbling, the energy of transition is the same for m = 0 → m = -1, m = 0 → m = 1 and only one line results.

For a single spin-1 nucleus interacting with an axially symmetric field gradient, the spectrum consists of a doublet with peaks separations given by:

Equation 3-2

$$\Delta\nu = \frac{3}{4}\left(\frac{e^2qQ}{\eta}\right)\left(3\cos^2\theta - 1\right)$$

where (e^2qQ) is the quadrupolar coupling constant and θ is the Euler angle between the principal axis system and the laboratory frame. If the deuteron undergoes rapid isotropic reorientation on the timescale of the quadrupolar interaction $1/(3e^2qQ/4h)$

then the electric field gradient at the nucleus, although present, is averaged to zero and there is no quadrupolar interaction to produce the doublet. A single resonance, centred at the Zeeman frequency, is observed. A *Pake doublet* arises (Figure 3-3) as the general case when the observed system exists as a powder sample with all molecular orientations. The doublet peak separation, $\Delta\upsilon$, is determined by the motions of the C-D bond and is varied by local axial rotation and changes in sample anisotropy (Figure 3-4).

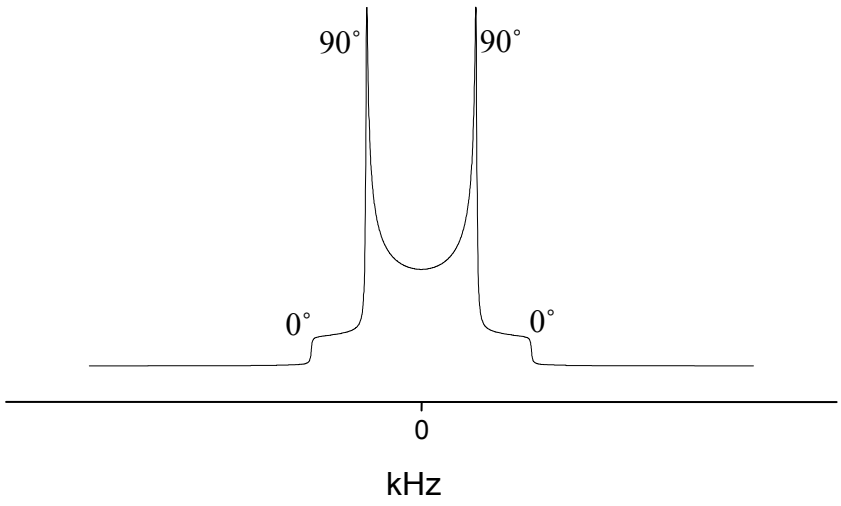

Figure 3-3 Powder pattern arising from orientation of the C-D bond at all possible angles with respect to the magnetic field with equal probability. The outer wings originate from the 0° orientation whilst the inner peaks arise from the 90° orientation of the C-D bond. $\Delta\upsilon_Q$ is the separation of the inner peaks.

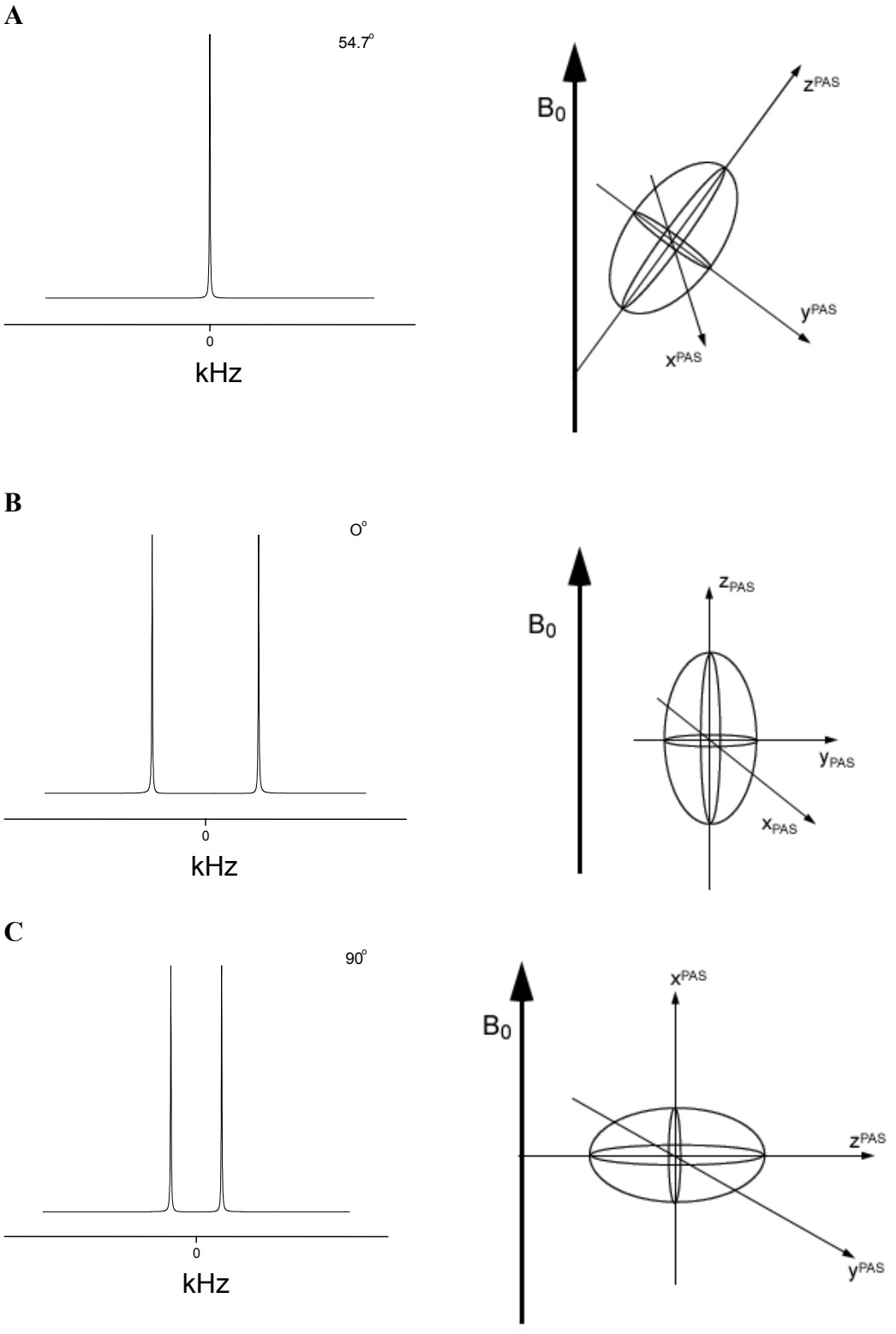

Figure 3-4 Simulated deuterium spectra showing the effect of orientation of the principal axis of the electric quadrupole tensor, which lies along the C-D bond, with respect to the magnetic field. These spectra arise when the z-axis of the Principal Axis System (PAS) of the tensor (and thus the C-D bond) oriented (A) at the magic angle (54.7˚), (B) parallel to (0˚) and (C) perpendicular to (90˚) the external field. Spectra simulated by Dr R. Verel.

The above examples are valid for a rigid sample whose deuterated groups are undergoing fast axial rotation about the director axis. In this study, the deuterium spectral lineshapes may be made more complex by exchange occurring on the quadrupolar timescale (10^6 Hz) between the bound state in the protein and the free state in the buffer. If there such intermediate exchange, the resultant lineshape is a convolution of the narrow and anisotropic components of the spectrum.

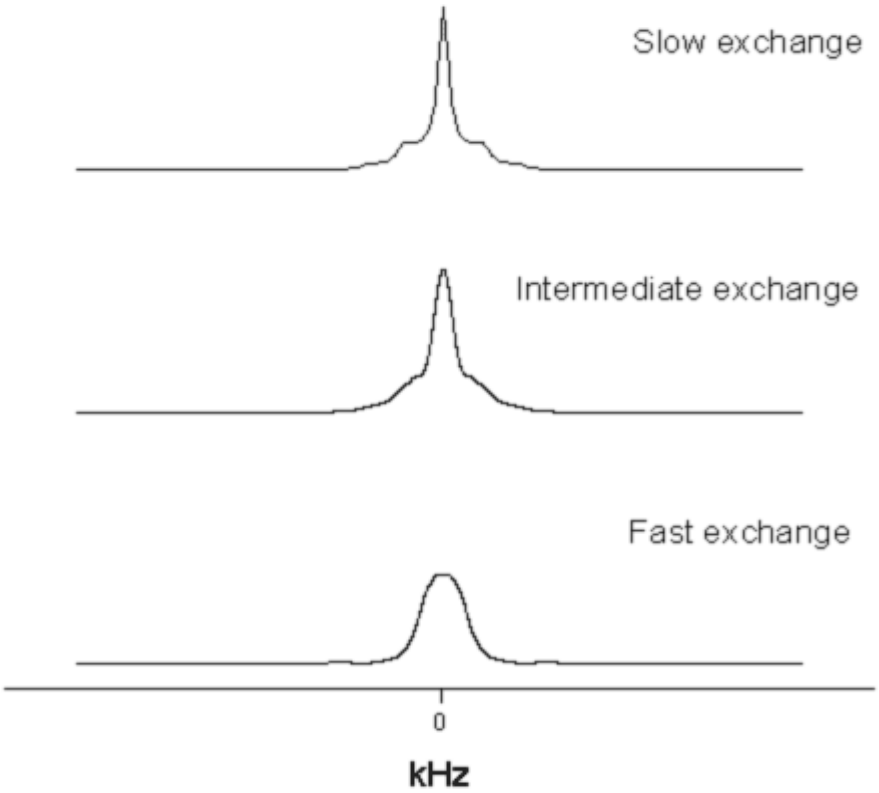

Figure 3-5 Simulated spectra illustrating the effect on the spectral lineshapes of rate of population exchange between a site of motional restriction and a site of free mobility. In the top spectrum there is slow exchange on the quadrupolar timescale (10^6 Hz) between the bound and free sites. The spectrum shows two components, a narrow line from the free species and a broad component from the bound population. As the rate of site exchange increases, the narrow central component broadens until the bound and free components are indistinguishable [148]. Spectra simulated by Dr D. Middleton.

In this study, exchange is prevented by freezing the sample (268 K) whilst avoiding freezing the free inhibitors in solution.

Aims of this study

The binding mechanism of reversible inhibitors of the gastric H/K-ATPase is poorly understood and the binding sites of these compounds are not clearly defined. Deuterium NMR can potentially provide dynamical information about the motional freedom of deuterium-enriched inhibitors and allows analysis of the motions of the labelled functional groups at the active site. A number of novel reversible inhibitors of the H/K-ATPase have been synthesised to contain ^{19}F for REDOR NMR structure determination (Chapter 4) and a variety of other substitutions have been made at the C8 position to examine the structure-activity relationship of the benzyl ring (see Chapter 2). The fluorinated compounds all exhibited inhibitory potency and substitution of the 8-aryl species by a cyclohexyl group demonstrated high activity. The deuterium spectra of SIPs with different activities titrated into gastric H/K-ATPase preparations were examined qualitatively for evidence of motional restriction of labelled groups at the binding site and thus to relate their function to mobility in the binding site. Control experiments were performed to verify if the spectrum was from inhibitor bound to H/K-ATPase. These experiments looked for liberation of the inhibitor into the surrounding medium by K^+-competition, and for association with lipids of the gastric membrane. An examination of the variation of the spectra of crystalline solid SIPs with temperature precedes the membrane work. The spectra determined the extent of axially-symmetric rotation available to the deuterated functional groups and to assess whether this rotation would complicate the membrane spectra.

Materials and Methods

Synthesis of TEMPO-ITC-labelled Substituted Imidazo[1,2-a]pyridines

As a complimentary experiment to the ^{2}H NMR studies of SIP dynamics in gastric membrane preparations, two spin-labelled analogues of SCH28080 were to be synthesised and the motional characteristics of the spin-label groups were to be compared to those examined by NMR. The first spin label was substituted at the C3 position of the imidazo fused ring (Figure 3-1B). The second spin label was to replace the phenylmethoxy group at the C8 position. In the first instance, the final compound had no inhibitory potency. In the second instance, synthesis of a primary amino intermediate (NH_2 in place of the oxygen of TMPIP) could not be conducted unambiguously and the final spin label product could not be separated from side products. Furthermore, the spin label was reduced and thus rendered impotent for ESR studies. The synthetic routes are presented below as a prelude to the synthetic steps describing isotopic enrichment of SIPs for ^{2}H NMR studies.

Generation of 3-amino-2-methyl-8-(phenylmethoxy)imidazo[1,2-*a*]pyridine and Labelling with TEMPO-ITC

2-methyl-8-(phenylmethoxy)imidazo[1,2-*a*]pyridine (DMPIP) (5 mmol), synthesised according to the methods outlined in Chapter 2 and continued here according to [125], in 50 mL tetrahydrofuran was added drop-wise to 15 mL *n*-butyl nitrate. The mixture was heated to reflux for 45 min, cooled and 50 mL absolute ethanol added. The mixture was concentrated to approximately 50 mL and poured into a 70 mL

volume of concentrated HCl and 10 g stannous chloride monohydrate (Aldrich Chemical Co., Gillingham, UK). The mixture was heated to 60 ˚C and then cooled to room temperature to be stirred for 1.5 hrs. The reaction was poured onto ice (500 g) and 100 g of 50 % NaOH solution was added to neutralise the mixture. The solution was extracted with chloroform (2 x 300 mL) to obtain pooled, then concentrated, organic phase extracts. These formed a brown oil that was separated on a Keiselgel 60 silica column (Merck, Darmstadt, Germany) eluting with 2:3 chloroform:ethanol. The product fraction was identified by ^{1}H NMR and reacted on without further purification.

To 37 mg of TEMPO-ITC (Aldrich Chemical Co., Gillingham, UK) was added an approximate 2 mole equivalent of 3-amino-2-methyl-8-(phenylmethoxy)-imidazo[1,2-*a*]pyridine (~22 mg, 0.09 mmol) in methanol. The reagents were stirred for 2.5 hrs at room temperature with periodic sampling to assess the extent of the reaction by TLC. The individual bands were solvated in ethanol and examined by ESR to identify spin-labelled compounds. Upon identifying the free TEMPO-ITC and ligand-TEMPO bands, the reagents were separated by preparative TLC and the silica corresponding to the position of the product band was removed from the plate and suspended in ethanol. The product band was filtered and the ethanol gently concentrated under reduced pressure. The concentration of spin-labelled ligand was estimated by ESR by reference to a standard curve generated using known concentrations of TEMPO-ITC. The final yield was estimated to be 0.133 μmol (0.15%) as a 265 μM concentration.

Generation of 2,3-dimethylimidazo[1,2-*a*]pyridine and Labelling with TEMPO-ITC

To 2,3-diaminopyridine (273 mg, 2.5 mmol) (Aldrich Chemical Co., Gillingham, UK) in 50 mL ethanol was added 3 mole equivalents 3-bromo-2-butanone (Lancaster Synthesis, UK) (1.13 g, 7.5 mmol) and the mixture was stirred under reflux for 20 hrs. After this time, a further 1 mole equivalent of 3-bromo-2-butanone was added and the reaction was stirred for a further 1 hr. The sample was allowed to cool and the solvent was removed by rotary evaporation under reduced pressure. The residue was dissolved in methanol and identified by Mass Spectrometry as a mixture of starting material and the desired product. The crude mixture was reacted with a further 2 mole equivalents of 3-bromo-2-butanone for a further 5 hrs. After this time, the reagents were separated on a Keiselgel silica column, eluting with 3:1 chloroform:methanol. The first eluted species readily yielded red needle-like crystals. These were redissolved in ethanol and cleaned with activated charcoal. The solvent was gently removed under reduced pressure. Clean, clear crystals were obtained from methanol. (10 % yield identified by Mass Spectrometry).

To 11 mg (52 μmol) TEMPO-ITC in cold ethanol (4 ˚C) was added an excess of 2,3-dimethylimidazo[1,2-*a*]pyridine (24 mg, 151 μmol). The reagents were allowed to stir at 4 ˚C under argon for 18 hrs. Sampling by TLC indicated a mixture of products and of TEMPO-ITC. The impure spin-labelled SIP could not be separated from its co-products and was found to be reduced when examined by ESR.

Synthesis of Deuterated Substituted Imidazo[1,2-a]pyridines

d_3-TM2FPIP (1-trideuteromethyl-2,3-dimethyl-8-(*o*-fluorophenylmethoxy)-imidazo[1,2-*a*]pyridinium iodide, d_3-DMPIP (1-trideuteromethyl-2-methyl-8-(phenylmethoxy)imidazo[1,2-*a*]pyridinium iodide, d_3-TMTFBIP (1-trideutero-2,3-dimethyl-8-(trifluorobutylmethoxy)imidazo[1,2-a]pyridine iodide, and d_3-TMCHIP (1-trideutero-2,3-dimethyl-8-(cyclohexylmethoxy)imidazo[1,2-*a*]-pyridinium iodide were synthesised according to the synthesis scheme described in Chapter 2 by first generating 2,3-dimethyl-8-(*o*-fluorophenylmethoxy)-imidazo[1,2-*a*]pyridinium, 2-methyl-8-(phenylmethoxy)imidazo[1,2-*a*]pyridine, 2,3-dimethyl-8-(trifluoro-butylmethoxy)imidazo[1,2-a]pyridine, and 2,3-dimethyl-8-(cyclohexyllmethoxy)-imidazo[1,2-*a*]pyridine. Methylation at the 1-position was generally achieved by reaction of the tertiary amine dissolved in acetone with 5 mole equivalents of d_3-iodomethane (Aldrich Chemical Co., Gillingham, UK). The mixture was heated under reflux until a white solid precipitate occurred. Upon removal of the solvent by rotary evaporation under reduced pressure, the solid was recrystallised from methanol to yield the iodide salt of the SIP quaternary amine.

d_7-TMPIP (1,2,3-methyl-8-(perdeuterophenylmethoxy)imidazo[1,2-a]pyridinium iodide were synthesised according to the scheme in §2.3.3 by addition of 1 mole equivalent benzyl-d_7 chloride to DMHIP (2,3-dimethylimidazo[1,2-a]pyridine-8-ol) respectively in N,N-dimethylformamide and 5 mole equivalents K_2CO_3. The 8-protected compounds were then reacted with iodomethane in the manner described above to produce the iodide salt of the SIP quaternary amine.

Preparation of GI Membranes for NMR

Gastric membranes were prepared according to a method modified from that of Sacconami [129]. GI membrane suspension containing 30 mg of protein was washed of sucrose by ultracentrifugation (240000 g, 60 min, 4 °C) in 20 mM TRIS-HCl (pH 7.4) buffer. In order to present the inhibitor with the greatest number of available binding sites, the NMR experiments were performed under conditions promoting the phosphorylated (E2-P) conformation. This form of the enzyme complex permits binding of the SIP to the high-affinity K^+-site in the extra-cytoplasmic surface of the protein [103, 104]. The presence of excess phosphate and chelating Mg^{2+} was applied to prevent turnover of the enzyme complex and concomitant loss of the SIP high-affinity binding site. Accordingly, the membranes were lyophilised overnight and resuspended in 20 mM phosphate buffer (10 mM $MgCl_2$, pH 7.4) in deuterium-depleted water. Prior to the NMR experiment, the protein suspension was pelleted by ultracentrifugation (240000 g, 60 min, 4 °C) and the membrane sample was placed in a 5mm quartz NMR tube cut to 3 cm lengths for incubation with the appropriate inhibitor.

Preparation of Gastric Membrane Lipids

GII membranes were pelleted by ultracentrifugation (240000 g, 60 min, 4 °C) and resuspended in acidified water (pH 3). The membranes were pelleted again and resuspended in water. The aqueous suspension was washed 5 times with a organic solvent preparation (3:1 chloroform:methanol) using a separating funnel. The cloudy organic lower phase was collected and pooled and centrifuged in a bench-top

centrifuge (2000 rpm, 5 min) to separate the organic and residual aqueous phase. A ring of insoluble matter was skimmed from the aqueous-organic phase interface. The mixture was returned to the separating funnel for a further wash with the organic preparation. The organic phases were pooled and backwashed with water. The organic phase was dried with anhydrous $MgSO_4$ and filtered through glass wool. The solvent was removed by rotary evaporation under reduced pressure and the final lipid sample was dried under high vacuum. The lipid was rehydrated overnight with deuterium-depleted 20 mM phosphate buffer (10 mM $MgCl_2$, pH 7.4) to afford a white slurry. Prior to incubation with deuterated SIP, the lipid suspension was pelleted and transferred to a 5mm diameter quartz NMR tube cut to 3 cm length.

Addition of Inhibitors to Membranes and Lipids

The maximum binding level for the SIP SCH28080 in sealed vesicles is 0.84 nmol/mg protein [154]. In leaky (lyophilised) membranes, the value is much higher [229]. The number of phosphorylation sites per mg protein is 1.6 nmole [230] and it has been estimated that there are 2.2 binding sites per phosphorylation site [154]. Thus it was assumed that 1 mg of total protein contained 2.5-3.0 nmoles inhibitor binding sites in the lyophilised membranes used in these experiments. Substituted imidazo[1,2-*a*]pyridines (SIPs) were introduced to membrane and lipid sample by dissolving the compound in deuterium-depleted phosphate buffer to the required concentration such that 3.5 nmoles SIP/mg protein were dispensed in a 40-50 μL aliquot (typically 2.6 mM). The buffer solution was thoroughly stirred into the protein suspension followed by incubation at 37 ˚C for 1 hr. The pyridinium iodide

salts were sparingly soluble and required warming the buffer and sonicating the sample until the solid had disappeared.

Broadline Deuterium NMR Measurements

^{2}H NMR measurements were performed at 500.13 Mhz on a Magnex wide bore (89 mm) spectrometer with an 11.7 T superconducting magnet, CMX Infinity console and static 5 mm single resonance probe. Spectra were obtained from samples contained in a sealed 5 mm diameter tube using the quadrupole echo sequence 90°_x-τ_1-90°_y-τ_2-acquire [Davis, 1976]. Deuterium 90˚ pulse lengths were typically 3.5 μs. The recycle time was 0.5–1.0 s. Temperature was controlled to ± 1 K by a Chemagnetics VT temperature control unit. Typically, 200000 acquisitions, accounting for 28 hours of acquisition time, were obtained for membrane samples. Previous activity assays had shown that the samples could survive thawing and refreezing.

Data analysis

To determine the populations of bound and free inhibitor a Lorentzian lineshape was fitted to the isotropic peak and subtracted from the integral of the spectral lineshape. The lineshape simulation algorithm was based on the probability density functions described by Seelig [138] and was written in C by Dr D. Middleton. The simulations permitted variation in bound and free populations and accommodated changes in site exchange rates.

Results and Discussion

Dynamics of d_3-Substituted Imidazopyridines in the Gastric Membrane

The temperature dependence of the deuterium spectra of solid crystalline *d_3*-TM2FPIP between 213 K and 293 K is shown in Figure 3-6. The powder pattern at 293 K shows a Pake doublet typical of an axially symmetric quadrupolar interaction for a CD_3 group undergoing free rotation about the N-C bond leading to an averaging of the static quadrupolar coupling for a CD_3 group deuteron (125 kHz) by over one third [138, 151]. There is a splitting, $\Delta\upsilon_Q$, of 36 kHz, with a rounding of the outer wings which indicates further averaging by molecular motion in the crystal lattice. As temperature is decreased, the splitting increases to 37 kHz at 268 K, 38 kHz at 258 K, and 39 kHz at 243K, 228 K and 213 K. There is a concomitant increase in the definition of the outer wings at temperatures below 258 K. At all temperatures, there is no central component attributable to rapid isotropic motion.

The variation of deuterium lineshape of *d_7*-TMPIP with temperature is shown in Figure 3-7. The spectra contrast with those obtained for *d_3*-TM2FPIP in that they show a complex powder pattern consisting of two overlapping Pake doublets. One pair of doublets ($\Delta\upsilon_Q$ = 29-32 kHz) arises from the phenyl deuterons engaging in 2-site flipping of the phenyl group while the other ($\Delta\upsilon_Q$ = 123-125 kHz) results from rigid methylene and phenyl deuterons [151]. The spectra show that the *d_7* benzyl group is motionally constrained in the crystal lattice and the reducing the temperature to 213 K has little freezing effect on the residual benzyl rotation in the molecule [152]. At 268 K there is no narrow central intensity arising from fast isotropic motions in the molecule.

A

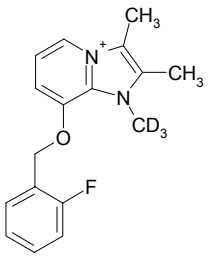

B

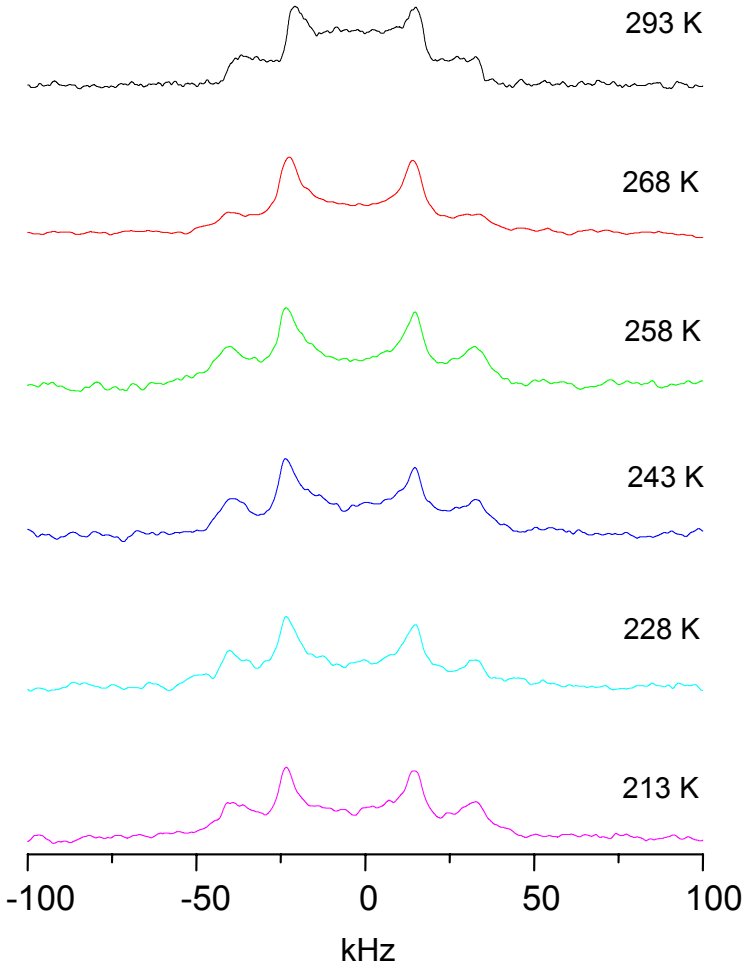

Figure 3-6 (A) Chemical structure of d_3-TM2FPIP. (B) Variable temperature deuterium NMR spectra of crystalline d_3-TM2FMPIP. Spectra as described in the text (4096 acquisitions).

A

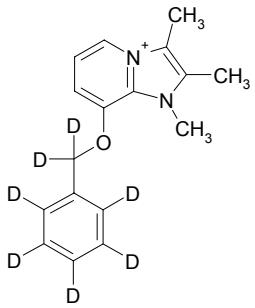

B

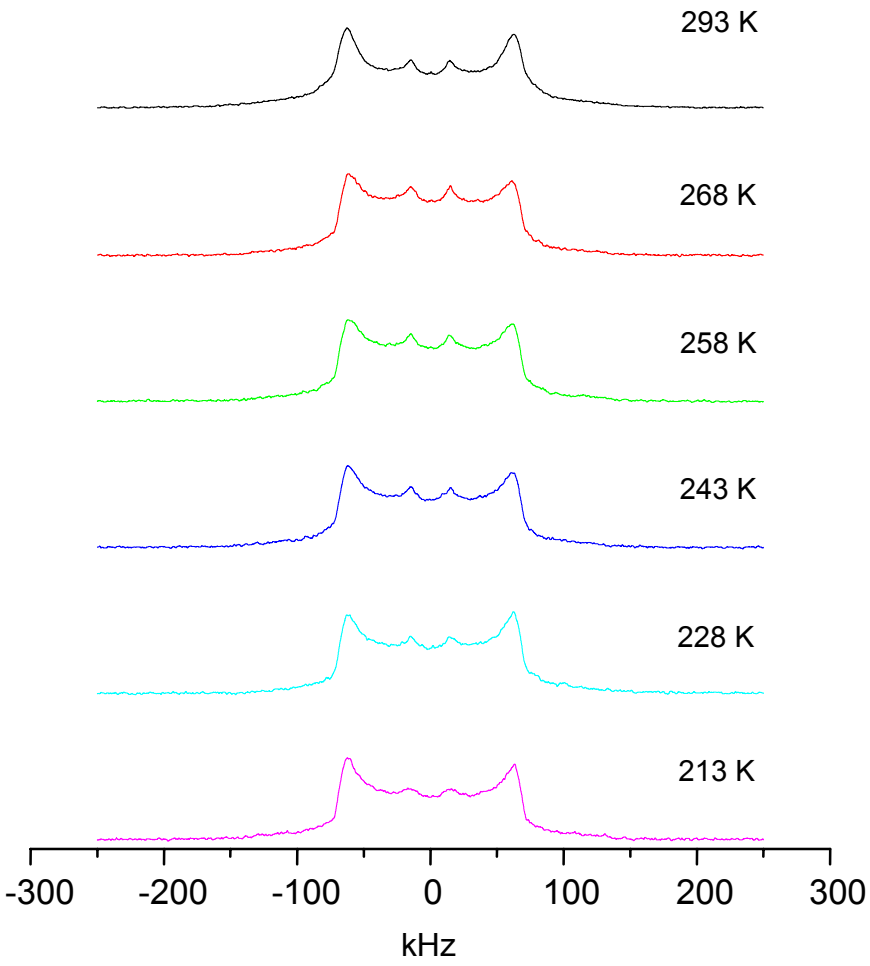

Figure 3-7 (A) Chemical structure of d_7-TMPIP. (B) Variable temperature deuterium NMR spectra of crystalline d_7-TMPIP. Spectra as described in the text (2048 acquisitions).

The temperature dependence of the deuterium spectra of d_3-DMPIP between 213 K and 293 K is shown in Figure 3-8. At all temperatures, the powder spectra exhibit splittings of the central intensities of 37-38 kHz indicating free rotation of the *N*-CD_3 group and further averaging of the quadrupolar coupling by vibrational motion in the crystal lattice. There is an improvement in the definition of the outer wings as temperature is reduced to 213 K. As with TM2FPIP, there is no central component attributable to fast isotropic motion.

Figure 3-9 shows the temperature dependence of the deuterium spectra of d_3-TMTFBIP between 213 K and 298 K. There are two components to the spectrum obtained at 298 K. A minor narrow central resonance ($\Delta\upsilon_Q$ = 1 kHz) is superimposed upon a doublet with a splitting of $\Delta\upsilon_Q$ = 36 kHz. Lowering the temperature to 268 K and 258 K reduces the contribution of the central resonance, which is attributed to residual solvent trapped in the crystal lattice. The powder patterns are characteristic Pake doublets reporting free rotation of the *N*-CD_3 methyl group. Additional molecular motions appear to be frozen out below 268 K as the definition of the outer wings improves.

The temperature dependence of the deuterium spectra of d_3-TMCHIP between 298 K and 213 K is shown in Figure 3-10. A minor narrow component ($\Delta\upsilon_Q$ = 2 KhZ) is superimposed upon a characteristic Pake doublet ($\Delta\upsilon_Q$ = 37 kHz). The intensity of the central resonance disappears by 243 K and may be attributed to solvent in the crystal lattice. The doublet separation remains unchanged as the temperature decreases but there is an improvement in the definition of the outer wings as additional molecular motion is frozen. At 268 K the contribution from the central intensity is minor and does not dominate the spectral lineshape.

A

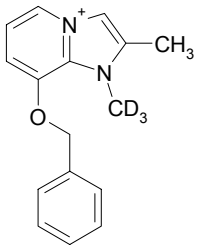

B

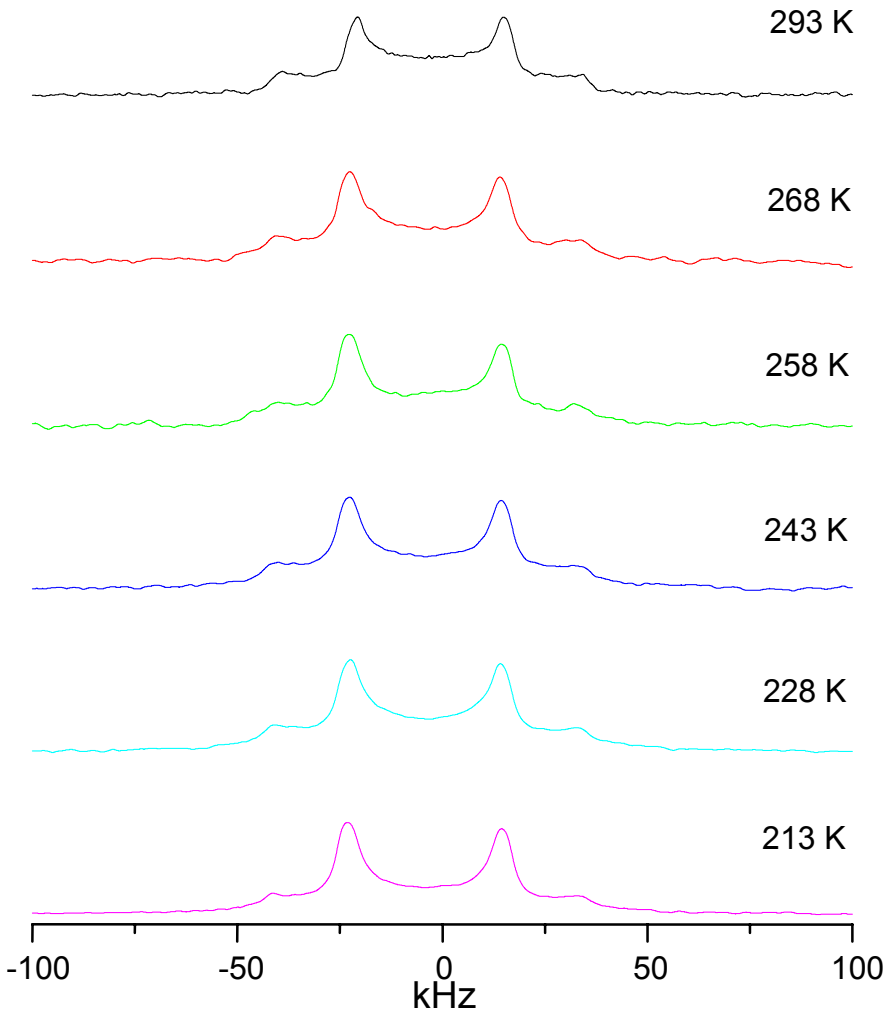

Figure 3-8 (A) Chemical structure of d_3DMPIP. (B) Variable temperature deuterium NMR spectra of crystalline d_3-DMPIP. Spectra as described in the text (1024 acquisitions).

A

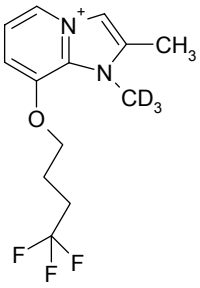

B

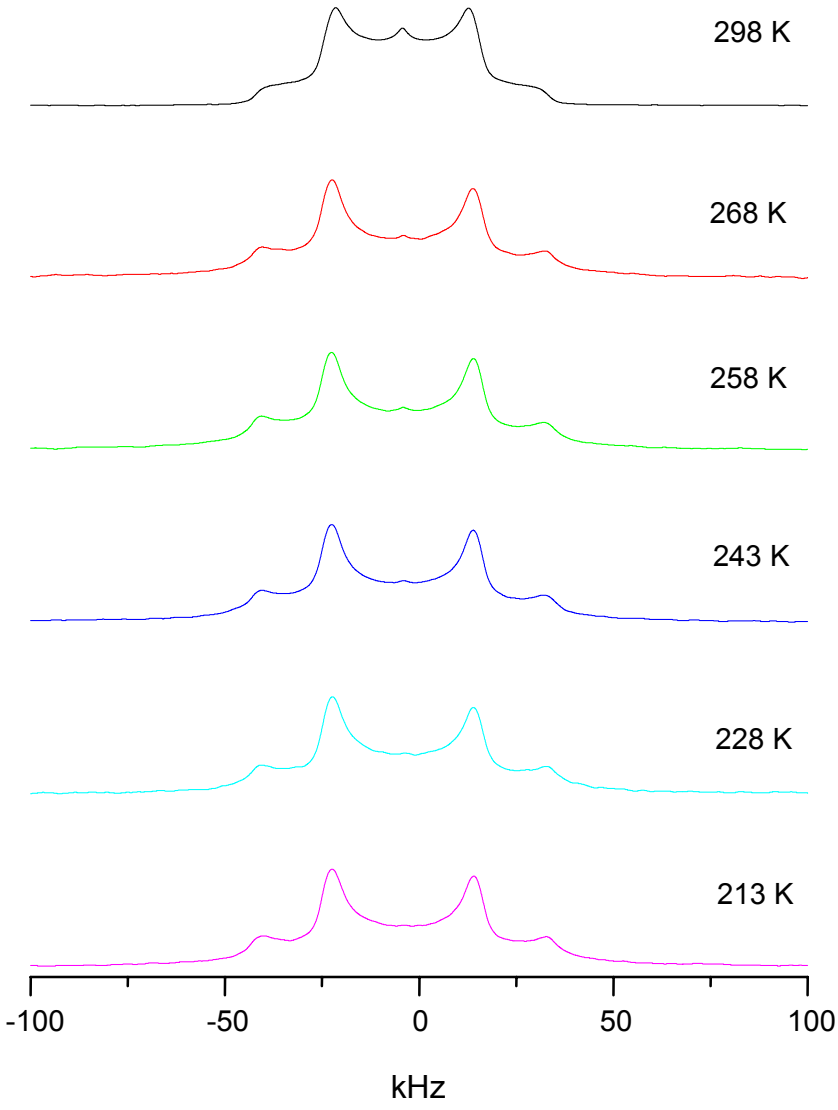

Figure 3-9 (A) Chemical structure of d_3-TMTFBIP. (B) Variable temperature deuterium NMR spectra of crystalline d_3-TMTFBIP. Spectra as described in the text (1024 acquisitions).

A

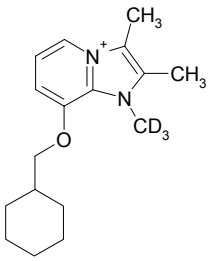

B

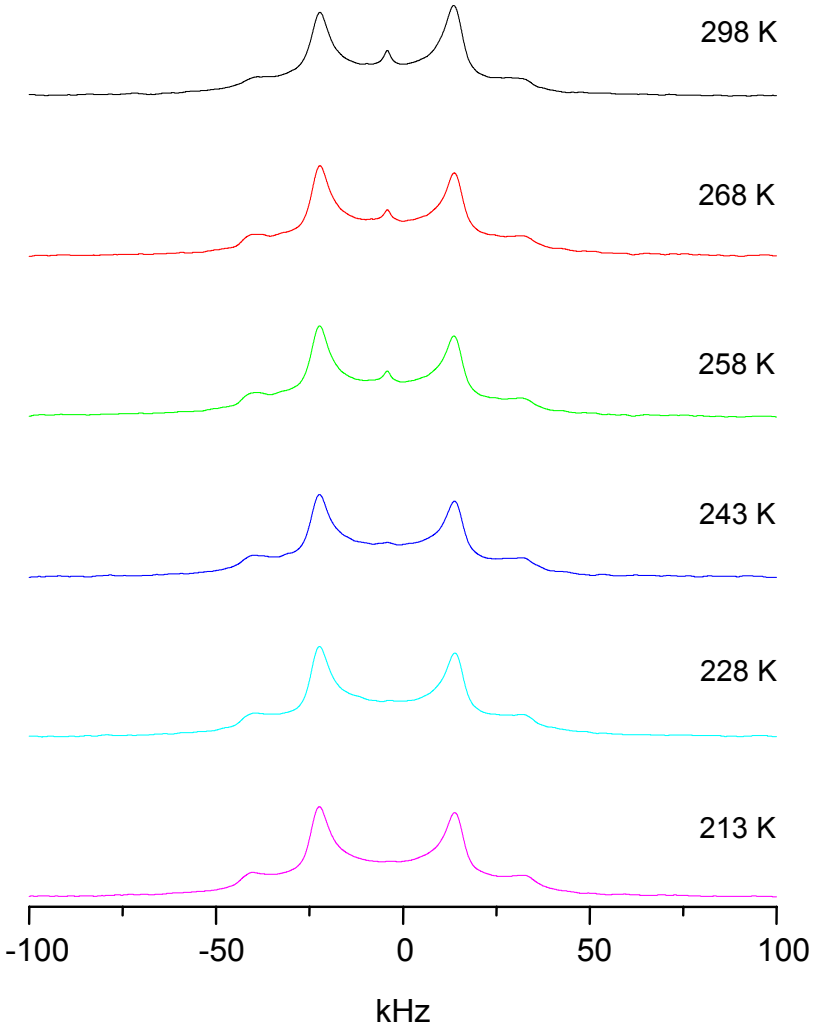

Figure 3-10 (A) Chemical structure of d_3-TMCHIP. (B) Variable temperature deuterium NMR spectra of crystalline d_3-TMCHIP. Spectra as described in the text (1024 acquisitions).

Gastric H/K-ATPase Membranes Labelled with d_3-TM2FPIP

Deuterium spectra of gastric membranes enriched with H/K-ATPase labelled d_3-TM2FPIP acquired at 268 K are shown in Figure 3-11. The spectrum of H/K-ATPase enriched membranes inoculated with d_3-TM2FPIP (IC_{50} = 5.0 μM) (Figure 3-11A) consists of two components in superposition, a narrow central line ($\Delta\upsilon_Q$ = 2 kHz) corresponding to highly mobile inhibitor, and a broad powder pattern ($\Delta\upsilon_Q$ = 37 kHz) ascribed to motionally-restricted inhibitor. Comparison of the spectrum with simulated spectra [138] presenting different proportions of the two components indicates that the powder (immobilised) component represents over 80% of the total spectral intensity and by implication, that 80% of the inhibitor population is immobilised at a binding site. Figure 3-11B shows the deuterium spectra of GI membranes containing d_3-TM2FPIP after addition of KCl. The broad spectral component has disappeared leaving only a single narrow line characteristic of free and highly mobile ligand. K^+ competes with imidazo[1,2-*a*]pyridines for the same high affinity site on the extracellular face of the H/K-ATPase [153, 154]. This observation suggests that the motionally restrained component corresponds to protein-bound ligand. To verify that the broad component does not arise from interaction with lipids and not protein, Figure 3-11C shows the deuterium spectrum of d_3-TM2FPIP added to a similar hydrated volume of extracted gastric lipid membranes. Only a single Lorentzian line from mobile inhibitor is observed. The line is narrow ($\Delta\upsilon_Q$ = 3 kHz) although broader than compared to that obtained after K^+ competition (Figure 3-10B). This indicates that K^+ competes out non-specific interactions with the gastric lipids but that the powder component arose exclusively from interaction of the inhibitor with H/K-ATPase at the high affinity site in the GI gastric membrane preparation.

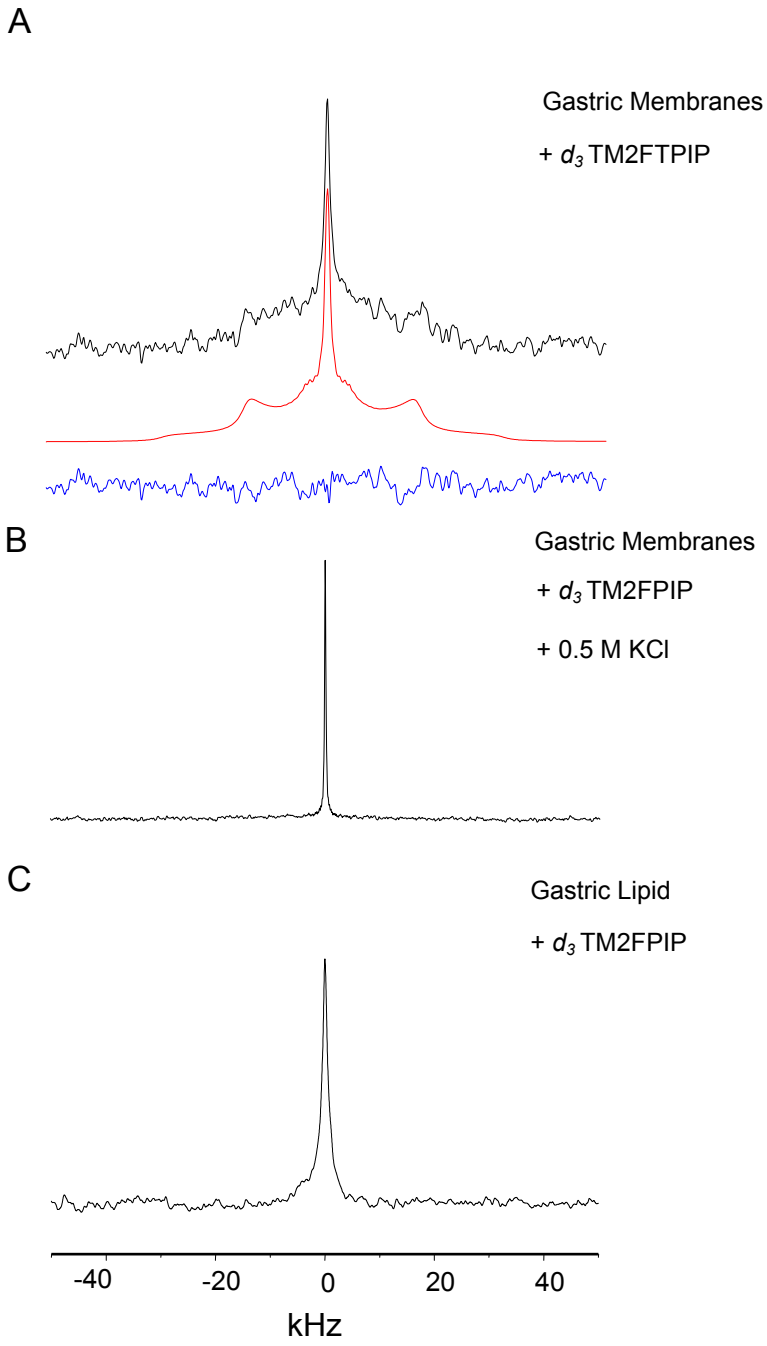

Figure 3-11 Deuterium NMR spectra of gastric membrane preparations inoculated with d_3-TM2FPIP. (A) H/K-ATPase membranes (30 mg protein) labelled with d_3-TM2FPIP. Simulated spectrum shown in red and difference spectrum in blue. (B) H/K-ATPase membranes as above following addition and incubation of 0.5 M KCl. (C) Gastric lipid labelled with d_3-TM2FPIP as above. Spectra acquired as described in materials and methods and result from averaging over 200000 acquisitions. Spectra acquired at 268 K.

Gastric H/K-ATPase Membranes Labelled with d_7-TMPIP

Deuterium spectra of gastric membranes enriched with H/K-ATPase labelled d_7-TMPIP acquired at 268 K are shown in Figure 3-12. The spectrum of H/K-ATPase enriched membranes incubated with d_7-TMPIP (IC_{50} = 2.8 μM) (Figure 3-12A) consists of two components in superposition, a narrow central line ($\Delta\upsilon_Q$ = 5 kHz) corresponding to highly mobile inhibitor, and a broad powder pattern with two sets of doublet peaks ($\Delta\upsilon_Q$ = 55 kHz and 108 kHz) ascribed to motionally-restricted inhibitor (c.f. Figure 3-7). The immobilised component exhibits a similar motional restriction to that displayed by the inhibitor in the crystalline sample but with evidence of an increase in secondary motional freedoms in an otherwise tight binding site in the protein. Motional averaging about a second or third bond axis would lead to further averaging of the coupling constant [155-157] and may account for the narrowing of the outer wings whereas this averaging results in a divergence of the inner wings resulting from the complex lineshape of the 2-site phenyl flipping. With simulation of the NMR lineshapes, motional models can be proposed to describe the phenyl ring dynamics in the binding site. Such analyses are beyond the scope of this qualitative study, however. Figure 3-12B shows the deuterium spectra of GI membranes containing protein-bound d_7-TMPIP after addition of KCl. The broad spectral component has disappeared leaving only a single narrow line (2 kHz) characteristic of free and highly mobile ligand. K^+ competes with imidazo[1,2-*a*]pyridines for the same high affinity site on the extracellular face of the H/K-ATPase [153, 154]. Apparent features in the baseline of this spectrum do not correspond to quadrupole splittings in the previous spectrum because the features they are not symmetrically distributed. These spectral artefacts are attributed to noise

in from the probe. Figure 3-12C shows the deuterium spectrum of d_7-TMPIP added to a similar hydrated volume of extracted gastric lipid membranes. Only a single line from mobile inhibitor is observed. The central intensity is broadened to the same extent as that of the mobile component in the GI-inhibitor spectrum in Figure 3-12A. The broadening of this line, compared to that obtained after K^+ competition may be taken to indicate non-specific interactions with the gastric lipids and that the broad component arose from interaction of the inhibitor with protein in the GI gastric membrane preparation. The results of this experiment support a binding mechanism for TMPIP whereby both the imidazo fused ring and the benzyl group are motionally restrained by the protein.

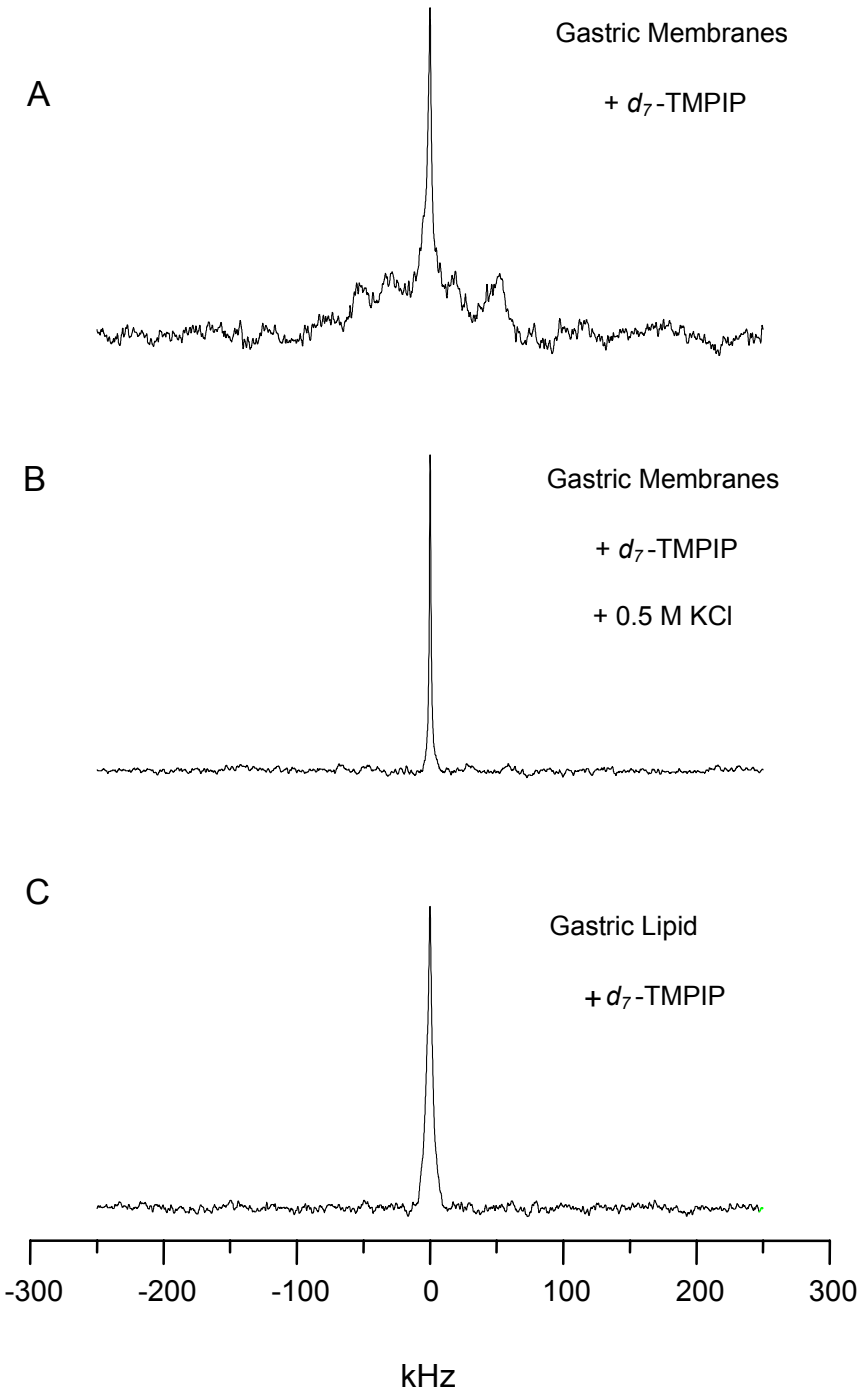

Figure 3-12 Deuterium NMR gastric membrane preparations inoculated with d_7-TMPIP. (A) H/K-ATPase membranes (30 mg protein) labelled with d_7-TMPIP. (B) H/K-ATPase membranes as above following addition and incubation of 0.5 M KCl. (C) Gastric lipid labelled with d_7-TMPIP as above. Spectra acquired as described in materials and methods and result from averaging over 200000 acquisitions. Spectra acquired at 268 K.

Gastric H/K-ATPase Membranes Labelled with d_3-DMPIP

Deuterium spectra of gastric membranes enriched with H/K-ATPase labelled d_3-DMPIP acquired at 268 K are shown in Figure 3-13. The spectrum of H/K-ATPase enriched membranes inoculated with d_3-DMPIP (Figure 3-13A) consists of two components. There is a single narrow central intensity (1 kHz) with a Lorentzian lineshape at the base characteristic of highly mobile inhibitor and a broader but low intensity component evident at the base. This spectrum indicates that DMPIP does experience some motional restraint by the protein but rather less than TMPIP. This may reflect the different IC_{50}s of the two ligands (> mM and 2.8 μM, respectively). Such an observation would be consistent with the condition that restraint of the imidazo ring in the binding site may be crucial for activity. There is little apparent change in the lineshape upon addition of KCl (Figure 3-13B), indicating that K^+ does not alter the binding properties of the ligand. The DMPIP analogue of SCH28080 has little inhibitory activity (IC_{50} > mM) and these data support the biochemical characterisation of the compound.

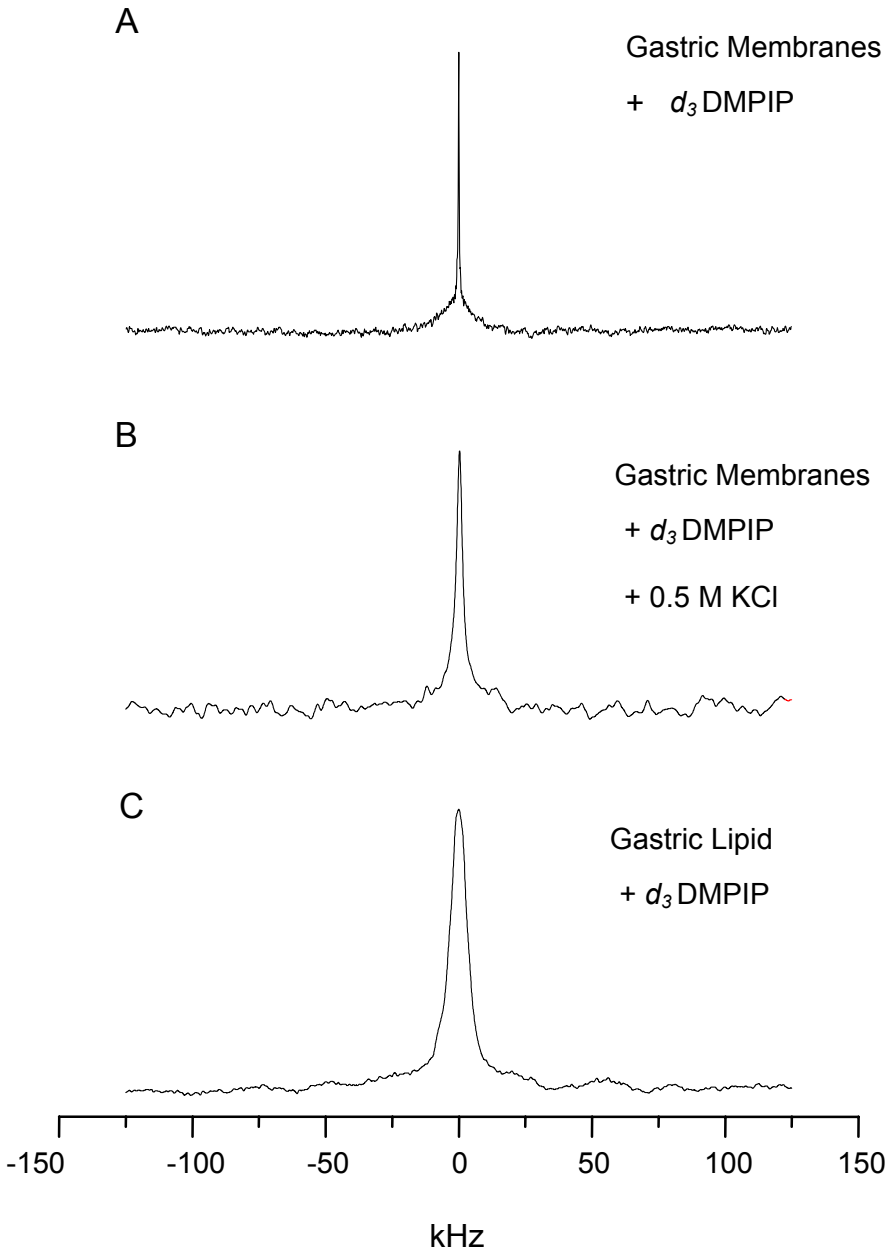

Figure 3-13 Deuterium NMR gastric membrane preparations inoculated with d_3-DMPIP. (A) 30 mg H/K-ATPase membranes labelled with d_3-DMPIP. (B) H/K-ATPase membranes as above following addition and incubation of 0.5 M KCl. (C) Gastric lipid labelled with d_3-DMPIP as above. Spectra acquired as described in materials and methods and result from averaging over 200000 acquisitions. Spectrum A is processed with less linebroadening than the other spectra. Spectra were acquired at 268 K.

The ligand appears to be retained by the H/K-ATPase to a lesser degree than TM2FPIP and is unsurprising therefore that introduction of K^+ into the system had little effect on this ligand population in the gastric membrane sample. Figure 3-13C shows the deuterium spectrum of d_3-DMPIP applied to a hydrated gastric lipid suspension of equal volume to the GI membrane preparation. The broadened lineshape is similar to those observed for both d_3-TM2FPIP and d_7-TMPIP incubated with gastric lipid and likewise indicates the motions of a highly mobile compound that may engage in weak interactions with the lipid component of the membrane.

Gastric H/K-ATPase Membranes Labelled with d_3-TMTFBIP

The deuterium NMR spectra of gastric membrane preparations labelled with d_3-TMTFBIP are shown in Figure 3-14. The broadline deuterium spectrum of H/K-ATPase enriched membranes incubated with d_3-TMTFBIP is shown in Figure 3-14A. The spectrum shows two poorly-resolved components. One component adopts a Lorentzian lineshape with a width at half-height of 3 kHz. The other component may exhibit a more motionally restricted species that contributes to the broadening of the lineshape. Biochemical characterisation of this compound has shown that it has no inhibitory potency in the range 10^{-3} – 10^{-9} M and the observed spectrum reflects an insubstantial population of d_3-TMTFBIP that is retained by the H/K-ATPase binding site. The lineshape Figure 3-14B shows the GI membrane sample containing d_3-TMTFBIP after addition of KCl. The spectrum shows a narrow central resonance with half-height width of 2 kHz that indicates free, mobile d_3-TMTFBIP. Incubation of the compound with gastric lipids produced a broadened (8 kHz) spectrum with a Gaussian lineshape. It appears that there is a non-specific interaction between the gastric lipids

and the SIP. d_3-TMFBIP does not inhibit the H/K-ATPase and the broadening of the central intensity of the GI membrane preparation may reflect a non-specific interaction with the gastric lipids. Addition of K^+ to the system, while not competing the compound from the H/K-ATPase, may change the charge distribution at the lipid-buffer interface such that retained d_3-TMFBIP is displaced from charged lipid headgroups that may concentrate the pyridinium cation. This experiment, taken with those preceding it appears to indicate a mechanism of binding whereby the primary interaction with the binding site is through the imidazo ring but further retention is determined by the nature of the C8-substituted group. The ^2H NMR experiments with d_7-TMPIP showed that the C8-group is bound to the same extent as in the crystalline solid. Here, d_3-TMFBIP cannot provide a C8-substituted ring system to retain the molecule in the binding site. The butyl group of d_3-TMFBIP provides neither the conjugate π electron system nor the steric volume of the phenylmethoxy- and fluorophenylmethoxy- substituents and the inhibitor potency suffers as a result.

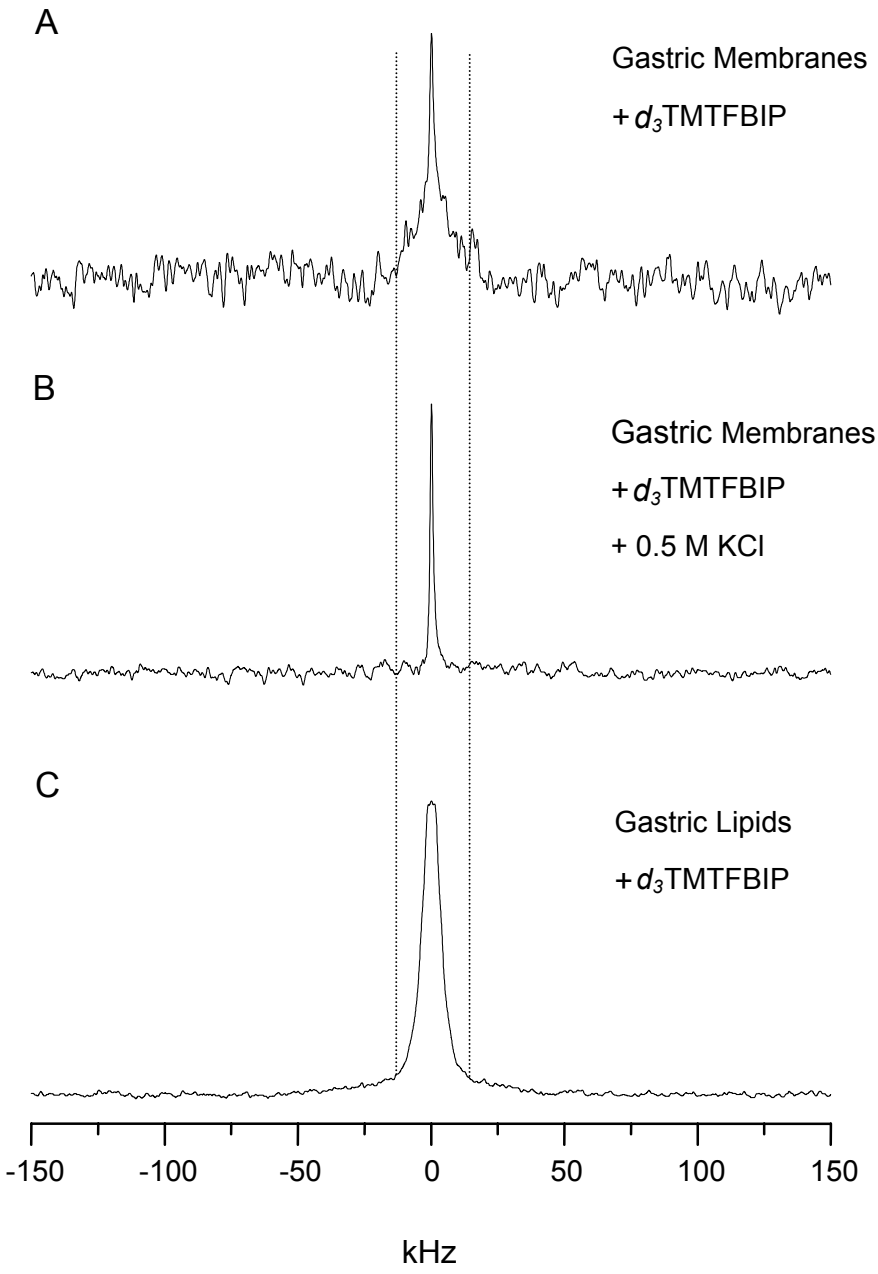

Figure 3-14 Deuterium NMR gastric membrane preparations inoculated with d_3-TMTFBIP. (A) H/K-ATPase membranes labelled with d_3-TMTFBIP (30 mg protein). (B) H/K-ATPase membranes as above following addition and incubation of 0.5 M KCl. (C) Gastric lipid labelled with d_3-TMTFBIP as above. The dotted lines illustrate the change in broadening of the spectral lineshape upon addition of K^+ to the membrane system and the similarity in linewidth between the GI membrane and lipid spectra. The spectra were acquired as described in Materials and methods and result from averaging over 200000 acquisitions. Spectra acquired at 268 K.

Gastric Membranes Labelled with d_3-TMCHIP

The spectra of d_3-TMCHIP-labelled gastric membranes (Figure 3-16) required a large number of acquisitions (>200000) to obtain a satisfactory signal using the echo delays employed previously. The deuterium NMR spectra of solid d_3-TMCHIP upon variation of the echo delay in the quadecho pulse sequence are shown in Figure 3-15.

A

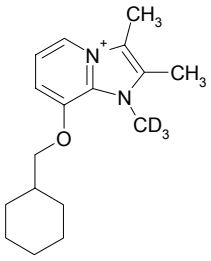

B

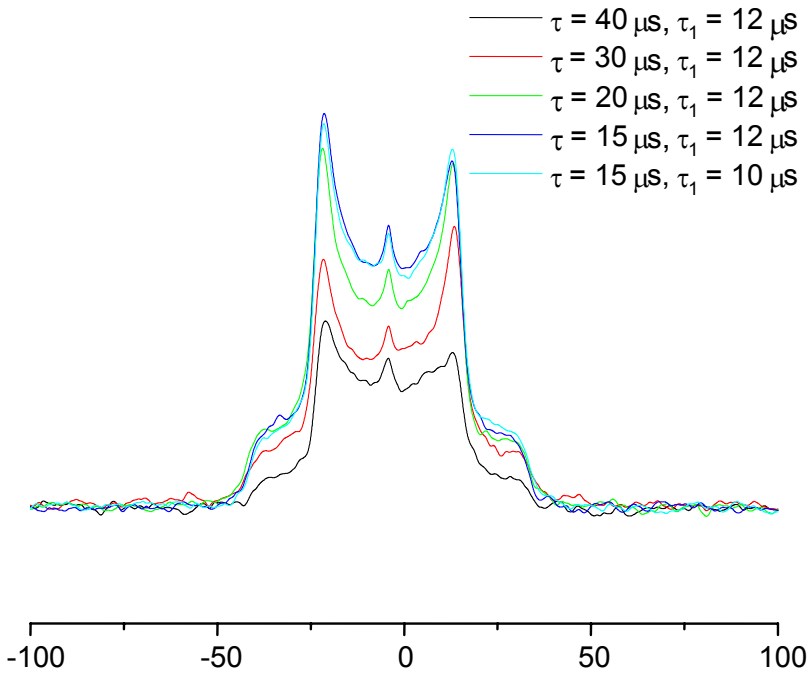

Figure 3-15 Deuterium NMR spectra of crystalline d_3TMCHIP with variation of interpulse delay, τ, in the quadrupole echo sequence. Spectra acquired at 268 K and as described in the text. (1024 acquisitions).

As the first delay, τ, in the echo sequence is decreased from 40 (black) to 15 μs (dark blue), it is seen that there is an improvement in spectral intensity of nearly 100% and 13% from 20 (green) to 15 μs (dark blue). For this experiment, delays of τ = 15 μs and τ_1 = 12 μs were chosen to improve signal intensity. There was no evidence of the ring-down of the probe being observed at these short echo delays. Reducing τ_1 from 12 to 10 μs produced no improvement in signal intensity but merely brought forward the observable full free induction decay by several data points.

Deuterium spectra of gastric membranes labelled with *d_3*-TMCHIP are shown in Figure 3-16. The spectrum of H/K-ATPase enriched membranes inoculated with *d3*-TMCHIP (Figure 3-16A) consists of two components in superposition, a narrow central line (3 kHz) corresponding to highly mobile inhibitor, and a broad powder pattern (33 kHz) ascribed to motionally-restricted inhibitor the methyl group of which is undergoing fast axially-symmetric rotation about the *N*-CD_3 axis. The binding mechanism of *d_3*-TMCHIP, which is a potent inhibitor (IC_{50} = 0.11 μM), does not contain an aromatic ring at the C8 position of the molecule (Figure 3-10A), allowing the possibility that inhibition of the protein by this compound, unlike other analogues of SCH28080, occurs in a manner that is not K^+-competitive. Figure 3-16B shows the spectrum of GI membrane containing *d_3*-TMCHIP after addition of KCl. The broad spectral component has disappeared and only a narrow line remains indicating that this SIP, with a cyclohexyl moiety in place of an aromatic system at C8, is indeed K^+-competitive. That the motional restriction is due to association with the protein and that the SIP has not been displaced from a strong association with lipids is demonstrated by the spectrum in Figure 3-16C.

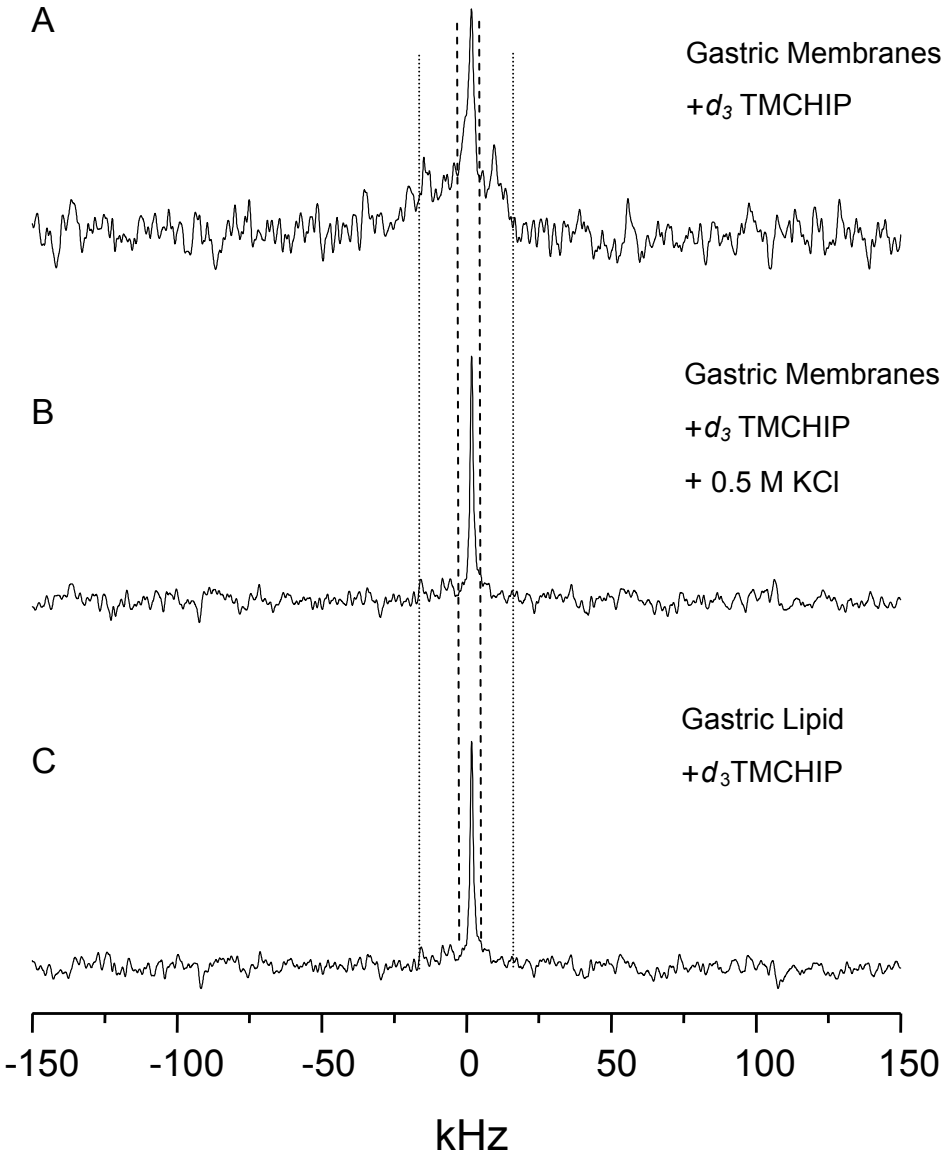

Figure 3-16 Deuterium NMR gastric membrane preparations inoculated with d_3-TMCHIP. (A) H/K-ATPase membranes (30 mg protein) labelled with d_3-TMCHIP. (B) H/K-ATPase membranes as above following addition and incubation of 0.5 M KCl. (C) Gastric lipid labelled with d_3-TMCHIP as above. The difference in spectral linewidths is illustrated by the dotted lines (broad component) and dashed lines (narrow component). Spectra acquired as described in materials and methods and result from averaging over 200000 acquisitions. Spectra acquired at 268 K.

When d_3-TMCHIP was added to a similar hydrated volume of gastric lipids a single narrow line is observed (2 kHz), indicating that the broad component in Figure 3-

16A arose from interaction of the inhibitor with the protein. There is little motional restriction due to association with the gastric lipid.

d$_3$-TMCHIP does not contain a system of conjugated π electrons that is characteristic of TMPIP (IC_{50} = 2.8 μM) and its fluorinated analogues and yet the cyclohexylmethoxy inhibitor exhibits inhibitory potency (IC_{50} = 0.11 μM) (see Chapter 2) and motional restriction in the protein. In the absence of a study of the deuterocyclohexyl equivalent of *d*$_7$-TMPIP it is not possible to be definitive about the binding mechanism of this compound. Since the compound is retained by the protein it is reasonable to assume that the C8-substituent is as motionally restricted as that of TMPIP and, as such, that binding of this part of the molecule is due to a steric, rather than electronic, component. Overall, it is seen that the imidazo ring is critical in binding. A small change (CH_3- → H-) produces a marked reduction in potency that is redeemed to only a small extent by the C8-aryl group of *d*$_3$-DMPIP (> mM). The binding pocket for the K^+-competitive SCH28080 analogues is able to tolerate variation in the nature of the electronic interaction that may be provided by this functional group. Biochemical analysis has shown that perfluorination of the 8-aryl group has little effect on the IC_{50} of the SIP (IC_{50} = 8.2 μM, see Chapter 2) and thus that cation-π interactions are not important for stabilisation of this group in the binding pocket [134]. Motional restriction of *d*$_3$-TMCHIP indicates that the π-π interaction is not crucial for binding this group. The saturated ring may still engage in CH-π interactions [158] and the influence of proximal aromatic residues should not be discounted. The role of this group in the binding mechanism may be primarily steric in nature. These ^{2}H NMR studies, coupled with the biochemical assays, allow a binding mechanism to be proposed whereby the substituted imidazo[1,2-*a*]pyridinium cation approaches the ligand binding site, possibly through a weak and

transitional association with the lipid bilayer, and is in the first instance drawn to the binding pocket by a protein-imidazo cation interaction. The ligand is then stabilised at its site of efficacy upon fulfilling a steric filtering constraint. If the C8-functional group does not occupy the correct volume the ligand is not retained by the binding site. Since a larger cyclohexymethoxy group, rather than a smaller fluorobutylmethoxy group, is accepted by the H/K-ATPase it is tempting to suggest that the inhibitor induces a mechanical change in the protein upon binding such that the larger group is retained. In the absence of further evidence at this stage, the proposal is offered with caution. The contention is supported by the acknowledgement that the cyclohexyl group may adopt the *boat* and *chair* conformations in the binding site (Figure 3-16). Both conformers are free of angle strain but the boat conformation is subject to both steric and torsional strain [159]. Furthermore, it is suggested that the cyclohexyl group emulates the planarity of its phenylmethoxy analogues by adopting the energetically favourable equatorial conformation with the methoxy group in the plane of the ring.

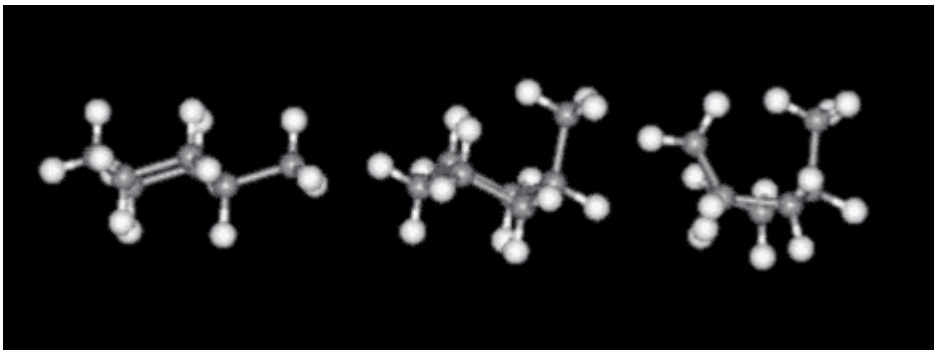

Figure 3-17 Schematic representations of (from left to right) the equatorial chair, axial chair and boat conformations of methylcyclohexane. The cyclohexylmethoxy functional group of TMCHIP is proposed to adopt the energetically-favourable equatorial chair conformation in the binding site of H/K-ATPase and thus occupy a similar space to that taken by the planar phenylmethoxy substituent of TMPIP and its fluorinated analogues.

Conclusions

This study established deuterium NMR as a sensitive reporter of the dynamics of substituted imidazo[1,2-*a*]pyridines associated with their target, the gastric H/K-ATPase. Analysis of the deuterium NMR spectrum has been valuable in both reporting the dynamics of the deuterated functional groups of the interaction of the SIPs with the GI membrane preparation and in validating the novel active analogues of SCH28080 as K^+-competitive and thus following a similar mechanism for binding the H/K-ATPase. The nature of binding of the potent inhibitors d_3-TM2FPIP and d_3-TMCHIP has been demonstrated to be both K^+ competitive in the manner of SCH28080 [153, 154] and constrained at the binding site. Both compounds produce Pake powder patterns when introduced into the GI membrane preparations. This indicates that the *N*-CD_3 undergoes rapid axially-symmetric rotation about the N-C bond axis but that this rotational averaging is not subject to further averaging by molecular vibration or motions propagated by the protein backbone on the timescale of the quadrupolar interaction. That there is no reduction in quadrupole splitting of the broad component in the membrane spectra as compared to the spectra obtained for the crystalline compounds demonstrates that the imidazo[1,2-*a*]pyridinium fused ring system is tightly retained at its site of action. The narrow central intensities are distinct from the broad feature and reflect the free SIP in the surrounding buffer. These data are supported by the studies with d_7-TMPIP. With this deuterated analogue, the motional restriction of the phenylmethoxy group of the molecule was demonstrated. Since the quadrupolar splittings of the doublet peaks for this compound in the membrane were reduced only slightly as compared to the crystalline d_7-TMPIP, it is possible to conclude that, despite their reversible

inhibition, both segments of these imidazo[1,2-*a*]pyridines are held tightly in the binding site of the H/K-ATPase with the C8 substitution permitting only a small amount of additional rotational freedom beyond that observed in the crystalline compounds.

The poor inhibitory potency of both d_3-DMPIP and d_3-TMTFBIP when titrated into gastric H/K-ATPase membrane preparations is illustrated in their deuterium spectra. Both these compounds are revealed to exist predominantly in the unbound population and give rise to narrow lineshapes which are little changed upon addition of K^+. All compounds exhibit a small population that interact in a non-specific fashion with the gastric membrane but this subgroup is a minor component of each spectrum and the motional restriction by this ligand-lipid interaction is not large.

The deuterium spectra indicate that both ring systems in the imidazo[1,2-*a*]pyridines are motionally constrained in the binding site of the H/K-ATPase. These results allow a mechanism to be proposed for the binding of SIPs to their high-affinity sites in the protein. It is suggested that the imidazo cation provides the primary influence in binding and that the C8 substitutions then determine the retention of the compound in the protein. Where the electronic and/or steric requirements of the C8 group are fulfilled but the imidazo fused ring system is poorly stabilised (d_3-DMPIP), the molecule acts as a poor inhibitor (IC_{50} > mM). Only a small population can be retained by the C8 substituent. When the imidazo fused ring system is adequately stabilised to localise the compound to the binding site but the C8 substitution is insufficient to retain the molecule (d_3-TMTFBIP), the compound exhibits no tight binding. The deuterium spectra obtained for d_3-TMCHIP in membrane preparations demonstrated that the nature of the interaction between the C8 functional group and neighbouring residues in the protein is not exclusively in a

manner previously suggested. Munson and co-workers [106], postulated that their photoactivated SCH28080 analogue, mDAZIP, might engage in π-π interactions with local aromatic residues. Whereas the study with TMCHIP does not discount this possibility for aryl SIPs, the absence of a conjugated system of π electrons in the C8 functional group provides that the binding pocket is sufficiently tolerant of a fully-saturated ring system at this position and of the additional volume occupied by the inhibitor as compared to the planar rings of the aromatic phenylmethoxy compounds.

The incorporation of ^{2}H- as a non-perturbing probe into SIPs has proven to be a valuable technique for providing information about the binding mechanism and dynamics of this pharmacologically important class of inhibitors without resorting to labelling with bulky spin labels for study by ESR. Deuterium NMR promises to be a useful technique in correlating inhibitory activity to binding mechanism and strength of retention of ligand retention at the binding site of the target membrane integral protein.

Chapter 4

^{13}C-^{19}F REDOR NMR STUDIES OF THE CONFORMATION OF SUBSTITUTEDIMIDAZO[1,2-A]PYRIDINES IN H/K-ATPASE ENRICHED MEMBRANES

Jude A. Watts, Anthony Watts, and David A. Middleton (2001) **A Model of Reversible Inhibitors in the Gastric H^+/K^+-ATPase Binding Site Determined by Rotational Echo Double Resonance NMR** *J. Biol. Chem*. **276**: 43197-43204

Introduction

There are many intrinsic difficulties in deriving structural information about membrane proteins and their ligands. The structural order imposed on membrane proteins and lipids is highly entropically unfavourable and, as such, there has been limited success with preparing well ordered crystalline arrays for diffraction studies (e.g. [32, 84, 160, 161]). The long correlation times associated with membrane proteins solubilised in detergents or reconstituted into small synthetic vesicles give rise to broad, poorly resolved solution state NMR spectra. Solid-state NMR with magic angle sample spinning (MAS) collapses such spectra to give well resolved isotropic chemical shifts but with concomitant loss of homonuclear and heteronuclear dipolar coupling and thus structural information. Inter-atomic distances may nonetheless be examined by application of particular analytical techniques such as rotational resonance [162] (See Chapter 1) and rotational echo double resonance (REDOR) NMR. These techniques reintroduce into the rotor-driven system dipolar couplings that exist between different non-perturbing NMR probes such as ^2H, ^{13}C,

^{15}N, ^{31}P and ^{19}F that are present in the system [43; 44; 173; 223; 224; 225]. The value of applying these methods to the study of ligands at their binding sites is that the structure of the protein target does not need to be known. Conformational information about the substrate at its active site may be obtained by site-specific labelling with non-perturbing NMR-sensitive nuclei and, as a process of rational drug design, the derived structural insight can be applied directly to improving the efficacy of the ligand [163]. REDOR NMR has also been used to determine internuclear distances between L-glutamate and glutamate-binding protein [164] and with the serine chemotaxis membrane receptor [165] to provide a large number of precise substrate-protein distance measurements. Assuming a stable scaffold for the protein itself (for instance, the transmembrane domain of the membrane integral protein) the structure of the ligand may impose constraints on the available orientations of transmembrane helices and the proximity of residues identified as important by site-directed mutagenesis studies [166]. Thus, where there is little known about the binding site of a ligand, the structure of the molecule can be used to build a model of the active site of its target.

Because their pharmacological activity is modulated by attendant reduction in gastric acidity, reversible inhibitors of the gastric H/K-ATPase such as SCH28080 (Figure 4-1) have aroused particular interest as potential drugs for the treatment of gastroesophagael reflux disease and gastric ulcer disease. The weak basicity of SCH28080 (pK_a = 5.5) concentrates the inhibitor in regions of high local acidity. The substituted imidazo[1,2-*a*]pyridine is protonated to form the active, K^+-competitive pyridinium cation. Methylation of SCH28080 at the N-1 position of the imidazo ring also produces an active pyridinium cation without imposing steric restraints which might affect binding to the H/K-ATPase [127].

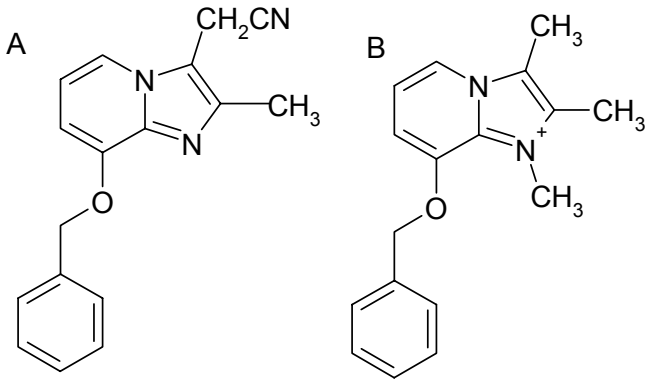

Figure 4-1 Schematic representation of the substituted imidazo[1,2-*a*]pyridines (A) SCH2808 and (B) TMPIP

The correlation between structure of substituted imidazo[1,2-*a*]pyridines and inhibitory potency *in vivo* and *in vitro* has been extensively studied [124-126]. The integrity of the 8-phenylmethoxy group was found to be important in retaining antisecretory and cytoprotective activity relative to SCH28080. Although introduction of an *o*-fluoro or *p*-fluoro substituent resulted in analogues with comparable oral antisecretory activity to the activity of the unsubstituted phenylmethoxy analogue, homologation (variation of the number of methylene groups between the oxygen atom and the phenyl ring) aromatic replacement and heteroatom replacement of the oxygen atom in the 8-phenylmethoxy group exhibited diminished antisecretory activity. Replacement of the cyanomethyl group of SCH28080 was also found to have a detrimental effect on activity but a simple analogue of SCH28080, 1,2,3-trimethyl-8-(phenylmethoxy)imidazo[1,2-a]pyridine (TMPIP) (Figure 4-1), where the cyanomethyl group is replaced by a methyl group has also been shown to be active (IC_{50} = 2.8 μM) [130]. TMPIP provides a convenient template for site-specific introduction of non-perturbing NMR-sensitive nuclei suitable for conformational studies of analogues of SCH28080 to complement the structural studies determined *in vitro* and *in vivo*.

Consider Figure 4-2. The structure of TMPIP is shown with the three torsion angles (ϕ_1, ϕ_2, ϕ_3) that are permitted conformational change. The fused imidazopyridine and phenylmethoxy rings substituent are rigid. Cross-polarization magic angle spinning (CP-MAS) NMR experiments have previously been performed on TMPIP in its binding site. The conformation of TMPIP was partially determined by calculating torsional angle ϕ_1 (=165˚ ± 15˚) indirectly from the a measurement of the internuclear distance between ^{13}C labels placed in the *N*-CH_3 and *O*-CH_2 groups of the inhibitor. Determination of ϕ_1 did not permit the complete structure of the bound inhibitor to be determined unambiguously, however. In this study, REDOR NMR has been used to impose further limits on the structure of this class of reversible inhibitors at their site of action and to provide the first structure of a reversible inhibitor at its binding site in the gastric H/K-ATPase.

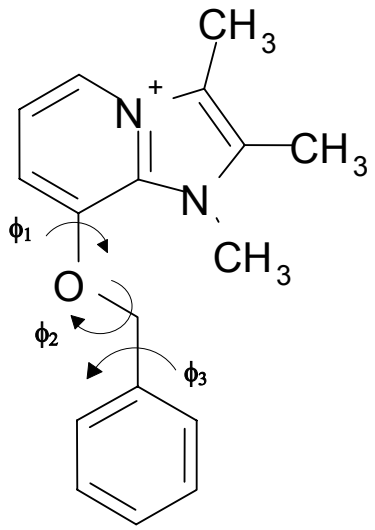

Figure 4-2 Chemical structure and definition of torsion angles (ϕ_1, ϕ_2, ϕ_3) of the 1,2,3-trimethyl-8-(phenylmethoxy)imidazo[1,2-*a*]pyridinium cation (TMPIP).

Rotational Echo Double Resonance (REDOR) NMR

Rotational Echo Double Resonance NMR is a powerful technique for measuring internuclear distances in the solid state [43, 44, 167]. The technique exploits the heteronuclear dipolar coupling between two different NMR-sensitive nuclei such as ^{19}F and ^{13}C. The dipolar coupling varies with internuclear distance and is thus useful for structure determination in solids.

Recalling Equation 3-12, the Hamiltonian describing the heteronuclear dipolar coupling may be stated as

$$H_D = \frac{\gamma_I \gamma_S}{r^3} \frac{\left(3\cos^2\theta - 1\right)}{2} \left(2\mathbf{I}_z\mathbf{S}_z\right) \qquad \textbf{Equation 4-1}$$

Where γ_I and γ_S are the gyromagnetic ratios of spins I and S, θ is the angle between the internuclear vector of length r and the applied magnetic field. The influence of the dipolar couplings is removed by magic-angle spinning (MAS) but it is possible to *recouple* these internal NMR interactions by applying suitable pulse sequences with timings synchronized to the sample rotation. The pulse sequence for the REDOR experiment is presented in Figure 4-3 as a four-rotor cycle dephasing period. A train of radio frequency pulses timed with the rotor cycles of the MAS rotor reintroduces dipolar coupling that is otherwise averaged by MAS sample rotation.

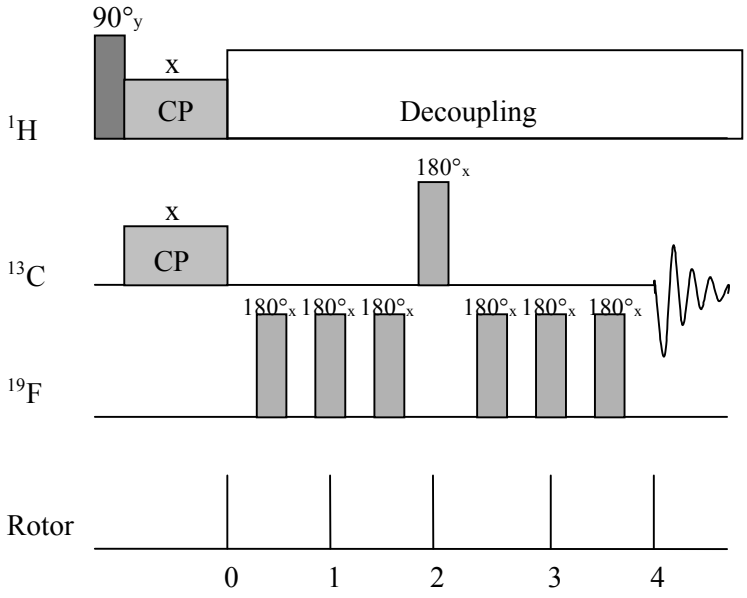

Figure 4-3 Pulse sequence for ^{19}F refocus, ^{13}C observe REDOR NMR. Transverse carbon magnetisation is produced by cross-polarisation (CP) transfer from dipolar-coupled protons. The 180° pulses at the ^{19}F frequency prevent rotational refocusing of the dipolar interaction. Incomplete refocusing of magnetisation results in a decrease in signal intensity, S, by an amount ΔS. The ^{13}C 180° pulse refocuses isotropic ^{13}C chemical shift differences at the beginning of data acquisition.

The first step of the REDOR sequence involves a cross-polarization (CP) step. Proton magnetization is used to enhance the polarisation of one of the heterospins (^{13}C). This spin is termed the "observed" spin. The protons are then dipolar decoupled with high-power (>80 kHz) throughout the remaining sequence. In the solid state, decoupling with rapid phase alteration leads to effective decoupling of the protons [168]. After the initial CP step, the resulting transverse magnetization evolves under the heteronuclear dipolar coupling. Due to MAS, the heteronuclear dipolar interaction is refocused after each completed rotor period. In this way, MAS achieves an averaging of the dipolar interaction. Application of π pulses to the "passive" spins (^{19}F) interferes with this averaging of the heteronuclear dipolar coupling. The observed spins accumulate phase which leads to a diminution of signal intensity in a distance-

dependent manner. The ^{13}C pulse in the middle of the evolution period refocuses isotropic chemical shifts.

To measure the extent of the dephasing, two experiments are performed with and without dephasing pulses. When π pulses are applied, a *dephased* signal (*S*) is detected which varies with dipolar coupling between the spins and the dephasing time (the number of rotor cycles before observation). Re-writing (in units of rad/sec) Equation 4-1, the heteronuclear dipolar interaction becomes [226; 167]

$$H_D = d(t)\mathbf{S}_Z\mathbf{I}_Z \qquad \textbf{Equation 4-2}$$

Due to MAS, the dipolar coupling constant is time-dependent.

$$d(t) = d\{\sin^2\beta\cos 2(\alpha+\omega_r) - \sqrt{2}\sin 2\beta\cos(\alpha+\omega_r t)\} \qquad \textbf{Equation 4-3}$$

The dipolar coupling is *d*, the sample spinning rate is ω_r, and α and β are the azimuthal and polar angles of the internuclear vector with respect to the spinning axis (Figure 4-4).

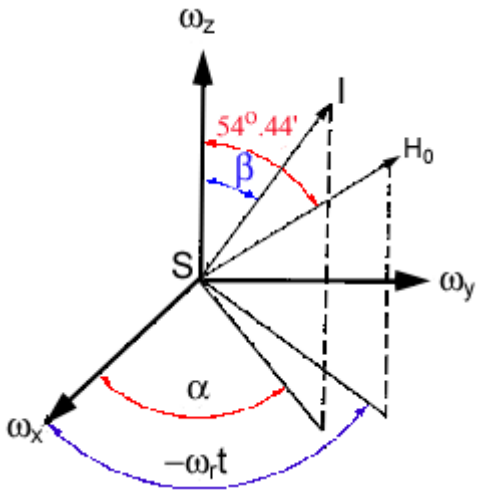

Figure 4-4 Definition of the angles in Equation 4-3 in the rotor frame rotating at the magic angle. I and S are the nuclei of interest. H_0 is the applied magnetic field [169].

The net dephasing angle, ϕ, for a single rotor period can be calculated by

$$\phi = \int_0^{T_{r/2}} \omega_d(t)dt - \int_{T_{r/2}}^{T_r} \omega_d(t)dt$$ **Equation 4-4**

where $\omega_d(t) = \pm d(t)/2$. Without ^{19}F dephasing pulses, the accumulated phase in the first half of the rotor period would be cancelled in the second half. With dephasing there is non-zero phase accumulation. Evaluation of Equation 4-4 for N_c rotor cycles gives a general term for the total phase accumulation

$$\phi = \frac{N_c T_r d}{\pi}\sqrt{2}\sin 2\beta \sin\alpha$$ **Equation 4-5**

A reference spectrum is obtained for each variation in rotor cycles. The ^{19}F π pulses are omitted and the dipolar interaction is completely refocused. The acquired *non-dephased* signal (S_0) is proportional to the integral detected spin signal. Both dephased and non-dephased regimes are subject to imperfections in the applied π-pulses and losses due to relaxation during the REDOR evolution periods. The ratio of $\Delta S/S_0$ eliminates these effects where

$$\frac{\Delta S}{S_0} = \frac{S_0 - S}{S_0}$$ **Equation 4-6**

The ratio $\Delta S/S_0$ = 1-cos(ϕ) for a single spin pair. For a powder sample, where all internuclear orientations must be included and all values of α and β summed over, the result is

$$\frac{\Delta S}{S_0} = \frac{1}{2\pi}\int_0^{\pi}\int_0^{\pi}\cos(\phi)\sin\beta\alpha d\beta$$ **Equation 4-7**

Where sin β is a geometric weighting factor. Universal curves may be generated for this ratio for the purpose of simulating to the REDOR data obtained in the NMR experiment (Figure 4-5).

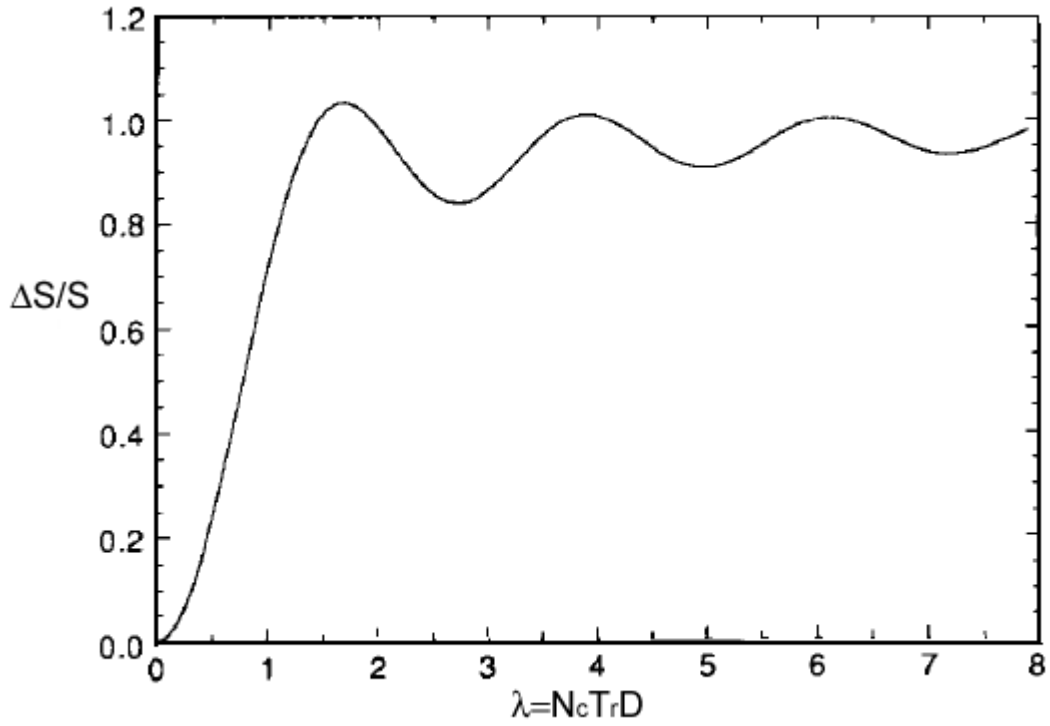

Figure 4-5 Variation of $\Delta S/S_0$ with the dimensionless parameter λ, a product of the number of rotor cycles (N_c), sample rotation period (T_r) and the dipolar coupling (D). Reproduced from [167].

Systematic variation of the number of rotor cycles and observing the signals both with and without the application of π pulsed dipolar dephasing in the REDOR experiment produces a time-domain REDOR dipolar dephasing signal from which internuclear couplings may be calculated directly. Since the dipolar coupling

Equation 4-8

$$d \propto \frac{\gamma_I \gamma_S}{2\pi r^3}$$

The interatomic distance between selectively labelled positions in a ligand may be measured and torsional angles for the molecule may be determined.

Aims of this study

From Equation 4-8 it can easily be seen that the dipolar coupling is dependent upon the internuclear distance and on the gyromagnetic ratios of the nuclei of the spin pair. The large gyromagnetic ratio of ^{19}F (25.18 x 10^7 $T^{-1}s^{-1}$) (c.f. $\gamma^{13}C$ = 6.73 x 10^7 $T^{-1}s^{-1}$) [170] allows the distances that can be measured using this nucleus to be greater than those for many homonuclear methods. In this study, a series of novel and biologically active analogues of TMPIP (TM2FPIP, TM4FPIP, TMPFPIP) (Figure 4-6) have been synthesised to contain ^{19}F in the phenylmethoxy ring.

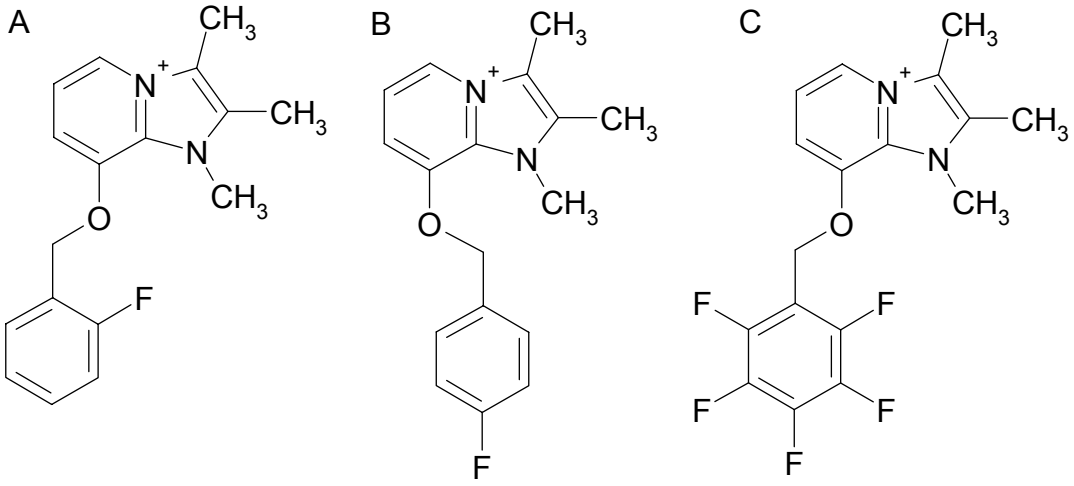

Figure 4-6 Schematic representation of fluorinated SIPs (A) TM2FPIP, (B) TM4FPIP and (C) TMPFPIP the structures of which were examined by REDOR NMR.

A constraint on torsion angle ϕ_1 (Figure 4-2) determined previously for TMPIP has been combined with new measurements probing the values of torsional angles ϕ_2 and ϕ_3 obtained by measuring the dipolar couplings between the *N*-$^{13}CH_3$ carbon and ^{19}F in the phenyl ring (Figure 4-7) using CP-MAS REDOR NMR. The structure of the bound inhibitor, and information on the binding site gained from site directed mutagenesis and photoaffinity labelling may then be used to describe models for SCH28080 and its analogues at the site of functional efficacy.

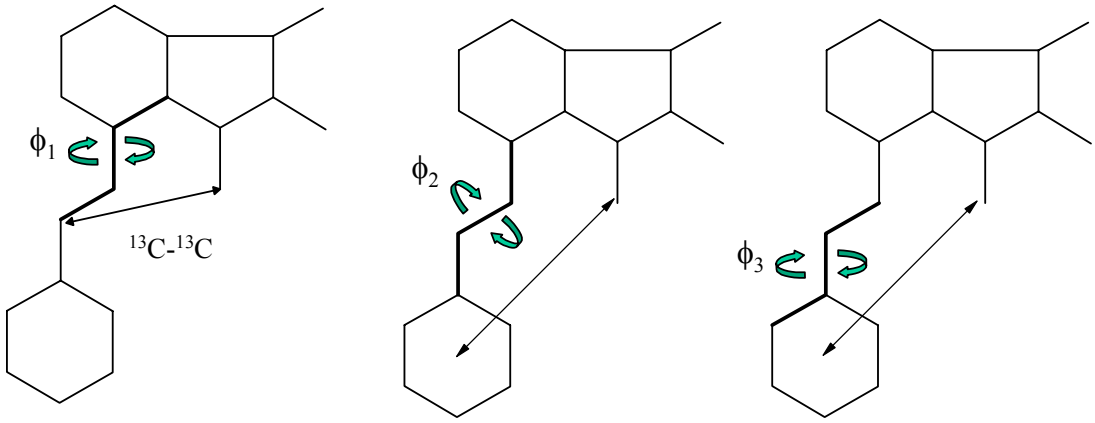

Figure 4-7 Representative structures of the 8-phenylmethoxyimidazo[1,2-*a*]pyridinium compound TMPIP showing the 3 torsional angles ϕ_1, ϕ_2 and ϕ_3, which define the complete three dimensional structure of the molecule. The structure on the left indicates a relationship between the separation of the *N*-CH_3 and CH_2 groups and the angle ϕ_1, which was measured by rotational resonance to be 165° ± 15° [130]. The arrows in the middle and right structures signify that angles ϕ_2 and ϕ_3 are related to distances between the *N*-CH_3 group and an undefined position within the aryl ring.

Materials and Methods

Synthesis of N-$^{13}CH_3$ *Labelled Substituted Imidazo[1,2-a]pyridines*

All compounds examined were derived from 2,3-dimethylimidazo[1,2-*a*]pyridine-8-ol which was synthesised by methods described in Chapter 2 and followed the synthetic route described by Kaminski [124]. The yields and NMR analysis are provided in Chapter 2. The ^{13}C-enriched quaternary ammonium compounds 1,2,3-trimethyl-8(*o*-fluorophenylmethoxy)imidazo[1,2-*a*]pyridinium iodide (TM2FPIP), 1,2,3-trimtheyl-8(*p*-fluorophenylmethoxy) imidazo[1,2-*a*]pyridinium iodide (TM4FPIP) and 1,2,3-trimethyl-8(pentafluorophenylmethoxy)imidazo[1,2-*a*]pyridinium iodide (TMPFPIP) (Figure 4-6) were prepared by reaction of the appropriate tertiary amine with 5 mole equivalents ^{13}C-methyl iodide (Aldrich Chemical Co., Gillingham, UK). The reaction was stirred under reflux until a precipitate had formed. The reaction was removed from the heat and allowed to cool with stirring. The mixture was filtered, washed with ether and recrystallised from methanol.

Sample Preparation for NMR

Lyophilised H/K-ATPase membranes (GI fraction) containing 30 mg protein were prepared as a pellet by centrifugation from a suspension in 20 mM phosphate buffer (10 mM $MgCl_2$, pH 7.4) at 100,000 g (30 min, 4 ˚C) and incubated with 0-300 μM of labelled inhibitor in 50 μL incubation medium (60 min, 37 ˚C). The maximum binding level for the SIP SCH28080 in sealed vesicles is 0.84 nmol/mg protein [154]. In leaky (lyophilised) membranes, the value is much higher [229]. The number of

phosphorylation sites per mg protein is 1.6 nmole [230] and it has been estimated that there are 2.2 binding sites per phosphorylation site [154]. Thus it was assumed that 1 mg of total protein contained 2.5-3.0 nmoles inhibitor binding sites in the lyophilised membranes used in these experiments. The pellet was transferred to a 6 mm external diameter zirconia MAS rotor fitted with Kel-F inserts to confine the sample to the centre of the rotor.

REDOR NMR Experiments

All solid state NMR experiments were performed on a Varian Infinity spectrometer operating at a magnetic field of 11.7 T at temperatures between 5 and -50 ˚C. CP-MAS experiments were performed by rotating the sample at a MAS frequency (υ_r) of 3-6 kHz. Hartmann-Hahn cross-polarization from ^{1}H to ^{13}C was achieved over a 1.6 ms contact time at a field of 65 kHz. REDOR experiments (^{13}C observe, ^{19}F-dephase) were conducted at a sample spinning frequency υ_r of 4500 Hz using a standard pulse sequence with rotor synchronized π pulses applied at the frequency of ^{13}C and^{19}F [171]. The π pulse length for both ^{19}F and ^{13}C was 9 μs. Numerical simulations of multiple-spin REDOR curves were carried out by adaptation of the general algorithms of Goetz and Schaefer [172] in a C++ routine written by Dr D A Middleton.

Results and Discussion

Structural Analysis of Solid Fluorinated SIPs by REDOR NMR

To validate the methodology for gastric membranes, the dipolar coupling between ^{13}C and ^{19}F in solid ^{13}C-TM2FPIP and ^{13}C-TM4FPIP was examined using heteronuclear dipolar-dephasing REDOR NMR. The dephasing curve, simulated to fit the REDOR $\Delta S/S_0$ data, for solid ^{13}C-TM2FPIP is shown in Figure 4-8.

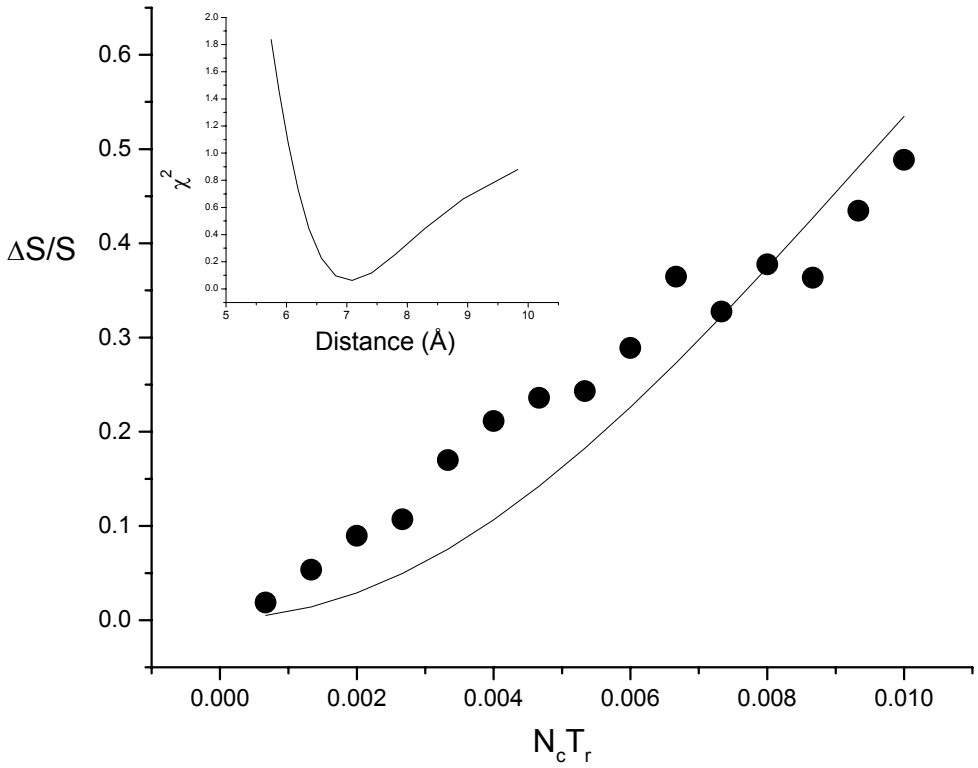

Figure 4-8 REDOR data (filled circles) and simulated dephasing curve for crystalline ^{13}C-TM2FPIP. Data are for 2-30 rotor cycles with 3 kHz (+/- 1 Hz) spinning speed. The calculated curve corresponds to r_{CF} = 7.1 Å with χ^2 = 0.0618. The variation of χ^2 with distance is shown in the inset.

The data indicate that the ^{13}C- and ^{19}F-labelled positions in this solid have an interatomic distance (r_{IS}) that permits dipolar coupling to be measured using REDOR

NMR (r_{IS} < 8 Å). A ^{13}C-^{19}F distance of 7.1 Å (χ^2 = 0.0618) is indicated by the best fit dephasing curve. This distance approaches the most extreme ^{13}C-^{19}F separation that may be adopted by the compound (Figure 4-9).

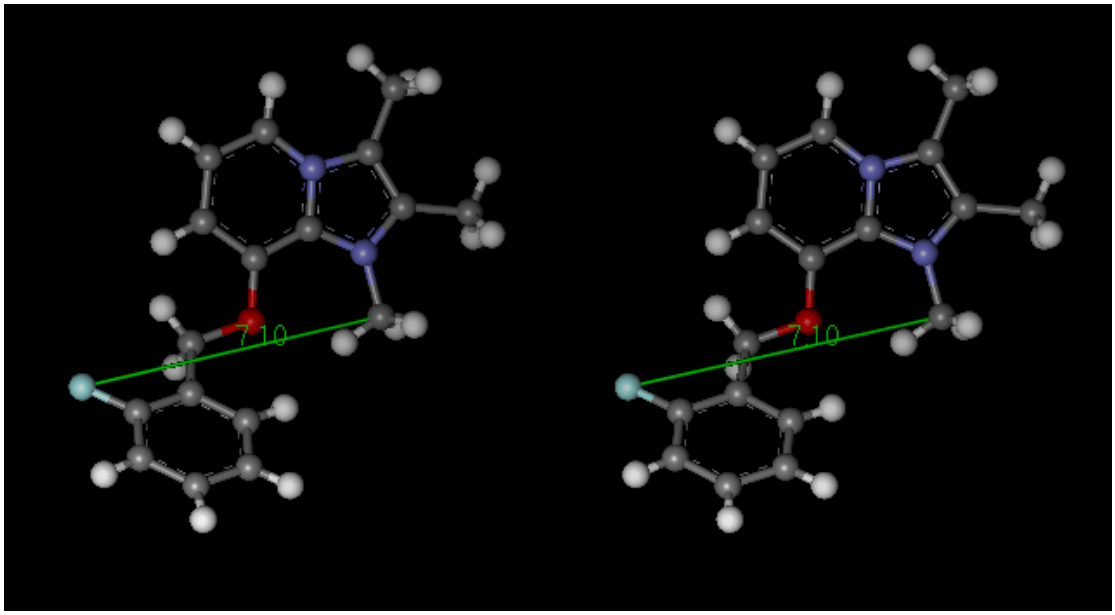

Figure 4-9 Stereoimage representation of the REDOR NMR-derived structural constraints imposed on crystalline TM2FPIP. The ^{13}C-^{19}F distance of 7.1 Å is indicated in green. The fluorine substitution on the phenyl ring is modelled to point away from the rest of the molecule. Parallelogram images were generated by Merge2.

The fluorine group points away from the body of molecule. Greater dephasing, suggesting a shorter apparent intramolecular ^{13}C-^{19}F distance, would arise from either smaller intermolecular or closer intramolecular ^{13}C-^{19}F separations, or a combination of the two interactions. Since the REDOR experiment was conducted on a crystalline solid sample not diluted by natural-abundance N-$^{12}CH_3$ and thus permitting intermolecular dephasing, this distance may represent the lattice conformation of the inhibitor. There are currently no diffraction structures for this compound to compare with the REDOR NMR measurements presented here.

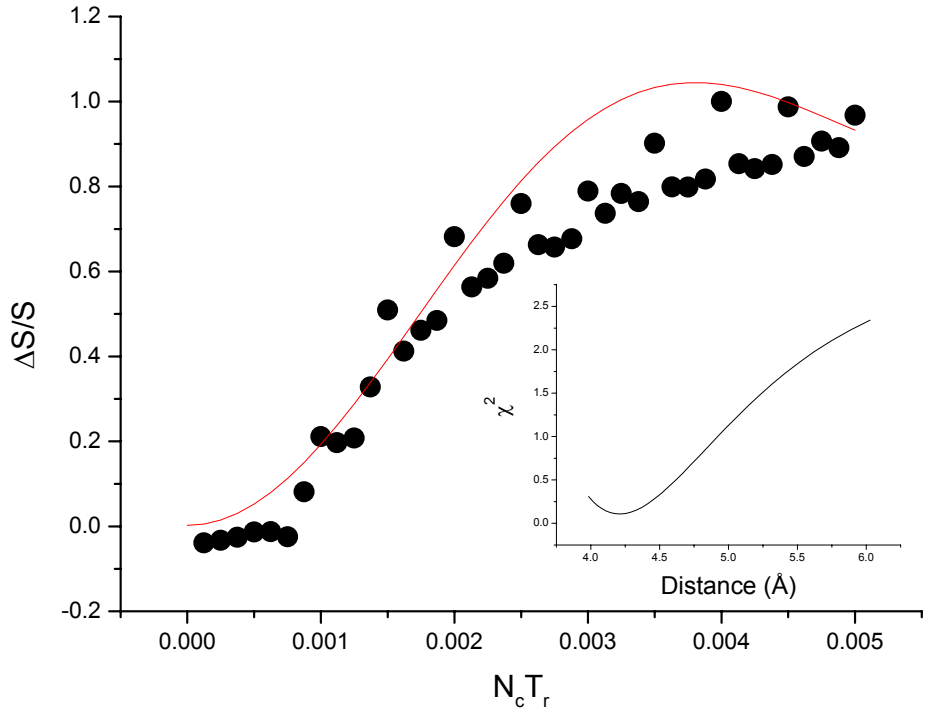

Figure 4-10 REDOR data (filled circles) and simulated dephasing curve for crystalline ^{13}C-TM4FPIP. Data are for 2-30 rotor cycles with 3 kHz (+/- 1 Hz) spinning speed. The calculated curve corresponds to r_{CF} = 4.2 Å with χ^2 = 0.107. The variation of χ^2 with distance is shown in the inset.

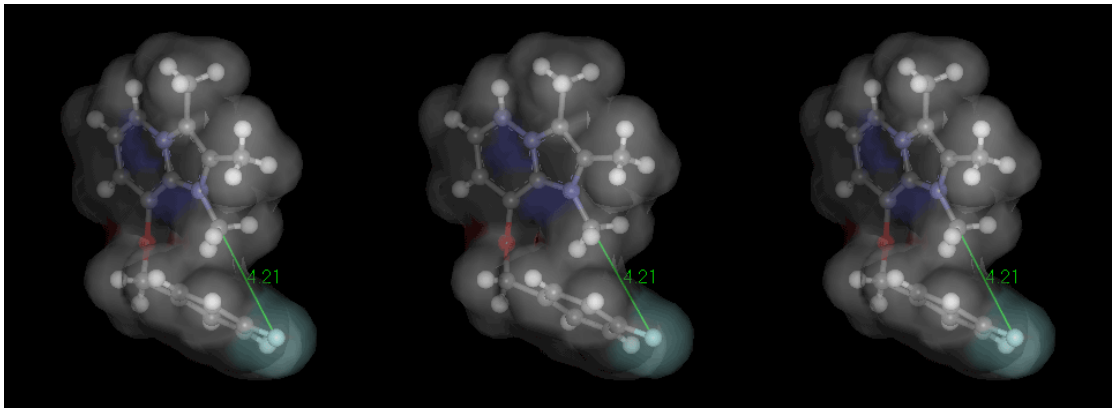

Figure 4-11 Stereoimage representations of the REDOR NMR-derived structural constraints imposed on crystalline TM4FPIP. The ^{13}C-^{19}F distance of 4.2 Å is indicated in green. The atomic van der Waals radii for the molecule are shown in transparent superposition on the ball-and-stick molecules. The inhibitor is required to adopt a sterically strained conformation that violates the van der Waals radii of proximal groups. To see the 4-fluorophenyl ring at the front, merge the middle and right images. To see 4-fluorophenyl ring from the rear, merge the middle and left. Parallelogram images were generated by Merge2.

The dephasing curve, simulated to fit the REDOR NMR data $\Delta S/S_0$ data, for solid ^{13}C-TM4FPIP is shown in Figure 4-10. The data indicate a ^{13}C-^{19}F interatomic distance of 4.2 Å (χ^2 = 0.107). Imposing this distance constraint on the structural model of the inhibitor generates a highly strained conformer whose residues violate van der Waal radii of neighbouring groups (Figure 4-11). This suggests that intermolecular, rather than intramolecular dephasing, leading to a shorter interatomic distance, is occurring in the ^{13}C-TM4PIP solid sample.

Structural Analysis of the H/K-ATPase-Inhibitor Complex by REDOR NMR

The structure of 8-(fluorophenylmethoxy)imidazo[1,2-*a*]pyridines in the H/K-ATPase has been probed by REDOR experiments that measure couplings between ^{19}F in the benzyl ring and ^{13}C (the observed nucleus) placed in the *N*-CH_3 group of the quaternary ammonium cation (Figure 4-12). In the cases of TM2FPIP and TM4PIP (Figure 4-6) the measured S/S_0 values can be converted directly into single ^{13}C-^{19}F internuclear distances [171], which are, in turn, functions of the relative orientations of the phenylmethoxy group and the imidazopyridine ring. However, numerical simulations of REDOR dephasing curves showed that measurement of a single distance between ^{13}C and ^{19}F at either the 2- or 4-position of the ring cannot provide sufficient information for determining the structure unambiguously. The structure could not be resolved from either of these distance measurements even after incorporating the pre-determined torsional angle ϕ_1 of 165˚ ±15˚ [130] as a constraint. To avoid such ambiguities in the structure analysis, the pentafluorophenylmethoxy compound was chosen for examination. The presence of five fluorine atoms in the aryl group potentially confers greater sensitivity of the REDOR experiment to molecular conformation. Moreover, the rotational symmetry of the aryl ring eliminates ambiguities associated with the possibility of the fluorine substituent lying *syn* or *anti* to the fused ring system as might arise with TM2FPIP. Nonetheless, once a model of the SIP has been determined using TMPFPIP, the monofluorinated compounds would be valuable in confirming the model as a future study.

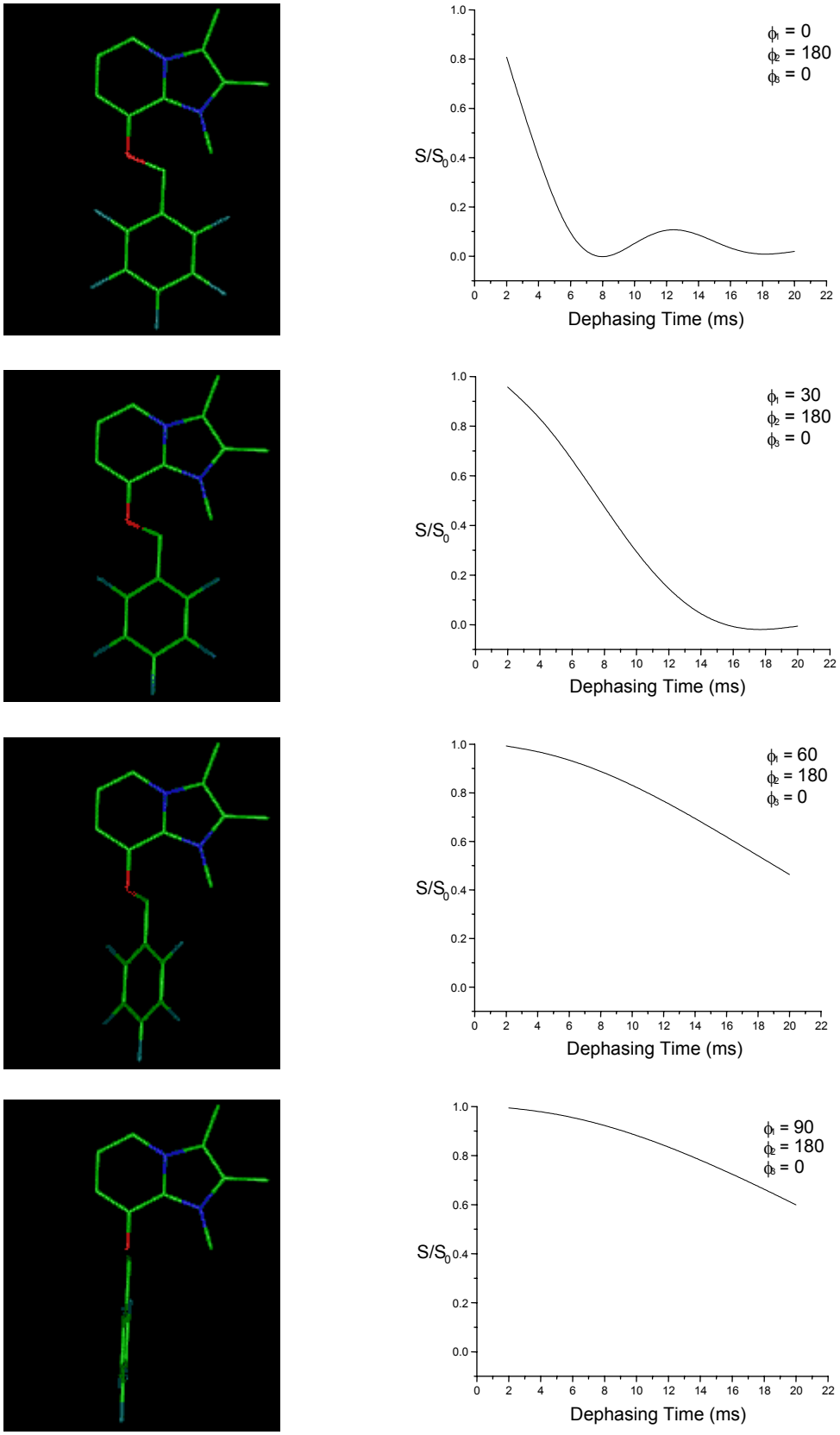

Figure 4-12 Illustrations of the relationship between simulated REDOR dephasing curves and the conformation of TMPFPIP. As torsional angle ϕ_1 (see Figure 4-7 for definition) is varied, S/S_0 versus dephasing time is calculated in a molecular reference frame defined with the z-axis along the *N*-$^{13}CH_3$ bond [174]. Simulations by Dr D. Middleton.

The combined effect of an ensemble of ^{19}F spins on the ^{13}C signal can be determined for any conformation of TMPFPIP by calculating the normalized co-ordinates of the individual spins in a molecular reference frame (Figure 4-12) [173, 174]. In practice, values of S/S_0 for any REDOR echo time are computed for many TMPFPIP conformations covering the entire conformational search space, to identify the structure or structures giving the closest fit to the results.

The analysis of the REDOR dephasing of ^{13}C by the five fluorine nuclei in the ring of ^{13}C-TMPFPIP is more complex than is the case for a simple spin pair (as with the monofluorinated species). There may be interference of homonuclear coupling between neighbouring ^{19}F nuclei in the ring, which attenuates the observed heteronuclear couplings between ^{19}F and ^{13}C [174]. In simple cases (e.g., homonuclear coupling of two ^{19}F nuclei), it is possible to calculate the extent of attenuation and to include compensatory factors in the numerical simulations of REDOR dephasing [175]. The structural analysis is more complex for ^{13}C-TMPFPIP because it is difficult to calculate the effect of the network of homonuclear coupling between the five phenyl ^{19}F nuclei on the REDOR experiment. The simulations of standard REDOR dephasing curves calculated for any given conformation of the ligand (e.g., the black lines in Figure 4-13) have neglected the effect of ^{19}F-^{19}F coupling, and therefore represent the *maximum* possible dephasing of ^{13}C as a result of heteronuclear coupling to ^{19}F. The *actual* dephasing for a given conformation (in the presence of ^{19}F-^{19}F coupling) cannot be determined accurately, but may fall anywhere between the maximum dephasing and zero dephasing depending on the interference of ^{19}F-^{19}F coupling. This point is illustrated for the calculated dephasing curves in Figure 4-13, in which the shaded areas of the graphs above the solid lines

represent regions of uncertainty in which the dephasing curves may lie when the ^{19}F-^{19}F coupling is non-zero.

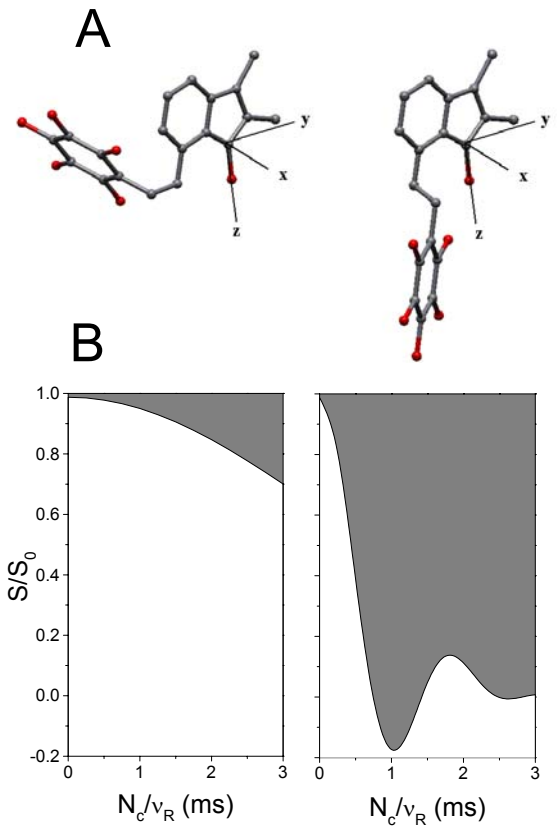

Figure 4-13 Illustration of the relation between two molecular conformations of ^{13}C-TMPFPIP (A) and the predicted response in a ^{13}C observe, ^{19}F diphase REDOR experiment. The dark lines in the graphs, forming the boundaries between the white and grey areas, show S/S_0 *versus* dephasing time for each of the two molecular conformations, calculated in a molecular reference frame defined by x, y and z using the algorithms of Goetz and Schaefer (33). The grey area of the graphs signifies uncertainties in each dephasing curve as a result of unquantifiable ^{19}F-^{19}F dipolar couplings.

The cross polarization MAS spectrum of ^{13}C-TMPFPIP bound in the gastric membrane preparation, the natural abundance spectrum of the gastric lipid preparation and the difference spectrum indicating the location of the inhibitor *N*-$^{13}CH_3$ signal are shown in Figure 4-14. The resonance from the site-specifically ^{13}C-enriched inhibitor is seen at 32 ppm and lies under the spectral region dominated by the resonances from the membrane lipids. Since the intensity of this resonance line will be diminished during the REDOR dephasing experiment it is critical that there is adequate signal

from the inhibitor in the difference spectrum for dephasing to be measured accurately. The difference spectrum indicates an intense signal presence from the inhibitor.

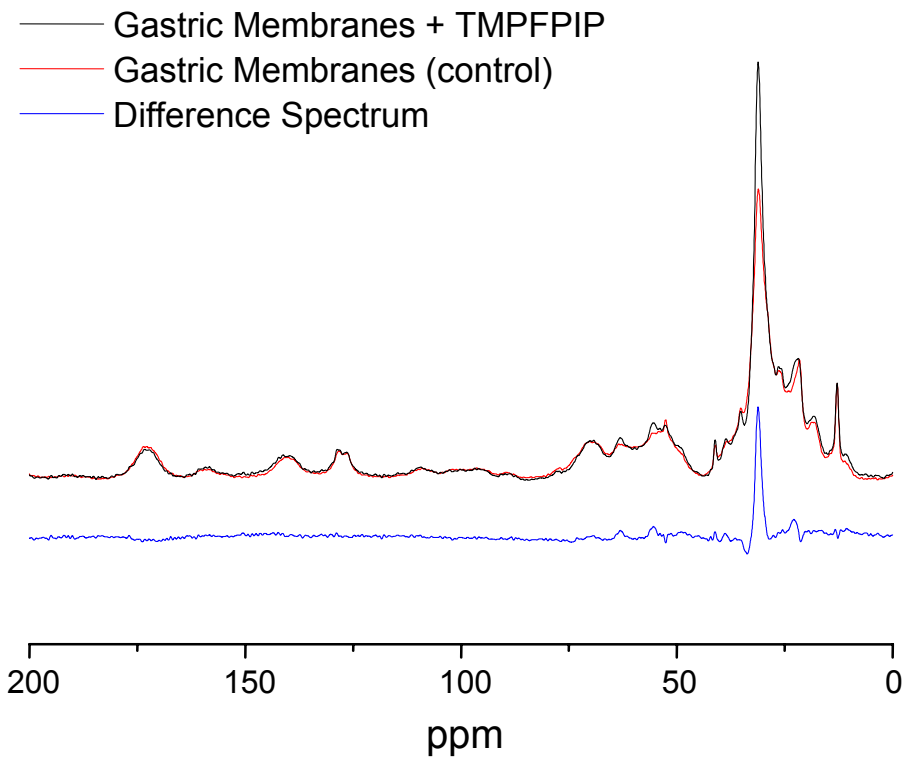

Figure 4-14 CP MAS ^{13}C NMR spectra of gastric membrane (30 mg protein) preparations with ^{13}C-TMPFPIP (3.5 nmol/mg protein) (black) and, as a control, without inhibitor (red). The difference spectrum is shown in blue and indicates a single resonance at 32 ppm due to the *N*-$^{13}CH_3$ of the inhibitor. Spectra acquired at 11.7 T (248 K, spinning frequency ω_r=4000 Hz ± 2 Hz).

The ^{13}C REDOR full-echo spectrum of ^{13}C-TMPFPIP bound to H/K-ATPase in a gastric membrane preparation is shown in Figure 4-14. A REDOR difference spectrum, obtained by subtraction of the dephased-echo spectrum from the full-echo spectrum (Figure 4-15) shows clearly the ^{19}F dephasing of the ^{13}C resonance line from [^{13}C]TMPFPIP at 32 ppm. Since the resonance line from the inhibitor lies under the intense peaks from the membrane lipids, to calculate S/S_0 it was necessary to first remove the interfering natural abundance background signal. Occlusion of the inhibitor resonance was achieved by subtraction of the corresponding full-echo and

dephased-echo spectra obtained before addition of inhibitor to the membranes. Using this approach, S/S_0 values were determined for three echo times, 1.0, 1.5 and 2.0 ms Table 4-1 and Figure 4-15.

Table 4-1 Variation of S/S_0 dephasing with dephasing time $N_c\upsilon_R$

N_c/υ_R (ms)	1.0	1.5	2.0
S/S_0	0.98	0.82	0.48

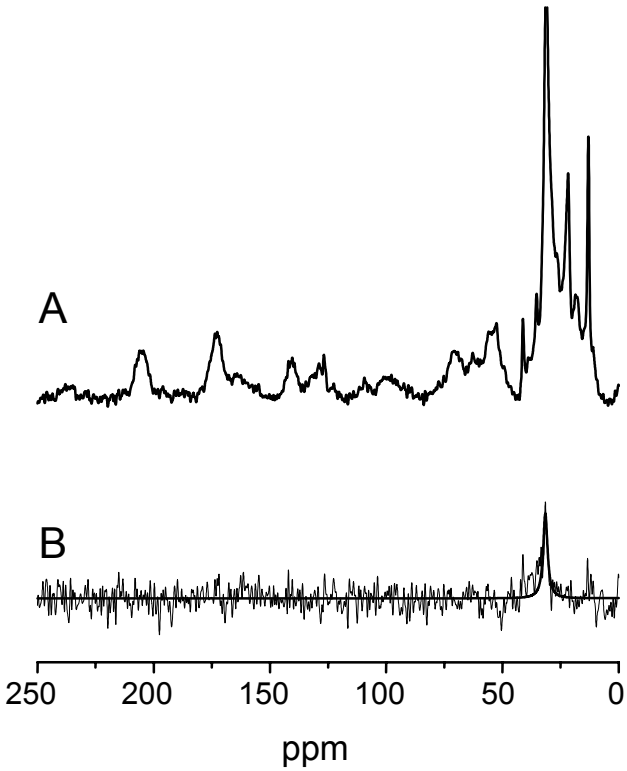

Figure 4-15 The proton decoupled ^{13}C CP-MAS NMR spectra (at 125 MHz) of GI membranes containing [^{13}C]TMPFPIP (A), and a ^{13}C observe, ^{19}F dephase REDOR difference spectrum of the same sample showing the resonance line from the *N*-$^{13}CH_3$ label of the bound inhibitor (B). Spectra were recorded at 248 K and the difference spectrum is the result of accumulation of 80,000 scans.

The molecular structure of ^{13}C-TMPFPIP in the binding site of H/K-ATPase was assessed by comparison of the observed REDOR dephasing with numerical simulations as described above. Values of S/S_0 at the three echo times were calculated for different combinations of the angles ϕ_1, ϕ_2 and ϕ_3 (Figure 4-7) defining

the conformational space of TMPFPIP. Calculations were based on 5° increments of ϕ_1 from 150° to 180° (the angular constraint determined independently from experiments on TMPIP [130]), 30° increments of ϕ_2 through 360° and 30° increments of ϕ_3 from 0° to 180° (full rotation was not necessary because of ring symmetry). The experimental REDOR data was accepted as being consistent with specific molecular conformations in the search space when the calculated S/S_0 values were greater than or equal to the corresponding experimental values. In this way, the analysis took into consideration the uncertainty in the interference from ^{19}F-^{19}F coupling, as described above.

The outcome of the analysis is represented in the three-dimensional graph in Figure 4-16. Each point on the graph represents a combination of the three torsional angles (i.e. molecular conformation) in the search space for which the predicted REDOR dephasing is favourably comparable with the observed response.

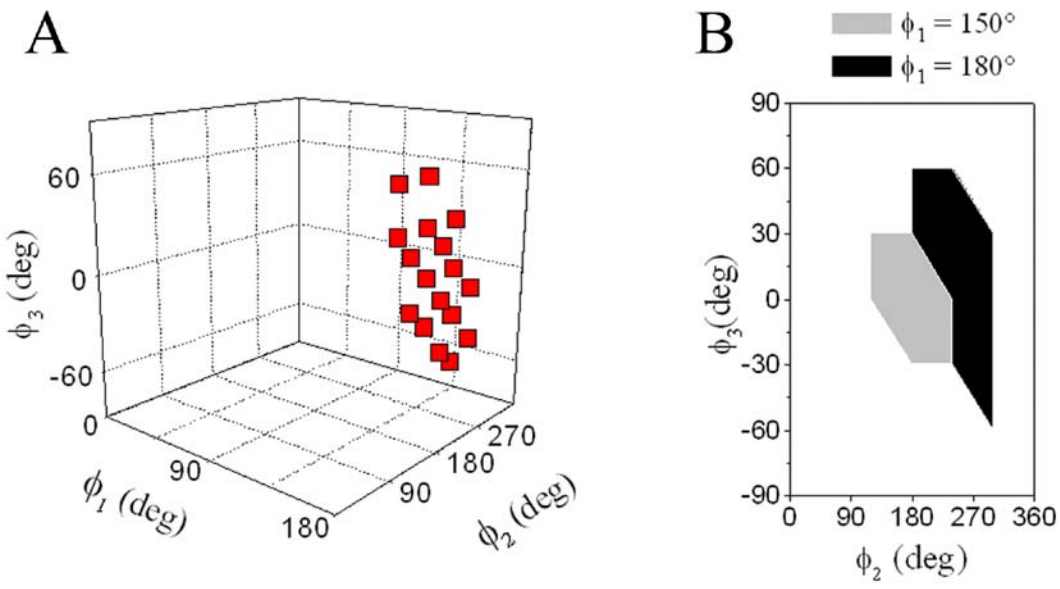

Figure 4-16 (A) Three-dimensional graph indicating combinations of the three torsional angles, ϕ_1, ϕ_2, and ϕ_3 (from a search space of 432 conformations), that are consistent with the experimental data. The permitted conformations are shown in Figure 4-17. (B) A two-dimensional representation of the torsional angle combinations shows the possible range of angles ϕ_2, and ϕ_3 when angle ϕ_1 is at the upper (180°) and lower (150°) limits of its range of excursion (*black* and *grey* regions, respectively).

The clustering of the points on the graph illustrates the small variance in the number of possible inhibitor conformations consistent with the experimental data. The limits on angle ϕ_1 (165° ± 15°) determined previously by rotational resonance NMR [130] were not reduced by the information provided here.

From the analysis of the REDOR experiment, limits could be placed on the angles ϕ_2 (180° ± 30°) and ϕ_3 (0° ± 60°) for the first time. Two molecular conformations of TMPFPIP are shown in Figure 4-17, which represent the two extreme structures in the conformational cluster represented in the graph (Figure 4-16).

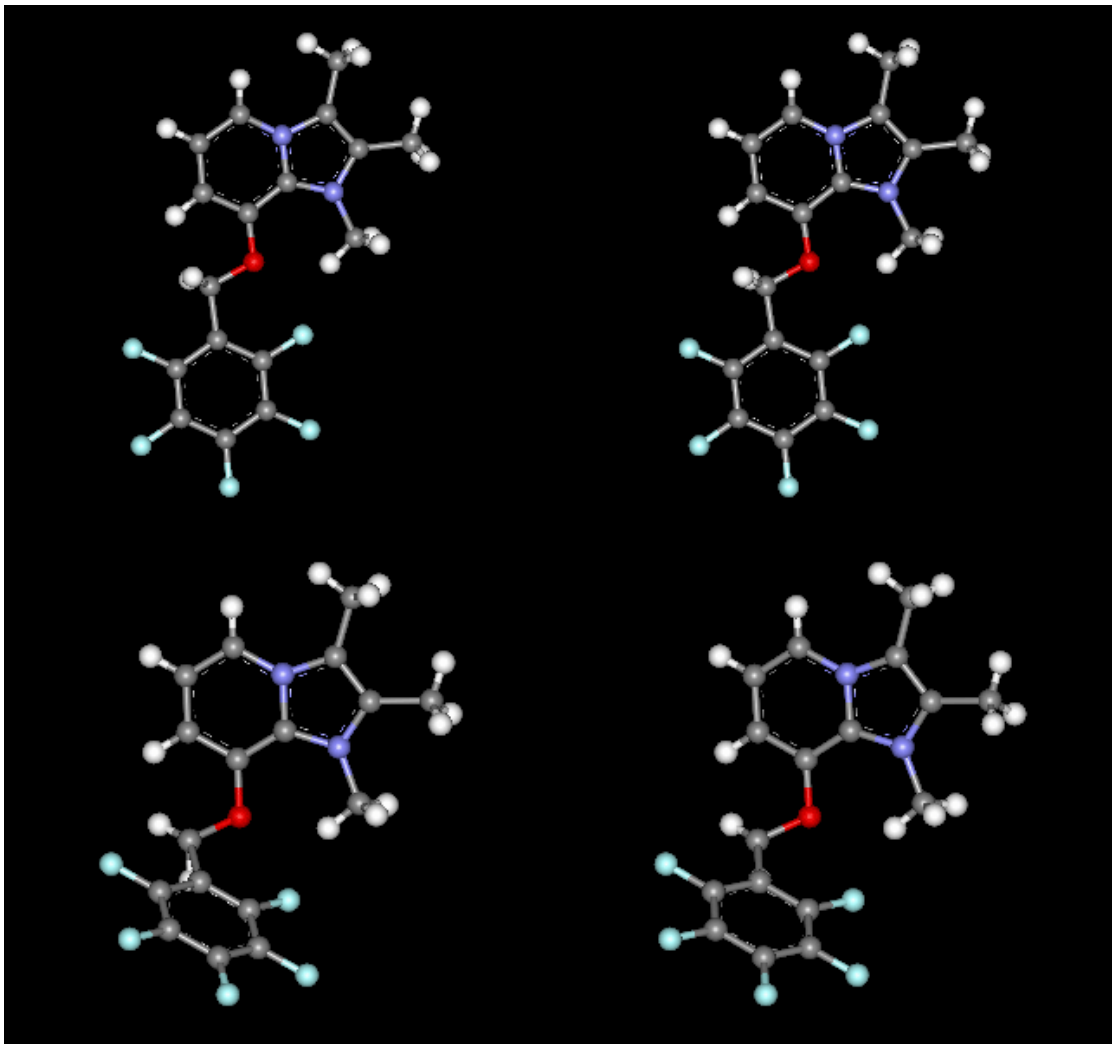

Figure 4-17 Stereoimage representations of the conformational extremes determined for TMPFPIP at its binding site in the gastric H/K-ATPase. The top figure shows the fully planar conformation and the bottom figure shows the slightly bowed shape. The torsional angle ϕ_1 (165° ± 15°) had been determined previously by rotational resonance NMR [130]. The REDOR NMR allowed limits to be placed on angles ϕ_2 (180° ± 30°) and ϕ3 (0° ± 60°). Parallelogram images were generated by Merge2.

One structure is fully planar, the other shows a slight curvature of the benzyl group relative to the fused ring. Although it is not possible to distinguish between the two conformations at this stage, all structures in the cluster share a common feature in that the benzyl ring lies extended away from the fuse ring system.

Conclusions

The cross-polarization magic-angle spinning NMR method REDOR has been used to determine ^{13}C-^{19}F distances in fluorinated analogues of SCH28080, the K^+ competitive reversible inhibitor of the gastric H/K-ATPase. The ^{13}C resonance from the inhibitor *N*-$^{13}CH_3$ group in the gastric membranes preparation, although dominated by the resonances of the membrane lipids, was sufficiently intense in the difference spectrum to provide successful dephasing measurements in a REDOR NMR experiment. A model of the active conformation of the pentafluorophenylmethoxy analogue of TMPIP has been generated from ^{13}C-^{19}F dipolar coupling measurements using REDOR NMR and represents the first structure of a reversible inhibitor in the binding site of the gastric H/K-ATPase. The conformational limits that are now imposed on the ligand give a valuable insight into the structural requirements for activity of this class of inhibitors and can provide the basis for modelling their interaction at the active site. Structural information on the H/K-ATPase is scarce but it is now possible to suggest a mechanism for inhibitor binding by comparing firm structural data for the inhibitor TMPFPIP with the dimensions of P2-type ATPases [74]. The perfluorophenylmethoxy analogue of SCH28080 may adopt only a limited range of conformations between the bowed and planar state. The C8-substituted ring system lies away from the fused ring system. These results are consistent with the ^2H-NMR data which indicated that the phenyl group is tightly bound by the binding site and thus limited in its range of molecular motions. The REDOR NMR data now reveal the structure to which this motional constraint is applied. It is possible to relate the steric requirement imposed on the C8 group for functional efficacy to the strict conformational constraints that the inhibitor

is exposed to in the binding site. A small, flexible group such as the butyl group of TMTFBIP, a SIP with no potency (Chapters 2 & 3), would permit too much mobility for the SIP at the binding site, effectively allowing the molecule to rattle in the binding pocket once the imidazo cation has localised the molecule to the binding site in the protein. Such a compound would not be able to wedge and blockade an interhelical space, for example, or to curve around several helices and efficiently prevent either protein conformation change or ion movement. A larger group such as a phenylmethoxy or cyclohexyl substituent is subject to a greater degree of steric constraint both intramolecularly and from the protein host. In the absence of high-resolution structural information for the H/K-ATPase it is not yet possible to assign an exclusive role to either the imidazo fused ring system or functional groups at C8 but this structural information, together with the structure-activity data described in Chapter 2 and the ligand dynamic studies of Chapter 3, forms the foundation for the model of the inhibitor in the putative H/K-ATPase binding site proposed in Chapter 5.

Chapter 5

A MODEL OF TMPFPIP AT ITS BINDING SITE IN THE GASTRIC H/K-ATPASE

Introduction

In drug design and development, it is desirable to understand both the contributions that the compound makes to its activity and the contributions that the target makes as a host. An iterative process of molecular refinement may be embarked upon whereby information about the ligand binding site directs the construction of the next generation of analogue. The new compound is examined for changes in potency and the target is consulted, through approaches such as site-directed mutagenesis, as to its association with the novel molecule. The drug may act as a probe of its target, especially when the binding site is poorly understood. With a reliable expression system, it is a comparatively more straightforward task to modify a membrane protein target through mutagenesis than it is to obtain high-resolution structural information for the protein. Furthermore, if the structure is known, this information may be used to reconcile site-directed mutagenesis studies and to impose structural constraints on a putative binding site for the ligand.

High resolution structural information is currently available for only a small proportion of membrane integral proteins (see Chapter 1). The structure of the

gastric H/K-ATPase has been refined by a combination of tryptic cleavage, peptide sequencing and *in vitro* translation [176]. Residues that are important for cation translocation have been identified by site-directed mutagenesis [107, 109, 111, 177-179]. The same technique, along with tryptinization and sequencing, has identified residues that are sensitive to covalent cationic thiophilic reagents (substituted benzamidazoles) [76, 98] and K^+-competitive reversible inhibitors (substituted imidazo[1,2-*a*]pyridines) [106, 109, 111, 177, 179-182]. The only framework of the H/K-ATPase that has been available upon which to hang these diverse strands of information is the low resolution electron diffraction structure of the protein at 8 Å [84]. Until recently, the two-dimensional crystal structures of the *Neurospora crassa* proton pump [183] and the sarcoplasmic reticular Ca-ATPase [184], both available to 8 Å, had been used [92] as templates for the positions of the putative H/K-ATPase transmembrane helices [77]. The boundaries of the transmembrane domain of the sarcoplasmic reticular Ca-ATPase is now known to 2.6 Å [74] and provides a convenient framework on which to reassess the membrane-integral region of the H/K-ATPase. From this construction it is possible to estimate the location of residues that are important for cation binding and that are sensitive to reversible inhibitors of the H/K-ATPase and to suggest a mechanism by which this class of inhibitors may bind the protein.

Aims of this study

The work in this chapter adopts a change in content and form from the preceding chapters. The aim of this study is to generate a working model that co-ordinates the chemical modification and site-directed mutagenesis data for the binding sites of inhibitors of the H/K-ATPase and NMR data of Chapters 3 and 4. The study proceeds with a review of the residues that have been determined to be involved in the binding site for SCH28080. The value of the high resolution structural data of the sarcoplasmic reticular Ca-ATPase [74] as a model is considered and the transmembrane regions are used to describe a putative arrangement for residues of the H/K-ATPase. The suggested locations of the sites of interactions between the protein and its SIP ligands are discussed and, ultimately, the structural NMR data obtained in Chapters 3 and 4 for the K^+-competitive reversible inhibitor TMPFPIP and functional data from Chapter 2 are applied to the topological arrangement of the H/K-ATPase to generate a model of this important class of H/K-ATPase inhibitors at their site of action.

Methods

Binary sequence analysis was performed using SIM [185] from sequences deposited with SWISS-PROT. The conformation restraints of TMPFPIP and, by analogy, its analogues were determined by ^2H and REDOR solid state NMR (Chapters 3 & 4). Site-directed mutagenesis studies and chemical modification of the protein are reviewed from the literature. Computational results were

obtained using software programs from Biosym/MSI (San Diego). Residue substitutions in the Ca-ATPase structure were performed with the *Biopolymer*® program. Graphical displays and van der Waals radii were produced from the *Insight*®*II* and WebLab Viewer Pro® molecular modelling systems from MSI.

The Binding Site of SCH28080

Residues that define the binding site of SCH28080

The region of the gastric H/K-ATPase responsible for binding the substituted imidazo[1,2-*a*]pyridine (SIP) SCH28080 is being defined by a number of distinct approaches. Figure 5-1 shows a suggested distribution of the transmembrane residues of the H/K-ATPase based on tryptic cleavage experiments (after [77]) and provides a useful reference for the sequence positions of the residues discussed in this section.

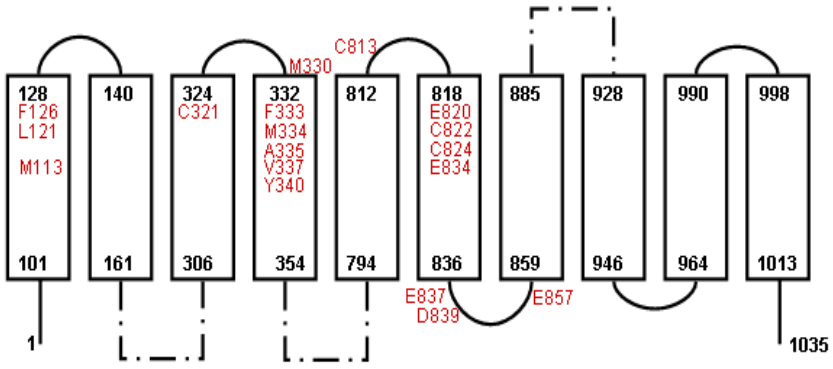

Figure 5-1 Schematic representation of the membrane-spanning regions of the gastric H/K-ATPase (based on [77]). Residues discussed in this chapter are indicated in red. Extended extramembrane domains shown by broken lines.

Chemical modification by a photoaffinity probe of a radioactive derivative of SCH28080 gave physical definition to the location of SIP binding [106]. From photoaffinity labelling experiments on [^{3}H]mDAZIP (Figure 5-2A), Munson and co-workers suggested that the phenylmethoxy ring of SCH28080 analogues participates in a π-π interaction with F126 in the putative first transmembrane region of the H/K-ATPase (M1) [106]. This type of interaction is broadly supported by functional studies showing comparable activities of TMPIP (Figure 5-2B) and its fluorophenylmethoxy analogues (see Chapter 2, Table 2-3 and Figure 5-2C). It is unlikely that the π-π interaction is the driving force for ligand stabilisation in the binding site. Studies of TMCHIP (Figure 5-2D) (See Chapter 2), a cyclohexyl analogue of TMPIP, showed the compound to be as active as its unsaturated analogues. This molecule does not have a conjugated π electron system in the C8 substitution and thus could not engage in a π-π stacking arrangement with close aromatic side-chains in the protein. A binding role for F196 or other proximal aryl groups is not to be discounted by the loss of a π-π binding partner in TMCHIP since the ring-saturated substituted imidazo[1,2-*a*] pyridine engage in CH-π interaction with neighbouring aromatic residues in the protein [158]. The nitrene-amino acid linkage was acid unstable in the [^{3}H]mDAZIP experiment and the precise residue labelled by the reagent could not be identified [92].

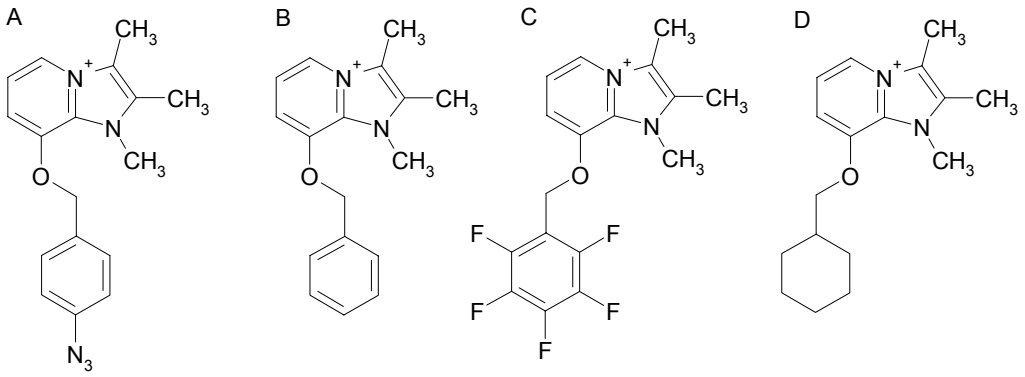

Figure 5-2 Chemical structures of substituted[1,2-*a*]pyridinium analogues of the K^+-competitive reversible inhibitor SC28080. (A) mDAZIP, (B) TMPIP, (C) TMPFPIP and (D) TMCHIP.

Other chemical modification experiments identified the transmembrane region of M6-M7 as important for cation binding by studies using the hydrophobic carboxylic activating reagent dicyclohexylcarbodiimide (DCCD) [177]. Sequence analysis of the ^{14}C-labelled peptides obtained from proteolytic digests suggested that at least one carboxyl residue (E857) at the M7 boundary was essential for cation binding-dependent activities [177].

Amino acid substitutions by site-directed mutagenesis have identified a number of residues in the membrane-spanning region of the gastric H/K-ATPase (Figure 5-1). The variation in apparent inhibitor constant, K_i, with each change has been found to have different degrees of influence. Some substitutions have a large effect, others a moderate, slight or no effect on sensitivity to SCH28080 [92] (Figure 5-3).

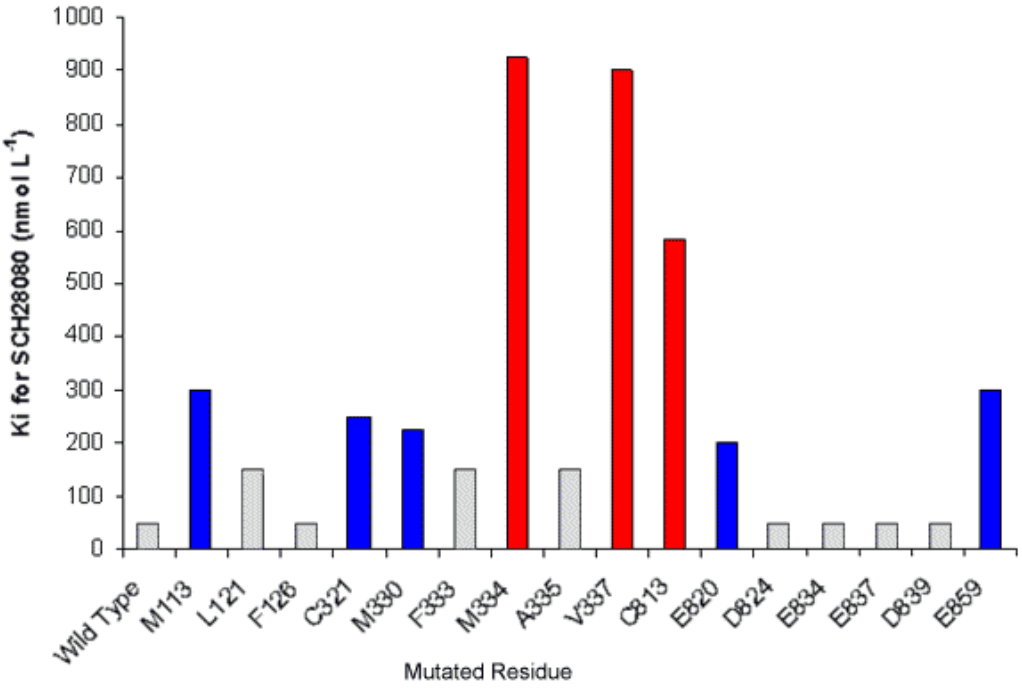

Figure 5-3 Overview of the effects of mutation of residues in the M1 - M6 transmembrane domain on the affinity for SCH28080 (K_i). Residue substitutions having a large effect on the binding affinity are shown in red. Those with a medium effect are shown in blue. Substitutions having a small effect are shown in grey. Definitions as classified by Munson and co-workers [92]. Data from [92, 107, 180, 186].

When the mutation influences K_i only, and leaves the Michaelis constant K_m unaffected, the substitution is regarded as changing the binding site of SCH28080 only. Some mutations alter K_m only. These mutations are considered to affect cation binding or to have some other structural effect on the protein. Site-directed mutagenesis has distinguished M113 as sensitive to SIP binding. M113 is proposed to be in the first transmembrane (M1) domain [77] (Figure 5-4). Munsons and coworkers suggested that the methylene group of M113 was the likely site of labelling with [^{3}H]mDAZIP following photolysis [92].

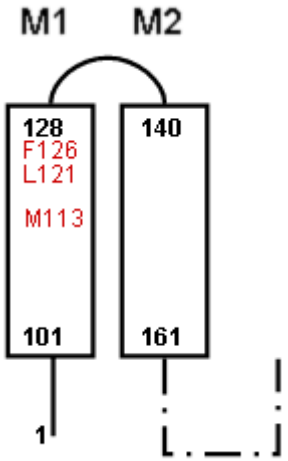

Figure 5-4 Overview of residues in M1 of the H/K-ATPase that have been studied by site-directed mutagenesis and chemical modification and are discussed in the text. See Figure 5-1 for an overview of the residues and membrane topology discussed in this section.

The M113 to leucine substitution had a large effect on K_i ($K_i \approx 300$ nmoles L^{-1} compared to 50 nmoles L^{-1} for the wild-type enzyme). Mutation of L121 to phenylalanine initiated a moderate 3-fold change in sensitivity to SCH28080 ($K_i \approx 150$ nmoles L^{-1}). F126 was found not to be directly involved in SCH28080 binding [107].

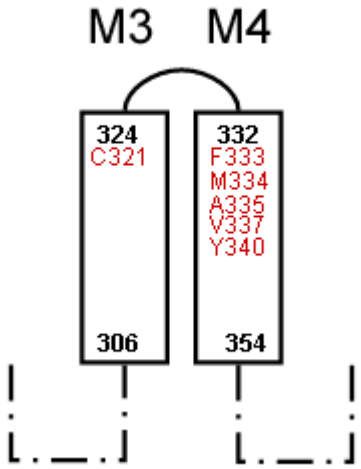

Figure 5-5 Representation of the M3/M4 residues discussed in the text. For an overview of the residues discussed in this section and for a suggested membrane topology for H/K-ATPase see Figure 5-1.

There have been a number of amino acid substitutions in the putative M3 and M4 transmembrane segments of the H/K-ATPase (Figure 5-5). Cysteine 321, a residue predicted to be lie within the centre of M3 [77], exhibits sensitivity to SCH28080. The C321A mutation had a mixed effect on K_m for NH_4^+ and K_i for SCH28080 ($K_i \approx 250$ nmoles L^{-1}). The effect is attributed to a conformational change in the protein. Considering the relative helix positions in the Ca-ATPase, C321 is distal to the proposed helical positions of L121 and C813 (see below) and would require the inhibitor to reside closer to the cytoplasmic interface of the transmembrane region, a proposition which is in conflict with localisation of SCH28080 to the extracellular face of the protein [103, 154].

Amino acid substitutions in the M4 region have generally had large effects on SCH28080 kinetics [182] (Figure 5-5). Mutation of M330, M334 and V337 produced competent enzyme with similar apparent K_m values for cation binding but variations in apparent K_i for SCH28080. The M330V mutation produced a 2-fold decrease in SCH28080 affinity. The decrease in SCH28080 affinity was 9-fold in both M334I and V337I mutations without significant effect on apparent K_m. A helical wheel view of this region of the transmembrane sequence placed M330, M334 and V337 facing into the M1-M6 helical space [182]. Replacement of F333 by leucine produced a modest reduction in affinity for SCH28080 (K_i = 220 nmoles L^{-1}) [92]. Few mutations in this region affect the cation binding affinity. The mutations A335G and Y340N produced a marked change in K_m [182] but these residues have been predicted by helical

wheel alignment to be presented from a different face of the helix to that of M334 and V337. Thus, it is suggested that residues in the extra-cytoplasmic region of M4 are important for binding SCH28080 since there is generally little change in K_m upon their mutation but large changes in K_i are observed.

A number of residues in the proposed M5 and M6 regions have been investigated by site-directed mutagenesis (Figure 5-6). Close to the extra-cytoplasmic face of M5 and M6, C813 has been determined to be the site of covalent reaction with the substituted benzamidazole omeprazole [98]. Preincubation of the protein with SCH28080 prevents modification of C813 by omeprazole [119]. A C813T mutation decreased the inhibitor affinity for SCH28080 about 6-fold (apparent K_i = 586 nmole L^{-1}) [186]. There was a concomitant 3-fold change in affinity for the counter-ion (K_m = 6.6) but no change in ATP affinity. Since cysteine does not provide oxygen for ion binding in its side chain, it is unlikely that this mutation affected an ion-binding site but rather induced a conformational effect.

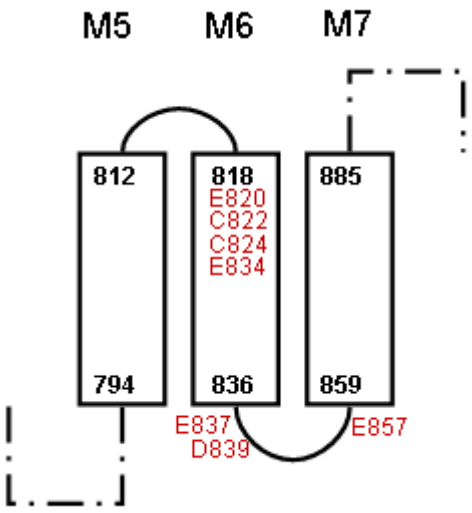

Figure 5-6 Schematic presentation of the M5-M6-M7 transmembrane domain of gastric H/K-ATPase showing the suggested locations of residues discussed in the text. An overview of the transmembrane region of the protein is presented in Figure 5-1.

Mutation of C822 to glycine, another binding site for substituted benzamidazoles, had no effect on SCH28080 binding [186]. The negatively charged residues in the fifth and sixth domains of the H/K-ATPase were examined by site-directed mutagenesis [109] [107] (Figure 5-6). Mutants D824R, E834Q, E837Q, and D839N showed no change in affinity for SCH28080 [109, 187]. The Mutant E822A (E822 is the rabbit analogue of rat E820) showed a sensitivity to SCH28080 that was 8 times lower than that of the wild-type enzyme [107]. This carboxyl residue was also implicated in K^+ binding [109] [107]. Furthermore, mutation of E820 suggests that sensitivity to the residue is conformation dependent. An increase in the phosphorylation level of the E820Q mutant was explained by assuming that during the catalytic cycle, the E2-P intermediate forms a complex with SCH28080 [179]. The role of E857 in binding SCH28080 was evaluated by site directed mutagenesis [180] in a study to compliment the experimental labelling with ^{14}C-DCCD [177]. Mutation

of the residue had a combined effect on cation and inhibitor sensitivity, discounting its function solely as a binding site for SCH28080.

The amino acid residues that were substituted by site-directed mutagenesis were generally chosen on the basis of divergence between Na/K- and H/K-ATPases [92]. The isoforms of the Na/K-ATPase have high homology (65%) to the H/K-ATPase and both enzymes require association with a β subunit [188]. SCH28080 does not inhibit the Na/K-ATPase and the difference in residues may account for the selectivity of this inhibitor. Although the differences in homology have not yet been fully explored, the available information provides a picture of the topology of the site in the H/K-ATPase that binds SCH28080 and its substituted imidazo[1,2-*a*]pyridine analogues. The spatial localisations of the residues involved in the ligand binding site are explored in the next sections.

The High-Resolution Structure of the Sarcoplasmic Endoreticular Ca-ATPase as a Template for the H/K-ATPase

In recent work [50], solid state NMR measurements were combined with results gained independently from site-directed mutagenesis studies [189], to provide a model for cardiac glycosides in the digitalis receptor site of the Na/K-ATPase. The 2.6 Å Ca-ATPase structure [74] (Figure 5-7) was used as a framework onto which ouabain-sensitive residues of the Na/K-ATPase were mapped by sequence threading.

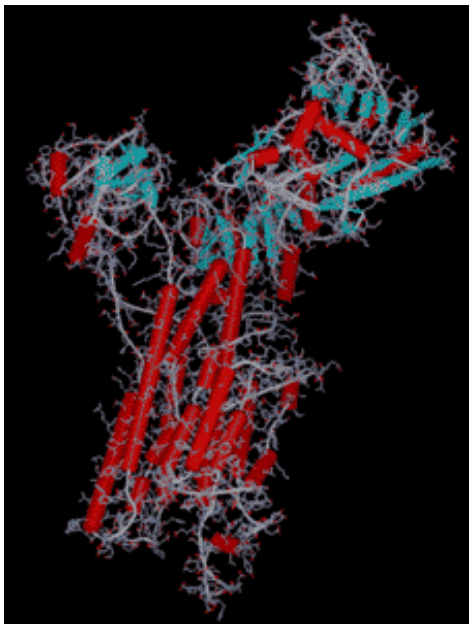

Figure 5-7 Side view of the sarcoplasmic endoreticular Ca-ATPase [74] showing the predominantly α helical transmembrane domain (lower part of image) and the large extramembranous region (mixed α helical/β sheet). (From co-ordinates deposited at the Protein Data Bank [190]).

The binding conformation of an ouabain analogue was determined by REDOR NMR and docked with the extracellular face of the putative Na/K-ATPase structure to suggest models for inhibitor binding. Analysis of the low resolution

crystals of the sarcolplasmic Ca-ATPase and *Neurospora crassa* H-ATPase [183, 184], formed the basis of an arrangement of the first six transmembrane segments of the gastric H/K-ATPase [92]. Similarly here, the high-resolution (2.6 Å) Ca-ATPase structure [74] has been used as a template of the H/K-ATPase from which to speculate a binding site, first taking into account the clear sequential and structural differences between the H/K-ATPase and the calcium pump.

The 10 transmembrane helices (M1 - M10) are believed to be a common feature of P-type ATPases [191], of which the gastric H/K-ATPase is an important member. The two-dimensional electron density maps of the homologous Ca-ATPase and *Neurospora crassa* [74, 183] validate protein digest and *in vitro* translation experiments on the H/K-ATPase [176] in this proposition. There is, however, little strong sequence identity between H/K-ATPase and the template Ca-ATPase. Within some regions, especially in the important transmembrane domain, of the H/K-ATPase, the identity with the Ca-ATPase is greater and can form the basis of a new paradigm for the topology of the membrane-spanning domain of H/K-ATPases. This work provides a novel interpretation of the location and boundaries of the H/K-ATPase transmembrane region that forms the binding site for SCH28080 and its analogues.

A description of the topology of the H/K-ATPase was provided by *in vitro* translation [176] (Figure 5-1) but there was no opportunity for scrutiny of the physical limits of the transmembrane domain of the H/K-ATPase. At the time,

there was no structural detail, low-resolution or otherwise, for the membrane region of the enzyme. Now, however, limits have been placed on the transmembrane helices of the rabbit sarcoplasmic reticular Ca-ATPase to a resolution of 2.6 Å. It is possible to reassess the working model of H/K-ATPase topology in light of this new information. Figure 5-8 shows the sequence alignment of the currently proposed M1 transmembrane region of the H/K-ATPase with the known helical boundaries of the Ca-ATPase.

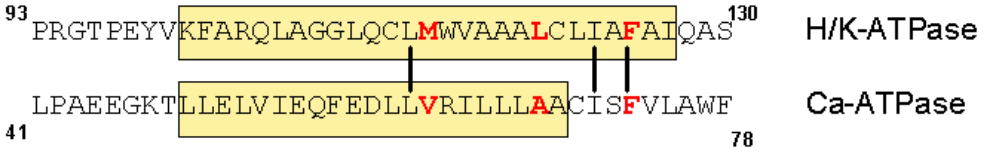

Figure 5-8 Sequence alignment of the putative M1 region of the H/K-ATPase and the known boundaries of the first transmembrane domain of the Ca-ATPase. Membrane-spanning regions shown in orange. Sequence identity indicated by black lines. Residues considered important for SCH28080 binding are highlighted in red. H/K-ATPase amino acid sequence from hog (SWISS-PROT accession number P19156) [192], Ca-ATPase from rabbit (SWISS-PROT accession number P20647) [193].

The helix described by M1 in the Ca-ATPase is of a similar length to that proposed recently by Melle-Milovanovic [77] (Figures 5-1 & 5-8). Upon alignment of these regions, it can be quickly seen that there is little sequence identity but, in regions, a number of analogous residues arises. Thus, between V116 and I128 of the H/K-ATPase and I64 and L75 of the Ca-ATPase there is an accumulation of hydrophobic alanines (47%, 17%), valines (8%, 8%), leucines (17%, 33%) and isoleucines (17%, 17% respectively) which has not been reported. Cysteine121 of the H/K-ATPase is proximal in position to C70 of the Ca-ATPase. Interestingly, the largely hydrophobic C-terminal region of this helix in the Ca-ATPase extends out of the body of the membrane domain

into the extra-cytoplasmic side (Figure 5-6). It is a compelling argument to regard conservation of hydrophobic residues in this exposed part of the transmembrane domain of both ATPases as validating the model of H/K-ATPase M1 generated by proteolysis studies. Threading of the sequence in this way places F126, implicated by photoaffinity labelling as close to the binding site of SCH28080 [106], at the position occupied by F73 in the calcium pump. By analogy to the position of F73 in the Ca-ATPase structure, it is proposed that F126 lies close to the membrane surface in the extracellular loop just outside the M1 membrane-spanning region, facing towards the body of the protein. In this way, the anchored aryl ring of TMPFPIP or SCH28080 allows for the imidazo[1,2-*a*]pyridinium ring to interact with M4 and M5/M6. Following this reasoning, M113 is necessarily within the membrane core and is placed at the position occupied by V62 in the Ca-ATPase. L121, mutation of which produced a moderate 3-fold change in sensitivity to SCH28080, is placed at the position occupied by A68.

There is little sequence identity between the proposed M3 region of the H/K-ATPase and the third transmembrane domain of the Ca-ATPase. The sequence alignment for these two regions is shown in Figure 5-9. It is possible to make two alignments. The first alignement is F311 - I322 of the H/K-ATPase with F256 - I267 of the Ca-ATPase (Figure 5-9A) and shares 33% sequence identity over 12 residues. The second alignement is I312 – I322 (H/K-ATPase) with I264 – I 269 (Ca-ATPase) and showing 50% identity over 6 residues (Figure 5-9B).

Figure 5-9 Sequence alignments of the M3 transmembrane region of the H/K- and Ca-ATPases. H/K-ATPase proposed transmembrane region and Ca-ATPase M3 domain shown in orange. Residues considered in the text are highlighted in red. Black lines indicate instances of sequence identity. (A) Sequence identity (33%) over 12 residues. (B) Sequence identity (50%) over 6 residues.

For the purposes of suggesting a location for C321 threaded onto the Ca-ATPase structure, the alignment spanning the larger stretch of residues will be considered as this is more likely to represent the location of the M3 helix in the H/K-ATPase than the shorter, localised region of homology. Furthermore, C321 can be placed at the position occupied by Ca-ATPase L266, the location of which is closer to the transmembrane space that appears to be important for SCH28080 binding.

Residues in the M4 region have been identified as important for SCH28080 binding. Figure 5-10 shows the sequence alignment of the currently proposed M4 transmembrane region of the H/K-ATPase with the known helical boundaries of the Ca-ATPase.

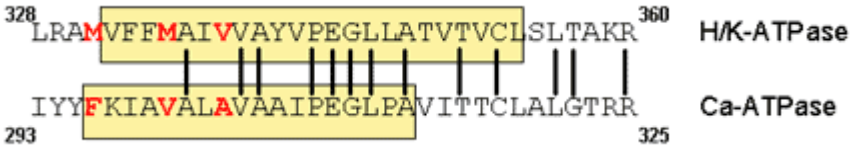

Figure 5-10 Sequence alignment of the putative M4 region of the H/K-ATPase and the known boundaries of the fourth transmembrane domain of the Ca-ATPase. Membrane-spanning regions are shown in orange. Sequence identity indicated by black lines. Residues that are sensitive to SCH28080 are highlighted in red. H/K-ATPase amino acid sequence from hog, Ca-ATPase from rabbit.

The sequence identity is 58% over the 19 residues between A301 and L319 and A336 and L354 of the Ca- and H/K-ATPases respectively. This alignment would place M330, M334 and V337 in the positions occupied by F296, V300 and A303 of the Ca-ATPase. The predicted topology of the H/K-ATPase is in close agreement at the N-terminal end of the domain if this threading scheme is adopted but the cytoplasmic terminus of the transmembrane region is several residues longer than the M4 helix of the Ca-ATPase. In addition, the K^+-sensitive residues A335 and Y340 occupy the positions of A304 and A309 in the Ca-ATPase. Over the six residues that extend beyond the C-terminal end of the Ca-ATPase M4 helix, there is 50% identity with the aligned sequence of the H/K-ATPase. It is suggested therefore that M330 and M334 lie just beneath the membrane surface at the sites occupied by F296 and V300 of the Ca-ATPase, V337 lies in the centre of the helix and that the H/K-ATPase C-terminal region of the M4 helix forms a loop by analogy to the C-terminal end of the Ca-ATPase M4 helix.

A number of models for the M5 and M6 domain have been proposed [77, 109, 194]. Figure 5-11 shows the sequence alignment of the putative H/K-ATPase M5/M6 region with that of the Ca-ATPase.

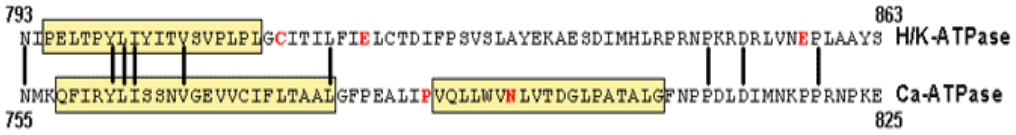

Figure 5-11 Sequence alignment of the putative M5/M6 region of the H/K-ATPase and the known boundaries of the fifth transmembrane domain of the Ca-ATPase. Membrane-spanning regions are shown in orange. H/K-ATPase M5 region is P794 – L812. Ca-ATPase Instances of sequence identity are indicated by black lines. Residues considered in the text are highlighted in red. H/K-ATPase amino acid sequence from hog, Ca-ATPase from rabbit.

There is evidence that the M5/M6 fragment forms a hairpin that is stabilised by the transported cation and is vulnerable to loss by trypsinization upon removal of K^+ ions [110]. This observation is supported by digestion of the Na/K-ATPase by trypsin in the presence of K^+. Following K^+ removal, M5/M6 were released into the medium [195]. These findings may reflect flexibility in this region. Since M5/M6 contains a number of hydrophilic and carboxylic residues, it is tempting to relate the opportunities for movement of the domain to a mechanism of counter-ion transport. The uncertainty of the sequence defining the hairpin has confounded reliable modelling of the M5/M6 region and explains the variety of suggested arrangements that have been proposed. There is 57% sequence identity between the short stretch Y800 and V806 (H/K-ATPase) and Y762 and V767 (Ca-ATPase) in the suggested M5 transmembrane region. The close sequence identity ends at this point and, if traced through the remainder of the suggested M6 domain, is not recovered. There is significant display of sequence identity if it is accepted that a frame-shift occurs between

G796 and L792 (Ca-ATPase) due to the insertion of some 11 residues. The result is an extended Ca-ATPase M5 helix and large interhelical loop and is illustrated in Figure 5-12.

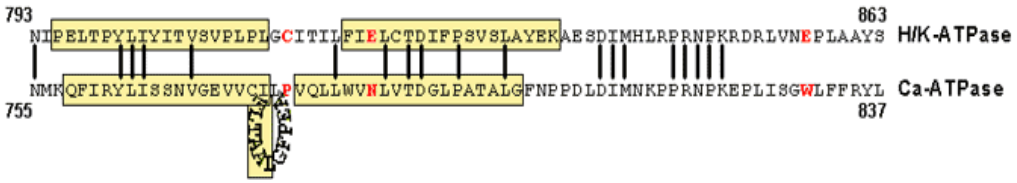

Figure 5-12 Sequence alignment of the putative M5/M6 region of the H/K-ATPase and a frame-shifted sequence of the M5 domain of the Ca-ATPase. The frameshifted region is shown as a loop. Membrane-spanning regions shown in orange. Sequence identity indicated by black lines. Residues considered in the text are highlighted in red. H/K-ATPase amino acid sequence from hog, Ca-ATPase from rabbit.

The accumulation of charged residues in the M5/M6 domain that have been determined to be important for cation binding may be reflected in the increase in M5-M6 interhelical space that this frame-shift creates. The expanded space may accommodate the large Ca^{2+} ion (N767, E770, T798, D799 contribute side-chain oxygen atoms [74]). The process of threading the H/K-ATPase sequence onto the structure of the Ca-ATPase is best approached from the M6 domain of the calcium pump. There is substantial identity between the two enzymes in the L818-K850 (H/K-ATPase) and L792-K824 (Ca-ATPase), suggesting that these 33 residues form a highly conserved structure in the membrane. If like charges are included (E838 ↔ D812), then the homology increases further for this long stretch of peptide. With the boundaries of the Ca-ATPase M6 helix established by high-resolution diffraction information [74], it is proposed that C813 (C814 in the hog sequence used here) takes the position occupied by P788 in the Ca-ATPase sequence. Cysteine 813 is within full reach of the imidazo[1,2-

a]pyridinium cation. Glutamate 820, mutation of which had a moderate effect on K_i, is placed at N795 in a marginal position for an interaction with SCH28080 and its analogues. The location of E857, which affected both K_i and K_m to a moderate extent [180], is proposed to occupy the position of W831 at the M7-cytoplasm interface.

Using the above considerations it is possible to suggest tentative positions of sites that are involved in the binding of substituted imidazo[1,2-*a*]pyridines such as SCH28080 and TMPFPIP. The sites that are important for binding this class of reversible inhibitor are shown in Figure 5-13. Residues have been classified as important for binding according to the criteria outlined by Munson and co-workers [92]. Upon site-directed mutagenesis, the apparent binding constant K_i of the inhibitor is changed by a large (>10-fold) amount without effecting K_m. It is apparent that the site forms a vestibule for the inhibitor such that the molecule could occupy the M1, M2, M4, M6 interhelical space.

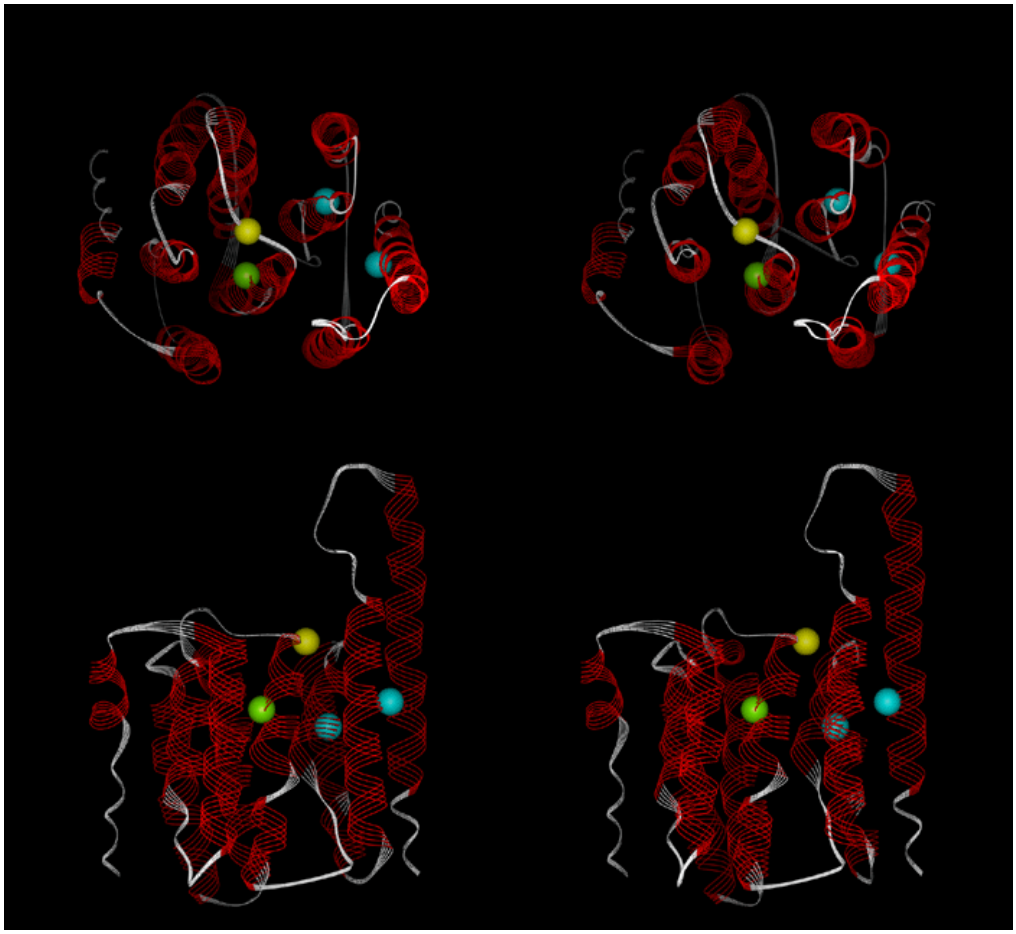

Figure 5-13 Stereoimage showing top and side views of the sites in the gastric H/K-ATPase that are important for binding substituted imidazo[1,2-*a*]pyridines. In the top images, the protein is seen from the extra-cytoplasmic side of the membrane. In the bottom images, the protein is shown with the extra-cytoplasmic face at the top. The N-terminal M1 helix is on the right. In sequence order: M113 & M334 (blue), C313 (yellow) and G820 (green). Mutation of these sites has a large reduced binding effect on the binding affinity of SCH28080 (see text for details). Graphical displays and residue substitutions were generated using *Biopolymer* and *InsightII* of Biosym/MSI. Further graphical processing was performed with WebLab ViewerPro from MSI.

Sites that are regarded as having a moderate or small contribution to binding SCH28080 and its analogues are shown in Figure 5-14. There appears to be a localisation of low-affinity sites in the M1, M3, M4 region. The position of E857 appears to be too far removed from the other sites to be a credible participant in ligand binding. The low-affinity binding sites appear to reside

within the outer half of the membrane. This localisation of auxiliary residues supports the contention that SCH28080 lies towards the extracellular face of the enzyme, overlapping with C813, the site of covalent reaction with omeprazole.

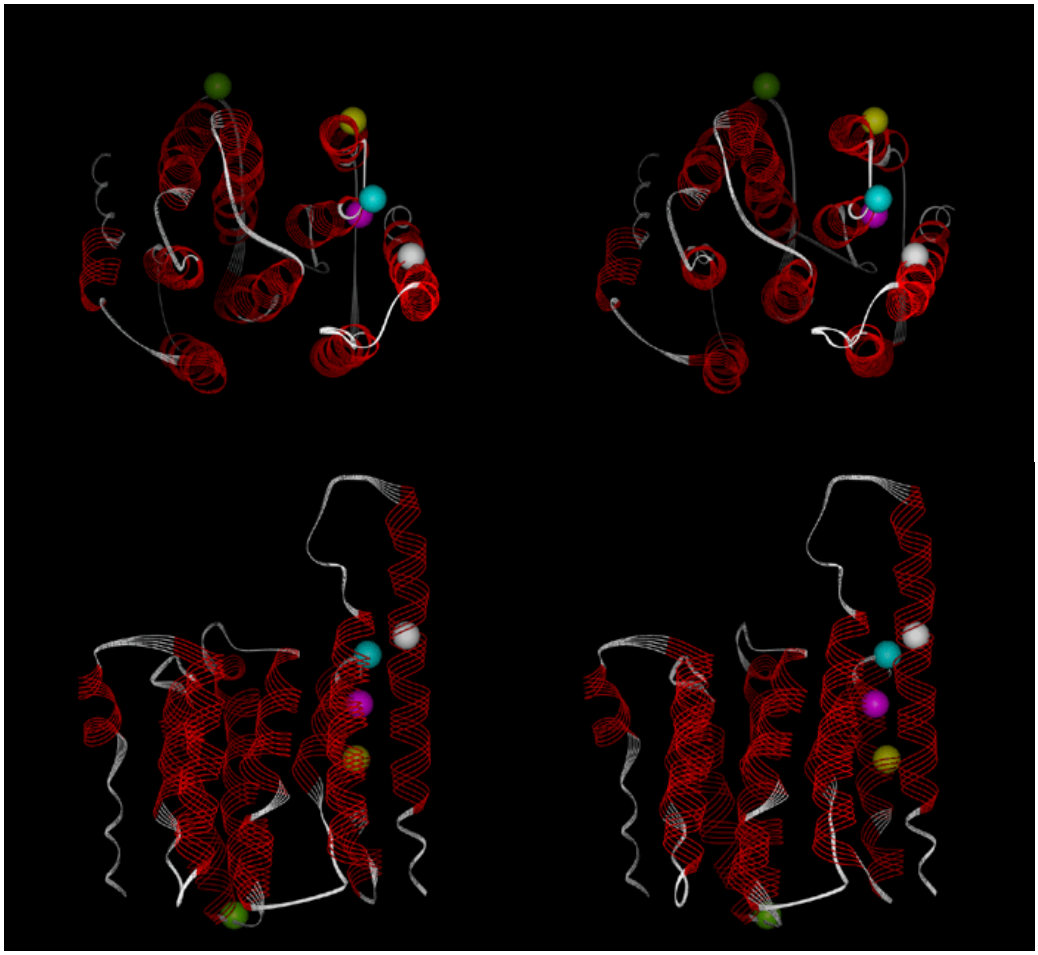

Figure 5-14 Stereoimage showing top and side views of the sites in the gastric H/K-ATPase that are auxiliary in binding substituted imidazo[1,2-*a*]pyridines. In the top images, the protein is seen from the extra-cytoplasmic side of the membrane. In the bottom images, the protein is shown with the extra-cytoplasmic face at the top. The N-terminal M1 helix is on the right. In sequence order: L121 (white), C321 (yellow), M330 (blue), F333 (pink), and G857 (green). Mutation of these sites has a moderate reduction in the binding affinity of SCH28080 (see text for details). Graphical displays and residue substitutions were generated using *Biopolymer* and *InsightII* of Biosym/MSI. Further graphical processing was performed with *WebLab ViewerPro* from MSI.

Models of Substituted Imidazo[1,2-a]pyridines at their Binding Sites in the Gastric H/K-ATPase

The structural constraints of TMPFPIP, a fluorinated analogue of SCH28080, a K^+-competitive reversible inhibitor of the gastric H/K-ATPase, at its binding site have been imposed on the compound using rotational echo double resonance (REDOR) NMR (see Chapter 4). The REDOR NMR structure of bound TMPFPIP was compared to the dimensions and arrangement of the H/K-ATPase extracellular face to assess how far the imidazo[1,2-a]pyridine moiety could extend toward the K^+ channel region. REDOR NMR experiments indicated that the active structure of TMPFPIP falls within a small conformational space between fully planar and slightly bow-shaped extremes (See Chapter 4). A bow-shaped conformation would allow the imidazo[1,2-*a*]pyridine to curve in the interhelical space between the neighbouring M1, M2, M4 and M6 transmembrane domains. A simple docking procedure minimising local van der Waals contacts but satisfying the site-directed mutagenesis and chemical modification data found two arrangements for the inhibitor could be accommodated in the protein. In the first model, TMPFPIP is placed with the imidazo fused cation ring interacting with C813 in the M5/M6 loop (Figure 5-15). The C813-cation distance is approximately 2.5 Å. The fluorophenylmethoxy ring is proximal to M330, F333 and M334 within the interhelical space and is modelled as being stabilised by the aromatic ring of F333. The C8-substitution, which may engage in a secondary, steric, interaction with the protein is buried in the interhelical space. This model reflects a binding

mechanism whereby the inhibitor, once localised to the binding pocket by the imidazo fused ring system, is retained by the C8 group.

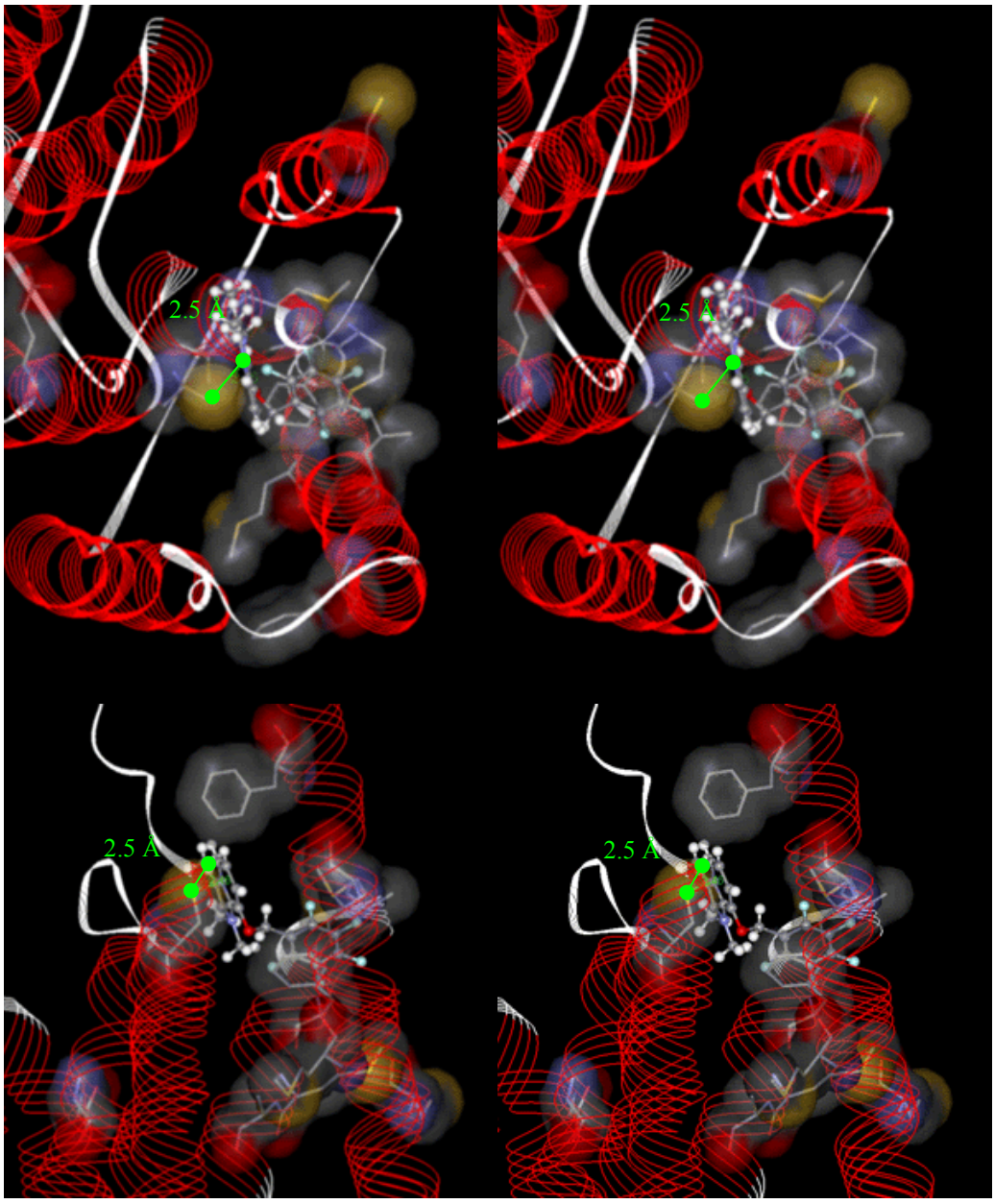

Figure 5-15 Stereoimage representation of a model of the SCH28080 analogue, TMPFPIP at its binding site in the gastric H/K-ATPase. Residues in the protein that have been implicated in inhibitor binding have been threaded onto the structure of the Ca-ATPase and are shown with Van der Waals surfaces. Top images show view from the extra-cytoplasmic face of the membrane. The reversible ligand, TMPFPIP, occupies the M1, M3, M4 interhelical space and associates with residues in M6. Bottom images show a side view with the extra-cytoplasmic face at the top of the protein. The inhibitor lies across the top of the transmembrane region and interacts with C813 in the M5/M6 loop. The putative M1 helix extends into the lumenal space on the right of the structure with F126 indicated near the top of the helix. Graphical presentations were generated using *Biopolymer* and *InsightII* from Biosym/MSI. Further processing was performed in *WebLab Viewer Pro* from MSI.

The bowed inhibitor is able to accommodate the requirement that it resides close to the membrane surface and that it interacts with residues identified by site-directed mutagenesis as important for ligand binding.

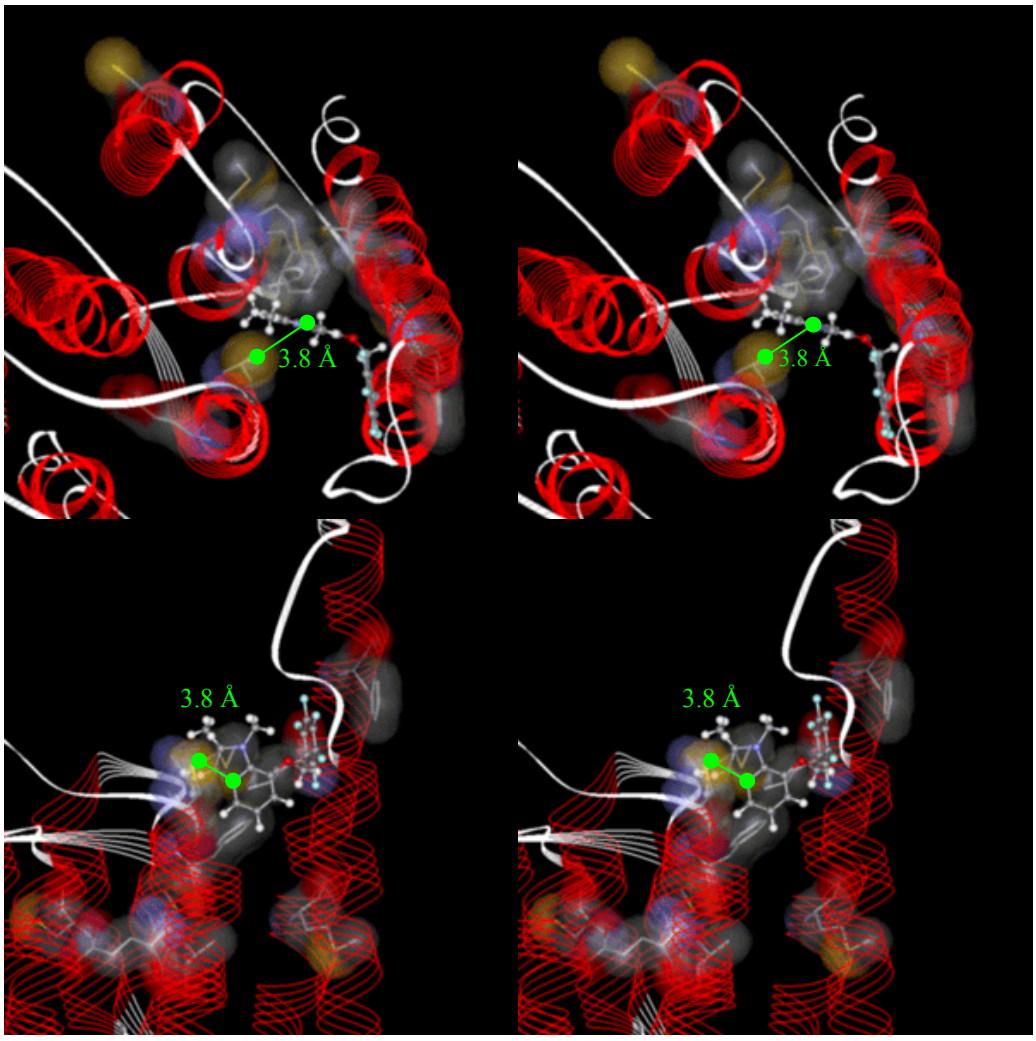

Figure 5-16 Stereoimage representations of a model of the SCH28080 analogue TMPFPIP at its binding site in the gastric H/K-ATPase. Residues in the protein that have been implicated in inhibitor binding have been threaded onto the structure of the Ca-ATPase and are shown with van der Waals surfaces. Top images show view from the extra-cytoplasmic face of the membrane. The reversible ligand, TMPFPIP, occupies the M1, M2, M4, M6 interhelical. Bottom images show a side view with the extra-cytoplasmic face at the top of the protein. The inhibitor lies across the top of the transmembrane region so as to interact with F126 in M1 and C813 in the M5/M6 loop. Helix M1 extends into the lumenal space on the right of the structure. Graphical presentations were generated using *Biopolymer* and *InsightII* from Biosym/MSI. Further processing was performed in *WebLab Viewer Pro* from MSI.

A model that places the fluorophenylmethoxy group of TMPFPIP close to F126, which was implicated by photoaffinity studies with [^{3}H]mDAZIP as a possible partner for π-π stacking, is shown in Figure 5-16. The inhibitor lies closer to the membrane surface than in the previous model and engages with C813, M330 and F333. The C813-cation distance is approximately 3.8 Å and the inhibitor is able to occupy the M1, M2, M6 interhelical space. This model allows a greater interhelical space to be blockaded by the inhibitor but the C8 functional interacts with few residues. This part of the molecule was determined by biochemical and ^{2}H NMR studies to be of secondary importance in defining inhibitor potency. Upon ligand binding, the inhibitor may be retained at the binding site by a localised conformational change in the protein as subtle as rotation of the aromatic group of F126 to associate with the phenylmethoxy group with greater efficiency.

It is with some caution that these suggestions are made. The homology between the H/K-ATPase and Ca-ATPase is unsatisfactory in many of the regions of interest in this study and, other than the shift described in the M5/M6 loop region, there has been no consideration of any evolutionary frame shifts leading to insertions or deletions of amino acids, which would have implications for the helical orientation of the residues under examination. These uncertainties have limited the faithfulness with which the SCH28080 analogue can be docked with the protein and the relative orientations of the molecules are for illustrative rather than definitive purposes. The models do provide a useful insight into the possible locations of residues that interact with this class of gastric H/K-ATPase

inhibitor and suggest that the binding site for the inhibitors lies within the outer region of the transmembrane domain in a binding pocket localised to C813. The models show that there is opportunity within the putative binding pocket for residues to accommodate variations in the phenylmethoxy group at the C8 position (refer to Figure 2-13 for definition). There appears to be little interaction with cation side-chains, supporting the biochemical observation that π-cation interactions between the inhibitor phenylmethoxy analogues are unimportant for ligand stabilisation. The models are also able to reconcile the chemical modification and site-directed mutagenesis data such that M1, M2, M3, M4 and M6 all contribute to retaining the inhibitor at its site of action in the enzyme.

Conclusions

The recent high-resolution structure of the sarcoplasmic reticular Ca-ATPase [74] has provided a useful template onto which the locations of residues in the gastric H/K-ATPase that have been implicated in the binding of SCH28080 and its analogues may be placed. Although suggestions have been made about the identity and location of residues that are important for binding K^+-competitive reversible inhibitors, the level of detail remains a matter of speculation until further structural information becomes available for the gastric H/K-ATPase. Structural information on the H/K-ATPase is scarce but it has nonetheless been possible to suggest a mechanism for inhibitor binding that involves the inhibitor partially spanning the extracellular surface of the protein. The imidazo fused ring cation is stabilised by interaction with C813 and methionine groups in M4 that are close to the surface of the transmembrane domain. The C8-substituted functional group may be buried successfully in the core of the intramembrane region or interact with residues at the extra-cytoplasmic face in a non-specific manner. The REDOR NMR-derived structure of TMPFPIP (Chapter 4) has allowed models to be proposed whereby this class of inhibitor adopts a bowed conformation to fit into the curved interhelical spaces and accommodates many of the limitations that have been imposed on the binding site by chemical modification and site-directed mutagenesis studies.

Chapter 6

DYNAMIC AND STRUCTURAL INFORMATION FROM MACROSCOPIC ORIENTATION OF NATIVE MEMBRANE SAMPLES

Work described in:
Williamson, P.T.F., Watts, J.A., Addona, G.H., Miller, K.W. and Watts, A. (2001) *PNAS* **98**(5): 2346 – 2351
and
Grobner, G., Taylor, A., Williamson, P.T.F., Choi, G., Glaubitz, C., Watts, J.A., de Grip, W.J., Watts, A. (1997) *Analytical Biochemistry* **254**: 132 – 138

Introduction

From Chapter 5 it was apparent that further structural information was required about the gastric H/K-ATPase in order to fully define the substituted imidazo[1,2-*a*]pyridine inhibitor binding site. Threading elements of the H/K-ATPase sequence onto the high-resolution structure of the sarcoplasmic reticular Ca-ATPase suggested that, although there was a concentration of SCH28080-sensitive residues in the M1-M6 transmembrane domain of the protein, there was opportunity for a number of different sites of interaction between the ligand and the protein. The knowledge of the conformational constraints of the fluorophenylmethoxy analogue of SCH28080, TMPFPIP, obtained by REDOR NMR allowed the inhibitor to be modelled in the transmembrane domain such that it lay across the M1-M4 interhelical space close to the extra-cellular surface of the membrane. In attempting to dock the ligand to the disperse binding residues in the protein, it was possible to suggest several orientations of the

ligand in the binding site that fulfilled some, but not all, of the binding obligations determined by site-directed mutagenesis. It follows that if the orientation of the substituted imidazo[1,2-*a*]pyridine could be established in the gastric H/K-ATPase, the model of the ligand at its high-affinity binding site could be further refined and the true contributions of each of the sites in the protein sequence that have been identified as important for inhibitor binding could be assessed with greater precision. It would be desirable therefore, to generate a macroscopically oriented gastric membrane sample suitable for determining the orientation of this class of inhibitors at their site of action. Orientational information has been obtained for lipids [196] and small peptides [197] in macroscopically ordered bilayer structures. This chapter describes work undertaken to develop a paradigm for the macroscopic orientation of native membrane systems for structural studies using solid state NMR techniques. The system under consideration is the nicotinic acetylcholine receptor from the electric organ of the electric ray *Torpedo nobiliana* for which medium resolution structural data is available from EM images (4.6 Å) [198], and on which the solid state NMR methods could be based, hence this choice of system.

The Nicotinic Acetylcholine Receptor (AChR)

The nicotinic acetylcholine receptor protein (AChR) is an example of a family of ligand-gated ion channels that allows neurotransmitters released from one cell to initiate an electrical signal that may propagate along the target cell membrane in neural tissue [199]. The *Torpedo* electric organ AChR complex is a 290 kDa

transmembrane glycoprotein composed of five homologous subunits, $\alpha_2\beta\gamma\delta$, that form a central ion channel [199]. An action potential invades the motor nerve ending at the motor endplate, resulting in the release from the synaptic cleft of a pulse of acetylcholine (ACh) and local concentration of the neurotransmitter increases ten-fold (0.1 – 1 mM) for less than 1 msec [199]. ACh diffuses through the cleft and binds the AChR at the post-synaptic cleft membrane where it may initiate an all-or-nothing opening of cation-selective channels through which there is a passive flow of Na^+ and K^+ ions. Electron diffraction studies have been used to resolve the structure of the receptor to 4.6 Å and to define how it is conformationally altered upon binding of ACh to the synaptic surface of the protein [198]. The resolution of the binding site is insufficient to enable the location, structure and orientation of the ligand to be determined with respect to the body of the protein.

Two ACh binding sites exist in the receptor found in muscle (and possibly also the neurone) [199] and interact in a positive, co-operative and non-equivalent manner [200]. The ligand binding sites have been investigated using the photoaffinity probes MBTA and DDF, and lophotoxin [201]. Amino acids labelled by DDF were conserved at homologous positions in the known α subunits of all but one of the muscle and neuronal receptors from all species investigated, while being absent from non-α subunits. The only known exception, the neuronal α5 subunit, does not form a functional AChR when injected into *Xenopus* oocytes with any other subunits. DDF labelled predominantly aromatic residues in three different regions of the α subunit and a *three loop* model of the agonist and competitive antagonist binding site has been proposed for the N-

terminal hydrophilic domain [202]. Adjacent cysteines, C192 and C193 of the *Torpedo* AChR subunit contribute to the affinity for agonists [203]. The presence of aromatic groups within the agonist binding site has been noticed in many choline-containing proteins and it may be the cation-π electron interactions, rather than binding through ionic interactions of charged molecules, that complex with the diffuse quaternary ammonium group of ACh. This view is supported by the observation that not only electrostatic, but hydrophobic interactions are required by macrocyclic compound in binding methyl-substituted ammonium groups [204].

The dynamics of a ligand at its binding site can give detailed information about the nature of the binding and the local environment of the ligand [148, 149, 205]. The well characterised lineshapes of deuterated compounds [206] allows a qualitative analysis relating to dynamics of a quaternary ammonium group such as that of ACh while in the agonist binding site of the AChR. Furthermore, the orientation of a ligand may be determined by exploiting the anisotropy of the deuterium spectrum. Combination of these features of the deuterium NMR spectrum provides a convenient system from which to determine the dynamics and orientation of ACh at its binding site in the receptor.

Information from the Deuterium Spectrum

An introduction to the deuterium NMR spectrum was given in Chapter 3. The analysis is extended here to examine the partial averaging of the quadrupolar interaction by rapid rotation about more than one bond. Recalling the axis of

rotation available to the deuterons of d_3-TM2FPIP [Figure 6-1A] and its analogues, the deuterons introduced into the quaternary ammonium group of the covalently linked ACh analogue [207] considered in this study, bromoacetylcholine (BrACh), have the opportunity to undergo rapid rotation about the C_3 and $C_{3'}$ axes [Figure 6-1B].

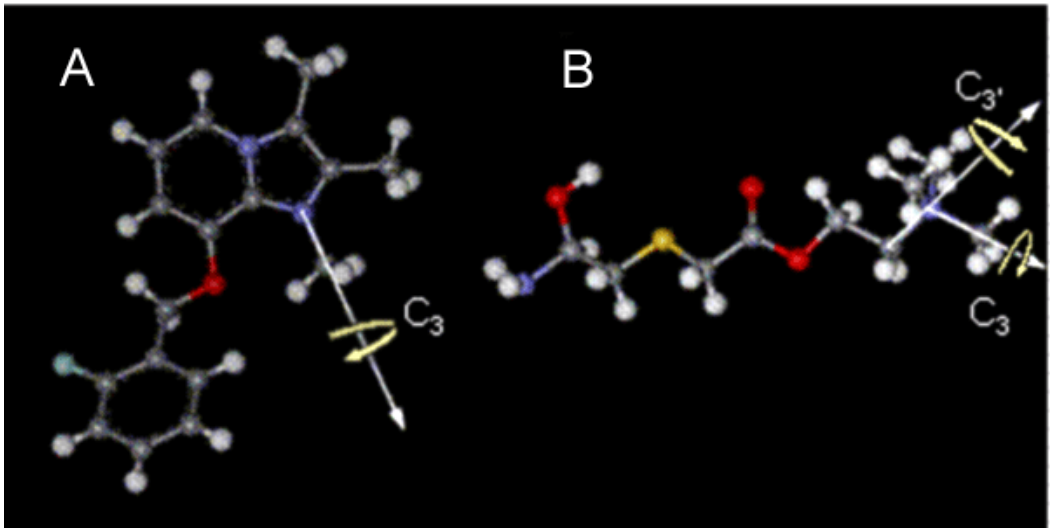

Figure 6-1 Schematic representation of the axes of rotation available to the deuterons in (A) d_3-TM2FPIP and (B) acetylcholine-d_9 (ACh). The CD_3- group in d_3-TM2FPIP may undergo fast axial rotation about the C_3 axis. The deuteromethyl groups in acetylcholine-d_9 may undergo fast axial rotation about the CD_3 bond axis (C_3) and the NC bond ($C_{3'}$).

From Equation 3-2 (Equation 6-1 below), the resonance position $\upsilon\pm$ of the $\Delta m = \pm 1$ transitions induced in a nucleus with spin = 1 by an external magnetic field is dependent upon the angle made between the deuterium bond vector and the applied magnetic field.

$$\Delta\nu_Q(\theta) = \nu_+ - \nu_- = 3\frac{(e^2qQ)}{2h}\frac{(3\cos^2\theta - 1)}{2}$$ **Equation 6-1**

To give a quadrupolar splitting, $\Delta\upsilon_Q(\theta)$. As stated previously (Chapter 3), the quadrupolar coupling constant for a static aliphatic deuteron is approximately 170 kHz.

In a rigid lattice, or in the slow exchange limit ($\tau_{ex} >> \Delta\upsilon_Q$), each C-D bond produces a separate resonance line and three quadrupole doublets arise from each magnetically equivalent C-D bond. When the jump frequency at which the $-CD_3$ group rotates about the C_3 axis from one configuration to another is fast ($k >> e^2qQ/h$, $\sim 10^{10}$ sec^{-1}) compared to the deuterium frequency ($\omega_0 = 10^7$ sec^{-1}), only the average molecular configuration is detected. There is a concomitant reduction in the quadrupolar splitting by a factor of $(3\cos^2\text{-}\rho)$ which is dependent upon the angle (ρ) between the deuterium bond and the axis of motional averaging [155]. In the bromoacetylcholine molecule, the deuterons introduced into the quaternary ammonium group are able to undergo rapid rotation about the C_3 and $C_{3'}$ axes (c.f. Figure 6-1). The quadrupolar coupling constant is scaled by both these rotational regimes and the resultant quadrupolar splitting is

$$\Delta\nu_Q = \frac{3e^2qQ}{16h}\overline{(3\cos^2\theta_{CD} - 1)}\,\overline{(3\cos^2\theta_{NC} - 1)}$$ **Equation 6-2**

where ρ has been substituted with the time-average angles between the C-D bond (θ_{CD}) and the N-C bond (θ_{NC}). By examining the quadrupolar splitting seen in the deuterium NMR spectrum, and comparing them to theoretically-computed lineshapes based upon Equation 6-2, it is possible to estimate the energetics of many of the dynamic processes occurring in the molecule.

In a uniaxially-oriented sample of AChR-enriched membranes labelled with BrACh, all deuterium bond vectors lie uniformly along the rim of a cone with an angle γ [Figure 6-3]. When the sample normal lies parallel to the applied magnetic field (α = 0˚), θ is defined by the cone angle γ (Figure 6-2). A *zero tilt* spectrum arises with quadrupole splitting

$$\Delta\nu_Q(\gamma) = \Delta\nu_Q{}^{powder}(3\cos^2\gamma - 1) \qquad \textbf{Equation 6-3}$$

If $\Delta\upsilon_Q^{powder}$ is known from the deuterium NMR powder pattern obtained from an unoriented powder sample, the angle of the deuterium bond vector relative to the macroscopic axis of ordering can be calculated. The positive and negative signs of $\Delta\upsilon_Q$ cannot be discriminated in the zero-tilt spectrum. Between cone angles γ of 35 and 90˚, only the magnitude of $\Delta\upsilon_Q(\gamma)$ can be determined. The sign of $\Delta\upsilon_Q(\gamma)$ is obtained by varying the tilt angle between the oriented sample and the magnetic field. As described by Ulrich and Watts [208], the contributions of γ and the changes in θ with variation in tilt angle can be simulated and compared to the resonance lines in the spectrum to determine the bond angle γ.

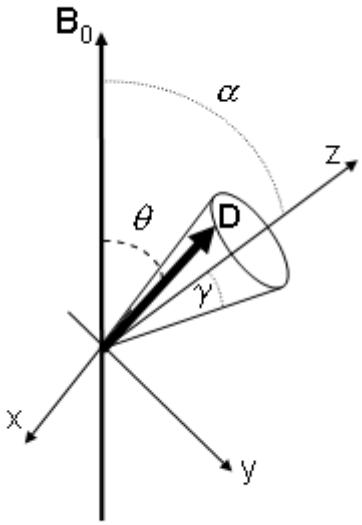

Figure 6-2 Representation of a uniaxially oriented sample showing the angle of inclination, α, relative to the spectrometer field B_0, the angle γ made between the deuterium bond and the axis of rotation, and θ the angle between the instantaneous angle made between the deuterium bond vector D and the applied field (adapted from [208])

The contribution of mosaic spread in the sample leads to a distribution of values around γ. By applying line-broadening functions to the lineshape simulation, it is possible to determine the mosaic spread of bond angle γ about the sample normal.

Information from the static ^{31}P NMR spectrum

^{31}P has a natural abundance of 100% and possesses a nuclear spin I = ½ which renders it a relatively sensitive nucleus to use with NMR spectroscopy. In particular, the interaction of lipids in oriented membranes with the magnetic field gives rise to spectra which are sensitive to mosaic spread and macroscopic orientation. The electron distribution around the ^{31}P nucleus is not symmetric.

This asymmetric environment is reflected in the chemical shift tensor and may be presented as a function of orientation with respect to the applied field. In a spherical distribution of all possible angles of the phosphorus nucleus, a powder pattern may be obtained [209] containing the three principal components of the chemical shift tensor σ_{11}, σ_{22}, and σ_{33}. Biological membranes in the Lα bilayer phase are characterised by rapid motions of the lipid molecules around the axis perpendicular to the bilayer surface (the director axis) and thus possess rotational averaging of the chemical shift anisotropy such that a new lineshape is produced that is described by the two components of a uniaxially averaged system $\sigma_{\parallel}$ and $\sigma_{\perp}$ [209]. The two extremes of the spectrum represent the anisotropic component of the chemical shift anisotropy ($\Delta\sigma$) which is given as:

$$\Delta\sigma = \sigma_{33} - \frac{1}{2}(\sigma_{11} + \sigma_{22}) = \sigma_{\parallel} - \sigma_{\perp}$$ **Equation 6-4**

It is possible to prepare planar-oriented lipid bilayers and biological membranes [138, 210] such that the director axis is perpendicular to the plane of the support. For the general case when the macroscopically-oriented membrane director axis makes an angle δ with the applied field [209]

$$\Delta\nu(\delta) = -\frac{2}{3}\Delta\sigma\left(\frac{3\cos^2\theta - 1}{2}\right)$$ **Equation 6-5**

Figure 6-3 illustrated the variation of the ^{31}P spectra upon orientation of powder samples and then variation in the tilt angle of the sample with respect to the applied field. Under the *zero-tilt* condition, where the lipid bilayers are oriented at 0˚ with respect to the magnetic field, the observed resonance lies at $\sigma_{\parallel}$. When the sample is tilted to be perpendicular to the magnetic field, the observed resonances appear at $\sigma_{\perp}$ (Figure 6-3).

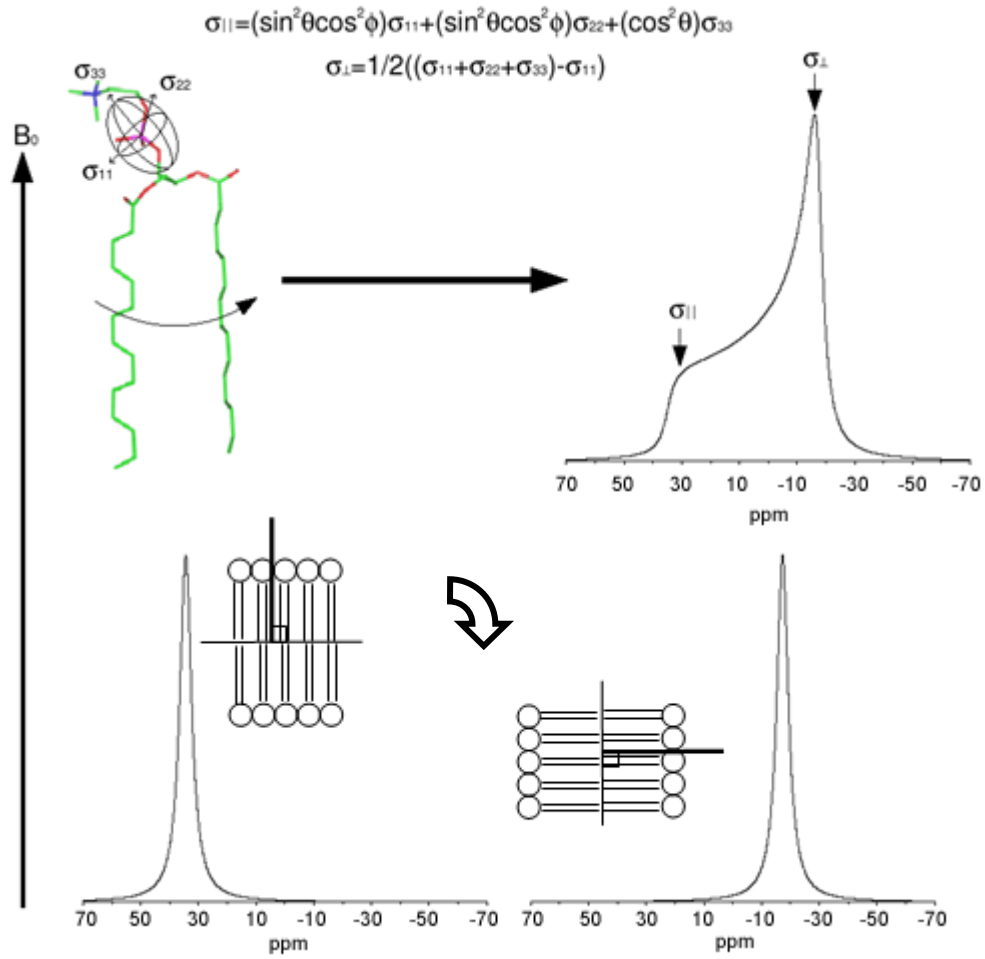

Figure 6-3 Illustration of the effect of macroscopic orientation of a lipid bilayer system on the ^{31}P spectral lineshape. Rotation of lipids about the long axis of the acyl chains (top left) leads to averaging of the principal components of the chemical shielding tensor (σ_{11}, σ_{22}, and σ_{33}) and an axially symmetric powder pattern results (top right). Upon macroscopic orientation of the bilayers by methods such as isopotential centrifugation, the parallel ($\sigma_{\parallel}$) and perpendicular ($\sigma_{\perp}$) components of the uniaxially oriented system can be isolated (bottom left and right respectively). Orientation of the membrane normal is shown as insets in the lower diagrams. This figure adapted from [211].

By fitting simulation lineshapes based on Equation 6-5 to the observed lineshapes, it is possible to estimate the degree of homogeneity of orientation of the biological membrane sample and thus to verify macroscopic ordering of the membrane system for oriented ^{2}H-NMR experiments.

Aims of this study

The aims of this study are to synthesise and characterise an *N*-methyl-deuterated acetylcholine analogue, BrAChBr-d_9 for site-specific labelling the AChR in the ACh binding site. Native membrane enriched with *Torpedo* AChR are oriented using a method based on isopotential spin-dry ultracentrifugation of membrane fragments onto a support. The quality of orientation is assessed by observation of static solid-state ^{31}P NMR of the membrane phospholipids. Having established macroscopic orientation of the membrane sample, the dynamics and orientation of the deuterated ACh analogue are determined using wide-line solid state ^{2}H NMR. This combination of dynamic and orientational information of the quaternary ammonium group of the covalently-bound ACh analogue will permit coherent description of the ligand at its binding site in a large, pharmacologically important membrane protein and establish a paradigm for orientational analysis of SCH28080 analogues in the gastric H/K-ATPase.

Materials and Methods

Synthesis of Bromoacetylcholine bromide-d_9 (BrAChBr-d_9)

Deuterated BrAChBr-d_9 was generated according to the method of Chiou [212]. Bromoacetyl bromide was added to dry choline-d_9 bromide under nitrogen. The product was precipitated from cold absolute ethanol, filtered through PTFE membranes and recrystallised from propan-2-ol. The purity was confirmed by ^{1}H NMR (δ = s 3.0 (9), d 3.6 (2), s 3.9 (2), d 4.5 (2)) and electrospray mass spectrometry (Fw = 233/235)

Purification and Labelling of Enriched Nicotinic Acetylcholine Receptor Membranes

Acetylcholine receptor (AChR) membranes were enriched from the electric organ of *T. nobiliana* according to the method of Sobel (Braswell) [213]. Membranes enriched with AChR were resuspended to a protein concentration of 1 mg/mL with 20 mM TRIS buffer (pH 7.2). the protein suspension was treated with 10 mM DFP to inhibit ACh esterase activity and to prevent non-specific binding of the ACh analogue to the esterase. The sample was treated with *N*-ethyl maleimide (3 mM NEM, 6 hrs, 4 °C) to modify free cysteine sulphydryl group. The incorporation of NEM was facilitated by freeze-thawing the suspension in liquid nitrogen. The suspension was washed with buffer as above and incubated with dithiothrietol (9 μM, 1 hr) to reduce the vicinal disulphide

bond. The suspension was serially washed and labelled with BrAChBr (1 mM, 1 hr). The sample was serially washed in buffer to remove free BrAChBr.

Orientation of Enriched Nicotinic Acetylcholine Receptor Membranes

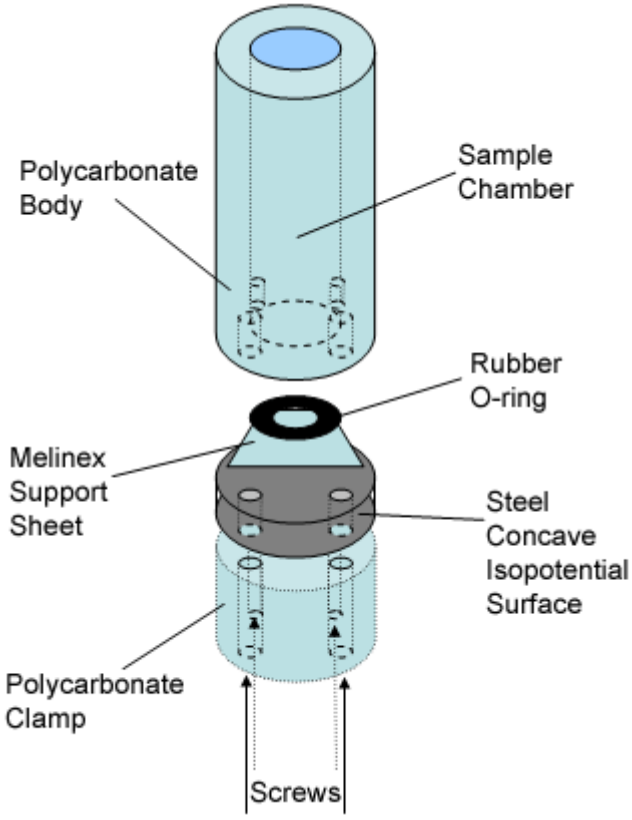

Figure 6-4 Isopotential centrifugation apparatus used for orienting native membranes onto Melinex supports in Beckman SW80 rotors. The membrane sample is placed in the sample chamber and the apparatus is inserted into a Beckman SW28 tube.

Nicotinic acetylcholine membrane suspensions were taken and oriented onto Melinex sheets (Agar Scientific, UK) using an isopotential spinning technique. 1 mL of receptor membranes (1mg/mL) was pelleted onto the Melinex support by centrifugation in isopotential spinning apparatus (Figure 6-4) (90000 g, 15 hrs, 4

˚C) without drying. Samples were then removed, dried and subsequently rehydrated (85% humidity, 20 ˚C, 3 hrs).

Static ^{31}P and ^{2}H NMR Spectroscopy

^{31}P NMR spectra were acquired at 161.92 MHz using a Bruker MSL 400 spectrometer with a static 8 mm double resonance probe. A standard Hahn-echo pulse was used to acquire spectra, with 25 kHz broadband proton decoupling during acquisition. 90˚ pulse lengths were typically 5 μs with an interpulse delay of 40 μs and recycle delay of 3.5 s. 2H powder spectra of crystalline BrAChBr-d_9 was acquired at 61.42 MHz using a 10 mm single resonance static probe. Temperature was regulated using a Bruker VT1000 temperature control unit to ± 1 K. ^{2}H spectra of both powder and orientated nicotinic membrane samples labelled with BrAChBr-d_9 were acquired on a CMX 500 Infinity machine at 75 MHz using a 10 mm single resonance static probe. A standard quadecho sequence was used to acquire spectra. 90˚ pulse lengths were 5 μs with an interpulse delay of 30 μs and recycle delay of 0.5 s.

Lineshape Simulations

Lineshape simulations for mosaic spread and angular dependence of the macroscopically oriented membranes were performed for both ^{31}P and ^{2}H spectra. The lineshape simulation algorithm was based on that of Ulrich and Watts [208] and modified by Dr C. Glaubitz. The simulation programme was

written in C++ using GAMMA and simulations were performed and interpreted by P. Williamson. The angular dependence of the deuterated quaternary ammonium group was determined by comparison of the oriented lineshapes to the experimental spectra.

Results and Discussion

Dynamics of Bromoacetylcholine-d_9 Bromide Bound in the Nicotinic Acetylcholine Receptor

The motional characteristics of the quaternary ammonium group in the crystalline ligand have been investigated as a function of temperature. The ^2H NMR spectra of crystalline BrAChBr-d_9 at temperatures between 293 K and 170 K are shown in Figure 6-5. It is immediately apparent that there is considerable variation in the spectral lineshapes of the solid ACh analogue as the temperature changes. There is considerable broadening of the lineshape as the temperature decreases. At 293 K, the spectral lineshape appears to exhibit two superimposed components. The sharp central intensity is dominated by a broad powder pattern with an inner splitting of 13 kHz, which is consistent with fast axial rotation about both the C_3 and $C_{3'}$ axes. The coincidence of the narrow peak with the rounded doublet suggests that the dynamics of the molecule are approaching an intermediate motional regime ($k = 10^3 - 10^6$ s^{-1}) [155-157, 206]. Between 273 K and 250 K there is a loss of intensity and broadening of the outer wings as the inner wings coalesce. At 250 K, the narrow intensity appears distinctly above a broad low intensity component. Broadening of the spectral features suggests that motion about the C3 or C3' axes has entered an intermediate time scale. Between 230 K and 190 K, there is disappearance of the narrow central intensity while there is improved definition of the outer wings.

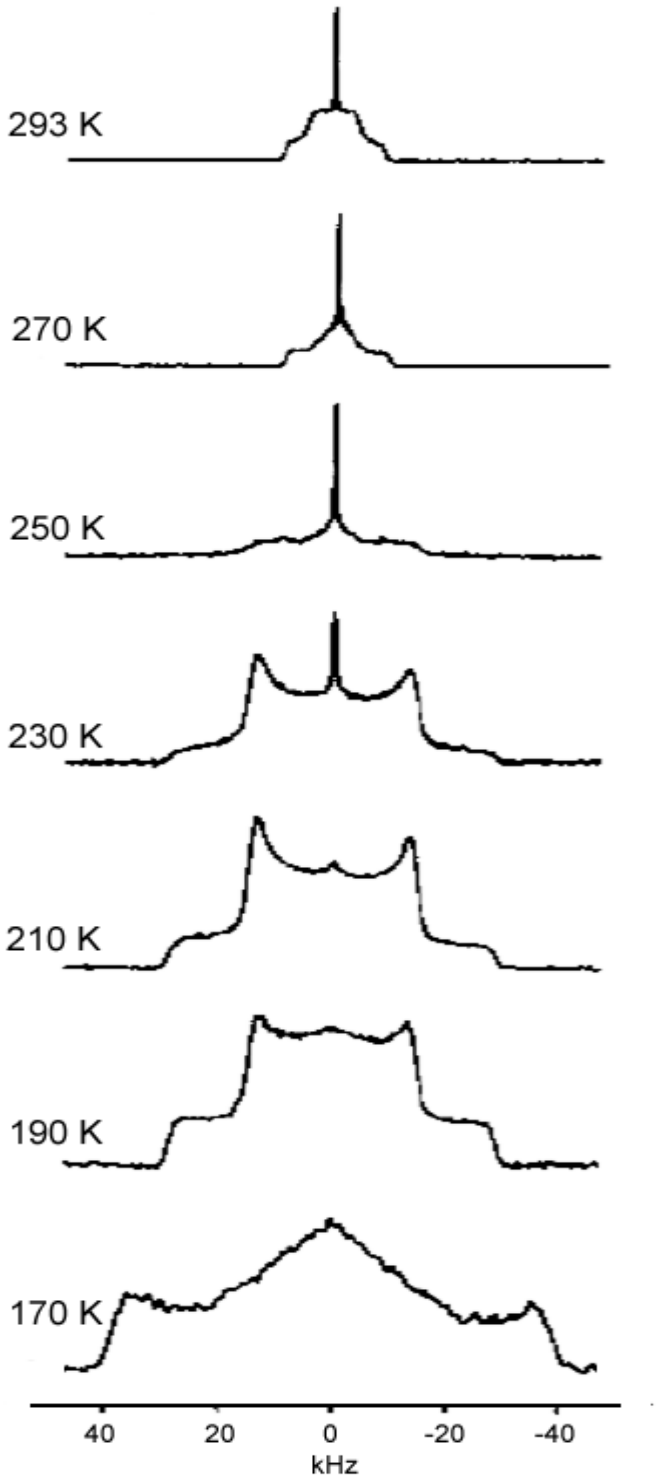

Figure 6-5 Variable temperature deuterium NMR spectra of crystalline BrAChBr-d_9. Spectra acquired as described in the text (1024 acquisitions).

At 230 K and then 210 K, the spectra increasingly adopt a powder-pattern lineshape that is dictated by single rapid rotation about the C_3 or $C_{3'}$ axis. There

is scaling of the quadrupolar coupling constant by ½(3cos$^2\theta$ - 1) in a manner reminiscent of the fast rotationally averaged spectra obtained for the crystalline d_3-methylated substituted imidazo[1,2-*a*]pyridines ($\Delta\nu_Q$) (Chapter 3). At 190 K, a broad central component appears between the inner wings and the quality of the outer wings begins to degenerate. Ultimately, as temperature is reduced to 170 K, the central component dominates the spectrum again but as a broad feature at the expense of the 40 kHz inner wings. The central component is coincident with a 80 kHz wide component consistent with the remaining axis entering an intermediate motional regime [155-157, 206].

Acetylcholine Receptor-Enriched Membranes labelled with Bromoacetlycholine bromide-d_9

The temperature-dependence of static deuterium spectra of native membranes enriched with AChR and labelled with BrAChBr-d_9 are shown in Figure 6-6. It is quite clear that variation of temperature has dramatic effects on the spectral lineshapes of the BrAChBr-d_9 in AChR membranes. At 278 K, the spectrum is dominated by a narrow resonance whose linewidth approaches the homogeneity of the magnet. Upon lowering the temperature the resonance broadens and at 253 K it has adopted a Lorentzian lineshape with a linewidth of 500 Hz. This change in linewidth reflects an increase in motional restriction of the quaternary group. The lineshape continues to broaden as the temperature is decreased to 233 K and the spectrum reveals wings with a splitting of 36 kHz, similar to that for crystalline BrAChBr-d_9 when motion about the C_3 or C_3' axes has been suppressed at lower temperatures. This observation is consistent with the

proposition that there is suppression of motion in the quaternary ammonium group at these temperatures.

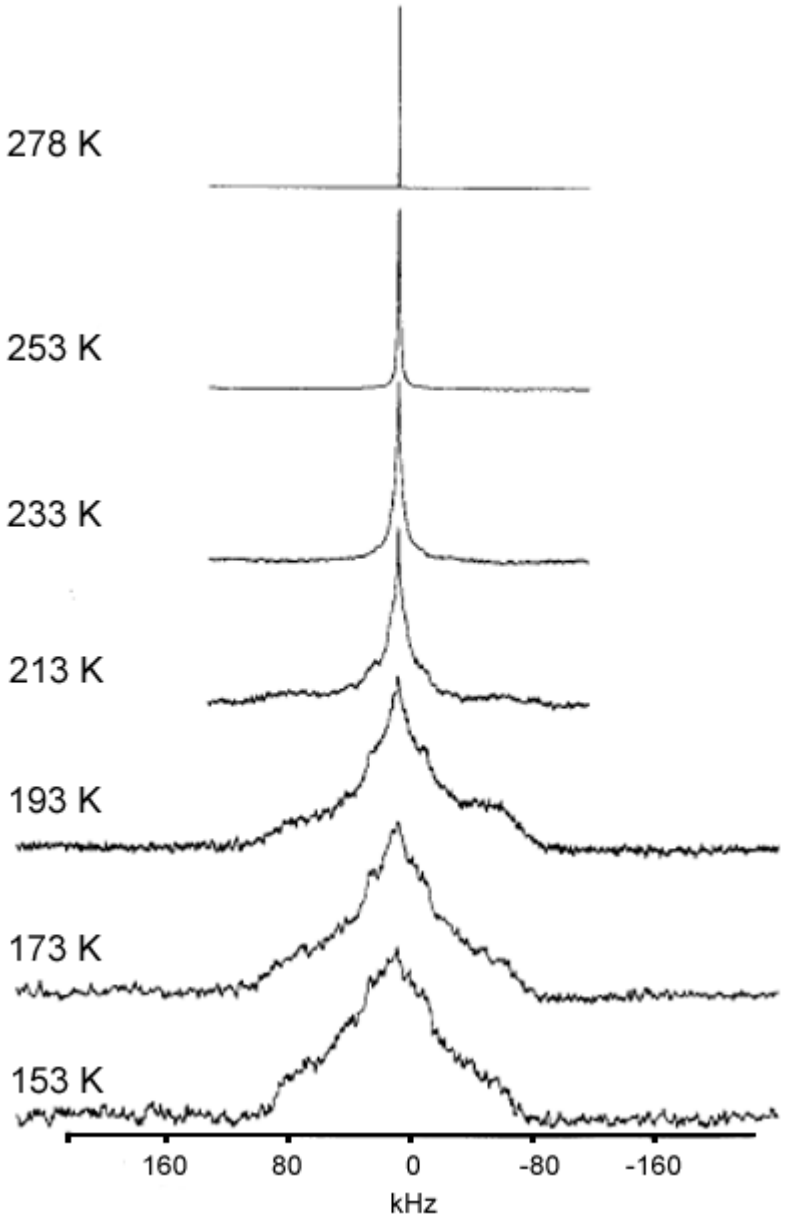

Figure 6-6 Variable temperature deuterium NMR spectra of native membranes enriched with 50 mg AChR labelled with the ACh analogue BrAChBr-d_9. Spectra acquired as described in text (60000 acquisitions).

With further decrease in temperature to 153 K there is a significant change in spectral features. Additional spectral components dominate the spectrum. In addition to the 36 kHz component, there appears to be two broader components

with apparent splittings of 76 kHz and 160 kHz. These broader features are less well resolved and this spectral insufficiency is attributed to inefficient excitation of the broad components due to limited power available during the experiments [214]. It is to be noted that these spectral features are broader than those obtained for the crystalline BrAChBr-d_9 sample at comparable temperatures, suggesting that there is greater immobilization of the d_9-quaternary ammonium group in the agonist binding site. The spectra of the inorganic salt trimethyl ammonium iodide [206] provide a useful comparison for the lineshapes obtained in this study. The membrane spectra obtained at 213 K and 153 K are similar to those obtained for the salt at similar temperatures and whose lineshapes were taken to reflect restricted motion about both C_3 and $C_{3'}$ axes of rotation. Thus, in this study the similarity in lineshape between the ligand-protein complex and the trimethyl ammonium iodide salt may reflect hindering of motion of the quaternary ammonium group when bound in the AChR. Although it is possible to conclude steric constraint of the quaternary ammonium group, a caveat must be entertained. Additional motions in the protein backbone and in the bilayer may occur on a timescale appropriate for influencing the ligand lineshapes. Even at low temperatures (213 K) there may be residual motion propagated from the protein that remains unfrozen. The nature of restriction of the ligand motion is difficult to assess. In the absence of a structure for BrAChBr-d_9 at its binding site, it is not possible to attribute the dynamics of ligand binding exclusively to interaction of the quaternary ammonium group with proximal residues or to steric constraints imposed by a conformation adopted by the ligand in the binding pocket. Electron diffraction data does indicate, however, that there is a high

degree of complimentarity between ACh and the available size and shape of the binding cavities [198]. Consideration of these structural data with structure-activity studies observing that minor modifications in ACh had profound negative effects on binding affinity of the ligand [215] supports the contention that motional restriction of ACh in the receptor is due to interaction with its high-affinity binding site.

Static ^{31}P NMR of Oriented AChR-Enriched Native Membranes

The static ^{31}P NMR spectra of oriented membranes were examined for the purposes of assessing the success of the isopotential centrifugation orientation protocol and in order to establish that the AChR-enriched membranes thus prepared were suitable for orientational studies of the ACh analogue with respect to the membrane normal by ^{2}H NMR. The ^{31}P NMR spectra of oriented membrane bilayers are shown in Figure 6-7. The 0˚ spectrum is broad and extends from 40 to 10 ppm with a main peak at 25 ppm. The breadth of this spectrum reflects the diverse chemical shift anisotropies of the different lipid species present in membranes derived from *Torpedo* electric organs whereby each lipid exhibits a slightly different chemical shift anisotropy [216] and also the chemical shift anisotropy of a mixed phosphatidyl-choline/phosphatidylethanolamine lipid system in the Lα bilayer phase [210]. Further contributions to the breadth of the spectrum arise from sample mosaic spread around the membrane normal. The spectrum at 0˚ also exhibits a resonance line at -12 ppm, indicating a small fraction of unoriented material.

Changing the tilt angle to 90˚ results in a shift in the 25 ppm resonance to -15 ppm as expected for macroscopically aligned lamellar membranes [210]. The central resonance at 0 ppm is observed in both 0˚ and 90˚ orientations and indicates either non-bilayer structures and small clustered particles or phosphorylated protein. Simulation of the lineshapes indicates an estimated mosaic spread of 30˚ ± 3˚ [210]. Thus, it is observed that isopotential centrifugation produced a well-oriented sample of this large membrane protein in a native bilayer system.

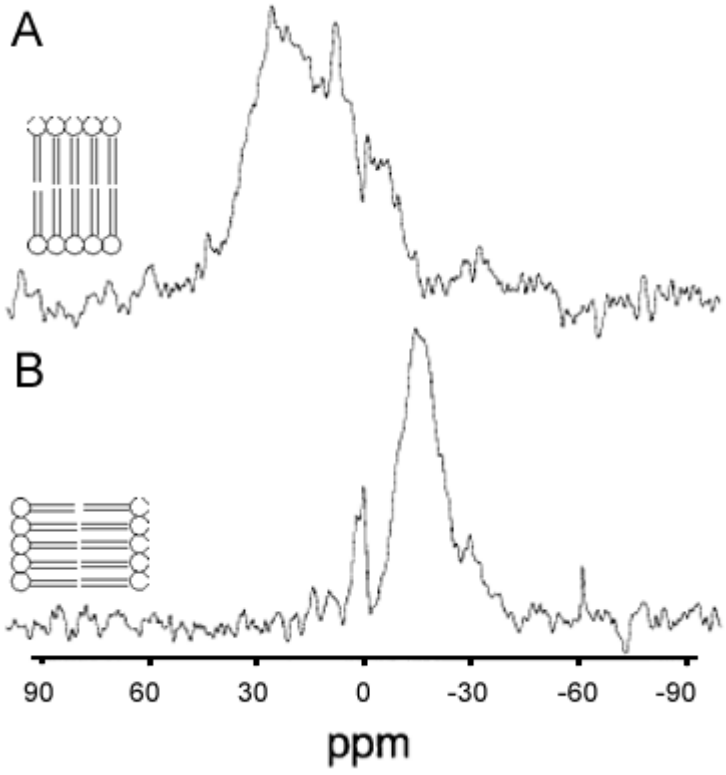

Figure 6-7 ^{31}P spectra of oriented AChR membranes labelled with BrAChBr-d_9. Spectra were recorded using two plates containing 2 mg protein each. Samples are oriented with the axis of motional averaging (A) parallel and (B) perpendicular to the applied field. Spectra acquired as in the text (4,000 acquisitions).

Static ^{2}H NMR of Bromoacetylcholine Bromide-d_9 in Orientated Nicotinic Acetylcholine Receptor Enriched Membranes

To determine the orientational dependence of BrAChBR-d_9 with respect to the membrane normal, ^{2}H spectra of AChR-enriched membrane preparations labelled with the ACh analogue were obtained at 0˚ and 90˚ with respect to the applied magnetic field. The spectra obtained at 0˚ and 90˚ are shown in Figure 6-8 (black spectra throughout). Figure 6-8A shows the 0˚ orientation, the spectrum of which consists of a central intensity of 30 kHz splitting superimposed on a broad component of 100 kHz. The 90˚ spectrum (Figure 6-8D) shows a relatively featureless lineshape that appears to consist of several contributory lineshapes. The spectrum is 50 kHz wide at the base and edges appear with a splitting of 30 kHz. The powder spectrum does not show a static lineshape at this temperature (153 K) it is nonetheless apparent that there is an orientational dependence of the sample with respect to the magnetic field that mirrors the macroscopic orientational ordering shown in the ^{31}P NMR spectra. Also shown in Figure 6-8 are overlays of simulated variation in γ, the tilt angle of the quaternary ammonium deuterium rotor, (Figures 6-8B (0˚) and 6-8E (90˚)) and the degree of mosaic spread in the sample (Figures 6-8C (0˚) and 6-8F (90˚)). Spectra were recorded and simulations performed and interpreted by P. Williamson. Simulation of the ^{2}H lineshapes to the 0˚ spectrum estimated an angle of 42˚ between the C3' axis and the membrane normal. A mosaic spread of 40˚ was estimated. Divergences from the simulated lineshapes and the experimental data

were greatest at the ± 50 kHz wings of the spectrum and were attributed to inefficient excitation of these broad spectral components in the experiment. In contrast, simulation of lineshapes to the 90˚ spectrum indicated that little divergence in tilt angle γ could be tolerated. Using a tilt angle of 42˚, a mosaic spread of 7.5˚ was estimated for this orientation.

In principle and assuming that BrAChBr-d_9 ligands adopt the same orientation at the binding sites, there should be good correlation between the mosaic spread estimated at these two tilt angle and the ^{31}P NMR spectrum. Inconsistencies, as estimated here, have been observed elsewhere in orientational studies of integral membrane proteins [217] and may be attributed to the proteins preventing better bilayer lipid alignment [139, 210]. The electron diffraction data of the AChR indicate that there is substantial homology between the ACh binding sites in the receptor [198, 218]. Furthermore, since the binding pockets are suggested to run normal to the membrane plane [198], it appears that the ligand can be accommodated such that the quaternary ammonium group make the suggested angle of 42˚ with the membrane normal. Figure 6-9 shows the suggested orientation of ACh in its binding pocket in the receptor protein.

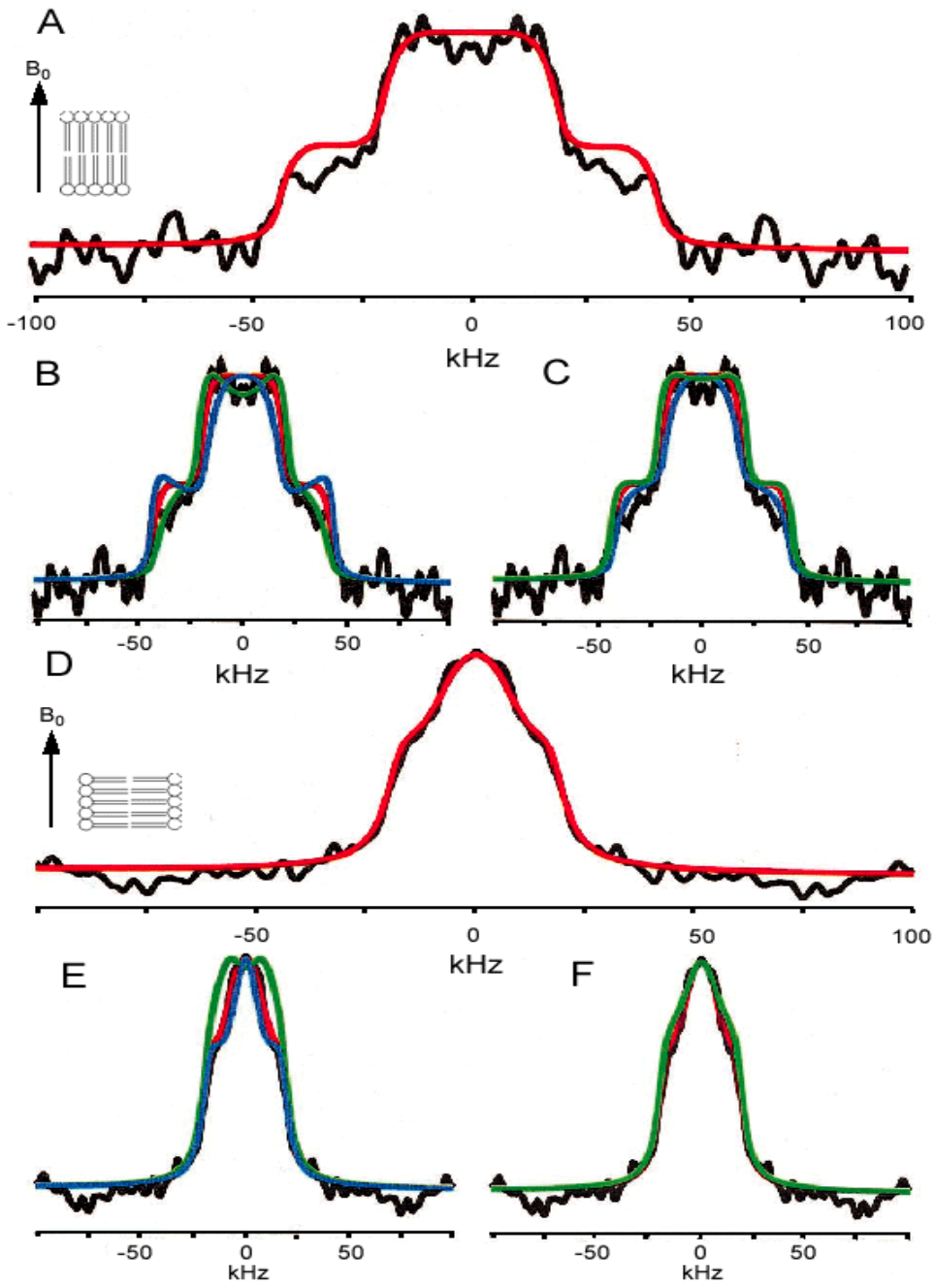

Figure 6-8 **^{2}H spectra of AChR-enriched oriented native membranes labelled with BrAChBr-d_9 at 153 K. Samples are oriented with the axis of motional averaging (A) parallel and (D) perpendicular to the applied field. Optimal simulated lineshapes are shown in red (A - F). The influence of small variation in γ, the angle made between the C3' axis of rotation and the membrane normal is shown in (B) for the 0° and (E) for the 90° orientations (the black line is the experimentally-derived spectrum, the red line is the best fit and the green and blue lines show +5° and -5° from best fit respectively). The estimated effect on the spectrum of the mosaic spread is shown in (C) for the 0° and (F) for the 90° orientations (black line is the experimentally-derived spectrum, the red line is the best fit and the green and blue lines show +5° and -5° from best fit respectively). Spectra acquired as in the text (80,000 acquisitions). Simulations performed and interpreted by P. Williamson. Figure adapted from [219].**

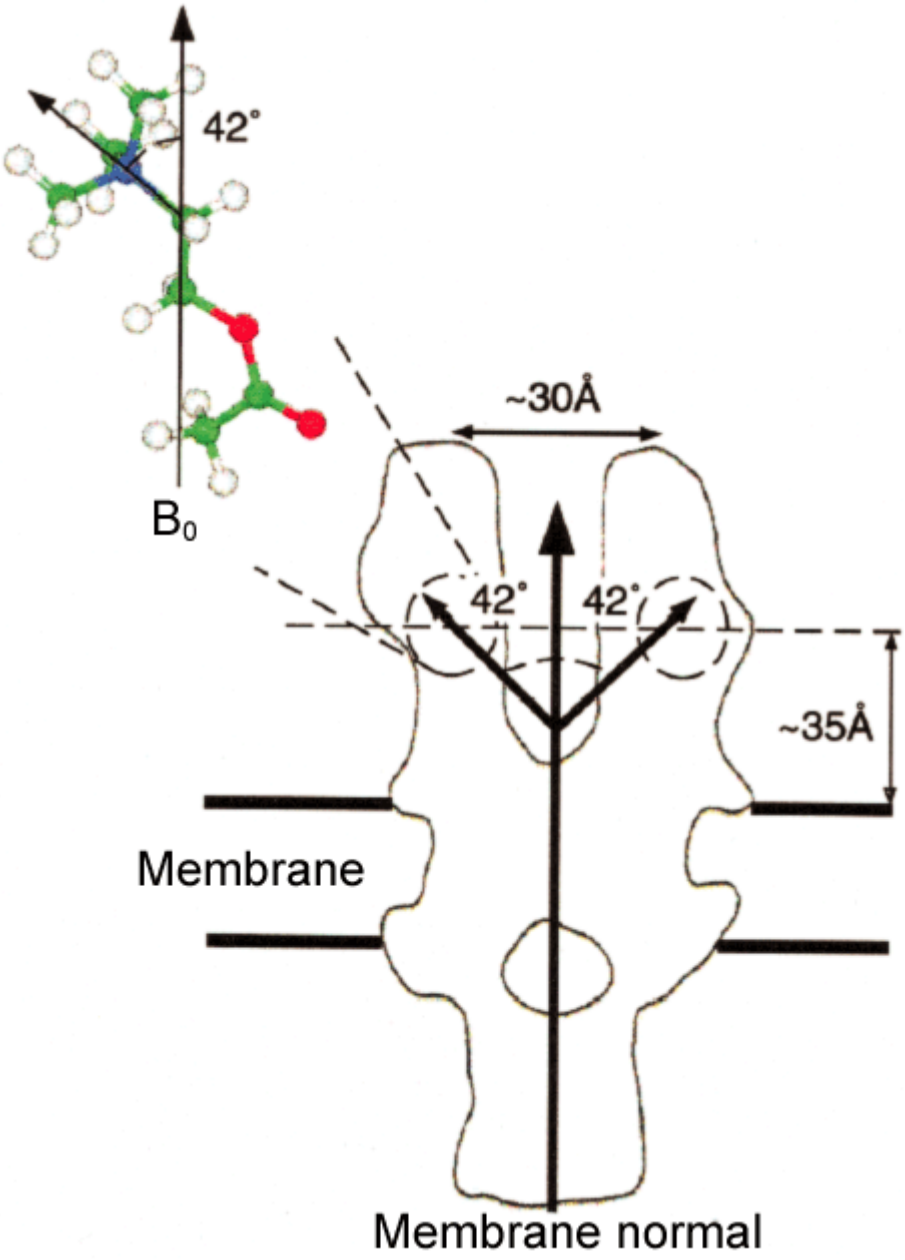

Figure 6-9 Schematic presentation showing the experimentally-determined relative orientation of acetylcholine with respect to the membrane normal in the binding pocket of the nicotinic acetylcholine receptor. The quaternary ammonium group of the ligand is angled at 42° ± 5° from the membrane normal. Only the absolute direction of the bond is undefined by these data [208] and the ligand may equally lie with headgroup pointing towards the core of the protein. Figure adapted from [219].

Conclusions

This study demonstrates that studies of macroscopically oriented membrane systems provide an elegant way of determining the orientation of a ligand at its binding site in a membrane protein. Orientation of model lipid bilayer systems has become routine when containing small peptides [220, 221] but the macroscopic orientation of large membrane proteins has proven to be more troublesome. Application of isopotential spin-dry ultracentrifugation is capable of preserving biological integrity and producing well-aligned samples for larger membrane proteins [210]. Exploiting the chemical shift anisotropy of the ^{31}P nucleus and the axially symmetric rotation of the bilayer phospholipids, it is possible to determine quickly the quality of the macroscopic alignment. The orientational dependence of a motionally-restricted ^{2}H may be coupled to this exercise in membrane alignment and the anisotropy present in the deuterium spectrum can be employed to determine the angle formed by the averaged bond vector. Here, native membranes enriched with the 290 kDa integral membrane protein, the nicotinic acetylcholine receptor, have been successfully oriented and the homogeneity of alignment has been verified by static ^{31}P NMR. Deuterium analysis of the powder membrane sample, labelled with the acetylcholine agonist analogue bromoacetylcholine-d_9 bromide, showed that under physiological conditions there was sufficient mobility in the system to average entirely the anisotropy present in the deuterium spectrum. This apparent motional freedom probably arises from molecular rearrangements and migration in the acetylcholine receptor and also motions propagated by the protein backbone on

the timescale of the NMR experiment (10^{-6} s). When the deuterium-labelled membranes are observed at temperatures where overall reorientation is suppressed, the spectral lineshapes indicate that the d_9-ligand experiences a restricted range of motions. Comparison of the membrane spectra with those of the crystalline ligands at comparable temperatures suggests that the ligand experiences sufficient immobilisation that the rotational averaging about the C_3 and $C_{3'}$ axes is hindered. The NMR data supports structure-activity experiment and the available structural information for the binding site that the ligand binding pocket has a high degree of complimentarity for the acetylcholine molecule and thus the quaternary ammonium group. In the absence of high-resolution structures for either the ligand or its binding pocket, it is not possible to attribute motional restriction exclusively to either conformational self-association or high-affinity interaction with proximal residues in the protein.

Macroscopic orientation of the AChR-BrAChR-d_9 complexed sample has permitted the orientation of the choline quaternary ammonium group to be fixed as 42˚ ± 5˚ with respect to the membrane normal at both agonist binding sites in the protein thus imposing constraints on a model of the molecule in its receptor. From this study and other recent investigations of G-protein coupled receptor proteins [217] and the erythrocyte anion exchange protein band 3 [222] it is clear that orientation of large membrane proteins is both possible and valuable in defining structural constraints for ligands of proteins for which there is little high-resolution structural information. This method has not been attempted with the gastric H/K-ATPase. Future experimental investigation of deuterated substituted imidazo[1,2-*a*]pyridines at their sites of inhibition in the gastric H/K-

ATPase by macroscopic orientation of the membrane sample and by exploitation of the anisotropy of the deuterium spectrum would provide valuable assistance in defining the binding mechanism for this important class of inhibitors. The information obtained would complement the structural limits obtained by the REDOR experiments and form a solid basis for future molecular dynamic simulations of this class of drug in the protein. Thus, modelling the antagonist binding site would be refined by solid state NMR methods and the process of rational drug design for treatment of gastroesophagael reflux disease and gastric ulceration would be propagated by another degree.

Chapter 7

CONCLUSIONS

The results of this thesis paint a coherent picture of the interactions of a class of K^+-competitive, reversible inhibitors, the substituted imidazo[1,2-*a*]pyridines (SIPs) with their target protein, the gastric H/K-ATPase. The work has progressed through several stages. The canvas was set by the synthesis of a variety of SIPs site-specifically labelled with fluorine and other functional groups to explore the binding interaction (Chapter 2). The subject of the painting has been the relationship between structure, functional group substitutions and inhibitory potency. Studies of the dynamics of ^2H isotopically-enriched analogues of SCH28080 (Chapter 3), an extensively studied SIP, when combined with biochemical characterisation of these novel SIP analogues, have provided a sketch upon which to draw a mechanism of SIP binding the enzyme. Solid state REDOR NMR has been successfully employed to add colour to the picture and has provided important structural constraints on the conformations adopted by SIPs in the H/K-ATPase binding site (Chapter 4). The data presented here have been of the first full structure of an inhibitor at its binding site in this pharmacologically important protein. The theme of the painting has been enhanced by a novel study relating site-directed mutagenesis and chemical modification information to the recent high resolution structure of a related P-type ATPase, the sarcoplasmic endoreticular Ca-ATPase [74], and the proposition of models of inhibitor bound in the gastric H/K-ATPase (Chapter 5).

Finally, orientational studies with another membrane protein, the nicotinic acetylcholine receptor, have determined the orientation of an analogue of acetylcholine in the binding pocket of the receptor (Chapter 6). A system has been established by which the unresolved question of the orientation adopted by SCH28080 and its analogues in the H/K-ATPase may be investigated.

Synthesis and Functional Characterisation of Reversible Inhibitors of the Gastric H/K-ATPase

In Chapter 2, a number of novel substituted imidazo[1,2-*a*]pyridines was successfully synthesised and characterised *in vitro*. There has been considerable diversity in the functional groups that have been investigated. SIPs are composed of two components joined by a short flexible linking region. Biochemical characterisation quickly established that the integrity of methylation in the imidazo fused ring system was critical for inhibitory activity. Simple substitution of a methyl group by hydrogen was sufficient to reduce activity dramatically (DMPIP, IC_{50} > 100 μM, c.f. TMPIP, IC_{50} = 2.8 μM). Modifications of the phenylmethoxy functional group were better tolerated. Indeed, disruption of the conjugated π-electron system of aromatic group upon introduction of fluorine into the ring system did little to change the potency of the SIP analogues (TM2FPIP, IC_{50} = 5.0 μM; TM4FPIP, IC_{50} = 2.7 μM). A perfluorinated ring, no longer able to engage in π-cation interactions, was nonetheless active to a similar extent as the fluorine-free system (TMPFPIP, IC_{50} = 8.2 μM). When the system of delocalised electrons was removed entirely from the C8 functional group, and thus the opportunity for π-π interactions between the ring and proximal aromatic

groups was denied, the resultant compound was still active (TMCHP, IC_{50} = 0.11 μM). Introduction of a small, flexible fluorobutyl group at this position produced a compound with no inhibitory potency within the range measured (mM – nM) (TMTFBIP, IC_{50} > mM). Thus, the respective roles of the two components of the SIP structure were sketched out. The imidazo group has a primary importance in ligand binding and stabilisation of the cation within the fused ring system may be the determinant of potency in the first instance. Provided that certain steric constraints were fulfilled, the C8 substitutions might still be active. Biochemical characterisation of the novel SIPs was insufficient to suggest how the protein might interact with the inhibitors and thus elaborate on the binding argument proposed thus far. The sketch has been filled by ^{2}H NMR studies of the SIPs in gastric membrane preparations.

^{2}H Solid State NMR of Inhibitors of the Gastric H/K-ATPase

^{2}H solid state NMR was employed to examine SIPs for two reasons. Firstly, by site-specific deuteration of the compounds in the synthetic route, the dynamics and motional freedoms of both components of the SIP analogues could be investigated. Secondly, the biochemical characterisation, as presented here, did not indicate whether the novel SIPs inhibited the protein in a K^+-competitive manner. *N*-methyl deuteration of the imidazo group of each SIP demonstrated that compounds with good inhibitory activity were subject to motional restraint of the imidazo functionality. The inhibitors demonstrated fast axially-symmetric rotational averaging of the CD_3- group that was apparently devoid of further

averaging by molecular mobility in the binding site. The same motional constraint was true of the perdeuterated phenylmethoxy group in d_7-TMPIP demonstrating that the phenylmethoxy group is granted little latitude for molecular vibration despite the promiscuity of the functional group at this position in permitting inhibitory potency. Furthermore, the ^{2}H NMR studies indicated that, at the temperature examined (268 K), exchange between the free and bound populations could be frozen without freezing the mobility of free ligand and introducing artefacts into the spectral lineshapes generated by the bound inhibitor. It was possible to demonstrate the K^+-competitive nature of the active inhibitors by displacing the ligand from the site of motional constraint upon introduction of K^+ into the sample. Furthermore, it was shown that motional restriction of potent inhibitors was due to interaction with H/K-ATPase and not the gastric lipid component of the membrane. Coupled with the biochemical characterisation of the novel SIPs, ^{2}H NMR has proved to be a powerful method for examining this system and a picture of the binding mechanism of this class of inhibitors is beginning to appear. Quite how the protein influences binding and imposes constraints on the ligand is emerging from the structural information obtained by solid state REDOR NMR.

^{13}C-^{19}F REDOR NMR Studies of the Conformation of Substituted Imidazo[1,2-a]pyridines in H/K-ATPase Enriched Membranes

The structure of TMPFPIP, a fluorophenylmethoxy analogue of TMPIP, was examined by REDOR NMR. In the absence of high-resolution structural information for the binding site of the protein to guide the design of inhibitors of the protein, it is necessary to work from the inside out. REDOR NMR permits the structural information to be obtained from compounds that have been site-specifically enriched to contain NMR-sensitive nuclei. In this study, the uses of fluorine have been several-fold. First, the favourable implications of the large ^{19}F gyromagnetic ratio have permitted intramolecular distances to be measured that might otherwise have been unfeasible using other methods (Chapter 4). Second, the small size of ^{19}F has permitted the atomic substitution to be relatively non-perturbing. Third, the 100% natural abundance of the NMR-sensitive isotope of fluorine has meant that enrichment of SIPs for this study has been considerably less expensive than if a ^{13}C-benzyl species had been used. REDOR NMR of GI gastric membrane preparations labelled with *N*-$^{13}CH_3$-^{19}F substituted TMPFPIP has provided the first complete structure for an inhibitor in the gastric H/K-ATPase without prior knowledge of the structure of the binding site in the enzyme. Indeed, it is the paucity of structural insight into the H/K-ATPase that has prompted a reassessment of the transmembrane topology of the H/K-ATPase and the generation of models of the newly-defined inhibitor in a putative binding site in the protein.

A Model of TMPFPIP at its Binding Site in the Gastric H/K-ATPase

The recent high-resolution structure of the sarcoplasmic endoreticular Ca-ATPase [74], a P-ATPase related to the gastric H/K-ATPase, has defined the boundaries of the transmembrane domain for the Ca-ATPase. Regions of sequence identity with the Ca-ATPase were identified in the H/K-ATPase and threaded onto the transmembrane backbone provided by the new structure. In this way, an original sequence alignment was generated and the spatial distribution of sites in the H/K-ATPase that had been identified as important for ligand binding was estimated. This hybrid of site-directed mutagenesis information, chemical modification analysis and structural detail formed the framework for proposing a binding site for the newly-defined SCH28080 analogue, TMPFPIP. In the course of the study, it was found that, although there is little gross sequence identity between the two proteins, within the transmembrane region there was sufficient alignment to redefine the boundaries of the transmembrane domain in the H/K-ATPase. Having suggested the relative positions of binding sites, two models were proposed, each fulfilling many of the criteria demanded by the mutagenesis studies and the modification analysis. By adopting a bowed conformation identified by REDOR NMR the SIP could plug the interhelical spaces between M1, M2, M3, M4 and M6 in such a way that might prevent conformational change in the protein and further K^+-translocation. Although illuminating, it is apparent that much greater structural detail is required for the H/K-ATPase before the validity of these models can be considered anything other than working hypotheses. The models may be refined in the meantime by defining the

orientation of the ligand in the binding site. To this end, another membrane protein, the nicotinic acetylcholine receptor, has been used to develop the methodology for reliable macroscopic orientation of native membrane samples for ^{2}H orientational studies. Having thus far painted a picture of substituted imidazo[1,2-*a*]pyridine binding in the gastric H/K-ATPase, it has been necessary to exploit another membrane system for which there is better-defined structural information.

Dynamic and Structural Information from Macroscopic Orientation of Native Membrane Samples

From the work in Chapter 5 it was apparent that further structural information was required about the gastric H/K-ATPase in order to define fully the substituted imidazo[1,2-*a*]pyridine inhibitor binding site. To this end, orientational information, coupled with the structure of the inhibitor, would be valuable in describing the binding site to a greater degree of accuracy. Orientational information may be obtained by exploiting the anisotropy of a motionally-restricted ^{2}H nucleus. In Chapter 3 it was established that the ligand is motionally restricted in the protein, suggesting that this system would be an ideal candidate for future orientational studies. There is to date little medium- or high-resolution information available for the gastric H/K-ATPase and because of this shortcoming, the nicotinic acetylcholine receptor, for which there is structural information to 4.6 Å [198] was chosen to refine a system for macroscopic orientation of native membrane samples and to determine the orientation of one of its ligands in the ligand binding pocket. The ^{31}P spectrum of

the oriented lipids membrane is sensitive to the quality of macroscopic orientation. This feature was exploited to determine the success of the isopotential centrifugation and partial rehydration protocol for orientation. Having established that acetylcholine receptor membranes could be oriented successfully, the behaviour of the acetylcholine analogue, bromoacetylcholine bromide-d_9, at different temperatures was examined in the crystalline form and in a powder sample of acetylcholine-enriched membranes. It was found that the analogue, when covalently bound to the receptor, was motionally restricted to a greater degree at low temperatures than when in the crystalline form. This observation suggested that the analogue is tightly constrained at the binding site but the mechanism could not be attributed exclusively to direct interaction with neighbouring residues in the protein or to steric constraints imposed by a conformation adopted by the ligand in the binding pocket. Upon macroscopic orientation of the membrane sample, it was possible to calculate the orientation of the deuterium-labelled quaternary ammonium headgroup in the acetylcholine analogue (42˚) with respect to the membrane normal. As a result, orientation of the ligand could be related to the known structure of the binding site and it was found that there was a good correlation between the two sources of information. Having established the applicability of orientation of large membrane proteins in this study, experimental investigation of deuterated substituted imidazo[1,2-*a*]pyridines at their sites of inhibition in the gastric H/K-ATPase by macroscopic orientation of the membrane sample and by exploitation of the anisotropy of the deuterium spectrum would provide valuable assistance in defining the binding mechanism for this compounds. Such a study would follow as a natural

progression from the work described in this thesis and, coupled with the synthesis and characterisation of an expanded range of SCH28080 analogues, would advance the iterative process of rational drug design for this important class of inhibitors and provide greater detail in the picture of ligand binding in the gastric H/K-ATPase.

BIBLIOGRAPHY

1. Shipley, G.G., *Recent X-ray Diffraction Srudies of Biological Membranes and Membrane Components*, in *Biological Membranes*. 1973, Academic Press Inc: London. p. 1-89.

2. Danielli, J.F. and D. H., J. Cell. Comp. Physiol., 1935. **5**: p. 495-508.

3. Singer, S.J. and G.L. Nicolson, *The fluid mosaic model of the structure of cell membranes.* Science, 1972. **175(23)**: p. 720-31.

4. Henderson, R. and P.N. Unwin, *Three-dimensional model of purple membrane obtained by electron microscopy.* Nature, 1975. **257**(5521): p. 28-32.

5. Simons, K. and E. Ikonen, *Functional rafts in cell membranes.* Nature, 1997. **387(6633)**: p. 569-72.

6. Luzzati, V., *Biological Membranes*, ed. D. Chapman. 1968, New York: Academic Press. 71-121.

7. Cullis, P.R. and B. de-Kruijff, *The polymorphic phase behaviour of phosphatidylethanolamines of natural and synthetic origin. A ^{31}P NMR study.* Biochim Biophys Acta, 1978. **513(1)**: p. 31-42.

8. Nicholls, D.G. and S.J. Ferguson, *Bioenergetics 2*. 2nd ed. 1992, London: Academic Press. 255.

9. Stryer, L., *Biochemistry*, in *Biochemistry*. 1988, W.H. Freeman & Co.: New York. p. 996.

10. Finean, J.B. and R.H. Michell, *Isolation, composition and general structure of membranes*, in *Membrane Structure*, J.B. Finean and R.H. Michell, Editors. 1981, Elsevier/North-Holland Biomedical Press: Amsterdam. p. 10.

11. Adam, G. and M. Delbruck, *Reduction of dimensionality in biological diffusion processes.* Struct. Chem. Mol. Biol., 1968: p. 198-215.

12. Kholodenko, B.N., J.B. Hoek, and H.V. Westerhoff, *Why cytoplasmic signalling proteins should be recruited to cell membranes.* Trends Cell Biol, 2000. **10(5)**: p. 173-8.

13. Watts, A., et al., *Membrane protein structure determination by solid state NMR.* Nat Prod Rep, 1999. **16(4)**: p. 419-23.

14. Hamm, H.E., *The many faces of G protein signaling.* J-Biol-Chem, 1998. **273**(2): p. 669-72.

15. Nathans, J. and D.S. Hogness, *Isolation, sequence analysis, and intron-exon arrangement of the gene encoding bovine rhodopsin.* Cell, 1983. **34**(3): p. 807-14.

16. Ji, T.H., M. Grossmann, and I. Ji, *G protein-coupled receptors. I. Diversity of receptor-ligand interactions.* J-Biol-Chem, 1998. **273**(28): p. 17299-302.

17. Dean, B., et al., *Changes in protein kinase C and adenylate cyclase in the temporal lobe from subjects with schizophrenia.* J-Neural-Transm, 1997. **104**(11-12): p. 1371-81.

18. Brys, R., et al., *Reconstitution of the human 5-HT(1D) receptor-G-protein coupling: evidence for constitutive activity and multiple receptor conformations.* Mol-Pharmacol, 2000. **57**(6): p. 1132-41.

19. Pronin, A.N., et al., *Synucleins are a novel class of substrates for G protein-coupled receptor kinases.* J-Biol-Chem, 2000. **275**(34): p. 26515-22.

20. Stryer, L., *The molecules of visual excitation.* Sci-Am, 1987. **257**(1): p. 42-50.

21. Gray Keller, M.P., M.S. Biernbaum, and M.D. Bownds, *Transducin activation in electropermeabilized frog rod outer segments is highly amplified, and a portion equivalent to phosphodiesterase remains membrane-bound.* J-Biol-Chem, 1990. **265**(25): p. 15323-32.

22. Ross, E.M., *Signal sorting and amplification through G protein-coupled receptors.* Neuron, 1989. **3**(2): p. 141-52.

23. Talcott, B. and M.S. Moore, *Getting across the nuclear pore complex.* Trends-Cell-Biol, 1999. **9**(8): p. 312-8.

24. Wilton, D.C., *Anionic phospholipids and the regulation of cell functions.* Biochem-Soc-Trans, 1998. **26**(3): p. 378-83.

25. Zachowski, A., *Phospholipids in animal eukaryotic membranes: transverse asymmetry and movement.* Biochem J. 1993 Aug 15; 294 (Pt 1)1 14, 1993.

26. Zwaal, R.F., P. Comfurius, and E.M. Bevers, *Platelet procoagulant activity and microvesicle formation. Its putative role in hemostasis and thrombosis.* Biochim Biophys Acta, 1992. **1180(1)**: p. 1-8.

27. Fadok, V.A., et al., *Exposure of phosphatidylserine on the surface of apoptotic lymphocytes triggers specific recognition and removal by macrophages.* J Immunol, 1992. **148(7)**: p. 2207-16.

28. White, S.H., *Membrane Protein Structure - Experimental Approaches*. Methods in Physiology, ed. T.A.P. Society. 1994: Oxford University Press.

29. Bank, P.D., *Protein Data Bank holdings*. 2001.

30. Bioinformatics, R.C.f.S., *PDB Current Holdings*. 2001.

31. Unwin, P.N. and R. Henderson, *Molecular structure determination by electron microscopy of unstained crystalline specimens.* J-Mol-Biol, 1975. **94**(3): p. 425-40.

32. Kuhlbrandt, W., D.N. Wang, and Y. Fujiyoshi, *Atomic model of plant light-harvesting complex by electron crystallography.* Nature, 1994. **367**(6464): p. 614-21.

33. Garavito, R.M., D. Picot, and P.J. Loll, *Strategies for crystallizing membrane proteins.* J Bioenerg Biomembr, 1996. **28(1)**: p. 13-27.

34. Landau, E.M. and J.P. Rosenbusch, *Lipidic cubic phases: a novel concept for the crystallization of membrane proteins.* Proc Natl Acad Sci U S A, 1996. **93(25)**: p. 14532-5.

35. Caffrey, M., *A lipid's eye view of membrane protein crystallization in mesophases.* Current Opinions in Structural Biology, 2000. **10**(4): p. 486-497.

36. Watts, A., et al., *Structural descriptions of ligands in their binding site of integral membrane proteins at near physiological conditions using solid-state NMR.* Eur-Biophysics-J, 1998. **28**: p. 84-90.

37. Bloom, M. and I.C.P. Smith, *Manifestations of lipid-protein interactions in deuterium NMR*. Progress in Protein-Lipid Interactions, ed. A. Watts and J.H. De Pont. Vol. 1. 1985, Amsterdam: Elsevier.

38. Seigneuret, M., et al., *High-resolution 13C NMR study of the topography and dynamics of methionine residues in detergent-solubilized bacteriorhodopsin.* Biochemistry, 1991. **30(16)**: p. 3885-92.

39. Raleigh, D.P., et al., J. Am. Chem. Soc., 1989. **111**: p. 4502-4503.

40. Raleigh, D.P., M.H. Levitt, and R.G. Griffin, Chem. Phys. Lett., 1988. **146**: p. 71-76.

41. Levitt, M.H., Raleigh, D.P., Creuzet, F., Griffin, R. G., *Theory and simulations of homunclear spin pair systems in rotating solids.* Journal of Chemichal Physics, 1990. **92**: p. 6347-6364.

42. Marshall, G.R., et al., J. Am. Chem. Soc., 1990. **112**: p. 963-6.

43. Guillon, T. and J. Schaefer, Adv. Magn. Reson., 1989. **13**: p. 57-83.

44. Guillon T, S.J., *Rotational-Echo Double-Resonance NMR.* Journal of Magnetic Resonance, 1989. **81**: p. 196-200.

45. Andrew, E.R., et al., Phys. Lett., 1963. **4**: p. 99.

46. Grobner, G., et al., *Observations of light-induced structural changes of retinal within rhodopsin.* Nature, 2000. **405(6788)**: p. 810-3.

47. Middleton, D.A., et al., *REDOR NMR on a hydrophobic peptide in oriented membranes.* J Magn Reson, 2000. **147(2)**: p. 366-70.

48. Ahmed, Z., et al., *A solid-state NMR study of the phospholamban transmembrane domain: local structure and interactions with Ca(2+)-ATPase.* Biochim Biophys Acta, 2000. **1468(1-2)**: p. 187-98.

49. Williamson, P.T.F., Watts, J.A., Addona, G.H. Miller, K.W., Watts, A., *Dynamics and orientation of N+(CD3)3-bromoacetylcholine bound to its binding site on the nicotinic acetylcholine receptor.* PNAS, 2001. **98**: p. 2346-2351.

50. Middleton, D.A., et al., *Structural insights into the binding of cardiac glycosides to the digitalis receptor revealed by solid-state NMR.* Proc Natl Acad Sci U S A, 2000. **97(25)**: p. 13602-7.

51. Middleton D, L.D.C., Peng X, Reid D, Saunders D, *Molecular conformations of the polymorphic forms of cimetidine from 13C solid-state NMR distance and angle measurements.* J. Am. Chem. Soc., 2000. **122**: p. 1161-1170.

52. Ernst, R.R., G. Bodenhausen, and A. Wokaun, *Principles of nuclear magnetic resonance in one and two dimensions.* 1989: Oxford Science Publications.

53. Datta, D., *A Comprehensive Introduction to Membrane Biochemistry*. 1987, Madison: Floral Publishing. 635.

54. Mavromoustakos, T., E. Theodoropoulou, and D.P. Yang, *The use of high-resolution solid-state NMR spectroscopy and differential scanning calorimetry to study interactions of anaesthetic steroids with membrane.* Biochim Biophys Acta, 1997. **1328(1)**: p. 65-73.

55. Therapeutics, A.C.o., *ASHP Therapeutic Guidelines on Antimicrobial*

Prophylaxis in Surgery. American Journal of Health-System Pharmacists, 1999. **56**: p. 1839-88.

56. Kimura, Y., et al., *Phospholamban regulates the Ca2+-ATPase through intramembrane interactions.* J Biol Chem, 1996. **271(36)**: p. 21726-31.

57. AstraZeneca, *Losec Administration*. 1999.

58. AstraZeneca, *AstraZeneca Annual Report.* 2000.

59. Sachs, G., *Acid inhibition and gastroesophageal reflux disease.* Yale-J-Biol-Med, 1999. **72**(2-3): p. 227-9.

60. Sorger, P. 2001.

61. Meyers, R.L. and R.C. Orlando, *In vivo bicarbonate secretion by human esophagus.* Gastroenterology, 1992. **103**(4): p. 1174-8.

62. Schade, C., G. Flemstrom, and L. Holm, *Hydrogen ion concentration in the mucus layer on top of acid-stimulated and -inhibited rat gastric mucosa.* Gastroenterology, 1994. **107**(1): p. 180-8.

63. Romell, B., et al., *Effects of carbachol and gastrin on 14C-aminopyrine accumulated in rabbit gastric glands and cells.* Scand J Gastroenterol, 1993. **28(6)**: p. 545-50.

64. Dajani, E.Z. and M.J. Klamut, *Novel therapeutic approaches to gastric and duodenal ulcers: an update.* Expert Opin Investig Drugs, 2000. **9(7)**: p. 1537-44.

65. (WHO), W.H.O., *The World Health Report 1996, Fighting disease, Fostering Development*. 1996, World Health Organisation: Geneva.

66. Scott, D., et al., *The life and death of Helicobacter pylori.* 1998.

67. Sachs, G., et al., *Gastric H,K-ATPase as therapeutic target.* 1988.

68. Hui, W.M., et al., *Maintenance therapy for duodenal ulcer: a randomized controlled comparison of seven forms of treatment.* Am J Med, 1992. **92(3)**: p. 265-74.

69. Nwokolo, C.U., et al., *Tolerance during 29 days of conventional dosing with cimetidine, nizatidine, famotidine or ranitidine.* Aliment Pharmacol Ther. 1990; 4 Suppl 129 45, 1990.

70. Robert, J.C., et al., *H+/K(+)-ATPase contents of human, rabbit, hog and rat gastric mucosa.* Biochim Biophys Acta, 1990. **1024(1)**: p. 167-72.

71. Silver, R.B. and M. Soleimani, *H+-K+-ATPases: regulation and role in pathophysiological states.* Am-J-Physiol, 1999. **276**(6 Pt 2): p. F799-811.

72. Wolosin, J.M., *Ion transport studies with H+-K+-ATPase-rich vesicles: implications for HCl secretion and parietal cell physiology.* Am J Physiol, 1985. **248(6 Pt 1)**: p. G595-607.

73. Shull, G.E. and J.B. Lingrel, *Molecular cloning of the rat stomach (H+ + K+)-ATPase.* J-Biol-Chem, 1986. **261**(36): p. 16788-91.

74. Toyoshima C, N.M., Nomura H, Ogawa H, *Crystal structure of the calcium pump of sarcoplasmic reticulum at 2.6 A resolution.* Nature, 2000. **405**: p. 647-655.

75. Skriver, E., A.B. Maunsbach, and P.L. Jorgensen, *Formation of two-dimensional crystals in pure membrane-bound Na+,K+-ATPase.* FEBS Lett, 1981. **131(2)**: p. 219-22.

76. Besancon, M., et al., *Membrane topology and omeprazole labeling of the gastric H+,K(+)-adenosinetriphosphatase.* Biochemistry, 1993. **32(9)**: p. 2345-55.

77. Melle Milovanovic, D., et al., *Regions of association between the alpha and the beta subunit of the gastric H,K-ATPase.* J-Biol-Chem, 1998. **273**(18): p. 11075-81.

78. Saccomani, G., et al., *Characterization of gastric mucosal membranes: IX. Fractionation and purification of K+-ATPase-containing vesicles by zonal centrifugation and free-flow electrophoresis technique.* Biochim Biophys Acta, 1977. **465**: p. 311-330.

79. Okamoto, C.T., et al., *Isolation and characterization of gastric microsomal glycoproteins. Evidence for a glycosylated beta-subunit of the H+/K(+)-ATPase.* Biochim Biophys Acta, 1990. **1037(3)**: p. 360-72.

80. Beggah, A.T., et al., *beta-subunit assembly is essential for the correct packing and the stable membrane insertion of the H,K-ATPase alpha-subunit.* J-Biol-Chem, 1999. **274**(12): p. 8217-23.

81. Horisberger, J.D., et al., *The H,K-ATPase beta-subunit can act as a surrogate for the beta-subunit of Na,K-pumps.* J Biol Chem, 1991. **266(29)**: p. 19131-4.

82. Gottardi, C.J. and M.J. Caplan, *Molecular requirements for the cell-surface expression of multisubunit ion-transporting ATPases. Identification of protein domains that participate in Na,K-ATPase and H,K-ATPase subunit assembly.* J Biol Chem, 1993. **268(19)**: p. 14342-7.

83. Shin, J.M. and G. Sachs, *Identification of a region of the H,K-ATPase alpha subunit associated with the beta subunit.* J-Biol-Chem, 1994. **269**(12): p. 8642-6.

84. Xian, Y. and H. Hebert, *Three-dimensional structure of the porcine gastric H,K-ATPase from negatively stained crystals.* J-Struct-Biol, 1997. **118**(3): p. 169-77.

85. Raussens, V., J.M. Ruysschaert, and E. Goormaghtigh, *Fourier transform infrared spectroscopy study of the secondary structure of the gastric H+,K+-ATPase and of its membrane-associated proteolytic peptides.* J-Biol-Chem, 1997. **272**(1): p. 262-70.

86. Lee, J., G. Simpson, and P. Scholes, *An ATPase from dog gastric mucosa: changes of outer pH in suspensions of membrane vesicles accompanying ATP hydrolysis.* Biochem Biophys Res Commun, 1974. **60(2)**: p. 825-32.

87. Helmich-de-Jong, M.L., et al., *Presence of a low-affinity nucleotide binding site on the (K+ + H+)-ATPase phosphoenzyme.* Biochim Biophys Acta, 1986. **860(3)**: p. 641-9.

88. Faller, L.D. and G.A. Elgavish, *Catalysis of oxygen-18 exchange between inorganic phosphate and water by the gastric H,K-ATPase.* Biochemistry, 1984. **23(26)**: p. 6584-90.

89. Walderhaug, M.O., et al., *Structural relatedness of three ion-transport adenosine triphosphatases around their active sites of phosphorylation.* J Biol Chem, 1985. **260(6)**: p. 3852-9.

90. Forte, J.G., T.E. Machen, and K.J. Obrink, *Mechanisms of gastric H+ and Cl- transport.* Annu Rev Physiol. 1980; 42111 26, 1980.

91. Sachs, G., et al., *The pharmacology of the gastric acid pump: the H+,K+ ATPase.* Annu Rev Pharmacol Toxicol. 1995; 35277 305, 1995.

92. Munson, K., et al., *Analysis of the membrane domain of the gastric H(+)/K(+)-ATPase.* J Exp Biol. 2000 Jan; 203 Pt 1161 70, 2000.

93. Esmann, M., *Occlusion of Rb+ by detergent-solubilized (Na+ + K+)-ATPase from shark salt glands.* Biochim Biophys Acta, 1985. **815(2)**: p. 196-202.

94. Vilsen, B. and J.P. Andersen, *Occlusion of Ca2+ in soluble monomeric sarcoplasmic reticulum Ca2+-ATPase.* Biochim Biophys Acta, 1986. **855(3)**: p. 429-31.

95. Rabon, E.C., et al., *Rubidium occlusion within tryptic peptides of the H,K-ATPase.* J Biol Chem, 1993. **268(11)**: p. 8012-8.

96. Rabon, E.C., et al., *Conformational transitions of the H,K-ATPase studied with sodium ions as surrogates for protons.* J Biol Chem, 1990. **265(32)**: p. 19594-9.

97. Pederson P, C.E., *Ion motive ATPases. I. Ubiquity, properties, and significance to cell function.* TIBS, 1987. **12**: p. 146-150.

98. Besancon, M., et al., *Sites of reaction of the gastric H,K-ATPase with extracytoplasmic thiol reagents.* J-Biol-Chem, 1997. **272**(36): p. 22438-46.

99. Kuipers, E.J., et al., *Atrophic gastritis and Helicobacter pylori infection in patients with reflux esophagitis treated with omeprazole or fundoplication.* N Engl J Med, 1996. **334(16)**: p. 1018-22.

100. Beil, W., I. Hackbarth, and K.F. Sewing, *Mechanism of gastric antisecretory effect of SCH 28080.* Br-J-Pharmacol, 1986. **88**(1): p. 19-23.

101. Beil, W., U. Staar, and K.F. Sewing, *SCH 28080 is a more selective inhibitor than SCH 32651 at the K+ site of gastric K+/H+-ATPase.* Eur-J-Pharmacol, 1987. **139**(3): p. 349-52.

102. Long, J.F., et al., *Gastric antisecretory and cytoprotective activities of SCH 28080.* J Pharmacol Exp Ther, 1983. **226(1)**: p. 114-20.

103. Wallmark, B., et al., *Inhibition of gastric H+,K+-ATPase and acid secretion by SCH 28080, a substituted pyridyl(1,2a)imidazole.* J-Biol-Chem, 1987. **262**(5): p. 2077-84.

104. Keeling, D.J., S.M. Laing, and J. Senn-Bilfinger, *SCH 28080 is a lumenally acting, K+-site inhibitor of the gastric (H+ + K+)-ATPase.* Biochem Pharmacol, 1988. **37(11)**: p. 2231-6.

105. Munson, K.B. and G. Sachs, *Inactivation of H+,K+-ATPase by a K+-competitive photoaffinity inhibitor.* Biochemistry, 1988. **27(11)**: p. 3932-8.

106. Munson, K.B., et al., *Identification of an extracytoplasmic region of H+,K(+)-ATPase labeled by a K(+)-competitive photoaffinity inhibitor.* J-Biol-Chem, 1991. **266**(28): p. 18976-88.

107. Asano, S., et al., *Mutational analysis of putative SCH 28080 binding sites of the gastric H+,K+-ATPase.* J Biol Chem, 1997. **272(28)**: p. 17668-74.

108. Asano, S., et al., *Mutational analysis of putative SCH 28080 binding sites of the gastric H+,K+-ATPase.* J-Biol-Chem, 1997. **272**(28): p. 17668-74.

109. Swarts, H.G., et al., *Role of negatively charged residues in the fifth and sixth transmembrane domains of the catalytic subunit of gastric H+,K+-ATPase.* J-Biol-Chem, 1996. **271**(47): p. 29764-72.

110. Gatto, C., et al., *Stabilization of the H,K-ATPase M5M6 membrane hairpin by K+ ions. Mechanistic significance for p2-type atpases.* J-Biol-Chem, 1999. **274**(20): p. 13737-40.

111. Swarts, H.P., C.H. Klaassen, and J.J. De Pont, *Involvement of glutamic acid 820 in K+ and SCH 28080 binding to gastric H+,K(+)-ATPase.* 1997.

112. Munson, K.B., N. Lambrecht, and G. Sachs, *Effects of mutations in M4 of the gastric H+,K+-ATPase on inhibition kinetics of SCH28080.* Biochemistry, 2000. **39**(11): p. 2997-3004.

113. Brimblecombe, R.W., et al., *Proceedings: The pharmacology of cimetidine, a new histamine H2-receptor antagonist.* Br J Pharmacol, 1975. **53(3)**: p. 435-36.

114. Fennerty, M.B., et al., *The diagnosis and treatment of gastroesophageal reflux disease in a managed care environment, Suggested disease management guidelines.* Arch Intern Med, 1996. **156(5)**: p. 477-84.

115. DeVault, K.R. and D.O. Castell, *Updated guidelines for the diagnosis and treatment of gastroesophageal reflux disease. The Practice Parameters Committee of the American College of Gastroenterology.* Am J Gastroenterol, 1999. **94(6)**: p. 1434-42.

116. Marks, R.D., et al., *Omeprazole versus H2-receptor antagonists in treating patients with peptic stricture and esophagitis.* Gastroenterology, 1994. **106(4)**: p. 907-15.

117. Robinson, M., et al., *Omeprazole is superior to ranitidine plus metoclopramide in the short-term treatment of erosive oesophagitis.* Aliment Pharmacol Ther, 1993. **7(1)**: p. 67-73.

118. Jansen, J.B., et al., *Effect of long-term treatment with omeprazole on serum gastrin and serum group A and C pepsinogens in patients with reflux esophagitis.* Gastroenterology, 1990. **99(3)**: p. 621-8.

119. Hersey, S.J., et al., *SCH28080 prevents omeprazole inhibition of the gastric H+/K+-ATPase.* Biochim-Biophys-Acta, 1988. **956**(1): p. 49-57.

120. Laemmli, U.K., *Cleavage of structural proteins during the assembly of the head of bacteriophage T4.* Nature, 1970. **227(259)**: p. 680-5.

121. Lowry, O.H., et al., *Protein measurement with the Folin-Phenol reagents.* J. Biol. Chem., 1951. **193**: p. 265-275.

122. LeBel, D., G.G. Poirier, and A.R. Beaudoin, *A convenient method for the ATPase assay.* Anal-Biochem, 1978. **85**(1): p. 86-9.

123. del-Valle, J.C., et al., *Impairment of H+-K+-ATPase-dependent proton transport and inhibition of gastric acid secretion by ethanol.* Am J Physiol Gastrointest Liver Physiol, 2001. **280(6)**: p. G1331-40.

124. Kaminski, J.J., et al., *Antiulcer agents. 1. Gastric antisecretory and cytoprotective properties of substituted imidazo[1,2-a]pyridines.* J-Med-Chem, 1985. **28**(7): p. 876-92.

125. Kaminski, J.J., et al., *Antiulcer agents. 2. Gastric antisecretory, cytoprotective, and metabolic properties of substituted imidazo[1,2-a]pyridines and analogues.* J-Med-Chem, 1987. **30**(11): p. 2031-46.

126. Kaminski, J.J. and A.M. Doweyko, *Antiulcer agents. 6. Analysis of the in vitro biochemical and in vivo gastric antisecretory activity of substituted imidazo[1,2-a]pyridines and related analogues using comparative molecular field analysis and hypothetical active site lattice methodologies.* J-Med-Chem, 1997. **40**(4): p. 427-36.

127. Briving, C., et al., *Inhibition of gastric H+/K+-ATPase by substituted imidazo[1,2-a]pyridines.* Biochim-Biophys-Acta, 1988. **946**(2): p. 185-92.

128. Hall, K., et al., *Location of the carbohydrates present in the HK-ATPase vesicles isolated from hog gastric mucosa.* Biochemistry, 1990. **29**(3): p. 701-6.

129. Saccomani G, S.H., Shaw D, Lewin M, Sachs G, *Characterisation of gastric mucosal membranes. IX Fractionation and purification of K+-ATPase-containing vesicles by zonal centrifugation and free-flow electrophoresis technique.* Biochimica et Biophysica Acta, 1977. **465**: p. 311-330.

130. Middleton, D.A., et al., *The conformation of an inhibitor bound to the gastric proton pump.* FEBS-Lett, 1997. **410**(2-3): p. 269-74.

131. Kumpf, R.A. and D.A. Dougherty, *A mechanism for ion selectivity in potassium channels: computational studies of cation-pi interactions.* Science, 1993. **261(5129)**: p. 1708-10.

132. Raine, A.R., et al., *Protein recognition of ammonium cations using side-chain aromatics: a structural variation for secondary ammonium ligands.* Protein Sci, 1995. **4(12)**: p. 2625-8.

133. Gasteiger, J. and M. Marsili, Tetrahedron, 1980. **36**: p. 3129-3228.

134. Ngola, S.M. and D.A. Dougherty, *Concerning the Effects of Aromatic Ring Fluorination on the Cation-π Interaction and Other Molecular Recognition Phenomena in Aqueous Media.* Journal of Organic Chemistry, 1998. **63**: p. 4566-4567.

135. Nowak, M.W., et al., *Nicotinic receptor binding site probed with unnatural amino acid incorporation in intact cells.* Science, 1995. **268(5209)**: p. 439-42.

136. Oldfield, E. *Recent advances in the study of bacteriorhodopsin dynamic structure using high field solid state NMR spectroscopy* Methods in Enzymology, 1982. **88**: p. 310-25

137. Seelig, J., in *Molecular Biology: Spin Labeling Theory and Applications*. 1976, Academic Press: New York. p. 373-410.

138. Seelig, J., *Deuterium magnetic resonance: theory and application to lipid membranes.* Q Rev Biophys, 1977. **10(3)**: p. 353-418.

139. Bloom, M. and I.C.P. Smith, *Manifestations of lipid-protein interactions in deuterium NMR*, in *Progress in Protein-Lipid Interactions*, A. Watts and D. Pont, Editors. 1985, Elsevier Science Publishers B.V. p. 61-88.

140. Bienvenue, A., et al., *Evidence for protein-associated lipids from deuterium nuclear magnetic resonance studies of rhodopsin-dimyristoylphosphatidylcholine recombinants.* J Biol Chem, 1982. **257(6)**: p. 3032-8.

141. Davis, J.H., *Deuterium magnetic resonance and relaxation in partially ordered systems.* Adv. Magn. Reson., 1989. **13**: p. 195-223.

142. Sixl, F. and A. Watts, *Deuterium and phosphorus nuclear magnetic resonance studies on the binding of polymyxin B to lipid bilayer-water interfaces.* Biochemistry, 1985. **24(27)**: p. 7906-10.

143. Ryba, N.J., C.E. Dempsey, and A. Watts, *Protein-lipid interactions at membrane surfaces: a deuterium and phosphorus nuclear magnetic resonance study of the interaction between bovine rhodopsin and the bilayer*

head groups of dimyristoylphosphatidylcholine. Biochemistry, 1986. **25(17)**: p. 4818-25.

144. Watts, A. and T.W. Poile, *Direct determination by 2H-NMR of the ionization state of phospholipids and of a local anaesthetic at the membrane surface.* Biochim Biophys Acta, 1986. **861(2)**: p. 368-72.

145. Van-Gorkom, L.C., et al., *Identification of trapped and boundary lipid binding sites in M13 coat protein/lipid complexes by deuterium NMR spectroscopy.* Biochemistry, 1990. **29(16)**: p. 3828-34.

146. Spooner, P.J. and A. Watts, *Reversible unfolding of cytochrome c upon interaction with cardiolipin bilayers. 1. Evidence from deuterium NMR measurements.* Biochemistry, 1991. **30(16)**: p. 3871-9.

147. Zhang, H. and R.G. Bryant, *Nuclear magnetic resonance spectra for l > 1 spins in dynamically heterogeneous systems with chemical exchange among environments.* Biophys J, 1995. **68(6)**: p. 2556-65.

148. Zhang, H. and R.G. Bryant, *Characterization of enzyme-bound ligand dynamics by solid-state NMR in the presence of ligand exchange: L-phenylalanine on carboxypeptidase A.* Biophys J, 1995. **68(1)**: p. 303-11.

149. Zhang, H. and R.G. Bryant, *Bound ligand motion in crystalline carboxypeptidase A.* Biophys J, 1997. **72(1)**: p. 363-72.

150. Evans, J.N.S., *Biomolecular NMR Spectroscopy*. 1995, Oxford: Oxford University Press.

151. Ulrich, A.S. and S.L. Grage, *2H NMR*, in *Solid State NMR of Polymers*, I. Ando and T. Asakura, Editors. 1998, Elsevier Science. p. 190-211.

152. Brouwer, E.B., et al., *Weak intermolecular interactinos and molecular recognition: structure and dynamics of the benzene and pyridine p-tert-butylcalix[4]arene inclusions.* J Physical Chemistry B, 1999. **103**: p. 10604-10616.

153. Mendlein, J. and G. Sachs, *Interaction of a K(+)-competitive inhibitor, a substituted imidazo[1,2a] pyridine, with the phospho- and dephosphoenzyme forms of H+, K(+)-ATPase.* J Biol Chem, 1990. **265(9)**: p. 5030-6.

154. Keeling, D.J., A.G. Taylor, and C. Schudt, *The binding of a K+ competitive ligand, 2-methyl,8-(phenylmethoxy)imidazo(1,2-a)pyridine 3-acetonitrile, to the gastric (H+ + K+)-ATPase.* J-Biol-Chem, 1989. **264**(10): p. 5545-51.

155. Penner, G.H., B. Zhao, and K.R. Jeffrey, *Molecular dynamics in the solid trimethylamine-borane complex: a deuterium NMR study.* Z. Naturforsch, 1994. **50a**: p. 81-89.

156. Ratcliffe, C.I. and J.A. Ripmeester, *2H nucelar magnetic resonance studies of motions in tetramethylammonium salts: the question of methyl reorientation.* Canadian Journal of Chemistry, 1986. **64**: p. 1348-1354.

157. Torchia, D.A., *Solid state NMR studies of protein internal dynamics.* Annual Review of Biophysics and Bioengineering, 1984. **13**: p. 125-144.

158. Takahashi, H., et al., *CH/Pi interactions as demonstrated in the crystal structure of host/guest compounds. A database study.* Tetrahedron, 2000. **56**: p. 6185-6191.

159. McMurry, J., *Organic Chemistry*. 3rd ed. 1992, Pacific Grove, CA: Brooks/Cole Publishing.

160. Cowan, S.W., et al., *Crystal structures explain functional properties of two E. coli porins.* Nature, 1992. **358(6389)**: p. 727-33.

161. McDermott G., et al., *Crystal structure of an integral membrane light-harvesting complex from photosynthetic bacteria.* Nature, 1995. **374**(6522): p. 517-512.

162. Peerson O, S.S., *Rotational resonance NMR of biological membranes.* Concepts in Magnetic Resonance, 1993. **5**: p. 303-317.

163. Spooner, P.J., et al., *Structural information on a membrane transport protein from nuclear magnetic resonance spectroscopy using sequence-selective nitroxide labeling.* Biochemistry, 1999. **38(30)**: p. 9634-9.

164. Klug, C.A., et al., *Closed form of liganded glutamine-binding protein by rotational-echo double-resonance NMR.* Biochemistry, 1997. **36**(31): p. 9405-8.

165. Wang, J., Y.S. Balazs, and L.K. Thompson, *Solid-state REDOR NMR distance measurements at the ligand site of a bacterial chemotaxis membrane receptor.* Biochemistry, 1997. **36**(7): p. 1699-703.

166. Watts, A., *NMR of drugs and ligands bound to membrane receptors.* Curr Opin Biotechnol, 1999. **10(1)**: p. 48-53.

167. Guillon, T., *Introduction to Rotational-Echo, Double-Resonance NMR.* Concepts in Magnetic Resonance, 1998. **10**(5): p. 277-289.

168. Bennett A, R.C., Auger M, Lakshmi K, Griffin R, *Heteronuclear decoupling in rotating solids.* J. Chem. Phys., 1995. **103**(16): p. 6951-6958.

169. Mattingly, S., *Introduction*. 2001.

170. Hore, P.J., *Nuclear Magnetic Resonance*. Oxford Chemistry Primers. Vol. 32. 1995, Oxford: Oxford University Press. 90.

171. Pan, Y., Guillon, T., Schaefer, J., *Determination of C-N internuclear distances by rotational-echo double resonance NMR of solids.* Journal of Magnetic Resonance, 1990. **90**: p. 330-340.

172. Goetz, J.M. and J. Schaefer, *Orientational information in solids from REDOR sidebands.* J-Magn-Reson, 1997. **129**(2): p. 222-3.

173. Goetz, J. and B. Poliks, Studelska, D., Fischer, M., Kugelbrey, K., Bacher, A., Cushman, M., Schaefer, J., *Investigation of the binding of fluoroluminazes to the 1-MDa capsid of luminaze synthase by 15N{19F} REDOR NMR.* J. Am. Chem. Soc., 1999. **121**: p. 7500-7508.

174. Goetz, J.M. and J. Schaefer, *REDOR dephasing by multiple spins in the presence of molecular motion.* J Magn Reson, 1997. **127(2)**: p. 147-54.

175. Espe, M.S., B.R. Mattes, and J. Schaefer, Macromolecules, 1997. **30**: p. 6307-6312.

176. Bamberg, K. and G. Sachs, *Topological analysis of H+,K(+)-ATPase using in vitro translation.* J Biol Chem, 1994. **269(24)**: p. 16909-19.

177. Rabon, E.C., M. Hoggatt, and K. Smillie, *Transmembrane carboxyl residues are essential for cation-dependent function in the gastric H,K-ATPase.* J-Biol-Chem, 1996. **271**(50): p. 32137-46.

178. Asano, S., et al., *Functional expression of gastric H+,K(+)-ATPase and site-directed mutagenesis of the putative cation binding site and catalytic center.* J-Biol-Chem, 1996. **271**(5): p. 2740-5.

179. Swarts, H.G., et al., *Conformation-dependent inhibition of gastric H+,K+-ATPase by SCH 28080 demonstrated by mutagenesis of glutamic acid 820.* Mol-Pharmacol, 1999. **55**(3): p. 541-7.

180. Rulli, S.J., et al., *Glu-857 moderates K+-dependent stimulation and SCH 28080-dependent inhibition of the gastric H,K-ATPase.* J-Biol-Chem, 1999. **274**(21): p. 15245-50.

181. Asano, S., et al., *A chimeric gastric H+,K+-ATPase inhibitable with both ouabain and SCH 28080.* J-Biol-Chem, 1999. **274**(11): p. 6848-54.

182. Munson, K.B., N. Lambrecht, and G. Sachs, *Effects of mutations in M4 of the gastric H+,K+-ATPase on inhibition kinetics of SCH28080.* Biochemistry, 2000. **39(11)**: p. 2997-3004.

183. Auer, M., G.A. Scarborough, and W. Kuhlbrandt, *Three-dimensional map of the plasma membrane H+-ATPase in the open conformation.* Nature, 1998. **392(6678)**: p. 840-3.

184. Zhang, P., et al., *Structure of the calcium pump from sarcoplasmic reticulum at 8-A resolution.* Nature, 1998. **392(6678)**: p. 835-9.

185. Xiaoquin, H. and W. Miller, *A Time-Efficient, Linear-Space Local Similarity Algorithm.* Advances in Applied Mathematics, 1991. **12**: p. 337-357.

186. Lambrecht, N., et al., *Comparison of covalent with reversible inhibitor binding sites of the gastric H,K-ATPase by site-directed mutagenesis.* J-Biol-Chem, 2000. **275**(6): p. 4041-8.

187. Swarts, H.P., C.H. Klaassen, and J.J. De-Pont, *Involvement of glutamic acid 820 in K+ and SCH 28080 binding to gastric H+,K(+)-ATPase.* Ann N Y Acad Sci. 1997 Nov 3; 834472 4, 1997.

188. Hasler, U., et al., *Role of beta-subunit domains in the assembly, stable expression, intracellular routing, and functional properties of Na,K-ATPase.* J Biol Chem, 1998. **273(46)**: p. 30826-35.

189. Lingrel, J.B., et al., *Cation and cardiac glycoside binding sites of the Na,K-ATPase.* Ann N Y Acad Sci., 1997. **834**: p. 194-206.

190. RCSB, *Research Collaboratory for Structural Bioinformatics*. 2001, RCSB.

191. Stokes, D.L., et al., *Comparison of H+-ATPase and Ca2+-ATPase suggests that a large conformational change initiates P-type ion pump reaction cycles.* Curr Biol, 1999. **9(13)**: p. 672-9.

192. Maeda, M., J. Ishizaki, and M. Futai, *cDNA cloning and sequence determination of pig gastric (H+ + K+)-ATPase.* Biochem-Biophys-Res-Commun, 1988. **157**(1): p. 203-9.

193. Khan, I. and A.K. Grover, *Cloning of internal Ca pump from rabbit stomach smooth muscle.* Nucleic Acids Res, 1990. **18(13)**: p. 4026.

194. Melle-Milovanovic, D., et al., *Structural aspects of the gastric H,K ATPase: the M5/M6 domain and alpha beta association.* Acta Physiol Scand Suppl., 1998. **643**: p. 147-162.

195. Lutsenko, S., R. Anderko, and J.H. Kaplan, *Membrane disposition of the M5-M6 hairpin of Na+,K(+)-ATPase alpha subunit is ligand dependent.* Proc Natl Acad Sci U S A, 1995. **92(17)**: p. 7936-40.

196. Morrison, C. and M. Bloom, *Orientation dependence of 2H nuclear magentic resonance spin lattice relaxaton on phospholipid and phospholipid cholesterol systems.* Journal of Chemical Physics, 1994. **101**: p. 1348-1354.

197. Opella, S.J., *NMR and membrane proteins.* Nat Struct Biol. 1997, 1997. **4**(Suppl): p. 845-8.

198. Miyazawa, A., et al., *Nicotinic acetylcholine receptor at 4.6 A resolution: transverse tunnels in the channel wall.* J Mol Biol, 1999. **288(4)**: p. 765-86.

199. Stroud, R.M., M.P. McCarthy, and M. Shuster, *Nicotinic acetylcholine receptor superfamily of ligand-gated ion channels.* Biochemistry, 1990. **29(50)**: p. 11009-23.

200. Changeux, J.P., A. Devillers-Thiery, and P. Chemouilli, *Acetylcholine receptor: an allosteric protein.* Science, 1984. **225(4668)**: p. 1335-45.

201. Galzi, J.L., et al., *Functional architecture of the nicotinic acetylcholine receptor: from electric organ to brain.* Annu Rev Pharmacol Toxicol., 1991. **31**: p. 37-72.

202. Galzi, J.L., et al., *Mutations in the channel domain of a neuronal nicotinic receptor convert ion selectivity from cationic to anionic.* Nature, 1992. **359(6395)**: p. 500-5.

203. Kao, P.N. and A. Karlin, *Acetylcholine receptor binding site contains a disulfide cross-link between adjacent half-cystinyl residues.* J Biol Chem, 1986. **261(18)**: p. 8085-8.

204. Dougherty, D.A. and D.A. Stauffer, *Acetylcholine binding by a synthetic receptor: implications for biological recognition.* Science, 1990. **250(4987)**: p. 1558-60.

205. Keniry, M.A., *Solid-state deuterium nuclear magnetic resonance spectroscopy of proteins.* Methods Enzymol. 1989; 176376 86, 1989.

206. Penner, G.H., et al., Canadian Journal of Chemistry, 1992. **71**: p. 417-426.

207. Damle, V.N., M. McLaughlin, and A. Karlin, *Bromoacetylcholine as an affinity label of the acetylcholine receptor from Torpedo californica.* Biochem Biophys Res Commun, 1978. **84(4)**: p. 845-51.

208. Ulrich, A.S. and A. Watts, *2H NMR lineshapes of immobilized uniaxially oriented membrane proteins.* Solid State Nuclear Magnetic Resonance, 1993. **2**: p. 21-36.

209. Seelig, J., *31P nuclear magnetic resonance and the head group structure of phospholipids in membranes.* Biochim-Biophys-Acta, 1978. **515**(2): p. 105-40.

210. Grobner, G., et al., *Macroscopic orientation of natural and model membranes for structural studies.* Anal Biochem, 1997. **254(1)**: p. 132-8.

211. Williamson, P.T.F., *The application of solid state nuclear magentic resonance to the study of ligand protein interactions*, in *Board of the Faculty of Biological Sciences*. 1999, University of Oxford: Oxford.

212. Chiou, C.Y. and B.V. Sastry, *Acetylcholinesterase hydrolysis of halogen substituted acetylcholines.* Biochem Pharmacol, 1968. **17(5)**: p. 805-15.

213. Braswell, L.M., K.W. Miller, and J.F. Sauter, *Pressure reversal of the action of octanol on postsynaptic membranes from Torpedo.* Br J Pharmacol, 1984. **83(1)**: p. 305-11.

214. Schmidt-Rohr, K. and H.W. Spiess, *Multidimensional solid-state NMR and polymers*. 3rd ed. 1999, London: Academic Press Limited. 478.

215. Michelson, M.J. and E.V. Zeimal, *Acetylcholine: An approach to molecular mechanism and action*. 1973, Oxford: Pergamon.

216. Barrantes, F.J., *The lipid environment of the nicotinic acetylcholine receptor in native and reconstituted membranes.* Crit Rev Biochem Mol Biol, 1989. **24(5)**: p. 437-78.

217. Grobner, G., et al., *Photoreceptor rhodopsin: structural and conformational study of its chromophore 11-cis retinal in oriented membranes by deuterium solid state NMR.* FEBS Lett, 1998. **422(2)**: p. 201-4.

218. Unwin, N., *The nicotinic acetylcholine receptor of the Torpedo electric ray.* J Struct Biol, 1998. **121(2)**: p. 181-90.

219. Williamson, P.T., et al., *Dynamics and orientation of N+(CD3)3-bromoacetylcholine bound to its binding site on the nicotinic acetylcholine receptor.* Proc Natl Acad Sci U S A, 2001. **98(5)**: p. 2346-51.

220. Bechinger, B., M. Zasloff, and S.J. Opella, *Structure and orientation of the antibiotic peptide magainin in membranes by solid-state nuclear magnetic resonance spectroscopy.* Protein Sci, 1993. **2(12)**: p. 2077-84.

221. Cross, T.A. and S.J. Opella, Current Opinions in Structural Biology, 1994. **4**: p. 574-581.

222. Taylor, A.M., et al., *Binding properties of the stilbene disulfonate sites on human erythrocyte AE1: kinetic, thermodynamic, and solid state deuterium NMR analyses.* Biochemistry, 1999. **38(34)**: p. 11172-9.

223. Li, Y. et al., *Conformation of Microtubule-Bound Paclitaxel Determined by Fluorescence Spectroscopy and REDOR NMR*. Biochemistry, 2000. **39**: p. 281-91.

224. Jaroniec, C.P. et al., *Measurment of ^{13}C-^{15}N distances in uniformly ^{13}C labelled biomolecules: J-decoupled REDOR* J. Am. Chem. Soc. 1999. **121**: p. 10237-8

225. Hirsh, D.J. et al., *A new monofluorinated phosphatidylcholine forms interdigitated bilayers.* Biophysical J. 1998. **75**: 1858-68

226. Slichter, C. P. *Principles of Magnetic Resonance* 1990. New York (Springer-Verlag).

227. Keniry, M. A., et al., *NMR studies of amino-acids and proteins. Deuterium NMR relaxation of deuteriomethyl-labelled amino-acids in crystals and in Halobacterium halobium and Escherichia coli cell membranes.* Biochemistry, 1984, **23**, 288-298.

228. Copie V., et al., *Deuterium solid state NMR studies of methyl group dynamics in bacteriorhodopsin and retinal model compounds: Evidence for a 6-s-trans chromophore in the protein*. Biochemistry, 1994. **33**: p. 3280-6.